# Molecular Beam Epitaxy Growth of Topological Materials

INAUGURAL-DISSERTATION

zur

Erlangung des Doktorgrades

der Mathematisch-Naturwissenschaftlichen Fakultät

der Universität zu Köln

vorgelegt von

Andrea Bliesener

*aus Dormagen*

Köln, 2020

| | |
|---|---|
| Berichtserstatter: | Prof. Dr. Yoichi Ando<br>Prof. Dr. Thomas Lorenz |
| Vorsitzender der Prüfungskommission: | Prof. Dr. Achim Rosch |
| Tag der mündlichen Prüfung: | 09.03.2021 |

# Contents

# Chapter 1

# Introduction

The band theory describing the electric conduction was developed in the 1920s by Bloch and further improved over the next decade [1]. Within this theory, solids were divided into metals and insulators. Insulators are materials with a fully occupied valence band separated by an energy gap from the empty conduction band, such that they do not allow the flow of free charges. However, in conductors there is no band gap between valence and conduction band. Here, electrons are free to move from the valence to the conduction band. Wilson later added the class of semiconductors which have a band gap size in between an insulator and conductor [2]. The discovery of the quantum Hall effect of a two-dimensional electron gas in 1980 by Klaus von Klitzing [3, 4] however suggested that there are more classes than only the three already mentioned. Intriguingly, by applying a perpendicular external magnetic field at low temperatures the bulk of the two-dimensional electron gas is an insulator while simultaneously conducting states are present at the edge of the sample. Duncan Haldane, David Thouless and Michael Kosterlitz all contributed remarkably to explain such a behavior in the framework of topological band theory and phases. They were awarded the Nobel Prize in Physics in 2016 „for theoretical discoveries of topological phase transitions and topological phases of matter “ [5]. Topological insulators (TIs) are the most prominent example of such a topological phase of matter. Like an ordinary insulator they have a bulk band gap but simultaneously host conducting states on their surface.

Topological insulators gained rapid interest after the works of Kane and Mele were published in 2005 [6, 7] and in which they introduced the quantum spin Hall effect in the absence of an external magnetic field as a 2D topological insulator. Shortly after, Bernevig *et al.* [8] theoretically proposed HgCdTe to be a topological insulator. The first experimental realization of a TI was achieved in 2007 by König *et al.* [9] in HgTe quantum wells. Following these exciting discoveries the

field of topological matter rapidly grew and the hunt for further topological materials went ahead. 3D topological insulators were first predicted in 2007 [10] and the 3D TI nature was experimentally confirmed by surface-sensitive angle-resolved photoemission spectroscopy (ARPES) on $Bi_{1-x}Sb_x$ crystals a year later [11]. The family of $Bi_2Se_3$, $Bi_2Te_3$ and $Sb_2Te_3$ was introduced as a second generation of 3D topological insulators and confirmed by ARPES experiments shortly after [12–14].

In order to enhance the surface dominated conduction and minimize the bulk contribution several approaches were suggested. Growing topological materials as thin films by molecular beam epitaxy (MBE) is a promising direction to achieve better crystal quality. The MBE technique opens up new possibilities in terms of thickness control, heterostructure growth or the precise doping of a material. This thin film deposition technique is introduced in chapter 3.
Chapter 4 of this work describes the growth of a bulk-insulating 3D topological insulator film by molecular beam epitaxy. $(Bi_{1-x}Sb_x)_2Te_3$ thin films are grown by combining $n$-type $Bi_2Te_3$ and $p$-type $Sb_2Te_3$ in the optimal ratio to engineer the bandstructure of the material [15].
Chapter 5 introduces an exciting phenomena which occurs when a topological insulator is doped with a magnetic element. Here, $(Bi_{1-x}Sb_x)_2Te_3$ is doped with vanadium. The vanadium-doping introduces a spontaneous magnetization into the topological surface states which breaks time-reversal symmetry and opens up a magnetic exchange gap. Tuning the Fermi level into this gap gives rise to the quantum anomalous Hall effect.
The following chapter 6 discusses the MBE-growth of $Sn_{1-x}In_xTe$ which is predicted to be a topological superconductor, another fascinating topological material [16, 17]. Topological superconductors are of particular interest because they are predicted to host Majorana fermions which are a building block for quantum computation [16, 18].
The final chapter of this thesis, chapter 7, presents another TI growth approach called selective area growth. By patterning substrates into nano-structures, topological insulator thin films are constricted into quasi-1D-structures. The prospect of realizing Majorana fermions at the end of selectively grown topological insulator nanowires by proximitizing them with a superconductor [19, 20] paves the way for many exciting applications in spintronics and quantum computation.

# Chapter 2

# Theoretical background

## Contents



This chapter gives a basic introduction into the topological phases discussed in this work. It starts with the theoretical concept of topological insulators, followed by magnetically doped topological insulators (with the focus on the quantum anomalous Hall effect) and the last section offers an overview on topological superconductivity.

## 2.1 Introduction into topological insulators

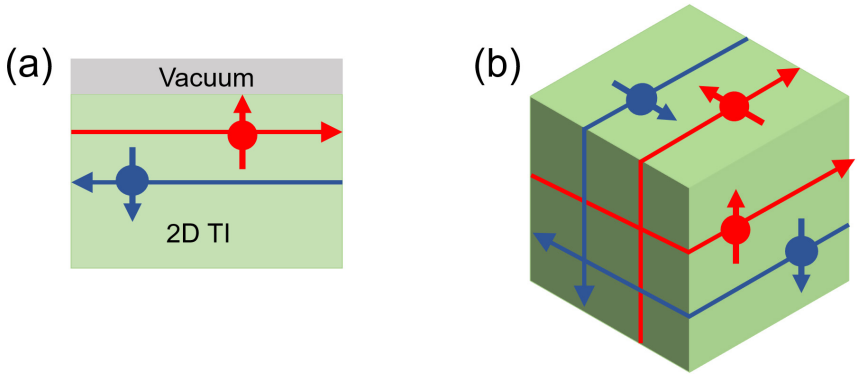


**Figure 2.1: Edge and surface states of 2D and 3D topological insulators.** (a) Schematic picture of a 2D topological insulator with 1D helical edge states. (b) Schematic picture of a 3D topological insulator with 2D helical surface states. The arrows indicate spin up (red) and spin down (blue).

Topological insulators (TI) are a new class of quantum materials with unique properties. They have an insulating bulk and metallic surface or edge states. A *2D topological insulator* hosts 1D edge channels, whereas a *3D topological insulator* exhibits 2D surface states on its boundary, as illustrated in Fig. 2.1. The surface or edge states feature gapless states in the electronic band structure, while the bulk exhibits an energy gap. The concept of the occurrence of gapless surface states is called bulk-boundary correspondence [21]. The surface states have a linear energy dispersion resembling Dirac electrons and are protected by time-reversal symmetry, which makes them robust against disorder. An odd number of Dirac cones appears per TI surface and the topological surface states are spin non-degenerate. They appear due to strong spin-orbit coupling (SOC) causing an inversion of the electronic bands (see Fig. 2.2). As a result of the large SOC, the spin of the electrons is locked to its momentum such that the electrons with opposite spin are separated along the TI edges (see Fig. 2.1).

### 2.1.1 Topology and quantum Hall effect

The term *topological* originates from a branch of mathematics which studies the properties of geometric objects under smooth deformations [22]. A common example is the coffee cup which can be smoothly transformed into a torus. The topological structure, or the genus (= the number of holes), of a torus and coffee cup is the same: $g = 1$. However, a sphere ($g = 0$) and a torus ($g = 1$) have a different genus such that they cannot be smoothly transformed into one another (see Fig. 2.3).

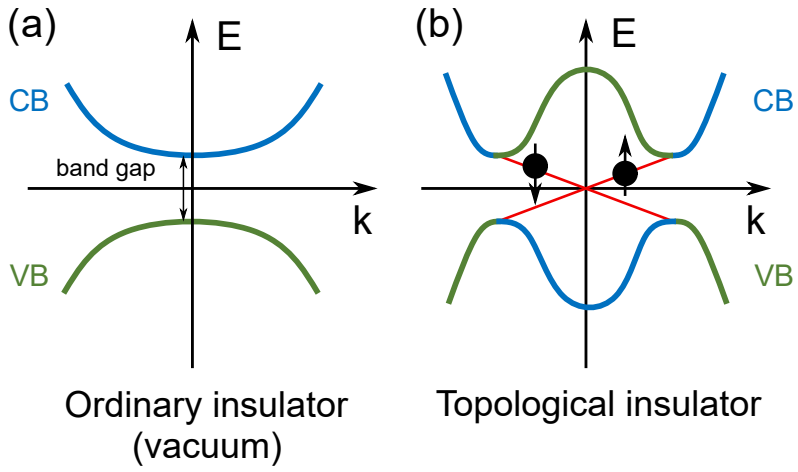


**Figure 2.2: Schematic of an ordinary and a topological insulator bandstructure.** (a) In an ordinary insulator the conduction (blue) and valence (green) band are separated by an energy gap. (b) In a topological insulator, the energy gap has been closed and re-opened again due to the inversion of the conductance and valence band. The conducting surface states (red) appear at the interface between a topological insulator and an ordinary insulator due to the non-trivial topological nature of the TIs.

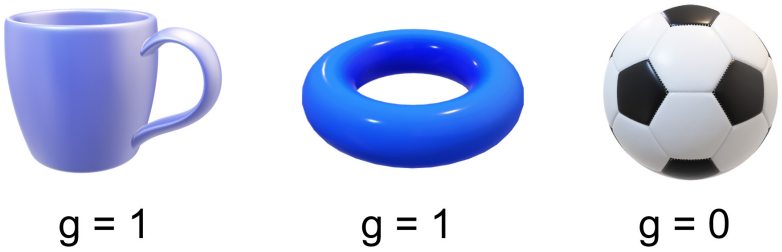


**Figure 2.3: Comparison of the genus of a cup, ball and torus.** The cup and the torus have genus $g = 1$ and can be transformed smoothly into one another, while the ball has genus $g = 0$ and thus is topologically different.

The first example of a system which was considered to be topological non-trivial (but time-reversal broken) was the *quantum Hall effect*. At high magnetic fields and low temperatures, the electrons in the bulk of a two-dimensional electron gas (2DEG) move in circular orbits with the cyclotron frequency $\omega_C$. At the boundary between the 2DEG and the vacuum, electrons skip along the edge since their circular path is interrupted, as sketched in Fig. 2.4. The electrons are constrained by the magnetic field to travel only in one direction which leads to a 1D chiral metallic edge state [23]. In 1980, von Klitzing showed that the Hall resistivity for such a system does not increase linearly with magnetic field, as it is the case for the ordinary Hall effect. Instead, the longitudinal conductivity becomes zero, while the Hall conductivity quantizes in units of integer multiples of $e^2/h$:

$$\sigma_{xy} = N\frac{e^2}{h}, \tag{2.1}$$

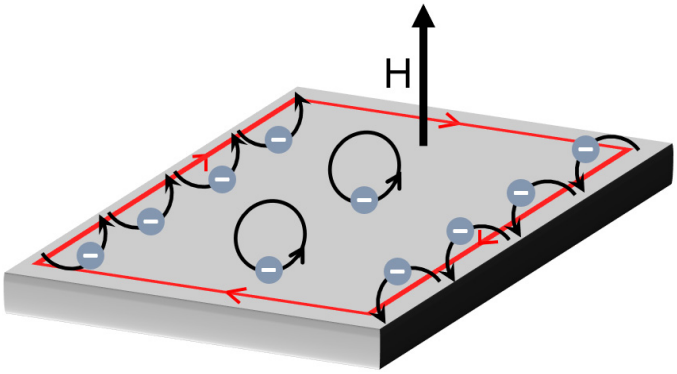


**Figure 2.4: Illustration of the quantum Hall effect** with the edge conductance carried by cyclotron orbits. (modified from [25])

with $N = 1, 2, 3...$, h = Planck's constant, e = elementary charge [3, 4]. Analogous to the mathematical description of the genus, a topological invariant $n \in \mathbb{Z}$ was introduced by Thouless, Kohmoto, Nightingale and den Nijs (TKKN) [24] to distinguish between topologically trivial ($n = 0$) and the topologically non-trivial quantum Hall ($n \neq 0$) state. Within the TKKN theory, it was found that the TKKN invariant $n$ is closely related to the integer $N$ in equation 2.1 and equal to the so-called Chern number.

### 2.1.2 Berry phase and Chern number

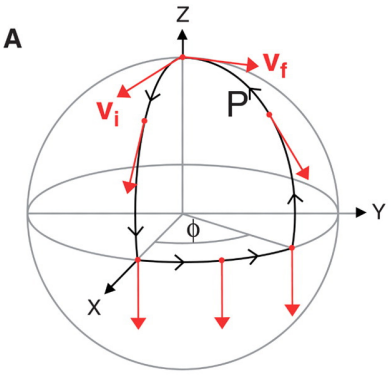


**Figure 2.5: Illustration of the geometric phase.** Parallel transport of a vector $\mathbf{v}_i$ on a spherical surface around a closed path P. Reprinted by permission from Science **317**, 5858, pp. 1889-1892 (2007), Observation of Berry's Phase in a Solid-State Qubit; P. J. Leek *et al.*, Copyright (2007), [26]

The Berry phase and the Chern number can both be used to characterize topological systems by applying mathematical concepts. The Berry phase is a geometric phase which a quantum mechanical system gains after completing a closed path in parameter space [21]. An intuitive classical example of such a geometric phase is demonstrated by the parallel transport of a vector depicted in Fig. 2.5. Here, the parallel transport of a vector $\mathbf{v}_i$ on a spherical surface starting from the north pole around a closed path P is shown. The vector $\mathbf{v}_i$ points towards south at all times. After completing the closed path P, the vector arrives back at the north pole. Here, the final state of the vector $\mathbf{v}_f$ has rotated by an angle $\phi$ in respect to its starting point, consequently it has gained an additional

phase. Berry presented a formulation of a quantum mechanical analogous of such a classical geometric phase in his work.
Consider a physical system which is described by the Hamiltonian $H = H(\mathbf{R})$, where $\mathbf{R} = \mathbf{R}(t)$ is a set of time-dependent parameters. The eigenvalues are given by $E_n(\mathbf{R})$ and the n-th eigenstate is written as $|n, \mathbf{R}(t)\rangle$, such that the Schrödinger equation for the system is given by [21]:

$$H(\mathbf{R}(t))|n, \mathbf{R}(t)\rangle = E_{\mathrm{n}}(\mathbf{R}(t))|n, \mathbf{R}(t)\rangle. \tag{2.2}$$

When $\mathbf{R}(t)$ adiabatically changes while moving along a closed path $C$, starting in a state $|n, \mathbf{R}(0)\rangle$, Berry showed that the time evolution follows $H(\mathbf{R}(t))|n, t\rangle = i\hbar\frac{\partial}{\partial t}|n, t\rangle$ and the time-dependent state is given by [27]:

$$|n, t\rangle = \exp\left(\frac{-i}{h}\int_0^t dt' E_n(\mathbf{R}(t'))\right)\exp(i\gamma_n(t))|n, \mathbf{R}(t)\rangle. \tag{2.3}$$

The first exponential term is conventionally called dynamical phase factor. Berry points the attention to the second exponential term in equation 2.3 [27]. When we consider $\mathbf{R}$ traveling along a closed path $C$ starting at a time $t = 0$ and ending at $t = T$, such that $\mathbf{R}(T) = \mathbf{R}(0)$, the Berry phase $\gamma_{\mathrm{n}}(C)$ is defined as [21]:

$$\gamma_n(C) = i\oint_C \langle n, \mathbf{R}|\nabla_R|n, \mathbf{R}\rangle d\mathbf{R}. \tag{2.4}$$

The term

$$\mathbf{A}_n(\mathbf{R}) = -i\langle n, \mathbf{R}|\nabla_{\mathbf{R}}|n, \mathbf{R}\rangle \tag{2.5}$$

is called the *Berry connection* and resembles the vector potential in electrodynamics. By applying Stoke's theorem, we can derive its curl, the *Berry curvature*, similar to the magnetic induction in electrodynamics, as:

$$\mathbf{B}_n(\mathbf{R}) = \nabla_{\mathbf{R}} \times \mathbf{A}_n(\mathbf{R}). \tag{2.6}$$

With equations 2.5 and 2.6, we can now rewrite the Berry phase in equation 2.4 as the integral

$$\gamma_n(C) = -i\oint_C d\mathbf{R} \cdot \mathbf{A}_n(\mathbf{R}) = -\int_S d\mathbf{S} \cdot \mathbf{B}_n(\mathbf{R}). \tag{2.7}$$

Berry found that the phase the system acquires while moving along the closed loop $C$ is independent of the surface which is calculated for the integral.

The *Chern number* is equal to the phase that a wavefunction accumulates when it travels along a closed loop, hence it is also referred to as a winding number. It is a topological invariant and can be written as:

$$Ch = \int_{\mathrm{BZ}} \frac{d^2\mathbf{k}}{2\pi} \left( \frac{\partial a_{\mathrm{ny}}}{\partial k_{\mathrm{x}}} - \frac{\partial a_{\mathrm{nx}}}{\partial k_{\mathrm{y}}} \right). \tag{2.8}$$

Here, the Berry connection is given by $a_n(\mathbf{k}) = -i\langle u_n(\mathbf{k})|\partial/\partial\mathbf{k}|u_n(\mathbf{k})\rangle$ with Bloch wavefunctions $|u_n(\mathbf{k})\rangle$, where $\mathbf{k}$ moves along a closed path. With Stoke's theorem one can rewrite equation 2.8 as:

$$Ch = \frac{1}{2\pi} \oint_{\partial \mathrm{BZ}} d\mathbf{k} \cdot a_n(\mathbf{k}). \tag{2.9}$$

The Chern number is used to classify topological trivial and non-trivial systems. It corresponds to the previously described genus $g$. In the case of a topological insulator, the Chern number is non-zero ($Ch \neq 0$). The wavefunction in a trivial insulator however will not acquire an additional phase $\gamma_n$ while moving in a closed path around the Brillouin zone, which gives a zero Chern number ($Ch = 0$). Thouless, Kohmoto, Nightingale and den Nijs [24] showed that the invariant $N \in \mathbb{Z}$ in equation 2.1 to describe the quantized Hall conductance has the same form as the Chern number. Given that the Chern number is a topological invariant, this helps to describe the quantum Hall effect. Considering the QH system shown in Fig. 2.4, the 2DEG material is topologically different ($Ch \neq 1$) from the insulator (vacuum) at its boundary ($Ch = 0$). Consequently, a gap has to close at the 2DEG-vacuum-interface and an edge state appears at the boundary due to the concept of bulk-boundary correspondence [21, 24, 28].

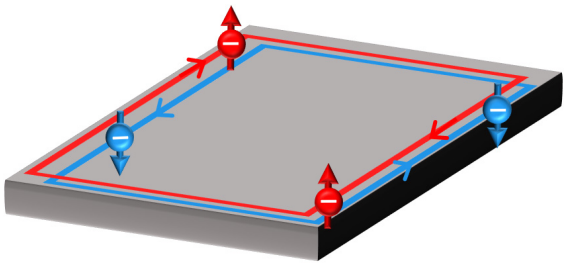

**Figure 2.6: Illustration of the quantum spin Hall effect.** Spin up and spin down carriers flow in opposite directions on the edge of the sample without an external magnetic field. (modified from [25])

### 2.1.3 Quantum spin Hall effect

High magnetic fields and low temperatures are two disadvantages of the quantum Hall effect. Furthermore, time-reversal symmetry is broken by an external magnetic field. It took until the works of Kane and Mele [6, 7] in 2005 and Bernevig and Zhang in 2006 [8, 29], in which they introduced the *quantum spin Hall effect (QSHE)* as a time-reversal invariant 2D topological insulator. Within this system, strong spin-orbit coupling plays an equivalent role to that of an external magnetic field in a quantum Hall system. Due to the spin-orbit coupling, the spin of the electrons is locked to its momentum such that the electrons with opposite spin are separated along the edges of the system. These edge states are called helical edge states. The QSHE can be seen as a superposition of two quantum Hall states with spin-polarized chiral edge channels, as illustrated in Fig. 2.6 [21]. Such a system was experimentally first realized in 2007 in HgTe quantum wells [9].

The helical edge channels in the quantum spin Hall insulator are protected by time-reversal symmetry which prevents backscattering. When an electron moves along an edge channel and meets a non-magnetic impurity, it is reflected and all the possible backscattering paths interfere destructively [17]. A schematic picture of the probable backscattering events is illustrated in Fig. 2.7. An electron can either move clockwise (top, blue) or anti-clockwise (bottom, red) around a non-magnetic impurity. Given that only the spin-down electrons can propagate backwards, the electron spin has to either rotate by $\pi$ or $-\pi$ to point in the other direction. The total phase difference of the two paths is now $\pi - (-\pi) = 2\pi$. Since the wavefunction of a spin-$1/2$-particle picks up a negative sign upon a rotation by $2\pi$, two backscattering paths always interfere destructively [17].

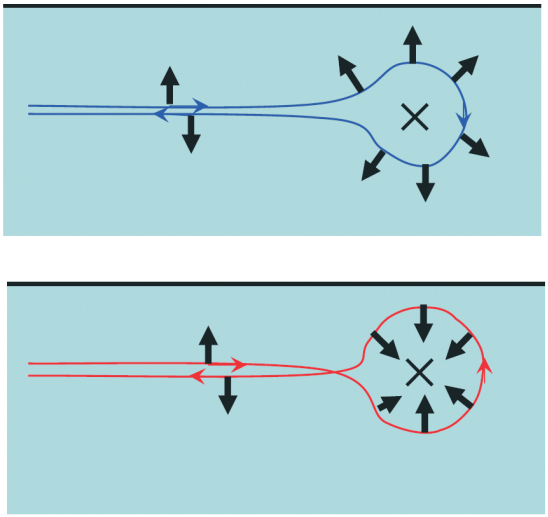

**Figure 2.7: Absence of backscattering at the quantum spin Hall edge.** An electron moves along a path on the quantum spin Hall edge and scatters at a non-magnetic impurity. The electron spin rotates by $\pi$ around the blue curve (top). The electron spin rotates by $-\pi$ around the red curve (bottom). The total phase difference is now $\pi - (-\pi) = 2\pi$, such that the paths interfere destructively and by this suppress backscattering. Reprinted figure with permission from X.L. Qi and S.C. Zhang, Rev. Mod. Phys **83**, 1057 (2011). Copyright 2011 by the American Physical Society; [17]

### 2.1.4 Time-reversal symmetry and $Z_2$ invariant

The quantum Hall state and the quantum spin Hall state are both topologically different from a trivial insulator. However, while time-reversal symmetry is broken by an external magnetic field in the case of the quantum Hall effect, it is not broken for the quantum spin Hall effect. In their work from 2005 [7], Kane and Mele introduced a new topological invariant to describe such a topological non-trivial systems in which the time-reversal symmetry is preserved. This invariant is characterized by the $Z_2$ classification, analogous to the classification within the TKKN formalism of the quantum Hall state [7]. An invariant $\nu_0$ within the $Z_2$ topology can distinguish a trivial ($\nu_0 = 0$) from a time-reversal invariant non-trivial insulator ($\nu_0 = 1$).
Lets first consider a time-reversal operator for spin-$1/2$-particles: $\Theta = -is_yK$. Here, $K$ is the complex conjugate and $s_y$ is the $y$-component of the spin operator. $\Theta$ has the important property $\Theta^2 = -1$ [21]. Time-reversal symmetry reverses the spin of an electron: $\Theta s_\uparrow = s_\downarrow$ and $\Theta s_\downarrow = -s_\uparrow$.

When $H$ is a Hamiltonian of a periodic system and preserves time-reversal symmetry, which implies that the Hamiltonian $H$ and the TR-operator $\Theta$ commute ($[H, \Theta] = 0$), then the Bloch Hamiltonian $H(\mathbf{k}) = \exp(-i\mathbf{k}\cdot\mathbf{r})H\exp(i\mathbf{k}\cdot\mathbf{r})$ fulfills [30]:

$$H(-\mathbf{k}) = \Theta H(\mathbf{k})\Theta^{-1}. \tag{2.10}$$

Equation 2.10 implies that in a system with time-reversal symmetry, for every eigenstate with momentum $\mathbf{k}$, the time-reversal state with momentum $-\mathbf{k}$ (and opposite spin) has the same energy and is an eigenstate as well. This is called the *Kramers theorem*. The two eigenstates must be at least two-fold degenerate [21,

28]. Spin-orbit coupling can split the degeneracy, but it is conserved at special points $\mathbf{k} = \Gamma_i$ in the Brillouin zone called *time-reversal invariant momenta (TRIM)*, where $+\mathbf{k}$ and $-\mathbf{k}$ are equivalent [21].

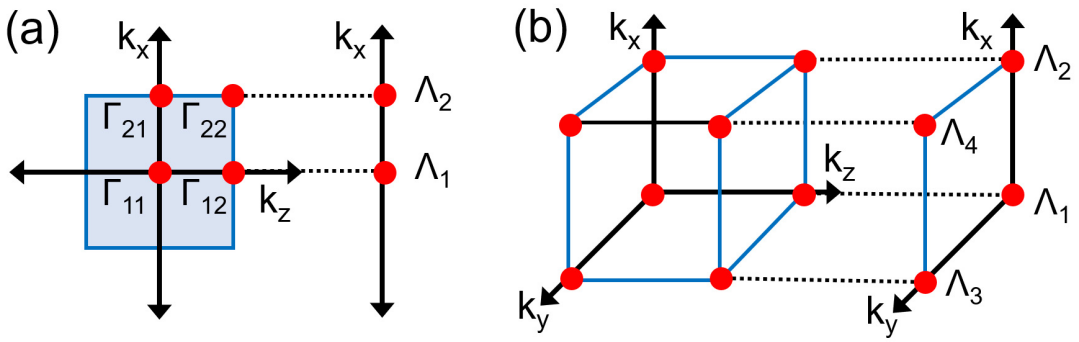


**Figure 2.8: Time-reversal invariant momenta (TRIM) in the Brillouin zone:** (a) The TRIM of the 2D bulk square Brillouin zone (red dots) $\Gamma_{ij}$ are projected onto the two edge momenta $\Lambda_a$. (b) The TRIM of the 3D cubic bulk Brillouin zone (red dots) $\Gamma_{ij}$ are projected onto the four 2D-surface momenta $\Lambda_a$. (modified from [31])

In two dimensions, four TRIM points in a square 2D Brillouin zone are projected onto the 1D edge (see Fig. 2.8(a)), while in three dimensions, there are eight distinct TRIM points in the 3D cubic Brillouin zone projected onto the 2D surface (see Fig. 2.8(b)) [7]. The $Z_2$ index reflects the number of times an edge state crosses the Fermi level between the TRIM points in the Brillouin zone. Depending on whether the number is even ($\nu_0 = 0$) or odd ($\nu_0 = 1$), the system is considered trivial or non-trivial [21]. Figure 2.9 shows the electronic dispersion in the Brillouin zone between two TRIM points $\Gamma_a = 0$ and $\Gamma_b = \pi/a$. The conduction and valence band are separated by an energy gap. Spin-degenerate points can be seen at the edge of the Brillouin zone at the TRIM points, whereas the degeneracy is split in-between, away from $\Gamma_a$ and $\Gamma_b$. In Fig. 2.9(a) the states at $k_x = 0$ and $k_x = \pi/a$ are connected as pairs and the bands cross the Fermi energy at an even number of points. The material is topologically trivial ($\nu_0 = 0$). The situation in Fig. 2.9(b) is different, since here the bands switch at the edge of the Brillouin zone and the Fermi energy is intersected only once (odd), which means the material is topologically non-trivial ($\nu_0 = 1$) and hosts metallic states on the boundary [7, 28].

These studies can now be generalized for three dimensions. 3D topological insulators with topological protected surface states were first predicted by Fu and Kane [10] in 2007 and experimentally confirmed a year later [11]. The basic building block material discussed in this thesis $(Bi_{1-x}Sb_x)_2Te_3$ (BST) is a 3D topological insulator.

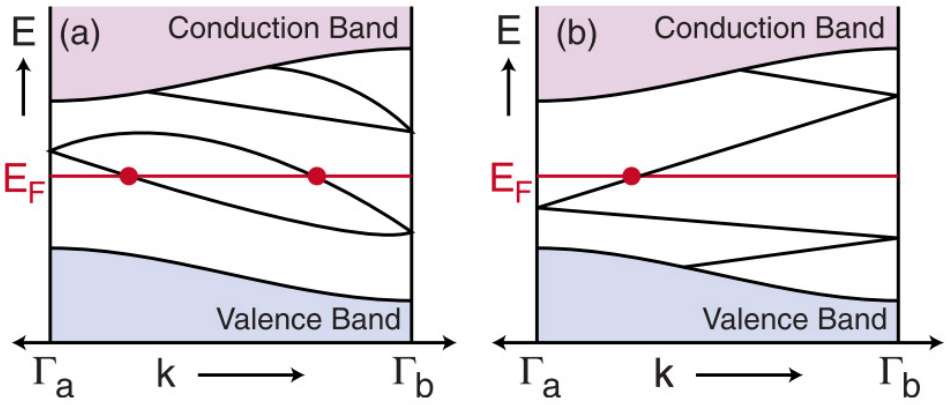


**Figure 2.9: Schematic of the 2D electronic dispersion between two Kramers degenerate points $\Gamma_a = 0$ and $\Gamma_b = \pi/a$:** (a) The number of surface states crossing the Fermi energy $E_F$ is even, which means the material is topologically trivial $\nu_0 = 0$. (b) The number of surface states crossing the Fermi energy $E_F$ is odd, which means the material is topologically non-trivial $\nu_0 = 1$. Note, that only half of the Brillouin zone from 0 to $\pi/a$ is shown, since the other half is the mirror image. Reprinted figure with permission from M. Hasan and C. Kane, Rev. Mod. Phys **82**, 3045 (2010). Copyright 2010 by the American Physical Society; [28]

The 3D cubic Brillouin zone hosts eight TRIM points sitting on the vertices of the cube (see Fig. 2.8(b)). They can be described by the primitive reciprocal lattice vectors $\Gamma_{i=(n_1 n_2 n_3)} = (n_1\mathbf{b}_1 + n_2\mathbf{b}_2 + n_3\mathbf{b}_3)$, with $n_j = 0, 1$ [31]. In the classification for the three-dimensional case, the number of topological invariants was increased to four $Z_2$-invariants $(\nu_0; \nu_1, \nu_2, \nu_3)$ [10, 30, 31]. The invariants are defined as:

$$(-1)^{\nu_0} = \prod_{n_i=0,1} \delta_{n_1,n_2,n_3} \tag{2.11}$$

$$(-1)^{\nu_{i=1,2,3}} = \prod_{n_{i\neq j}=0;n_i=1} \delta_{n_1,n_2,n_3}, \tag{2.12}$$

with the parity invariant $\delta_i = \prod_{m=1}^{N} \xi_m(\Gamma_i)$ [31]. Here, $\xi_m \pm 1$ is the parity eigenvalue of the m-th occupied band at the TRIM point $(\Gamma_i)$.

Fu, Kane and Mele distinguish 16 different classes of topological insulators in their paper [10] and introduce strong ($\nu_0 = 1$) and weak ($\nu_0 = 0$ and any of $\nu_i$ for $i = 1, 2, 3$ is odd) topological insulators. When all four invariants are zero ($\nu_0 = \nu_1 = \nu_2 = \nu_3 = 0$), the system is a trivial insulator.

Figure 2.10 shows a schematic of the Fermi circle in the 2D surface Brillouin zone of a 3D topological insulator with four TRIM points $\Gamma_{1,2,3,4}$. The Brillouin

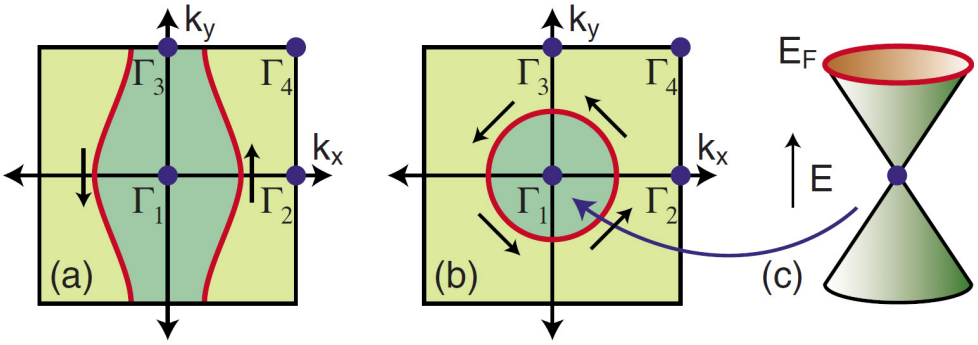


**Figure 2.10: Schematic of the Fermi surface in the Brillouin zone.** (a) An even number of TRIM points are enclosed by the Fermi surface in a weak topological insulator. (b), (c) Fermi circle in the surface Brillouin zone of the simplest strong topological insulator with a single TRIM point enclosed by the Fermi surface. Reprinted figure with permission from M. Hasan and C. Kane, Rev. Mod. Phys **82**, 3045 (2010). Copyright 2010 by the American Physical Society; [28]

zone of a weak topological insulator is illustrated in Fig. 2.10 (a). An even number of TRIM points is enclosed by the Fermi surface. For the strong topological insulator, an odd number of Dirac points have to be enclosed by the Fermi surface. The surface Brillouin zone of the simplest strong topological insulator is illustrated in Fig. 2.10 (b) and shows that the Fermi surface encloses a single TRIM point.

## 2.2 Magnetically doped topological insulators

### 2.2.1 Introduction to the Hall family

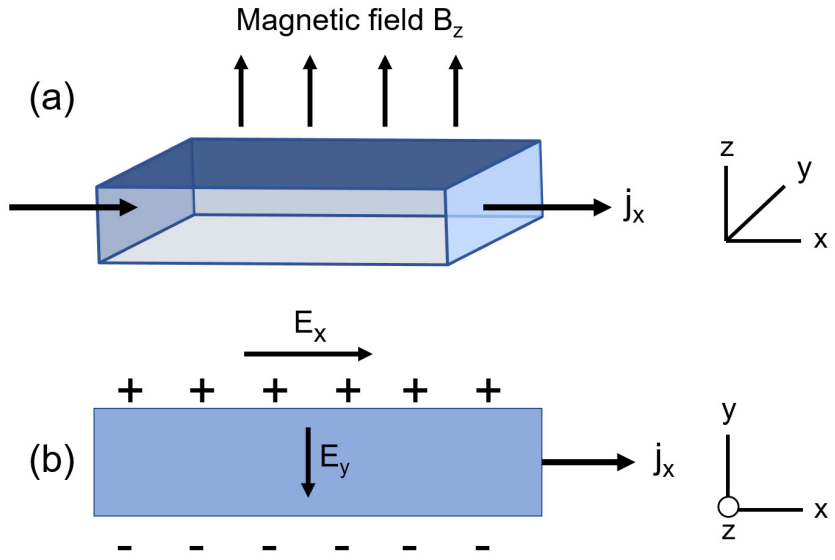


**Figure 2.11: Schematic illustration of the ordinary Hall effect:** (a) Current flows in $x$-direction through a sample placed in a magnetic field in $z$-direction. (b) Electrons accumulate on one side of the sample, while positive charges are present on the opposite side due to the Lorentz force. (adapted from [32])

The *ordinary Hall effect (OHE)* was discovered by Edwin Hall in 1879 [32, 33]. When a current runs through a conducting sample in a homogeneous magnetic field, the charges accumulate on the edges of the sample and by this generate a voltage. In Fig. 2.11(a) a transverse magnetic field is applied to a sample in $z$-direction while a current $j_x$ is applied in longitudinal $x$-direction. Due to the Lorentz force $F_L$, the electrons are deflected in the negative $y$-direction (see Fig. 2.11(b)):

$$F_{\mathrm{L}} = -\frac{e}{c} v \times H. \tag{2.13}$$

The transverse electric field $E_y$ will balance the Lorentz force once it is in equilibrium and the current is flowing in $x$-direction only. Now the electric field $E_y$ will generate a voltage across the sample with $U_H = \frac{E_y}{W}$, with W being the width of the sample.

The ratio of the electrical field $E_y$ and the current density $j_x$ is called magnetoresistance $\rho$:

$$\rho = \frac{E_x}{j_x} \tag{2.14}$$

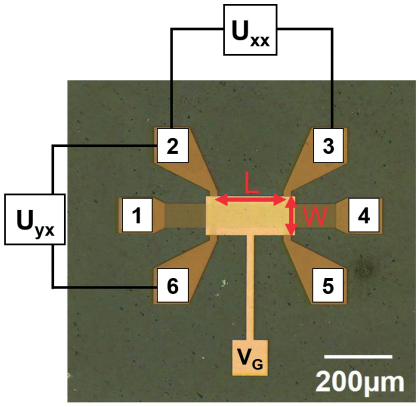


**Figure 2.12:** Optical image for a standard Hall bar device. The current flows from contact 1 to 4. The longitudinal (transversal) voltage is measured between contact 2 and 3 (5 and 6). Additionally, a gate is added to this device. L and W depict the length and width of the Hall-bar.

Another important quantity is the Hall coefficient $R_H$. It relates the induced transverse electrical field $E_y$ to the magnetic field (see equation 2.15). Since $E_y$ points to the negative direction, the Hall coefficient $R_H$ should be negative as well. In the case of positive charges, the sign will be reversed. Thus, by measuring the Hall coefficient one can determine the carrier type and concentration $n$:

$$R_H = \frac{E_y}{j_x B} = -\frac{1}{ne}. \tag{2.15}$$

The Hall coefficient can be easily extracted from the slope d/dB $R_{xy}$ of the Hall resistance $R_{xy}$ in magnetic field, with $R_{xy} = R_H \frac{B_z}{d}$.

Using the Hall coefficient one can now calculate the mobility of the carriers with:

$$\mu = \frac{1}{R_H \rho}. \tag{2.16}$$

In the scope of this work, the resistance is often defined as the sheet resistance $R_\square = {}^{R_{xx}W}/_{L}$ with the longitudinal resistance $R_{xx}$ and width W and length L between the Hall contacts. An optical photo of a typical Hall-bar device used for transport measurements in this thesis is shown in Fig. 2.12.

Two years after the discovery of the ordinary Hall effect, Hall noticed that the effect is ten times larger in a ferromagnetic material (FM). The reason for this is the spontaneous magnetization of the ferromagnetic material and this effect was later known as the *anomalous Hall effect (AHE)* [34]. The AHE can be measured in zero magnetic field, since the ferromagnetic material keeps its magnetization. The external magnetic field which is necessary in the OHE, is replaced by an internal magnetization in the anomalous Hall effect. Its origin lies in the spin-orbit coupling and appears in materials with broken time-reversal symmetry [35]. It was experimentally found that the relation between Hall resistivity $\rho_{xy}$ and applied magnetic field behaves differently in a ferromagnetic and non-magnetic

material. It behaves linearly in non-magnetic materials. However, in ferromagnetic materials the resistivity increases in low magnetic fields and saturates for higher fields. In this case the most common empirical relation for the Hall resistance is given by a term for the ordinary Hall and for the anomalous Hall contribution [35]:

$$\rho_{xy} = R_0 H + R_\mathrm{A} M(H), \tag{2.17}$$

where the Hall coefficient $R_0$ mainly depends on the carriers and the anomalous Hall coefficient $R_\mathrm{A}$ depends on material specific parameters and particularly the longitudinal resistivity $\rho_{xx}$.

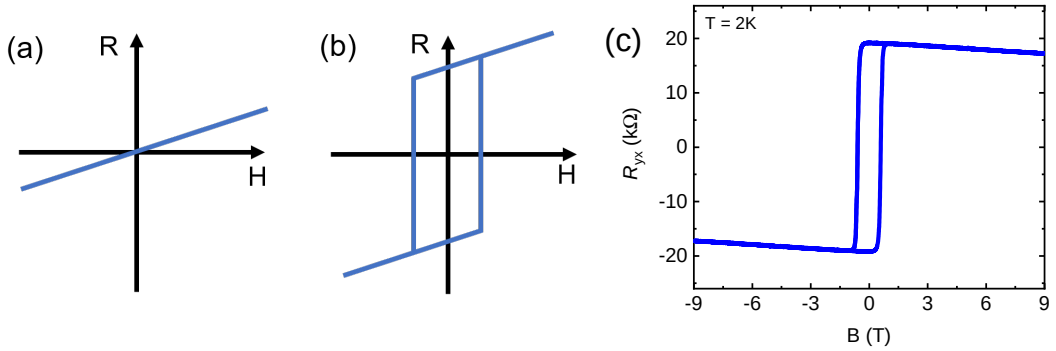


**Figure 2.13: Ordinary Hall effect and anomalous Hall effect.** (a) Classical relation between magnetic field and resistance of the ordinary Hall effect. (b) Relation between magnetic field and resistance of the anomalous Hall effect. (c) Measurement of a vanadium-doped $(Bi_{1-x}Sb_x)_2Te_3$ film which shows a hysteresis loop indicating a ferromagnetic order. Both, the ordinary and the anomalous Hall contribution can be identified in the measurement result. (modified from [36])

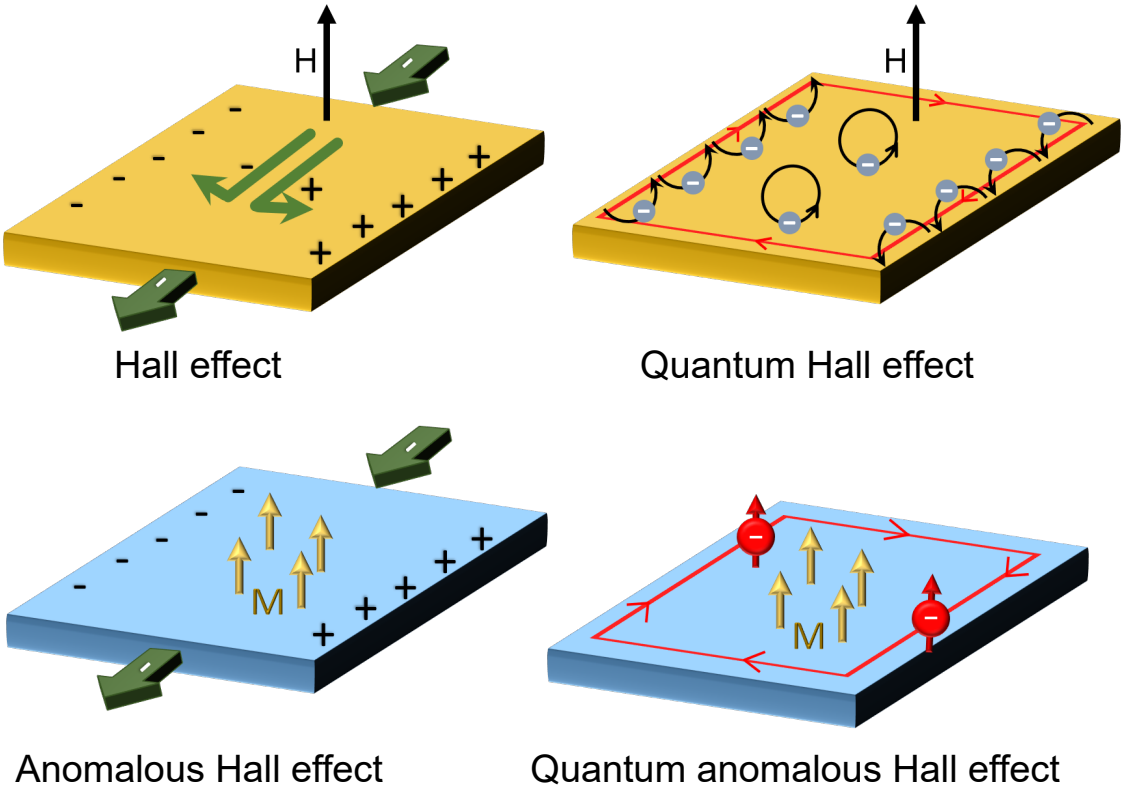


**Figure 2.14: Schematic illustration of the Hall family:** ordinary Hall effect (OHE, top left), quantum Hall effect (QHE, top right), anomalous Hall effect (AHE, bottom left) and quantum anomalous Hall effect (QAHE, bottom right). M is the intrinsic magnetization and H is the external magnetic field. (modified from [25, 37])

### 2.2.2 Quantum anomalous Hall effect

#### 2.2.2.1 Introduction into the quantum anomalous Hall effect

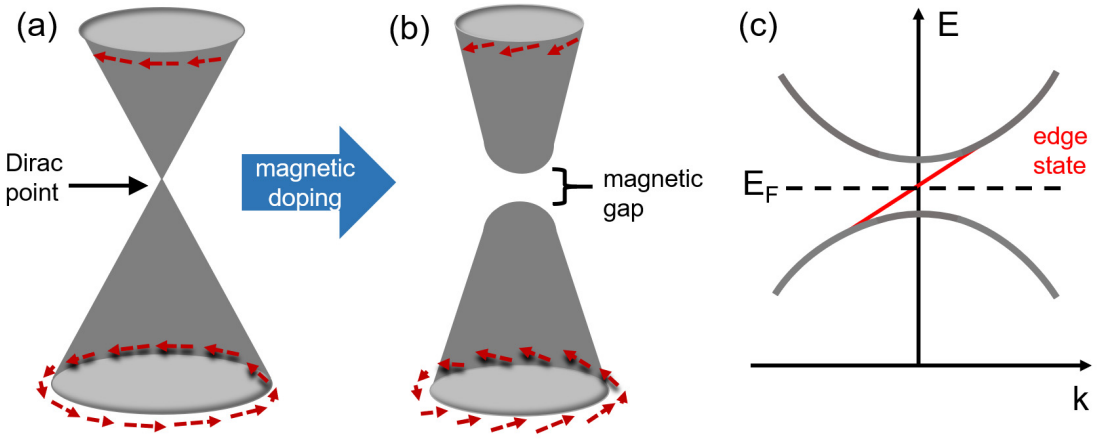


**Figure 2.15: Schematic of the Dirac dispersion of the topological surface states of a topological insulator and the gaped dispersion in a magnetic topological insulator.** (a) Dirac-like dispersion of a topological insulator. (b) Introducing magnetic dopants breaks the time-reversal symmetry and opens an exchange gap in the topological surface states. (c) When the Fermi level is within the magnetic exchange gap, a chiral edge mode appears on the edge of the sample.

The quantum anomalous Hall effect is the quantized version of the anomalous Hall effect and hosts dissipationless edge current similar to the case of the quantum Hall effect, however, it does not require an external magnetic field (see Fig. 2.14). Even though Haldane proposed the QAHE already in 1988 [38], it took until the discovery of topological insulators and the achievement of the quantum spin Hall effect [9] to stir up the realization of a concrete system which exhibits the quantum anomalous Hall effect [39].

Magnetic doping of a topological insulator induces a spontaneous magnetization into the topological surface states which breaks time-reversal symmetry (TRS). Breaking the TRS in a system leads to the opening of a magnetic gap in the Dirac dispersion. When the Fermi level is within the magnetic exchange gap, a chiral edge mode appears on the edge of the sample and the Hall conductivity is quantized in units of $e^2/h$ (see Fig. 2.15) [39–45].
The quantum anomalous Hall effect can be constructed from a 3D magnetic topological insulator [43, 45–47]. As illustrated in Fig. 2.16, the out-of-plane magnetization $M_z$ leads to the opening of a magnetic exchange gap $m$ in the top and bottom surface of a 3D topological insulator. The 2D surface states of such a magnetically doped 3D topological insulator can be mathematically described by the

following Dirac Hamiltonian [40, 46]:

$$H = v_{\mathrm{F}}(-k_y\sigma_x + k_x\sigma_y) \pm m\sigma_z. \tag{2.18}$$

Here, $\mathrm{v_F}$ is the Fermi velocity, $m$ is the magnetic exchange gap along the out-of-plane axis, $k_x$ and $k_y$ are momenta and $\sigma_x$, $\sigma_y$ and $\sigma_z$ are the Pauli matrices for the spin. $\pm$ represents the top and bottom surface. Solving the Schrödinger equation for this Hamiltonian results in the energy dispersion [28]:

$$E = \pm\sqrt{v_{\mathrm{F}}^2 + m^2}, \tag{2.19}$$

which has an energy gap $2|m|$ at $k = 0$.

The normal vectors along the out-of-plane magnetization axis for the top and bottom surface point in opposite directions, resulting in a positive gap $+m$ for the top surface and a negative gap $-m$ for the bottom surface, as shown in Fig. 2.16 [46]. Due to their opposite magnetization direction, the two surfaces belong to a different topological class. The bulk-boundary correspondence now imposes the occurrence of a gapless, metallic edge state carrying a quantized conductance $e^2/h$ at the interface between top and bottom surface [46, 47].

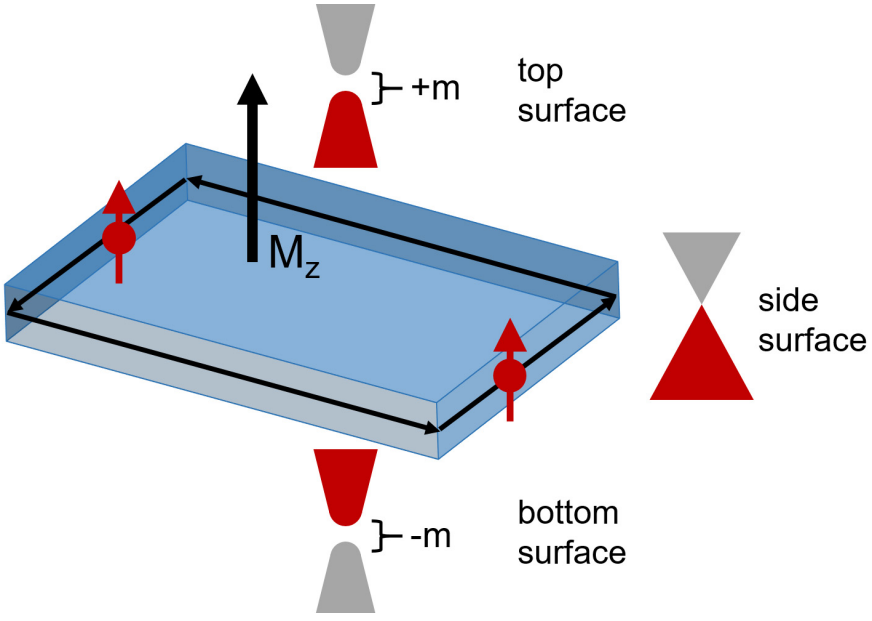


**Figure 2.16: Schematic of a magnetic topological insulator with out-of-plane magnetization** $M_z$. Due to the time-reversal symmetry breaking by introducing a magnetization, the top and bottom surface of the magnetically doped topological insulator have a gap $\pm m$ opening, while a 1D chiral edge mode forms at the boundary in between.

The experimental signatures of the quantum anomalous Hall effect are a quantization of the Hall resistivity $\rho_{yx}$ in units of $h/e^2$, while the longitudinal resistivity $\rho_{xx}$ vanishes:

$$\rho_{xx} = 0 \tag{2.20}$$

$$\rho_{yx} = \frac{h}{e^2} \tag{2.21}$$

Accordingly, the conductivities are given by:

$$\sigma_{xx} = \frac{\rho_{xx}}{\rho_{xx}^2 + \rho_{yx}^2} = 0 \tag{2.22}$$

$$\sigma_{yx} = \frac{\rho_{yx}}{\rho_{xx}^2 + \rho_{yx}^2} = \frac{e^2}{h} \tag{2.23}$$

The experimental steps to achieve the quantum anomalous Hall effect in a topological insulator film are [45]:

- Grow a thin, bulk-insulating topological insulator film.
- Introduce long-range ferromagnetic order by doping the film with magnetic atoms. This will break the time-reversal symmetry of the TI and open an energy gap at the Dirac point.
- Tune the Fermi level into the magnetically induced energy gap.

#### 2.2.2.2 Magnetism in magnetically doped topological insulators

Magnetism in topological insulators can in general be realized by either the magnetic proximity effect or by doping the TI with magnetic dopants. It was predicted that ferromagnetism in topological insulators can be established by chemical doping with 3d transition metal elements [39, 48, 49].

In the first experiments in which materials such as $Bi_2Se_3$, $Bi_2Te_3$ and $Sb_2Te_3$ were magnetically doped, they were treated like diluted magnetic semiconductors [50–53]. The knowledge gained in these studies was transferred to transition metal-doping of topological insulators. Neighboring magnetic dopants in magnetically doped semiconductor can be aligned by the *Ruderman-Kittel-Kasuya-Yosida (RKKY)* interaction. In this coupling mechanism, magnetic ions couple indirectly via free conduction electrons (see Fig. 2.17 (a)) [54]. The disadvantage of this type of mechanism is that free electrons can disturb the quantum anomalous Hall effect by introducing additional conduction channels [37, 55].

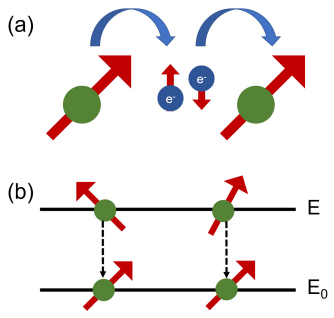


**Figure 2.17:** (a) RKKY coupling mechanism: Magnetic ions couple indirectly via free electrons. (b) Van Vleck coupling mechanism: Magnetic ions couple indirectly via interaction between occupied and unoccupied electron bands. (modified from [37])

Yu *et al.* [39] predicted *Van Vleck* mechanism as another possible mechanism for magnetic exchange. This type of magnetism is a quantum mechanical second order perturbation effect without any itinerant carriers (see Fig. 2.17 (b)) [56]. In their work, Yu *et al.* assumed that the magnetic exchange among local moments is carried by electrons upon doping $Bi_2Se_3$, $Bi_2Te_3$ or $Sb_2Te_3$ with 3d transition metals such as chromium or iron. The free energy of the system in an external magnetic field H is considered to be [39]:

$$F_{\text{total}} = \frac{1}{2}\chi_L^{-1}M_L^2 + \frac{1}{2}\chi_e^{-1}M_e^2 - J_{\text{eff}}M_L M_e - (M_L + M_e)H, \tag{2.24}$$

with the spin susceptibility $\chi_L$ ($\chi_e$) and the magnetization $M_L$ ($M_e$) of the local moments (band electrons). $J_{\text{eff}}$ is the magnetic exchange coupling between local moments and band electrons. It was found that the Van Vleck mechanism can give rise to a large spin susceptibility of the band electrons $\chi_e$, so that they directly couple to the magnetic moments and thus result in a non-zero magnetization

without an external magnetic field H. This spin susceptibility for temperatures much less than the band gap can be written as:

$$\chi_e^{zz} = \sum_{E_{nk}<\mu; E_{mk}>\mu} 4\mu_0\mu_{\mathrm{B}}^2 \frac{\langle nk|\hat{S}_z|mk\rangle\langle mk|\hat{S}_z|nk\rangle}{E_{mk} - E_{nk}}. \tag{2.25}$$

Here, $\mu$ is the Fermi energy, $\mu_0$ is the vacuum permeability, $\mu_{\mathrm{B}}$ is the Bohr magneton, $\hat{S}_z$ is the electron spin operator and $|mk\rangle$ and $|nk\rangle$ are Block wavefunctions in the conduction and valence band. In an ordinary insulator, valence and conduction band are separated by an energy gap such that $|mk\rangle$ and $|nk\rangle$ do not mix and $\chi_e$ is minimal [47]. However, in the $Bi_2Se_3$ family the strong spin-orbit coupling causes a band inversion of valence and conduction band, and hence the mixing of the $|mk\rangle$ and $|nk\rangle$ wavefunctions. This leads to a large matrix element $\langle nk|\hat{S}_z|mk\rangle$ which contributes to the van Vleck spin susceptibility. Chang *et al.* [57] claimed to have found indications for Van Vleck interaction in 5 nm-thin $Cr_{0.22}(Bi_xSb_{1-x})_{1.78}Te_3$ films. In their work, the bismuth-antimony ratio was changed to tune the carrier type, while the Cr-dopants and film thickness was kept constant. The Curie temperature $T_{\mathrm{C}}$ was almost constant regardless of the change from $n$- to $p$-type. Additionally, they observe no change in the coercive field $H_{\mathrm{C}}$ in the gate-voltage dependent measurement of the anomalous Hall effect measurements.

## 2.3 Topological superconductivity

### 2.3.1 Introduction into topological superconductivity

After the discovery of the time-reversal invariant (TRI) topological insulators [7], the study of their superconducting counterpart, the *topological superconductors*, gained interest [58, 59], even though Read and Green proposed a non-trivial 2D $p + ip$-superconductor already in 2000 [60]. Several approaches to engineer a topological superconductor have been proposed. Among them doping a topological insulator to achieve a bulk superconductor, as it was found in $Cu_xBi_2Se_3$ [61, 62], or, following a proposal by Fu and Kane [63], proximitizing a topological insulator with a superconductor and thus inducing superconductivity into the TI surface states. The second approach will be discussed in detail in chapter 2.3.5 and chapter 6. Particularly the prospect of topological superconductors hosting Majorana fermions, which are a building block for quantum computation, makes this material class interesting [16, 18].

Just like topological insulators, topological superconductors exhibit gapless excitation on their boundary. These excitation are not electrons or holes as it is the case for TIs, but superpositions of both. They are called Bogoliubov quasiparticles or Bogolons. The surface states are called Andreev bound states and depend on the symmetries a material holds. Topological superconductors can be classified foremost by such symmetries [64].
Topological superconductors can be time-reversal breaking or time-reversal invariant. A 2D chiral topological superconductor which breaks time-reversal symmetry, can be seen as the superconducting variant of the quantum Hall effect, as illustrated in the top row of Fig. 2.18 [17, 65]. Whereas the quantum Hall insulator is classified by the Chern number, time-reversal breaking topological superconductors are categorized by an integer [60]. The quantum Hall state with Chern number $N$ hosts $N$ chiral edge states. The 2D chiral superconductor in comparison exhibits $N'$ chiral Majorana edge states which exhibit half the degree of freedom of the QHE. The same comparison can be drawn for the quantum spin Hall effect and its superconducting analogous, the helical superconductor, shown in the bottom row of Fig. 2.18. Here, fermions with spin up are in a $p_x + ip_y$ state, while spin down fermions are in the $p_x - ip_y$ state [17].

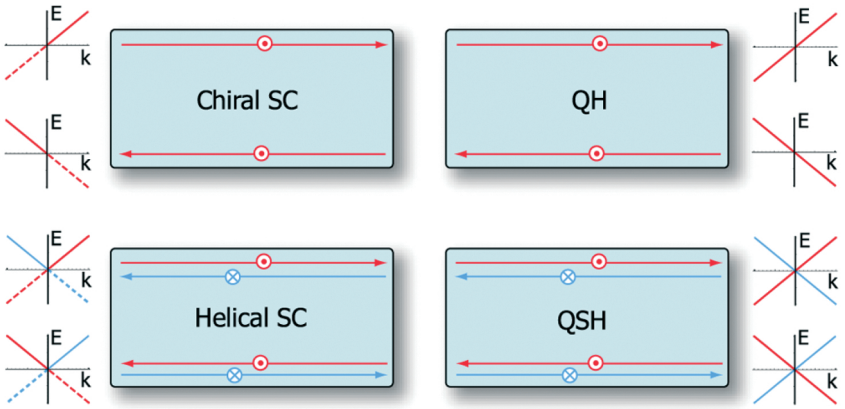


**Figure 2.18: Schematic comparison of the quantum Hall state and a 2D chiral superconductor (top row); the quantum spin Hall state and a 2D helical superconductor (bottom row).** In the top row, both systems exhibit TR-broken symmetry and host chiral edge modes. Bottom row: TRS is present in both systems and they exhibit helical edge states. Reprinted figure with permission from X.L. Qi *et al.*, PRL **102**, 187001 (2009). Copyright 2009 by the American Physical Society; [58]

### 2.3.2 Short recap: Conventional superconductivity

Certain materials become superconducting when cooled down below a critical temperature $T_{\mathrm{C}}$ which manifests in a vanishing resistance. This phenomena was discovered in 1911 by Heike Kamerlingh Onnes when he cooled down a mercury wire and found that its resistance suddenly vanishes at a critical temperature of 4.2 K [66]. Further investigation of the superconducting state demonstrated a critical current $I_{\mathrm{C}}$ which is defined as the maximum current that can flow at zero resistance. The magnetic properties of superconductors were investigated by Meissner and Ochsenfeld [67]. They showed in 1933 that a magnetic field cannot enter a superconductor below a critical temperature $T_{\mathrm{C}}$ and up to a critical field $H_{\mathrm{C}}$, which makes superconductors perfect diamagnets with a susceptibility of $\chi = -1$. Additionally, a characteristic length called London penetration length $\lambda_{\mathrm{L}}$ was later found, which defines a narrow region at the boundary of a superconductor in which the magnetic field can enter but decays exponentially [68].
Bardeen, Cooper and Schrieffer developed a theory to explain the origin of superconductivity known as the *BCS-theory*. It was published in 1957, 46 years after the experimental discovery of superconductivity [69, 70]. The BCS-theory describes how so-called Cooper pairs of electrons are created and annihilated in a superconductor as a result of interactions between phonons and electrons. This interaction overcomes the Coulomb repulsion and a minimum energy of $E_{\mathrm{g}} = 2\Delta(T)$ (with the energy gap $\Delta$) is required to break a Cooper pair apart [71].

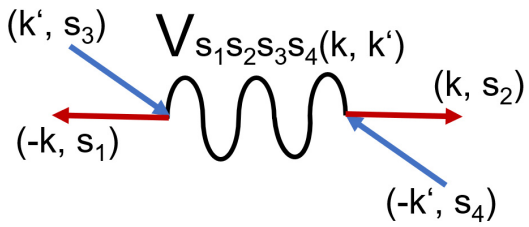


**Figure 2.19:** Illustration of the pairing interaction $V_{s_1 s_2 s_3 s_4}(\mathbf{k}, \mathbf{k}')$ (modified from [64, 73])

### 2.3.3 The Bogoliubov-de Gennes equation

A single-band Hamiltonian can be written as [16, 72]:

$$H = \sum_{\mathbf{k},s_1,s_2} \epsilon_{s_1 s_2}(\mathbf{k}) c^\dagger_{\mathbf{k}s_1} c_{\mathbf{k}s_2} + \frac{1}{2} \sum_{\mathbf{k},s_1,s_2} \left( \Delta^*_{s_1 s_2}(\mathbf{k}) c_{\mathbf{k}s_1} c_{-\mathbf{k}s_2} + \Delta_{s_1 s_2}(\mathbf{k}) c^\dagger_{\mathbf{k}s_1} c^\dagger_{-\mathbf{k}s_2} \right). \quad (2.26)$$

The electrons with spin $s$ and momentum $\mathbf{k}$ are represented by the annihilation $c_{\mathbf{k}s}$ and creation $c^\dagger_{\mathbf{k}s}$ operators, and the spin-dependent energy operator $\epsilon_{s_1 s_2}(\mathbf{k})$. Within the BCS theory, the formation of Cooper pairs results in a non-zero expectation value $< c_{\mathbf{k}s_1} c_{-\mathbf{k}s_2} >$ and $< c^\dagger_{\mathbf{k}s_1} c^\dagger_{-\mathbf{k}s_2} >$. Thus, the pairing potential $\Delta_{s_1 s_2}(\mathbf{k})$ can be defined as:

$$\Delta_{s_1 s_2}(\mathbf{k}) = - \sum_{\mathbf{k}',s_3,s_4} V_{s_1 s_2 s_3 s_4}(\mathbf{k}, \mathbf{k}') < c_{\mathbf{k}'s_3} c_{-\mathbf{k}'s_4} > . \quad (2.27)$$

Here, $V_{s_1 s_2 s_3 s_4}(\mathbf{k}, \mathbf{k}')$ describes the pairing interaction between electrons. Two electrons in the states $(\mathbf{k}, s_1)$ and $(-\mathbf{k}, s_2)$ interact, owing to the scattering by phonons, and end up in the states $(\mathbf{k}', s_3)$ and $(-\mathbf{k}', s_4)$ as illustrated in Fig. 2.19.

Equation 2.26 can be rewritten by introducing the *Bogoliubov-de Gennes (BdG) Hamiltonian* $H_{\mathrm{BdG}}$:

$$H = \frac{1}{2} \sum_{\mathbf{k},s_1,s_2} \begin{pmatrix} c^\dagger_{\mathbf{k}s_1} & c_{-\mathbf{k}s_1} \end{pmatrix} H_{\mathrm{BdG}}(\mathbf{k}) \begin{pmatrix} c_{\mathbf{k}s_2} \\ c^\dagger_{-\mathbf{k}s_2} \end{pmatrix}. \quad (2.28)$$

Within equation 2.28, the BdG-Hamiltonian is given by a $4x4$-matrix and a four component vector $(c^\dagger_{\mathbf{k}s_1}, c_{-\mathbf{k}s_1})$ :

$$H_{\mathrm{BdG}}(\mathbf{k}) = \begin{pmatrix} \epsilon_{s_1 s_2}(\mathbf{k}) & \Delta_{s_1 s_2}(\mathbf{k}) \\ \Delta^\dagger_{s_1 s_2}(\mathbf{k} & -\epsilon_{s_1 s_2}(-\mathbf{k})^t \end{pmatrix}. \quad (2.29)$$

The Bogoliubov-de Gennes Hamiltonian underlies *particle-hole symmetry*, which means that every eigenstate at energy $E$ and wavevector $\mathbf{k}$ has a corresponding eigenstate at $-E$ and $-\mathbf{k}$. The particle-hole symmetry exchanges electrons

with holes. One can define an anti-unitary particle-hole operator $P$ which anti-commutes with the BdG-Hamiltonian:

$$P = \begin{pmatrix} 0 & 1_{2x2} \\ 1_{2x2} & 0 \end{pmatrix} K, \tag{2.30}$$

where $1_{2x2}$ is the unit matrix and $K$ the complex conjugation operator.

Applying the operator $P$ to the BdG-Hamiltonian $H_{\mathrm{BdG}}(\mathbf{k})$ results in:

$$PH_{\mathrm{BdG}}(\mathbf{k})P^{-1} = -H_{\mathrm{BdG}}(-\mathbf{k}). \tag{2.31}$$

Lets assumes that $\begin{pmatrix} u_s(\mathbf{k}) \\ v_s^*(-\mathbf{k}) \end{pmatrix}$ is an eigenvector of the BdG Hamiltonian 2.29 with energy $E$. Diagonalizing equation 2.29, results in the eigenequation:

$$H_{\mathrm{BdG}}(\mathbf{k}) \begin{pmatrix} u_s(\mathbf{k}) \\ v_s^*(-\mathbf{k}) \end{pmatrix} = E(\mathbf{k}) \begin{pmatrix} u_s(\mathbf{k}) \\ v_s^*(-\mathbf{k}) \end{pmatrix}. \tag{2.32}$$

Applying the particle-hole operator $P$ on equation 2.32, gives:

$$H_{\mathrm{BdG}}(\mathbf{k})P \begin{pmatrix} u_s(-\mathbf{k}) \\ v_s^*(\mathbf{k}) \end{pmatrix} = -E(-\mathbf{k})P \begin{pmatrix} u_s(-\mathbf{k}) \\ v_s^*(\mathbf{k}) \end{pmatrix}. \tag{2.33}$$

Thus, both energy eigenvalues $E(\mathbf{k})$ and $-E(-\mathbf{k})$ are eigenvalues of the BdG-Hamiltonian and, consequently, $H_{\mathrm{BdG}}$ is symmetric around zero energy which is the Fermi level. One can now diagonalize $H_{\mathrm{BdG}}$ and write the set of four eigenvalues as $(E_1(\mathbf{k}), E_2(\mathbf{k}), -E_1(-\mathbf{k}), -E_2(-\mathbf{k})$ with $E_i(\mathbf{k}) \geq 0)$. Equation 2.28 can now be re-written as:

$$H = \sum_{\mathbf{k},i=1,2} E_i(\mathbf{k}) \alpha_{\mathbf{k}i}^\dagger \alpha_{\mathbf{k}i}. \tag{2.34}$$

Here, $\alpha_{\mathbf{k}i}^\dagger$ is the creation and $\alpha_{\mathbf{k}i}$ is the annihilation operator of quasiparticles in the superconducting state, the so-called Bogoliubov quasiparticles or Bogolons.

Pair potentials are classified by their spin angular momentum. The spin is the only degree of freedom in the simple case discussed so far. Cooper pairs are generally formed by pairing two spin-$1/2$ electrons, such that the spin angular momentum is either 0 (for a spin-singlet) or 1 (for a spin-triplet). The pair potential of a spin singlet has to be antisymmetric ($\Delta_{ss'} = -\Delta^T(-\mathbf{k})$) and is written as:

$$\Delta_{ss'}(\mathbf{k}) = i\psi(\mathbf{k})[s_y]_{ss'} = \begin{pmatrix} 0 & \psi(\mathbf{k}) \\ -\psi(\mathbf{k}) & 0 \end{pmatrix}. \tag{2.35}$$

Here, $\psi(\mathbf{k})$ is an even function of $\mathbf{k}$: $\psi(\mathbf{k}) = \psi(-\mathbf{k})$.

The spin triplet however has a symmetric pair potential:

$$\Delta_{ss'} = id(\mathbf{k}) \cdot [\mathbf{s}s_y]_{ss'} = \begin{pmatrix} -d_x(\mathbf{k} + id_y(\mathbf{k})) & d_z(\mathbf{k}) \\ d_z(\mathbf{k}) & d_x(\mathbf{k} + id_y(\mathbf{k})) \end{pmatrix}. \tag{2.36}$$

The $\mathbf{d}$-vector is an odd function of $\mathbf{k}$: $\mathbf{d}(\mathbf{k}) = -\mathbf{d}(-\mathbf{k})$.

### 2.3.4 2D spinless chiral $p$-wave superconductor

One can now use the mathematical concept from the previous chapter to describe a prototypical topological superconductor. The chiral 2D $p$-wave pairing is often called $p + ip$ - pairing. The Hamiltonian can be written as:

$$H = \int d^2\mathbf{r} \left[ \psi^\dagger \left( -\frac{\nabla^2}{2m} - \mu \right) \psi + \frac{\Delta}{2} \left[ e^{i\phi} \psi \left( \frac{\partial}{\partial x} + i \frac{\partial}{\partial y} \right) \psi + h.c. \right] \right]. \tag{2.37}$$

The phase factor of the pair potential is given by $\phi$. Fourier transformation to the $\mathbf{k}$-space and using $\Psi^\dagger(\mathbf{k}) = [\psi^\dagger(\mathbf{k}), \psi(-\mathbf{k})]$ gives the BdG-Hamiltonian:

$$H = \frac{1}{2} \int \frac{d^2\mathbf{k}}{(2\pi)^2} \Psi^\dagger(\mathbf{k}) H_{\mathrm{BdG}}(\mathbf{k}) \Psi(\mathbf{k}). \tag{2.38}$$

The BdG-Hamiltonian $H_{\mathrm{BdG}}(\mathbf{k})$ is given by a $2x2$ matrix:

$$H_{\mathrm{BdG}}(\mathbf{k}) = \begin{pmatrix} \epsilon(k) & \Delta^*(\mathbf{k}) \\ \Delta(\mathbf{k}) & -\epsilon(k) \end{pmatrix}, \tag{2.39}$$

where the kinetic energy $\epsilon(k) = \dfrac{k^2}{2m} - \mu$ and the pair potential $\Delta(\mathbf{k}) = i\Delta e^{i\phi}(k_x + ik_y)$ are scalars.

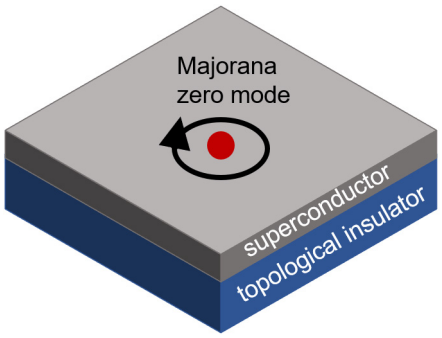


**Figure 2.20: Illustration of the Fu-Kane-proposal from 2008.** Placing a superconductor on top of a topological insulator is expected to induce superconductivity into the surface states of the TI which are predicted to host a Majorana zero mode. [63]

### 2.3.5 Proximity induced superconductivity on the surface of a 3D topological insulator

Fu and Kane proposed in 2008 that superconductivity can be induced into the surface state of a topological insulator by the proximity effect [63]. The resulting 2D superconductor is different to an ordinary superconductor since its surface states are not spin degenerate and they only have half the degree of freedom compared to an ordinary metal [28].

The Hamiltonian of the two-dimensional surface states of a three-dimensional topological insulator can be written as:

$$H_0(\mathbf{r}) = \psi^\dagger(-iv_\mathrm{F}\sigma \cdot \nabla - \mu)\psi(\mathbf{r}) \tag{2.40}$$

with the Pauli matrices $\sigma = (\sigma^x, \sigma^y)$ and the field operators $\psi \begin{pmatrix} \psi_\uparrow(r) \\ \psi_\downarrow(r) \end{pmatrix}$.

By placing an $s$-wave superconductor on top of a topological insulator, Cooper pairs can tunnel into the surface states (SS) of the topological insulator due to the proximity effect and a pairing potential

$$H_{\mathrm{scpair}}(\mathbf{r}) = \Delta_0 e^{i\phi}\psi^\dagger_\uparrow(\mathbf{r})\psi^\dagger_\downarrow(\mathbf{r}) + h.c. \tag{2.41}$$

is induced into the surface states. Here, $\Delta_0 e^{i\phi}$ depends on the phase of the superconductor. By adding equations 2.40 and 2.41, the following Hamiltonian is obtained:

$$H = \frac{1}{2}\int d^2\mathbf{r}\Psi^\dagger\mathcal{H}\Psi, \tag{2.42}$$

with the Nambu notation

$$\Psi = \begin{pmatrix} \psi_\uparrow \\ \psi_\downarrow \\ \psi^\dagger_\downarrow \\ -\psi^\dagger_\uparrow \end{pmatrix} \tag{2.43}$$

and the Bogoliubov-de-Gennes Hamiltonian

$$H = \begin{pmatrix} -iv_{\mathrm{F}}\sigma \cdot \nabla - \mu & \Delta_0(\cos\phi - i\sin\phi) \\ \Delta_0(\cos\phi + i\sin\phi) & iv_{\mathrm{F}}\sigma \cdot \nabla + \mu \end{pmatrix}. \tag{2.44}$$

The expression in the diagonal of the BdG-Hamiltonian 2.44 represents the kinetic energy terms, while the off-diagonal elements describe the pair potential. One can now define a polar angle in the momentum-space representation $\theta_k$ by introducing $\mathbf{k} = k_0(\cos\theta_k, \sin\theta_k)$ and additionally apply the transformation $c_k = \frac{1}{\sqrt{2}}(\psi_{\uparrow k} + e^{i\phi_k}\psi_{\downarrow k})$ to diagonalizes the kinetic energy term. The resulting Hamiltonian is given by:

$$\mathcal{H} = \sum_k \Big[(v_F k_0 - \mu)c_k^\dagger c_k + \frac{1}{2}\big(\Delta e^{i(\phi+\phi_k)}c_k^\dagger c_{-k} + H.c.\big)\Big]. \tag{2.45}$$

The pairing term $e^{i(\phi+\phi_k)}$ can be written as $e^{i\phi}(k_x + ik_y)$. This expression resembles the 2D $p$-wave $p_x + ip_y$ superconductor which is a prototypical topological superconductor [58].

# Chapter 3

# Experimental methods

## Contents



In this chapter the various growth and characterization techniques used in this thesis are presented. The first part discusses the thin film deposition by molecular beam epitaxy (MBE). The setup of the ultrahigh vacuum MBE chambers used in the scope of this work is shown and the basic principles of film growth is introduced. The second part of this chapter describes various methods used to characterize the structural and electrical properties of the grown films.

## 3.1 Thin film deposition

### 3.1.1 Molecular beam epitaxy (MBE)

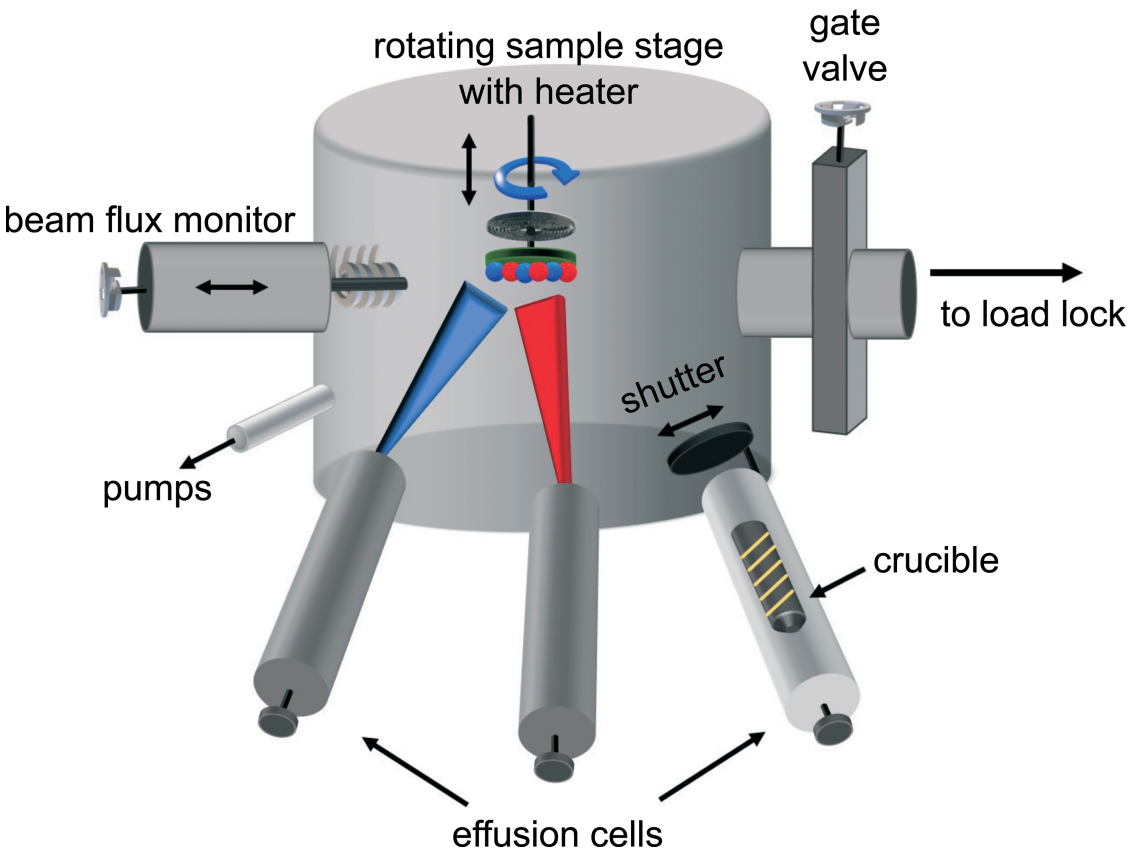


**Figure 3.1: Schematic illustration of a MBE chamber used to grow topological insulator thin films.**

Molecular beam epitaxy is a versatile thin film growth technique which takes place in ultrahigh vacuum (UHV). The UHV regime requires a pressure lower than $10^{-9}$ mbar. The mean free path of gas molecules for this pressure range is in the kilometer range, which is far larger than the diameter of a MBE chamber [74]. In a solid source MBE system, elements are heated in effusion cells from which they are evaporated. The evaporated materials travel as non-interacting molecular beams from the effusion cell to the substrate where they condense and the film growth takes place. A schematic illustration of a MBE chamber is depicted in Fig. 3.1. In general, an ultrahigh vacuum MBE chamber consists of a load lock chamber to introduce or remove samples into/from the MBE chamber and a main growth chamber which is constantly kept at ultrahigh vacuum conditions. As a consequence of the UHV conditions the main advantage of the MBE technique is a very clean film growth with extremely low contamination. Another advantage of the MBE growth is the slow deposition rate (typically

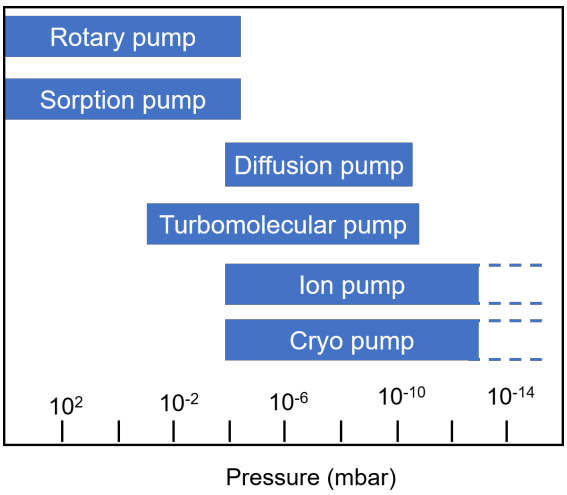


**Figure 3.2:** Pressure ranges in which different pumps can be used (adapted from [75])

a few Å $\mathrm{min}^{-1}$). The slow growth mode ensures a higher quality epitaxial film growth as long as the surface absorbed molecules have a high enough diffusion on the substrate surface. Additionally, MBE growth provides a precise control of the chemical composition and doping of the grown film. Furthermore, the film thickness can be accurately controlled in the atomic-layer range. Another advantage is that the grown films have a smooth surface, an attribute important for achieving higher surface carrier mobility which is crucial for topological insulator materials.

The materials discussed in this work were grown in three different MBE systems: Two chambers designed by Eiko (MBE1 and MBE2) and a chamber constructed by MBE Komponenten (MBE3). A combination of pumps is needed to achieve the UHV pressure regime, while the pressure is monitored by several pressure gauges. Both Eiko chambers can reach background pressures in the main growth chamber lower than $10^{-9}$ mbar, whereas the MBE3 chamber is able to achieve a background pressure of $10^{-11}$ mbar. The difference in pressure between the chambers results primarily from the pumps which are connected to the systems. Both Eiko chambers are equipped with rotary pumps to generate a pre-vacuum and turbo pumps to achieve ultrahigh vacuum conditions. MBE3 additionally has an ion getter pump in the growth and preparation chamber, and a cryogenic pump in the main growth chamber which significantly improve the vacuum conditions (see Fig. 3.2) [75]. To further reduce the background pressure, the chamber walls are cooled by water or liquid nitrogen, which helps to trap residual gases.

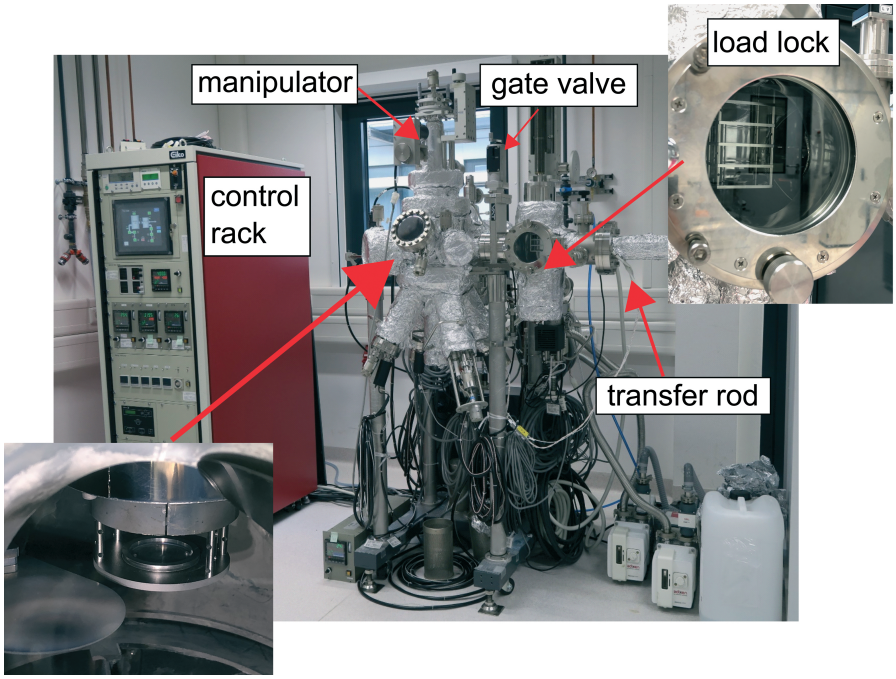


**Figure 3.3: Picture of the MBE2 chamber.** The control rack to monitor the pumps and evaporator temperatures is shown on the left of the central photo. The inset on the lower left shows the inside of the main chamber with the sample holder on the sample stage visible while the shutter is open. The inset on the upper right displays the load lock with several stages to store sample holders.

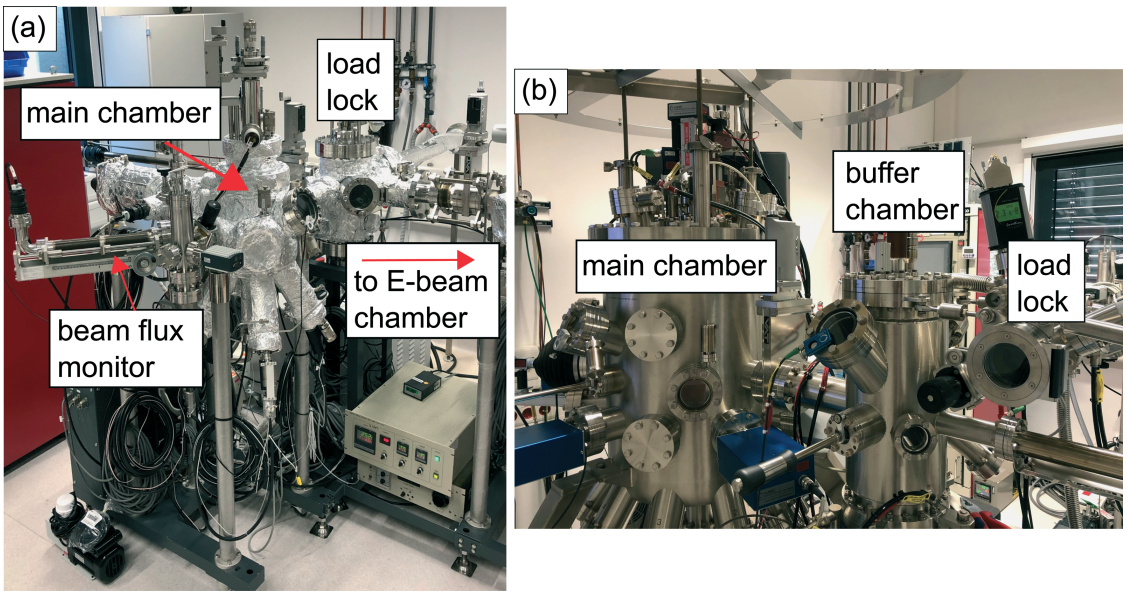


**Figure 3.4: Pictures of the MBE1 and MBE3 chambers.** (a) MBE1 is similar to MBE2. Additionally, this system has an attached MBE chamber which is equipped with an electron-beam evaporator. (b) MBE3 is equipped with an additional buffer chamber situated between main growth chamber and load lock.

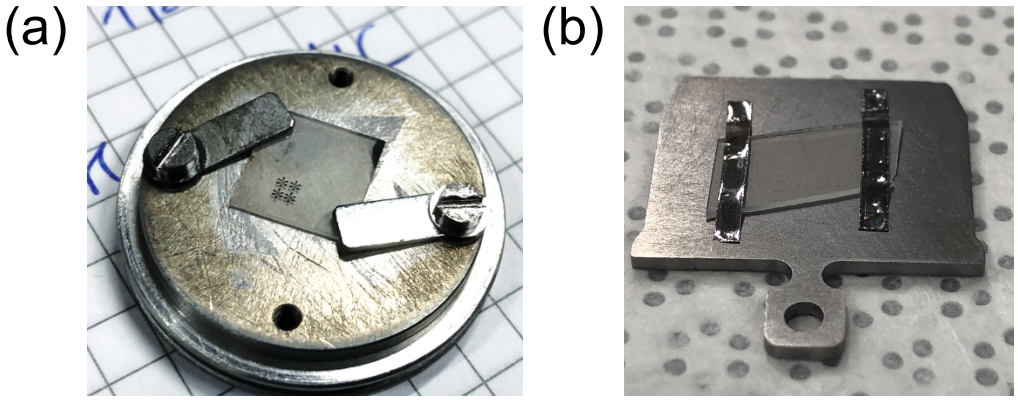


**Figure 3.5: Pictures of the sample holders used in the MBE chambers:** (a) Molybdenum sample holder used in Eiko chambers MBE1 and MBE2. The substrate is fixed with 1 µm-thick tantalum stripes. (b) Tantalum Omicron style sample holder for MBE3. The substrate is fixed by spot welded tantalum stripes.

The substrate is mounted on a sample holder (Eiko type for MBE1 and MBE2, Omicron style for MBE3). For the Eiko sample holder, the substrate is fixed by tantalum stripes which are tightly screwed to provide good thermal contact between substrate and sample holder, whereas the substrates on the Omicron sample holders are spot welded with tantalum stripes (see Fig. 3.5). Molybdenum and tantalum are selected as materials for the sample holder components due to their high temperature resistance and low vapor pressure. After mounting the substrate, the sample holder is introduced face down into the MBE system via a load lock chamber with a background pressure of approximately $10^{-7}$ mbar.

The load lock chamber is frequently exposed to ambient conditions. It is separated from the main growth chamber by a gate valve and thus allows introducing substrates while keeping UHV conditions in the growth chamber. It additionally can be used for sample storage under vacuum conditions.

From the load lock chamber, the substrate is then transferred using a linear transfer rod into the main growth chamber and placed on the sample stage. This stage is rotatable to ensure a homogeneous distribution of incoming material and can additionally be heated by a graphite heater. The substrate temperature is controlled by a standard thermocouple and can reach up to 1000 °C. MBE3 has an additional preparation chamber situated between load lock and growth chamber which is used to anneal and clean the substrates before transferring them into the main growth chamber.

Both Eiko MBE chambers contain four ports for evaporation cells which can be configured depending on the particular growth system. Four effusion cells are attached to MBE1, while MBE2 is equipped with three effusion cells and one four-pocket electron-beam evaporator. MBE3 can host up to 12 different evaporators.

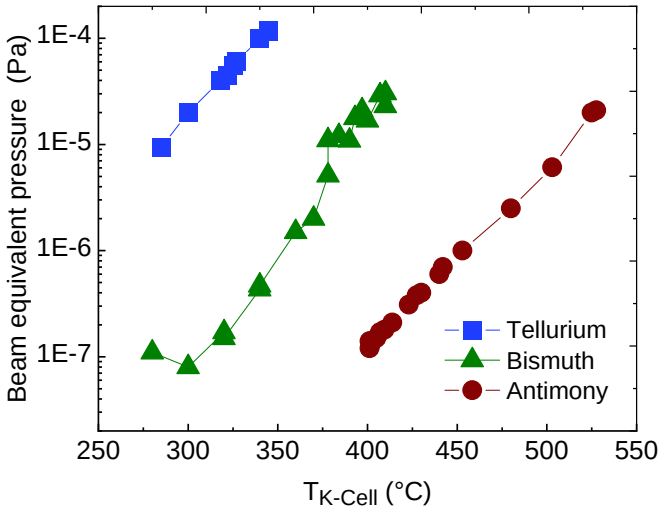


**Figure 3.6:** Beam equivalent pressure recorded in the MBE1 chamber as a function of the respective effusion cell temperature for tellurium (blue squares), bismuth (green triangles) and antimony (red spheres).

The effusion cells contain crucibles usually made out of alumina, tungsten or pyrolytic boron nitride (PBN) depending on the chemical they contain. They are filled with high purity materials ($> 6N$). A heating tungsten or tantalum filament is wrapped around the crucible and a thermocouple is mounted close by to record the temperature and regulate the heater power via a proportional-integral-differential (PID) feedback loop. The evaporated materials sublimate into the gas phase and travel towards the substrate in form of a molecular beam. Each effusion cell, as well as the sample stage, is equipped with a shutter, which can close the cell/substrate off and as such stop the evaporation of a particular material or the overall film growth.

The amount of evaporated material is controlled by the temperature of the evaporation cell. It is determined by the beam equivalent pressure (BEP) which is measured using an ion gauge (beam flux monitor). The beam flux is given by the number of molecules of an element which condense on a surface unit per time [75, 76]. To measure the beam flux, the ion gauge is inserted into the growth chamber right below the sample stage and the difference between background pressure with evaporator shutter closed and opened is noted. The beam equivalent pressure for bismuth, antimony and tellurium for different effusion cell temperatures in the MBE1 chamber is shown in Fig. 3.6. Such a graph is obtained for every MBE chamber and can be used to set the effusion cell temperature in order to evaporate a certain amount of material. To have a good control over the growth conditions, the fluxes should be monitored closely since they change over time as the material in the effusion cell is depleted.

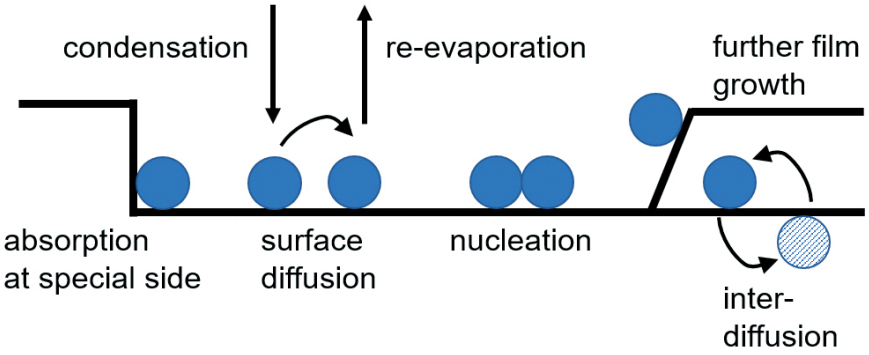


**Figure 3.7: Schematic illustration of growth dynamics occurring during thin film growth:** absorption, condensation, diffusion, re-evaporation, nucleation and inter-diffusion (adapted from [75])

### 3.1.2 Growth dynamics

Different processes are involved in thin film growth using the molecular beam epitaxy technique [75, 77, 78]. The most important processes which take place once the molecular beam arrives at the substrate surface, are illustrated in Fig. 3.7. Materials are evaporated from effusion cells in the MBE chamber and are transported in form of a molecular beam to the (heated) substrate where they condense on the surface and chemically react with each other. These processes strongly depend on the substrate temperature.

If the substrate temperature is too high or the absorption energy of the substrate atoms is low such that the incoming material can not stick to the surface, the incoming atom might immediately re-evaporate. If the substrate temperature allows the arriving atom to condenses on the substrate surface, there are two possibilities: The atom either remains at the initial position or is only weakly bonded and still mobile enough to diffuse along the surface. The diffusion length depends on the substrate temperature. If the atom moves along the surface of the substrate and encounters a defect or step edge, it might get absorbed at this imperfection. Depending on the substrate and the arriving molecules, both can exchange positions during an interdiffusion process. Newly arriving molecules can nucleate with atoms which are already sitting on the surface and chemically react with each other. This nucleation center is where the film growth begins [75].

Depending on the various growth parameters, such as substrate cleaning, deposition rate or temperature, the molecules on the substrate can form a single crystalline, amorphous or polycrystalline film. Among these, the single crystalline film shows uniformly arranged crystal structure across the whole film.

In order to grow a single crystalline film, the substrate temperature and deposition rate need to be optimized. For instance, if the substrate temperature is too low, the mobility of the incoming molecule is too low in order to form a a single crystalline film. Consequently, the grown film islands will be randomly oriented, resulting in a polycrystalline or amorphous growth. In addition to the correct substrate temperature, the growth rate has to be rather slow (typically a few $\text{Å}\,\text{min}^{-1}$) in order to achieve a single crystalline film. The molecules need time to diffuse along the surface and nucleate before new material arrives at the surface [79].
A phenomenological illustration of the growth process is shown in Fig. 3.8. One can distinguish between three growth modes: layer-by-layer growth (Frank van der Merve, FM), layer-plus-island growth (Stranski-Krastanov, SK) and island growth (Vollmer-Weber, VW) [75].
The interaction strength between atoms and substrate, and furthermore the atoms among each other, determines which growth mode takes place. Additionally, the deposition rate, substrate temperature and surface morphology of the substrate play an important role.
The characteristic of the layer by layer growth (FM) is that a new film layer starts growing only once the underlying film layer is complete. The interaction between atoms of a certain layer is weaker than the interaction between the layer and the substrate. The opposite interaction takes place in the Vollmer-Weber growth. Here, material clusters are formed from nucleation centers and grow into islands on the substrate surface. The bonding between the atoms is stronger among each other than between atoms and substrate. The Stranski-Krastanov growth process is a combination of the FM and VW mode. In this case, usually a few monolayers are grown in the layer-by-layer mode, followed by the appearance of island growth on top of the continuous film. When the film thickness is large enough, the islands tend to merge and cover the complete substrate surface [75].

### 3.1.3 Substrate selection and preparation

The interaction between substrate surface and grown film plays a crucial role for the MBE growth. While growing, the film mimics the atom arrangement of the substrate, hence the orientation and crystal structure of the grown film matches the structure of the substrate. This process is called epitaxy. An important factor in the growth process besides crystal orientation and surface geometry, is the lattice mismatch between substrate and film. The interaction between film and

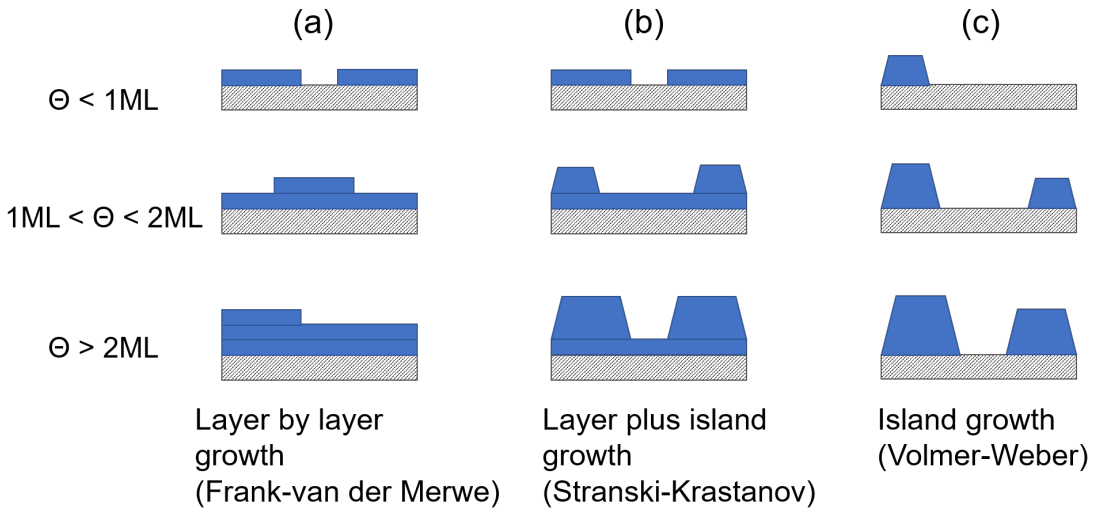


**Figure 3.8: Schematic illustration of the three growth modes on a substrate (dashed line).** Θ represents the coverage on the substrate in monolayers (ML). (a) Layer by layer or Frank-van der Merwe mode, (b) Layer plus island growth or Stranski-Krastanov mode, (c) Island growth or Volmer-Weber mode (adapted from [75])

substrate can create misfits and stress during the film growth. By carefully choosing an appropriate substrate, stress at the interface between film and substrate can be minimized [77, 78]. The growth mechanism of topological insulator materials relies on the so called van der Waals (vdW) epitaxy. The weak van der Waals bonds allow for a larger lattice mismatch between film and substrate while still remaining a high-quality film growth. It is also easier to grow heterostructures of different materials in this manner [80, 81]. For that reason, the MBE growth of topological materials was performed on various substrates including CdS (0001) [82, 83], Si(111) [84], $BaF_2$ [85], InP [86], GaAs [87, 88], $Al_2O_3$ (0001) [15, 89] and Si(111) [90].

The lattice mismatch between a sapphire substrate and a $Bi_2Te_3$ film is approximately 9% [91]. Despite the large mismatch, it is still possible to grow a single crystalline epitaxial film due to the van der Waals growth mechanism. An exemplary structural characterization of a $Bi_2Te_3$ film grown on a sapphire substrate in the MBE1 chamber is shown in Fig. 3.9. The atomic force microscopy (AFM) image displayed in Fig. 3.9(a) shows flat triangular terraces with sharp edges, which is an indication for high-quality epitaxial film growth. The height profile in Fig. 3.9(b) taken along the white line in the AFM image, reveals the typical quintuple layer height in this material of 1 nm [13]. Additionally, the x-ray diffraction (XRD) pattern in Fig. 3.9(c) indicates an epitaxial $Bi_2Te_3$ film growth, which shares hexagonal crystal structure of the sapphire along the $c$-axis.

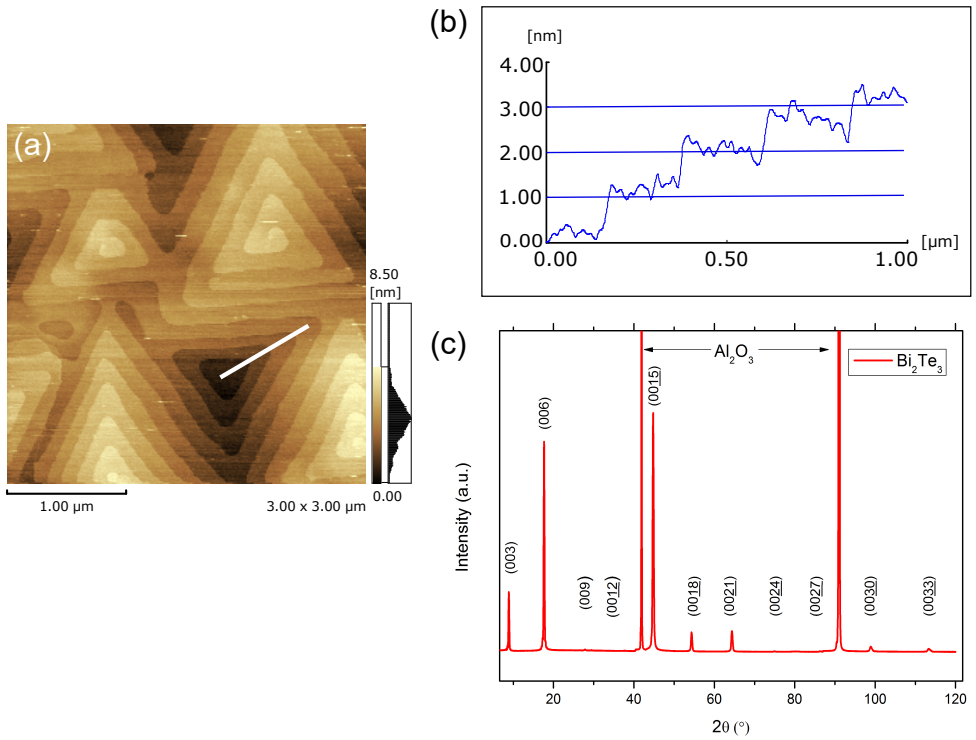


**Figure 3.9: Structural characterization of a $Bi_2Te_3$ film grown on $Al_2O_3$.** (a) AFM image (3x3 µm) of a $Bi_2Te_3$ film grown on $Al_2O_3$ with flat terraces visible. (b) Height profile along the white line in the AFM image gives step heights of 1 nm. (c) XRD pattern of a $Bi_2Te_3$ film grown on $Al_2O_3$, only the (00l)-peaks from film and substrate are visible.

Aside from the structural parameters of the substrate, a clean, contaminate free substrate with a smooth surface is essential for high-quality film growth. Even small contamination and impurities can influence the crystalline growth of a film. Different methods can be used to remove specific residues from the substrate surface such as particles or thin film layers of contaminates. Generally, these methods can be divided into wet chemical cleaning and dry cleaning [92, 93].

In the scope of this work, two different substrates were used: sapphire $Al_2O_3$ (0001) and iron-doped indium phosphide InP (111)A. Both substrates are epi-ready prepared and (semi-)insulating, which is important to perform transport measurements. For the sapphire cleaning, a combination of wet-chemical and dry cleaning was established, whereas the InP substrates were only chemically wet cleaned.

**Preparation of the sapphire substrate**

Sapphire is chemically very stable and can be annealed at high temperatures due its high melting point of 2053 °C [94]. These properties ensure that there is no chemical reaction between substrate and film. Furthermore, it is an insulator which allows electrical transport measurements of the grown film without additional transport through the substrate.

The as-received epi-ready sapphire wafers are spincoated with a layer of protective photoresist before cutting them into smaller pieces which fit the sample holders. First, the sapphire is cleaned in an ultrasonic bath with acetone and isopropanol (IPA) to remove the protective resist and further residues at the surface. Acetone and IPA are known to remove organic contaminants, but they alone rarely remove all contamination from the sapphire surface [93]. Consequently, the sapphire is further cleaned by oxygen, argon and $CF_4$ reactive-ion etching (RIE) plasma for 1 minute each. Approximately 8 nm to 10 nm of the sapphire thickness are etched in this cleaning step. The prepared substrates are loaded into the MBE chamber and annealed up to 950 °C in UHV conditions to further remove adsorbates and contaminants from the surface. The substrates are afterwards kept at 400 °C until the film growth procedure begins. This cleaning method has shown to be successful in achieving a contaminate free, smooth surface.

The x-ray diffraction pattern and atomic force microscopy image measured on a sapphire substrate cleaned by the described cleaning procedure are shown in Fig. 3.10. Both measurements confirm the single crystalline phase and low surface roughness of less than 1 nm of the cleaned substrate.

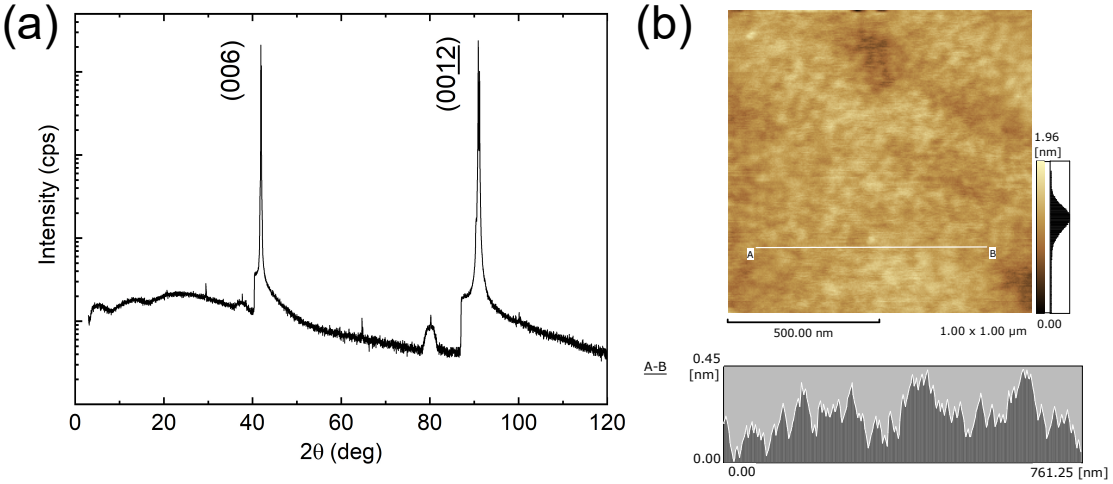


**Figure 3.10: XRD and AFM measurement of a cleaned sapphire substrate.** (a) XRD pattern of a cleaned sapphire substrate. Only the (00l) peaks can be identified. (b) AFM image (1x1 µm) and height profile indicate a surface roughness of less than 1 nm.

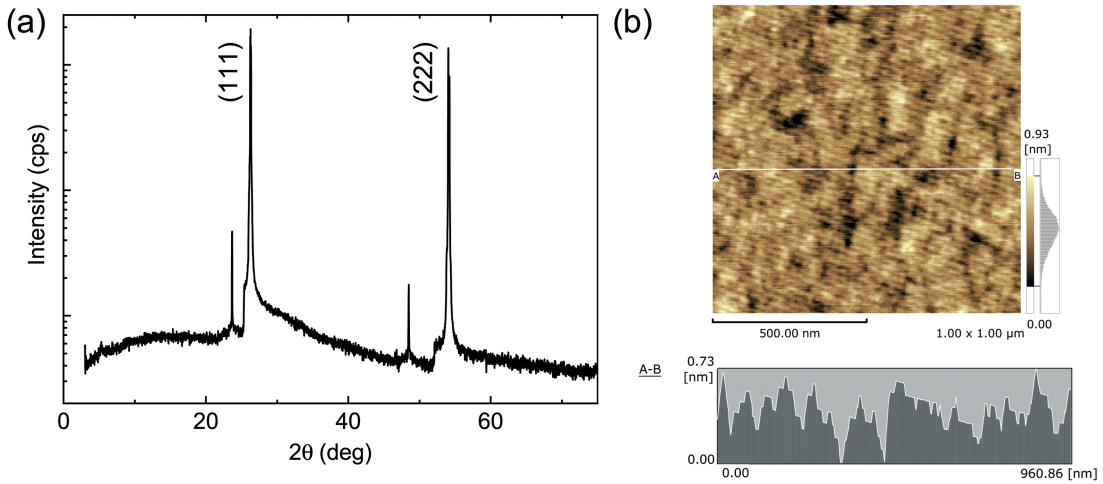


**Figure 3.11: XRD and AFM measurement of a cleaned InP substrate.** (a) XRD pattern of the InP substrate reveals a single crystalline phase. (b) AFM image (1x1 µm) and height profile show a surface roughness of less than 1 nm.

**Preparation of the InP substrate**

The epi-ready InP pieces are cleaned in acetone and IPA using an ultrasonic bath. No plasma cleaning by RIE is used for the InP pieces, since the substrate surface will be heavily damaged in the process. Figure 3.12 shows two AFM images of a InP substrate which was exposed to 1 minute argon (a) or 1 minute $CF_4$ plasma (b). The AFM image shown in Fig. 3.12 (a) was taken after the InP was exposed to argon RIE and the height profile taken along the middle of the AFM image reveals a surface roughness of approximately 40 nm. Figure 3.12 (b) shows an AFM image measured on a InP substrate which was treated by $CF_4$ in the RIE machine. Small holes are visible all across the substrate surface and the surface roughness is approximately 2 nm. In both cases the surface is too heavily damaged to allow for a flat crystalline film growth.

Indium phosphide has a surface oxide layer which can be thermally adsorbed by annealing the sample. However, if the sample is annealed at too high temperatures, the raised temperatures lead to the decomposition of phosphorus from the sample and leave indium pillars on the surface [95, 96]. This behavior is illustrated in Fig. 3.13. Here, the InP substrate was annealed in the MBE chamber from 375 °C to 650 °C while the pressure in the chamber was continuously monitored by the beam flux monitor. While heating the substrate up to 650 °C, the pressure increased by two orders as shown in Fig. 3.13 (a). This increase in pressure indicates the evaporation of material in the MBE chamber. An optical picture of the damaged film after annealing can be seen in the inset of Fig. 3.13(a). The damage is even more apparent in the AFM image depicted in Fig. 3.13(b). Here, indium pillars of up to approximately 500 nm height are visible in the AFM image and the height profile taken along the white line. To prevent such damage of the InP substrate, the annealing temperature has to be carefully calibrated for each MBE chamber. The optimized annealing temperature was found to be 350 °C for MBE1 and MBE2, and up to 550 °C for MBE3. The varied optimized temperatures found for the individual chambers result from different substrate heaters, sample holders and sample manipulators used for the respective MBE chambers. A InP substrate which was cleaned by the optimized process for MBE2 was investigated by XRD and AFM measurements. The exemplary results of these measurements are shown in Fig. 3.11. The XRD pattern shown in Fig. 3.11 (a) reveals a single crystalline phase and the AFM image and height profile in Fig. 3.11 (b) indicate a surface roughness of less than 1 nm.

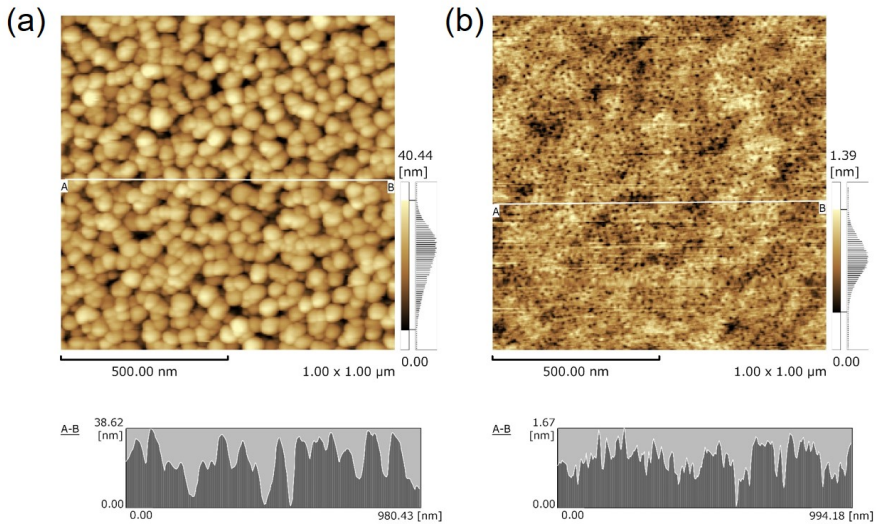


**Figure 3.12: AFM images (1x1 µm) of a InP substrate treated with RIE plasma:** (a) InP treated with 50 W argon plasma for 1 minute. The surface is visibly damaged with a surface roughness of approximately 40 nm. (b) InP treated with 50 W $CF_4$ plasma for 1 minute. Small holes are visible all across the substrate surface.

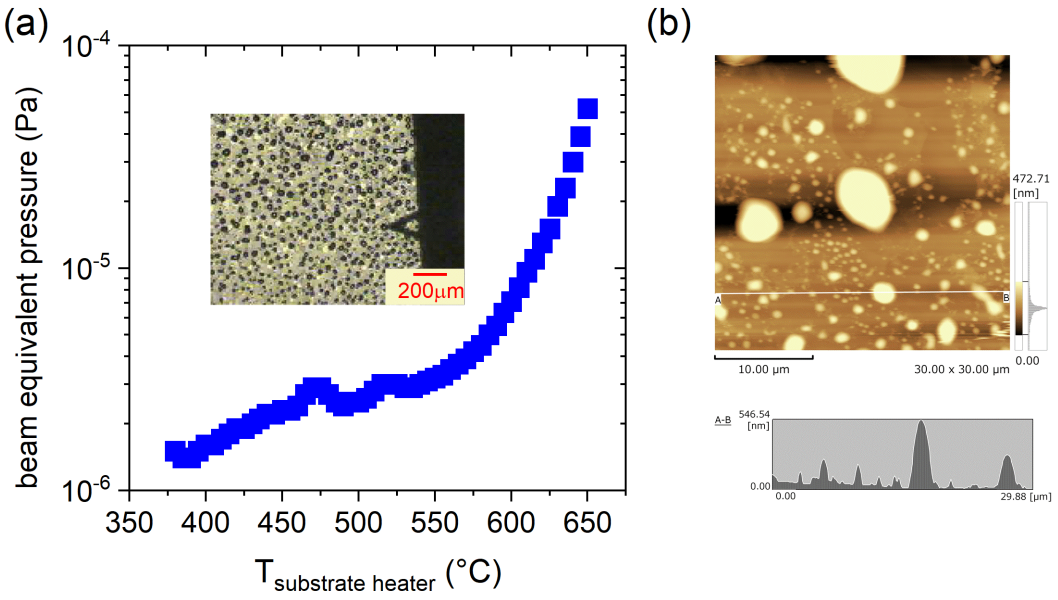


**Figure 3.13: Annealing of an indium phosphide substrate in the MBE chamber:** (a) The beam equivalent pressure in the chamber measured in relation to the substrate temperature. The pressure rises two orders of magnitude with the temperature increasing from 375 °C to 650 °C. The inset shows an optical image of the damaged InP substrate due to high temperatures. (b) AFM image (30x30 µm) of the annealed InP substrate.

## 3.2 Thin film characterization techniques

After growing a thin film by molecular beam epitaxy, the films are characterized using several methods and instruments. The structural properties are checked using atomic force microscopy (AFM), x-ray diffraction (XRD) and energy-dispersive x-ray spectroscopy (EDX). The magnetic and electrical properties are studied by transport measurement at low temperatures. The grown films are patterned into predefined shapes by microfabrication. Within the microfabrication process, usually a dielectric layer is deposited by atomic layer deposition (ALD) and parts of the film are etched by reactive-ion etching (RIE). ALD is furthermore used to deposit a layer of $Al_2O_3$ after film growth to protect the grown film from oxidization.

### 3.2.1 Atomic force microscopy (AFM)

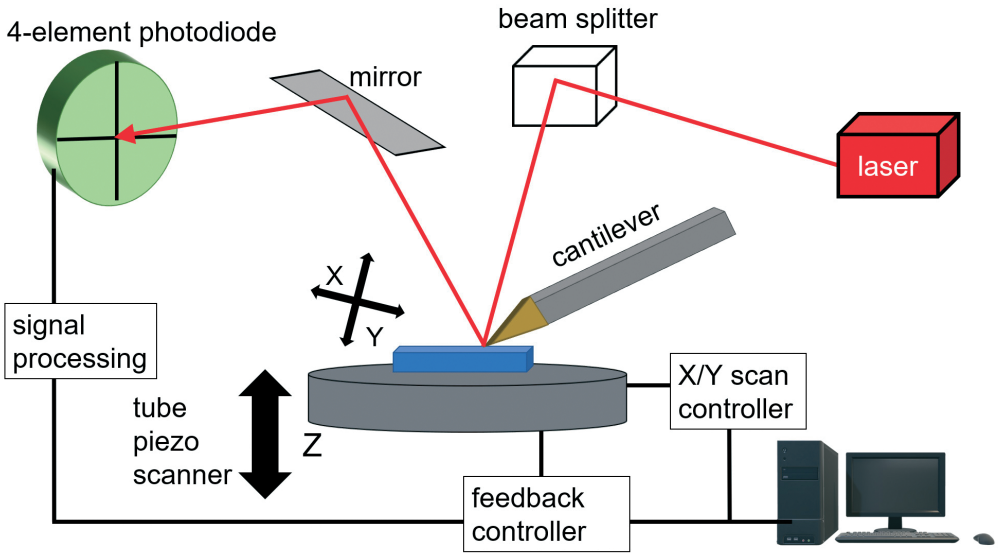


**Figure 3.14: Schematic drawing of the AFM set up by Shimadzu used in this thesis** (modified from [97])

Atomic force microscopy (AFM) is a type of scanning probe microscopy and a technique to observe the topography of a sample's surface in real space. A nanometer sized sharp probe tip, attached to a silicon cantilever, is brought into close proximity to the sample surface. The tip is moved laterally across the sample surface and the interaction between tip and surface is recorded. This interaction is measured by monitoring the variation or displacement in $z$-direction in amplitude of the cantilever. Therefore, a laser beam is focused on the backside of the cantilever and reflected onto a position-sensitive photo-diode (see Fig. 3.14).

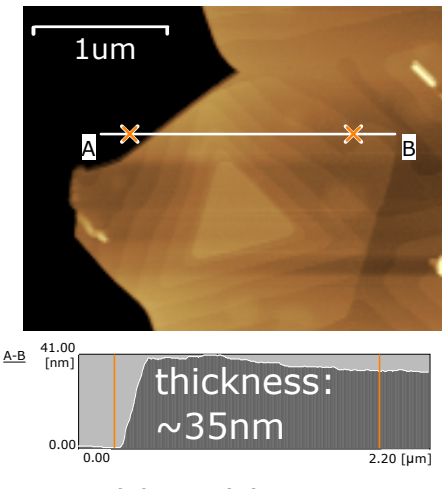


**Figure 3.15: Typical AFM image (3x3 µm) of a 35 nm-thin $Bi_2Te_3$ film grown in the scope of this work.** The atomic force microscope is used to check the morphology of the grown film and to determine the thickness by measuring the height difference along a scratch in the film. The height profile recorded along the white line in the AFM image is depicted below the image.

All AFM images shown in this thesis were measured in the so-called *contact mode* using a Shimadzu SPM 9700 scanning probe microscope. In this mode, the sample surface is scanned while the force between surface and cantilever is kept constant by a feedback loop which compares a user defined operating point and the current vertical displacement of the tip. The cantilever is acting as a spring which is deflecting according to the interaction between the tip and the sample (spring constant $k$ in this case 0.15 N m$^{-1}$ to 0.57 N m$^{-1}$). After starting the measurement, the cantilever is lowered to make contact with the sample surface until the force between tip and sample overcomes the spring constant of the cantilever. The sample features at different heights influence the cantilever deflection and the subsequent reflected beam. This variation is recorded by the photo-diode. Together with the sample position which is determined by the x-y-z-piezo scanner, a topography image of the sample surface can be resolved [97, 98].

A typical AFM image taken on a $Bi_2Te_3$ film grown in the scope of this thesis is shown in Fig. 3.15. The atomic force microscope measurement is used to verify a good morphology of the grown film and additionally to determine its thickness. For this purpose, the height profile along a scratch in the grown film is measured as shown by the height profile scan below the AFM image in Fig. 3.15.

### 3.2.2 X-ray diffraction (XRD)

X-ray diffraction (XRD) is a widely used non-destructive method to study the crystal structure of a material. A crystalline sample consists of a periodic array of atoms with a typical inter-atom spacing in the Angstrom range, which is in the same order as the wavelength of x-rays [99]. When a monochromatic x-ray beam hits the sample, the x-rays will scatter. The periodic atomic planes cause the

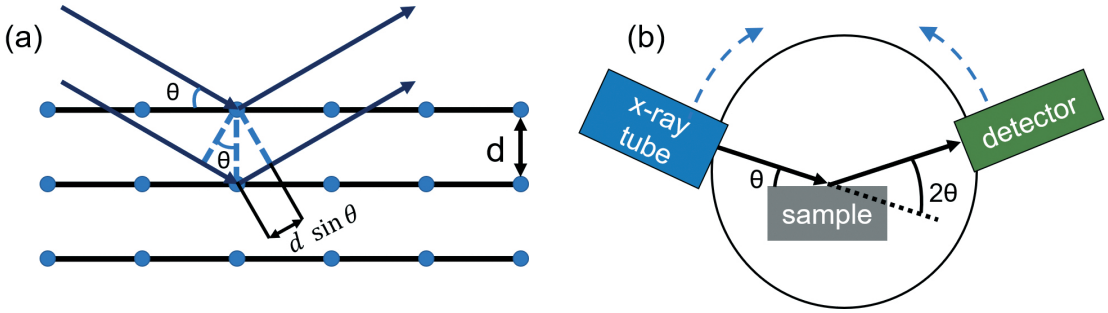


**Figure 3.16:** (a) Schematic drawing to explain Bragg's Law: Two x-ray beams interfere constructively when the difference of the traveled path $2d\sin\theta$ equals to an integer of the wavelength $n\lambda$. (b) Schematics of the experimental setup. X-rays are produced in a x-ray tube and arrive at the sample, where they scatter. The intensity is recorded by the detector. Both the x-ray tube and the detector may rotate while the sample is static. (adapted from [32, 99])

incident x-ray beams to interfere with one another while they leave the crystal. The reflected x-rays which are in phase, will interfere constructively if they fulfill Bragg's law [32]:

$$2d\sin\theta = n\lambda. \tag{3.1}$$

Here $2d\sin\theta$ is the path difference for x-rays which are reflected from adjacent planes, $\lambda$ denotes the wavelength of the x-rays and $2\theta$ is the angle between the crystallographic plane and the reflected x-ray beam, $n$ is an integer (see Fig. 3.16(a)).

The films characterized by x-ray diffraction in this thesis all share the same rhombohedral crystal symmetry and a growth along the $c$-direction (see the crystal structure depicted in Fig. 4.1). Using the Bragg equation, it is possible to derive the lattice parameter of these films. The equation to calculate the $d$-spacing for rhombohedral systems is given by [99]:

$$\frac{1}{d^2} = \frac{h^2+k^2}{a^2} + \frac{l^2}{c^2} \tag{3.2}$$

with the lattice parameters $a = b$ and $c$, and the Miller indices $h$, $k$, $l$.

Equations 3.1 and 3.2 now allow to calculate the $c$-lattice parameter of the grown topological insulator films by using (with $h = k = 0$):

$$\frac{1}{d^2} = \frac{l^2}{c^2} \Longleftrightarrow c = \frac{n\lambda}{2d\sin(\theta)}l \tag{3.3}$$

In order to analyze the structure of the grown samples, so called $\theta$-$2\theta$ scans are performed. Here, $\theta$ is the incident angle of the x-ray beam, while the detector position, depicted by the angle $2\theta$, and the intensity (as counts per second) are

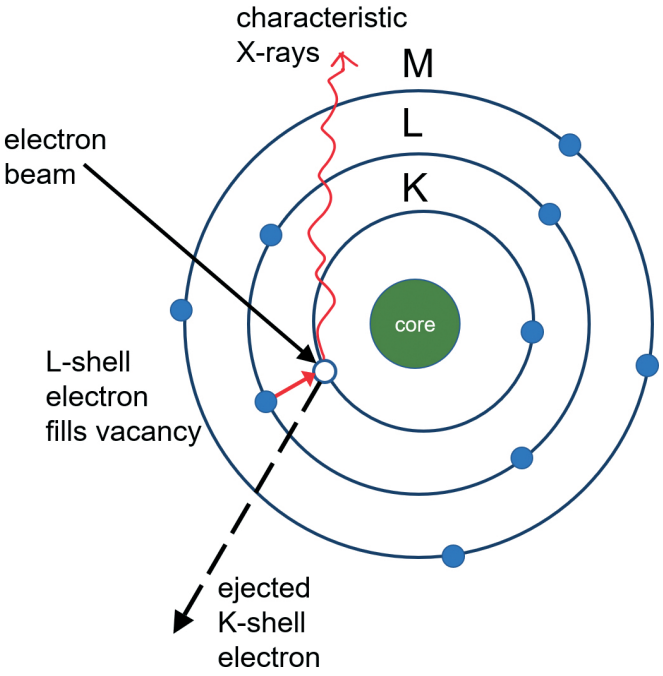


**Figure 3.17: Schematic illustration of energy-dispersive x-ray spectroscopy (EDX).** A K-shell electron interacts with an incoming electron and is ejected. An electron from an outer L-shell fills the created vacancy while emitting a photon with an element specific characteristic x-ray wavelength. (adapted from [100])

recorded during the measurement (see Fig. 3.16(b)). With this type of scanning mode it is possible to obtain details about the crystal structure and composition of the measured sample [99].

The XRD experiments shown in this work were performed using a Rigaku Ultima IV diffractometer. The x-ray beam is generated from a copper source at the Cu-$K_\alpha$ line with $\lambda$=1.540 56 Å.

### 3.2.3 Energy-dispersive x-ray spectroscopy (EDX)

Energy-dispersive x-ray spectroscopy (EDX) is a technique to identify the chemical composition of materials. A EDX system is usually attached to a scanning electron microscope (SEM) in order to select the position on the sample which is supposed to be analyzed.
A x-ray beam is focused on the sample and interacts with it. The incoming electrons carry enough energy to remove electrons from inner orbitals of the atom. An electron from an outer shell, for example the L-shell, will then fill the created vacancy and emit a photon while doing so. The emitted photon has an element specific energy (*characteristic x-rays*). Therefore, the energy spectrum of the emitted photons provides information of the chemical composition of the sample. The emitted photon energy $K_\alpha$ is given by $\Delta E = hf$, with the Planck's constant $h$ and the frequency of the emitted photon $f$, and it is equal to the energy difference between K- and L-shell. A detector records the spectrum and compares it

to spectra taken on standard element samples. The areas of the measured peaks in the energy spectrum are a measure of the amount of a specific element. The EDX software then automatically calculates the atomic percentage of a certain element [101, 102].

Since the samples measured in this thesis are of rather low thickness, it is important to use low acceleration voltages of 5 kV to 10 kV to decrease the penetration depth of the incoming x-rays and hence increase the surface sensitivity of the EDX measurement. A typical energy spectrum of a $Bi_2Te_3$ film grown on sapphire is shown in Fig. 3.18. The individual emission lines for bismuth, tellurium, aluminum and oxygen are labeled.
The EDX measurements shown in this work were performed using an Oxford Instruments AztecOne system with a x-act Silicon Drift Detector combined with a Jeol JSM-6510 scanning electron microscope.

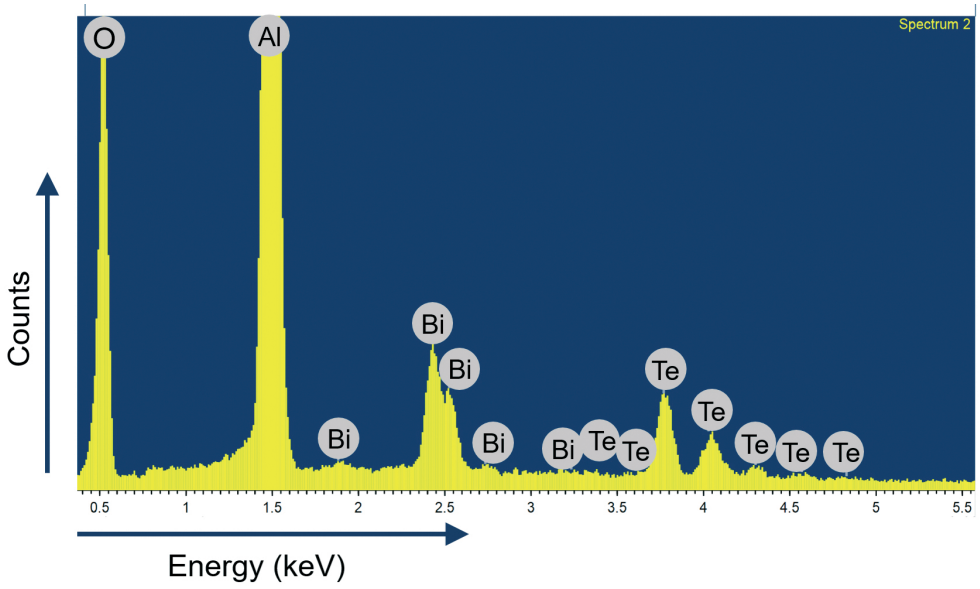


**Figure 3.18: EDX spectrum of a $Bi_2Te_3$ film grown on sapphire.** The characteristic x-ray emission lines for Bi, Te, Al and O are labeled.

### 3.2.4 Microfabrication

The microfabrication of the devices studied in this thesis mainly consists of several key techniques including lithography, wet or dry etching, and standard lift off process, which are described in detail as follows.

**Lithography**

Photolithography is a microfabrication technique used to transfer a designed pattern onto a sample. In this work, a maskless micro pattern generator (Heidelberg $\mu$ PG 101) with a structure resolution down to 0.6 µm is used. As a first step, the sample is spin-coated with a layer of positive photoresist AZ1505. After baking the resist at 100 °C for 1 minute, the sample is loaded into the lithography machine. Here, following the specified pattern design, parts of the resist are exposed to a 2 mW laser beam. The exposed parts of resist are chemically different from the non-exposed areas and can be removed in the consecutive developing step in a TMAH (TetraMethylAmmoniumHydroxide) based solvent. With this technique, one can repetitively define resist structures to be used in the lift-off and etching process, both of which are central in realizing final devices. Schematics of these processes are shown in in Fig. 3.19 and Fig. 3.20.

**Etching:** The etching schematic is illustrated in Fig. 3.19. To start with, the substrate is coated with photoresist (a) and exposed to the laser beam (b). After the development, some parts of the film are still protected by photoresist (c). In order to remove unwanted regions of a film, the part which is not protected by photoresist will be etched by either chemical wet-etching (in a solution of $H_2O_2$ 3 : 1 $H_2SO_4$) or dry (plasma) etching (d). After stripping off the resist in acetone and isopropanol, the final structure is left ((c)-(e)).

**Lift-off:** The lift-off schematic is displayed in Fig. 3.20. Again, the sample is coated with resist and subsequently exposed to the laser beam and developed ((a)-(c)). Afterwards, typically a metal layer is deposited onto the whole surface of the sample (d). To initiate the lift-off process the sample is placed in a solvent solution, for example acetone or N-Methyl-2-pyrrolidone (NMP). During the lift-off process, the remaining resist is washed out by the solvent and thereby lifts the metal parts covering these regions (e). The metal part with no underlying resist remains on top of the film (f). This technique is for example used to create metal contact pads.

The results of the microfabrication processes should be monitored by checking the devices in a microscope. Figure 3.21 shows such typical optical images of the microfabrication processes described above. Figures 3.21 (a) and (b) display the etching step. In (a) a Hall-bar device is protected by resist, while the surrounding film is not protected. After wet etching, the unprotected film is completely removed (see Fig. 3.21(b)). A result of a lift-off process can be seen in Fig. 3.21 (c)

and (d). A Hall-bar-patterned film is shown in (c). The sample was coated with resist and only the arms of the Hall bar were exposed by the laser beam. The resist in this area was dissolved during development, while the rest of the sample is still covered with resist (green color). Afterwards, this sample was sputtered with 40 nm gold. To start the lift-off process, the sample was then placed in NMP solvent and the resist below the gold was dissolved. The final structure, in which the gold only remains on the arms of the Hall bar, is shown in figure (d).

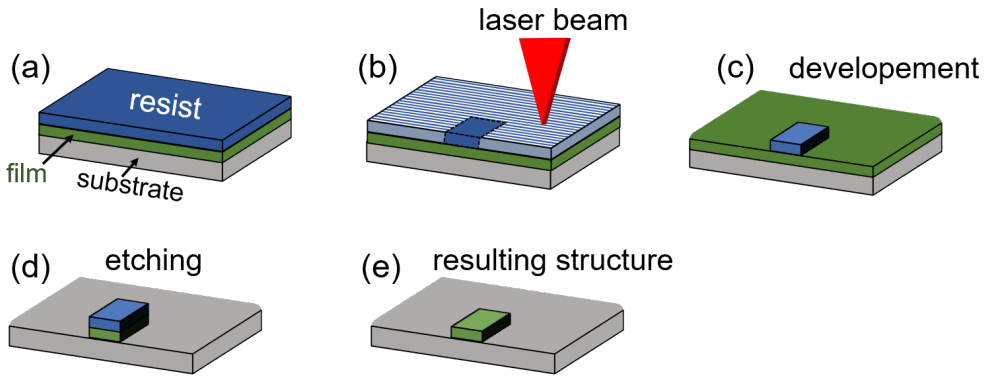


**Figure 3.19: Microfabrication scheme including etching:** (a) Substrate and film covered with resist. (b) Laser exposure. (c) Development, the exposed part of the resist is dissolved. (d) The part of the film which is not protected by resist is etched away. (e) The final structure remains after stripping of the resist.

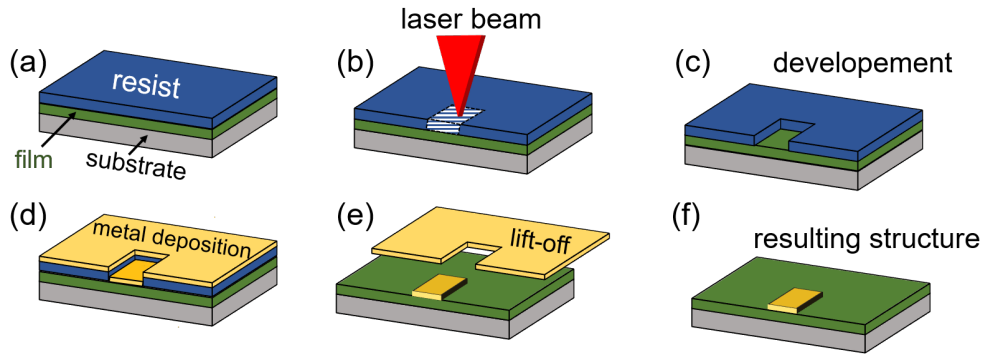


**Figure 3.20: Microfabrication scheme including lift-off:** (a) Substrate and film covered with resist. (b) Laser exposure. (c) Development, the exposed part of the resist is dissolved. (d) Metal is deposited on the whole surface of the substrate, including the region which is nor covered with resist. (e) The resist is removed by a solvent and lifts the metal off. (f) Final structure after lift-off remains.

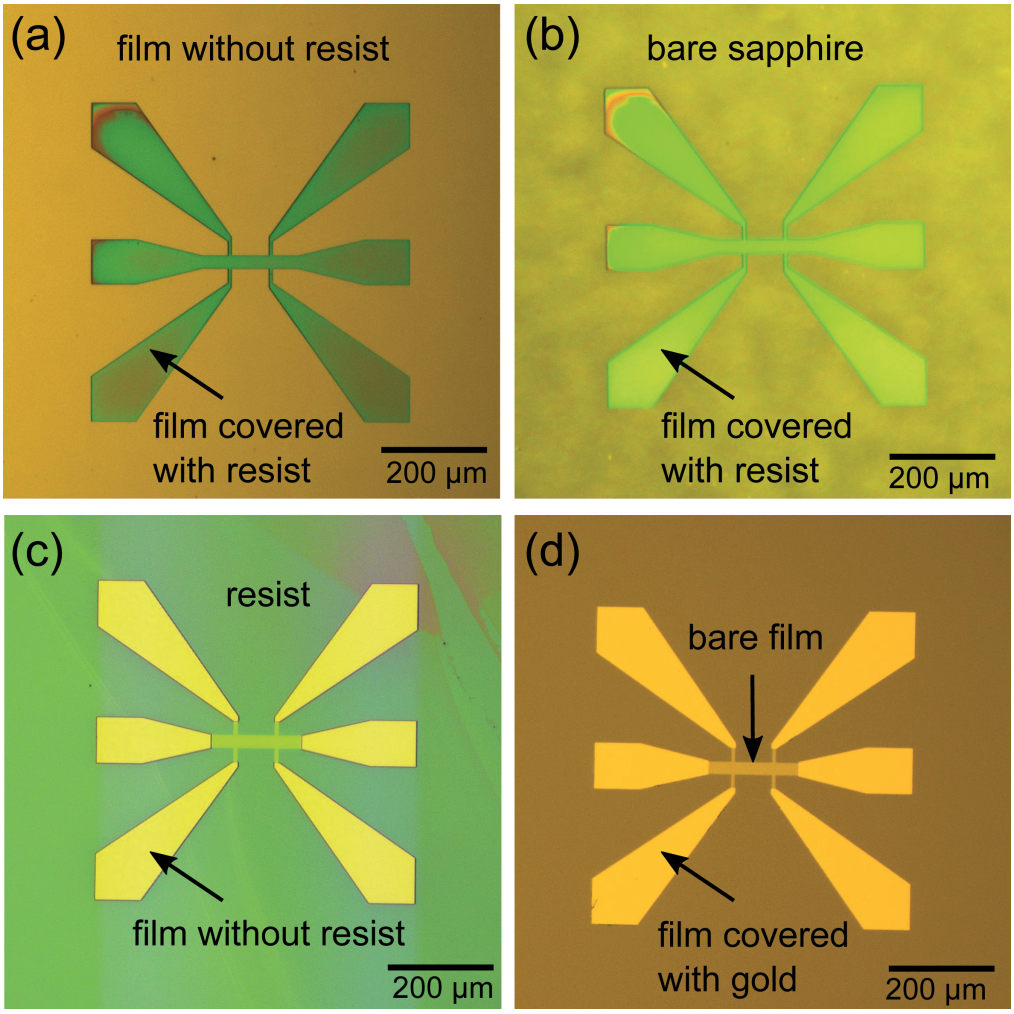


**Figure 3.21: Microscope pictures of a etching (a,b) and lift-off (c,d) process:** (a) Hall bar devices after laserlithography and development. The Hall bar itself is still protected by resist (green color). (b) Sample after wet etching, the Hall bar is still protected by resist, the surrounding film is etched and bare sapphire can be seen. (c) The sample is covered in resist, except the arms of the Hall bar, where the resist was removed during developing. (d) The whole film is covered by 40 nm gold. After lift-off, only the Hall bar arms are covered with 40 nm gold. The rest of the gold was lifted off in NMP. This leaves bare BST film as seen in the middle of the Hall bar device.

**Atomic layer deposition (ALD)**

Atomic layer deposition (ALD) allows to grow thin films from the vapor phase. The growth is performed atomic layer by layer in a self-limiting reaction [103, 104]. In the scope of this work an Ultratech Savannah setup is used to deposit $Al_2O_3$ as a dielectric layer during microfabrication and as a capping layer to protect the MBE-grown films from oxidization.

The basic principle of ALD deposition consists of sequential pulses of different gases which react on a film or substrate. The film is placed on a heated plate in the reaction chamber during the growth. Here, it is important to keep the heater temperature low at a temperature of 80 °C during deposition since higher temperatures influence the transport properties of the topological insulator film [105].
The formation of a $Al_2O_3$ film is shown in Fig. 3.22 [103, 106, 107]. Here, water $H_2O$ and a precursor, trimethylaluminium (TMA or $Al(CH_3)_3$), are alternately introduced as non-overlapping pulses into the reaction chamber. Subsequently, the chamber is purged after each pulse by an inert gas (typically $N_2$) to remove excess precursor and reaction products.
The first pulse introduces $H_2O$ into the chamber which results in a hydroxyl (OH)-terminated surface (a). The next pulse adds TMA, which reacts with the hydroxyl on the surface while releasing methane $CH_4$ (b). Excess TMA and methane are removed by inert gas being introduced into the reactor chamber in a subsequent step while the substrate surface is now covered by $AlCH_3$ (c). Again, water is introduced into the chamber (d) and reacts with the methyl-group $CH_3$ of the $AlCH_3$. It forms Al-O-Al oxygen bridges and additional hydroxyl groups (e). The excess precursor and reaction products are subsequently flushed out of the reactor chamber by yet another purge with an inert gas. After this full cycle, the hydroxyl bonds from the beginning are reproduced on top of a $Al_2O_3$ layer and allow for a repetition of the growth cycle until the desired $Al_2O_3$ film thickness is grown (f).

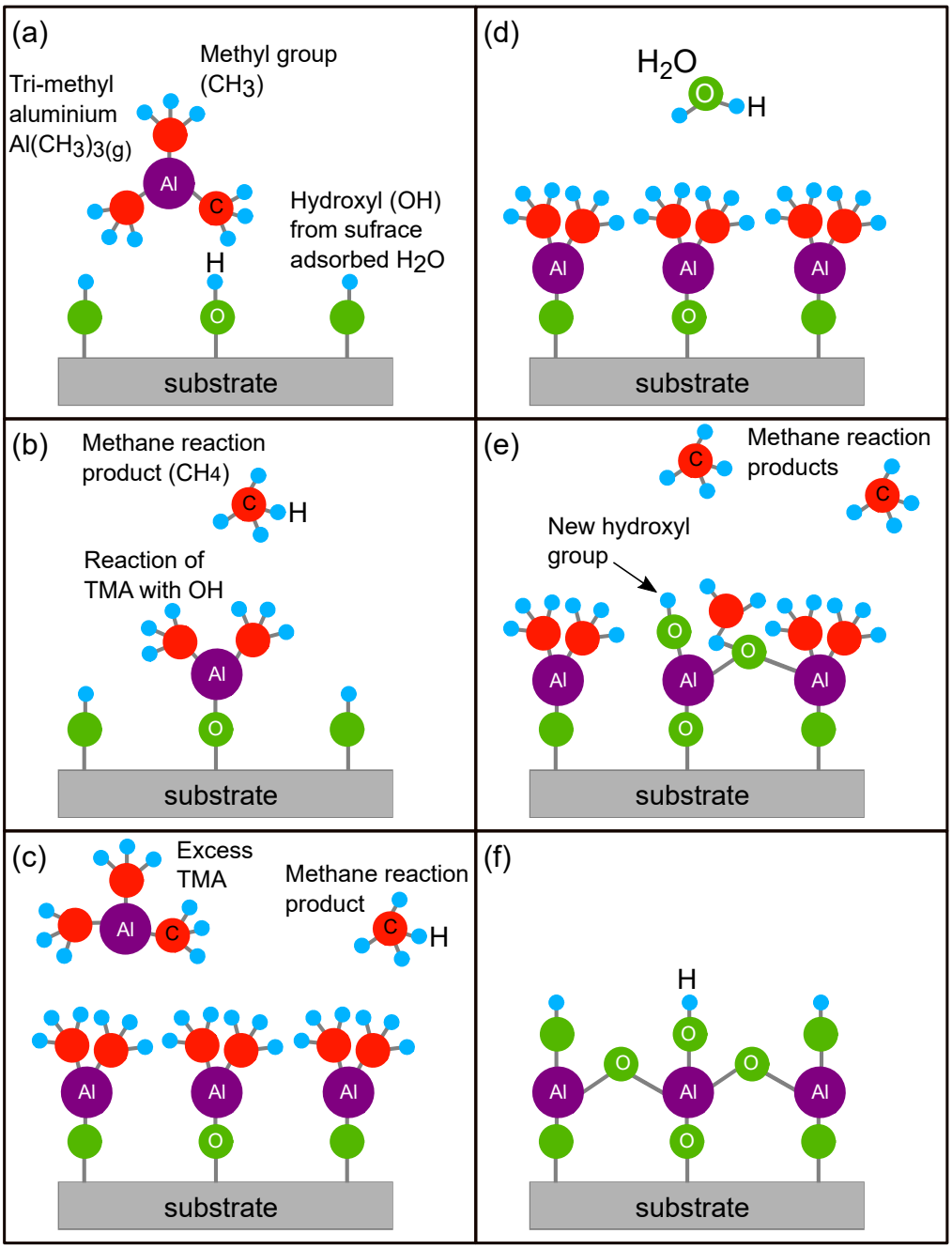


**Figure 3.22: Schematics of an atomic layer deposition (ALD) process of growing $Al_2O_3$.** Alternating pulses of $H_2O$ and a precursor TMA, separated by inert gas purging, are introduced into the reactor chamber where they react on a substrate/film surface. The ALD growth cycle can be repeated until the desired $Al_2O_3$ film thickness is grown. (modified from [106])

### Reactive ion etching (RIE)

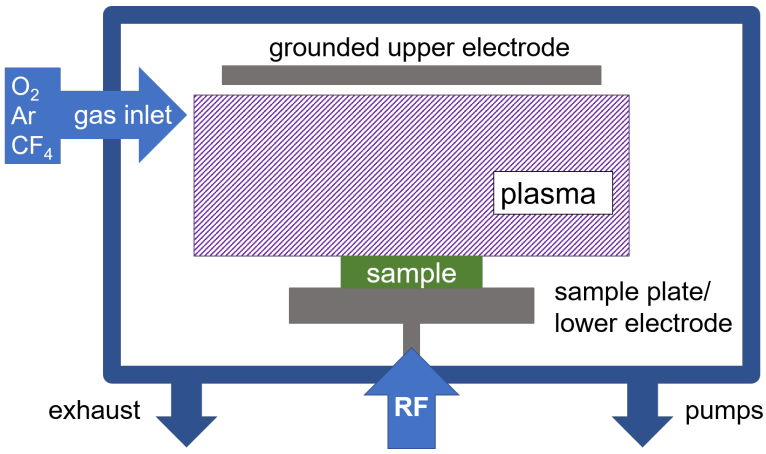


**Figure 3.23: Schematic of a reactive ion etching (RIE) chamber** (modified from [108, 109])

Reactive ion etching (RIE) is a common dry etching technique which is used in microfabrication. In the scope of this work, an Oxford PlasmaPro80 RIE is used to clean the sapphire substrates (see chapter 3.1.3) and during microfabrication. The machine consists of a vacuum chamber (p$\sim 10^{-6}$ Torr) in which the sample is loaded onto a table. Several gases can be introduced to the reactor chamber.

The scheme of a typical reactive ion etching (RIE) configuration is illustrated in Fig. 3.23. After placing the sample on the sample plate, the reactor chamber is evacuated. The sample plate acts as a lower electrode and is powered by an RF generator (usually 13.56 MHz) [108]. A second electrode is situated in the upper region of the reactor chamber and is grounded. The plasma is generated from the reaction gases (here: oxygen ($O_2$), argon (Ar) or carbon tetraflouride ($CF_4$)) by ionizing the gas and thus providing free electrons. Considering that the mobility of electrons is higher than the ion mobility, the lower electrode acquires a negative DC self-bias voltage while the plasma itself is positively charged by positive ions [109, 110]. Hence, the ions are accelerated with energies in the same order as the RF induced DC bias from the plasma to the negatively charged lower electrode and the sample placed on the plate [108, 111].

Each of the introduced gases has a different etching characteristic. Generally, a distinction is made between isotropic and anisotropic etching. Here, isotropic etching is performed by chemical etching during which ions from the generated plasma react chemically with the sample. Anisotropic etching is performed by physical etching by bombarding the sample with ions [109]. In the scope of this

work, oxygen $O_2$ is mainly used to etch polymers, particularly photoresist [109]. The halogen-based $CF_4$ is a known etchant for silicon based materials such as $Si_3N_4$ or $SiO_2$ [111]. Argon is a noble gas and as such not chemically reactive, but it is chosen for anisotropic etching by ion bombardment [109].

### 3.2.5 Transport measurement setup

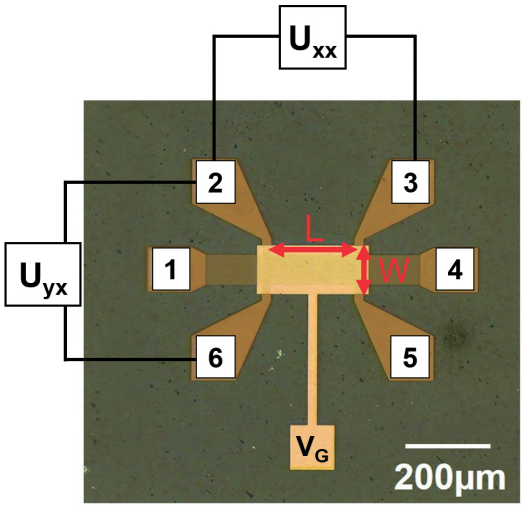


**Figure 3.24: Schematic illustration of a typical Hall bar measurement device and setup with contacts 1-6 and an additional gate.** The length $L$ and width $W$ of the Hall bar are indicated.

The measurement of electrical and magnetic properties is an important characterization tool for the materials grown in the scope of this work. The basic method to determine the carrier concentration, carrier type and mobility of the grown film is the Hall measurement technique at low temperatures (see chapter 2.2.1). A typical Hall bar device is shown in Fig. 3.24. Here the current is applied from contact 1 to contact 4. The transverse Hall resistance is measured between contact 2 and 6 (contact 3 and 5), while the longitudinal resistance is measured between contact 2 and 3 (contact 6 and 5). Furthermore, a top gate can be added to the specific device in order to apply a gate voltage and tune the Fermi level of the sample. The samples are attached on a sample holder and 0.025 mm-thin, annealed gold wires are used to make an electrical contact from the sample to the sample holder. The sample holders used for the transport measurements are shown in Fig. 3.25. The sample holder used for the PPMS setup can electrically connect up to 12 contacts, while the sample holder for the dilution refrigerators offers up to 24 pins.

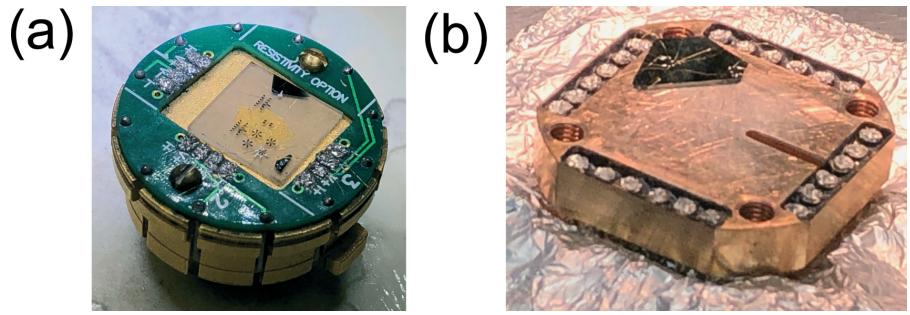


**Figure 3.25: Photographs of the sample holders used for transport measurements.** (a) Photo sample which is electrically connected by gold wires to a PPMS sample puck with 12 available pins. (b) Sample holder with 24 available electrical pins used for the Heliox and Triton measurements.

The low temperature transport measurements shown in this thesis were performed in different measurement setups. For measurements performed at temperatures in the range between 2 K to 300 K, a Quantum Design Physical Property Measurements System (PPMS) is used. This fully automated system is convenient to operate and ideal for daily transport measurements. It consists of a dewar which contains a 9 T superconducting magnet cooled by liquid helium. The sample is placed on a so called puck which is inserted into a vacuum isolated tube inside of the dewar. It is cooled by helium gas which flows through the sample chamber and can be heated by resistive heating.

In the case of $Sn_{1-x}In_xTe$ films, discussed in chapter 6, the critical temperature $T_c$ is lower than 2 K, which requires a different cryogenic setup. Temperatures down to $\sim$ 300 mK are achieved by a Helium-3-insert (Oxford Instruments Heliox) using $^3$He for cooling. The cooling power is directly related to the pressure, and the vapor pressure becomes exponentially lower with decreasing temperature $\dot{Q} \propto P \propto \exp^{-1/T}$ [112]. This means that a liquid can be cooled by pumping on it. The condensation stage of the cryostat is called 1 K pot. After condensing the helium, the vapor above the liquid helium is pumped by a sorption pump which acts like a cryo pump. This provides the cooling power necessary to cool down the cryostat. The cryostat will stay at the base temperature for a limited time. Once all of the $^3$He is evaporated, the sorption pump has to be heated up to 30 K in order to condense the $^3$He again.

To observe the quantum anomalous Hall effect (see chapter 5) even lower temperatures are needed. A mixture of liquid $^3$He and liquid $^4$He is necessary to achieve temperatures down to 10 mK. $^3$He and $^4$He have characteristic thermodynamic properties, depicted in Fig. 3.26. The helium mixture separates into two

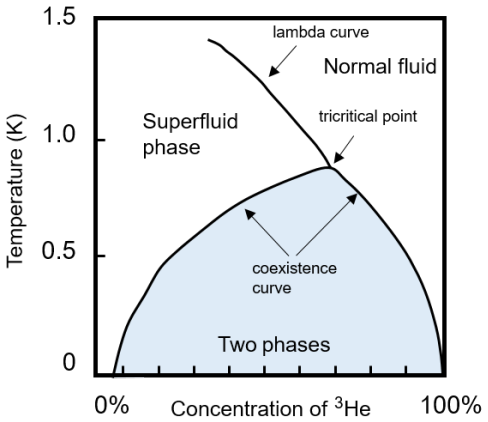


**Figure 3.26:** Phase diagram of the liquid $^3$He and $^4$He mixture (modified from [113])

liquid phases, separated by a phase boundary, upon cooling it below 870 mK: a phase which is rich in $^3$He (concentrated phase) and a phase which is rich in $^4$He (dilute phase) [113]. The $^4$He-rich phase contains at least 6.6% $^3$He at any temperature. The $^3$He-rich region contains a large fraction of pure $^3$He and its concentration depends on the temperature. In the dilution refrigerator the diluted phase is situated at the bottom of the so-called mixing chamber which is connected to the distillation unit. $^3$He is removed in a closed cycle from the diluted phase through the still. Pumping on the still, which is at 0.7 K, removes $^3$He since its vapor pressure at this temperature is around 1000 times higher than the vapor pressure of $^4$He [113]. To compensate the loss of $^3$He, $^3$He flows from the concentrated into the diluted phase across the phase boundary and provides the cooling power for the dilution refrigerator. A dry dilution refrigerator (Oxford Instruments Triton 200) with a base temperature of $\sim$ 10 mK is used in the scope of this work. Instead of pre-cooling the dilution refrigerator with liquid helium, a pulse-tube cooler is used to pre-cool the dry dilution refrigerator to prepare the necessary low temperatures for the $^3$He/$^4$He dilution circuit [114].The 1 K pot is replaced by an additional heat exchanger which, together with a Joule-Thomson stage, condenses the $^3$He.
More detailed information on the cryogenic setup can be found in references [112, 113].

# Chapter 4

# MBE growth and characterization of $(Bi_{1-x}Sb_x)_2Te_3$ films

## Contents



In this chapter the growth of the topological insulator $(Bi_{1-x}Sb_x)_2Te_3$ (BST) is introduced. BST films are the basic building block for the material systems discussed in the following chapters of this thesis. The optimization process to grow thin films with good morphology and bulk insulating transport properties is explained. The films are grown by MBE and characterized by atomic force microscopy (AFM) and x-ray diffraction (XRD). The transport measurements are performed in a Physical Property Measurement System (PPMS).

## 4.1 Introduction

The first 2D topological insulators (TI) were theoretically predicted in 2005 by Kane and Mele in graphene [6] and in 2006 in HgCdTe quantum well structures by Bernevig *et al.* [8]. The first experimental realization was achieved in 2007 by the Molenkamp group in HgTe quantum wells [9].

In the same year, the 3D topological insulator with topological protected surface states was predicted by Fu and Kane [10] and the 3D TI nature was experimentally confirmed by surface-sensitive angle-resolved photoemission spectroscopy (ARPES) on $Bi_{1-x}Sb_x$ crystals a year later [11].

The search for new 3D TI materials continued, and in 2009 the bismuth-based compounds $Bi_2Se_3$, $Bi_2Te_3$ and $Sb_2Te_3$ were predicted as a second generation of materials with topological surface states consisting of a single Dirac cone at the $\Gamma$ point of the surface Brillouin zone [13]. ARPES and scanning tunneling microscope (STM) measurements on $Bi_2Te_3$ [14, 115] and $Bi_2Se_3$ [12] indeed showed two bands with a linear dispersion forming a single Dirac cone in the bulk band gap.

Despite the successful proof of the existence of the topological surface states in these materials, it is still challenging to grow materials with no bulk contribution at all. Most of the grown topological insulators exhibit non-negligible bulk carrier densities which were observed in ARPES and transport experiments. Especially in magneto-transport the influence of remaining bulk carriers is problematic [116, 117]. The two channels of the bulk and surface carriers cause a non-linear Hall response. Here, the bulk carriers overlay the contributions by the surface states by a parallel channel [118–121]. In order to achieve surface-dominated conduction in topological insulator materials, the carrier density has to be decreased. Brahlek *et al.* [122] estimated the carrier concentration which corresponds to conduction dominated by the topological surface states in $Bi_2Se_3$ to be $n_{\mathrm{TSS}} \approx 5 \times 10^{12}\,\mathrm{cm}^{-2}$. There are various strategies to achieve high-quality bulk-insulating TI materials. Growing topological insulator thin films in an MBE chamber has several advantages, which were already discussed in chapter 3.1.1. Among them, the high crystal quality of the thin films, the precise control of the film thickness (which is an intuitive approach to minimize bulk contributions and maximize conduction from the surface states), the easy implementation of doping the films or the possibility of combining different TI materials in heterostructures. Furthermore, pre-patterned nano-structure can be grown in an MBE chamber to achieve surface dominated transport. The first results of MBE grown TI films were shown by Zhang *et al.* in 2009 by growing $Bi_2Se_3$ films on Si(111) substrates [123].

An established method to reduce the carrier contribution and obtain bulk-insulating materials, is doping the TI material. For instance, doping $Bi_2Te_3$ with calcium or tin can tune the material from a hole-doped into an electron-doped transport regime [124]. A disadvantage of this method is that the dopants can introduce defects and disorder [14, 125, 126].
Electrical gating is a way to achieve surface states-dominated conduction by moving the position of the Fermi level $E_F$ through the band gap. Here, either the TI material has to be thin enough so the gate can sufficiently move the Fermi level, or it is necessary to apply a back and top gate in order to achieve the independent tuning of both TI surfaces. The gating behavior of TI materials was for instance studied for $Bi_2Se_3$, $Bi_2Te_3$ and the ternary compound $(Bi_{1-x}Sb_x)_2Te_3$ [127–130].

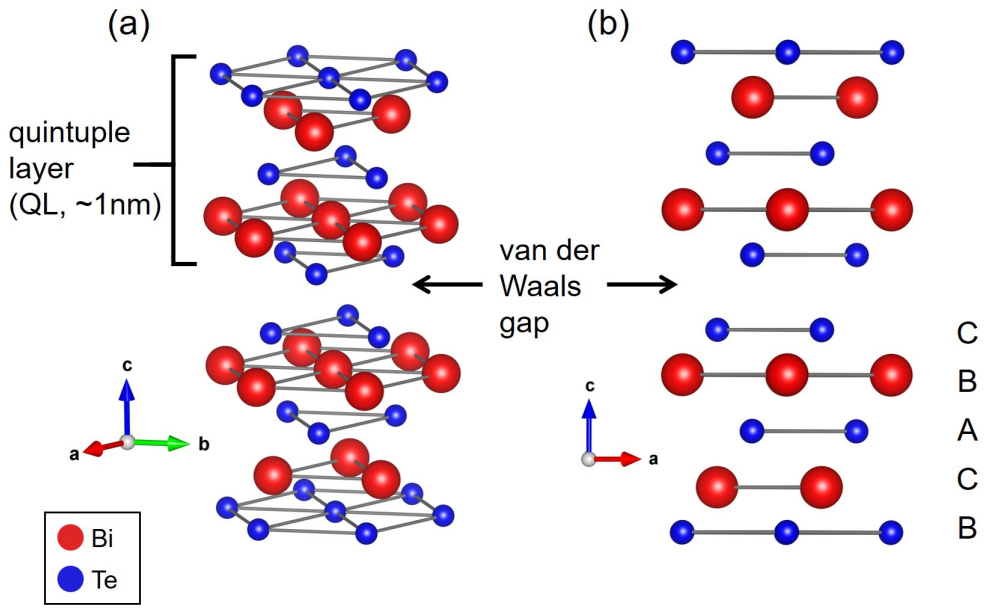


**Figure 4.1: Crystal structure of $Bi_2Te_3$:** (a) Schematic illustration of the tetradymite crystal structure of $Bi_2Te_3$ with two quintuple layers shown and the van der Waals gap between Te layers in the middle. For the $Sb_2Te_3$ crystal structure, the bismuth is replaced by antimony. In the case of BST, the antimony will partially substitute for bismuth. (b) Side view of the layer structure along the c-axis.

Band structure engineering of topological insulator materials presents another approach to reduce the bulk carriers and control the surface states. The ternary compound $(Bi_{1-x}Sb_x)_2Te_3$ (BST) acts as a mixture of $Bi_2Te_3$ and $Sb_2Te_3$, which have close lattice constants and share the same crystal structure. Both materials have a rhombohedral crystal structure with the space group $D^5_{3D}$ (R=$\bar{3}$m)

as displayed in Fig. 4.2. In the case of $(Bi_{1-x}Sb_x)_2Te_3$, antimony will partially substitute for bismuth [13].

The basic building block of a 3D TI material with a tetradymite crystal structure is the quintuple layer (QL). A QL consists of five covalently bonded atom layers along the (001)-direction and has a layer height of $\sim$1 nm. Each atom layer has a 2D hexagonal lattice which is stacked in an ABC order (Te(1)-Bi-Te(2)-Bi-Te(1)). Two quintuple layers are coupled by weak van der Waals bonds, whereas two adjoining layers within a quintuple layer are covalently bonded which results in a far stronger bond. The van der Waals coupling is the reason why TI materials with a tetradymite crystal structure are easy to cleave in crystal form, and in the case of thin film growth adds a flexibility to the choice of growth substrate [13]. A look at the band structure of $Bi_2Te_3$ and $Sb_2Te_3$ highlights the motivation to fabricate a ternary compound. As displayed in Fig. 4.2, $Bi_2Te_3$ is generally $n$-type doped. The bandstructure of $Bi_2Te_3$ reveals that the Dirac point is buried in the bulk valance band, and furthermore the Fermi level lies in the bulk conduction band. $Sb_2Te_3$ on the other hand is usually $p$-type doped. Figure 4.2 shows that here the Dirac point lies in the bulk gap. Antimony vacancies and Sb-Te anti-site defects introduce hole-type bulk carriers which results in the Fermi level lying in the bulk valence band [15]. The individual bandstructures of $Bi_2Te_3$ and $Sb_2Te_3$ suggest that by combining the two materials and alloying them in the correct ratio, one can tune the Fermi level by charge compensation and shift the Dirac point into the band gap, to eventually obtain a fully bulk insulating 3D topological insulator [13, 15, 90, 131].

## 4.2 Sample growth and characterization

### 4.2.1 $(Bi_{1-x}Sb_x)_2Te_3$ sample growth by molecular beam epitaxy

The $(Bi_{1-x}Sb_x)_2Te_3$ (BST) films are grown on epi-ready $Al_2O_3$ (0001) substrates. The sapphire is cleaned using the recipe described in chapter 3.1.3. After transferring the sapphire into the growth chamber of the MBE system and *in-situ* annealing it up to 950 °C, the substrate is kept at 400 °C until the beginning of the growth process. At this temperature it is guaranteed that no contaminants will stick to the sapphire surface [132].

To initiate the growth process, the bismuth, antimony and tellurium sources are heated up. Bismuth and tellurium are evaporated from regular Knudsen cells, whereas for the evaporation of antimony a thermal cracking cell is used

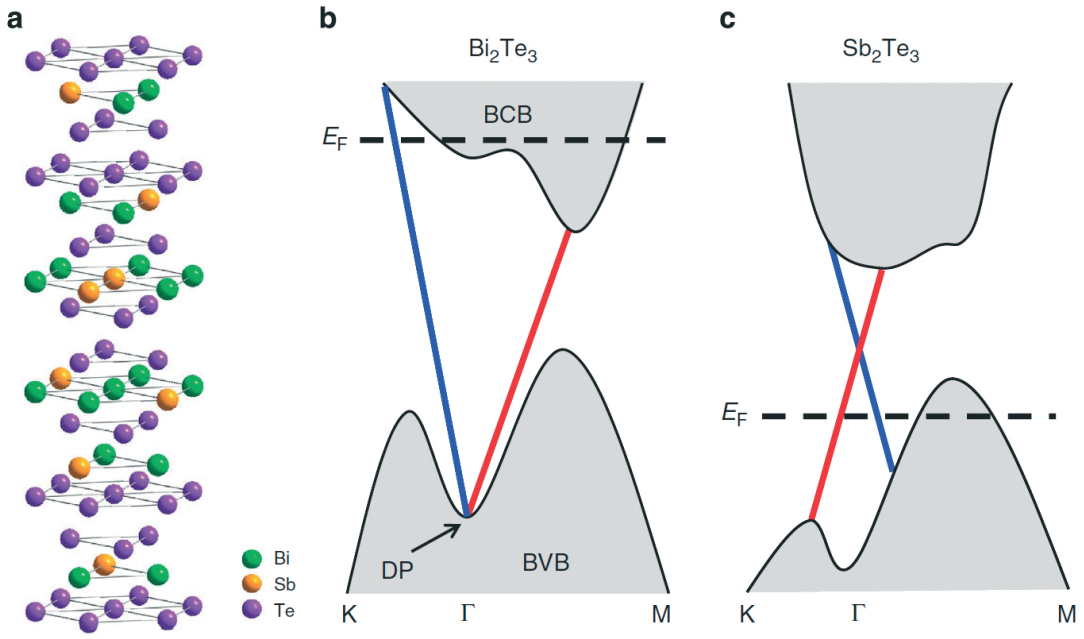


**Figure 4.2:** Schematic illustration of (a) the crystal structure of $(Bi_{1-x}Sb_x)_2Te_3$ and the electronic bandstructure of (b) $Bi_2Te_3$ and (c) $Sb_2Te_3$. Reprinted by permission from Springer Nature: Nat Commun **2**, 574 (2011), Band structure engineering in $(Bi_{1-x}Sb_x)_2Te_3$ ternary topological insulators, Zhang *et al.*, Copyright (2011); [15]

to ensure a better flux control of this high vapor pressure material. Antimony was found to be primarily evaporated in larger molecules such as tetrameric $Sb_4$ [133, 134]. The thermal cracker source first evaporates antimony tetrameters from a crucible, and subsequently breaks the large antimony clusters in a hot cracking zone of the evaporator into mainly smaller $Sb_2$-dimers [135]. The respective fluxes of the materials are measured with a beam flux monitor and can be adjusted by increasing or decreasing the evaporator temperature. The chemical composition of the grown film is determined by the flux ratios Bi/Sb and Te/(Bi+Sb). The $x$ value in $(Bi_{1-x}Sb_x)_2Te_3$ can be changed by varying the temperatures of the bismuth/antimony evaporators and accordingly the material fluxes. Once the fluxes are calibrated, the substrate temperature is decreased from 400 °C to the growth starting temperature and Bi, Sb and Te are co-evaporated, with roughly 10 times more tellurium than bismuth and antimony fluxes combined. The tellurium-rich growth condition leads to the desired stoichiometry in the grown film [85, 134, 136, 137].

The thin film growth is performed by applying a two-step-growth method. The first quintuple layers of the film are deposited while slowly ramping the substrate temperature from the starting temperature $T_1$ to a higher temperature $T_2$. The substrate temperature is afterwards kept at $T_2$ for a certain time depending

on the desired film thickness. During the temperature ramping, the sticking of the incoming atoms is high enough to condense on the substrate surface, but the mobility of the atoms is still low. The diffusion length of the atoms is larger at the higher end temperature $T_2$ and the film quality is improved. The growth rate is primarily dictated by the bismuth and antimony fluxes, while the excess tellurium will desorb from the film surface at the given growth temperature. Once the deposition of the materials is finished, the sample is cooled to a temperature lower than 100 °C and can afterwards be transferred into the load lock chamber.

### 4.2.2 *Ex-situ* structural characterization by x-ray diffraction and atomic force microscopy

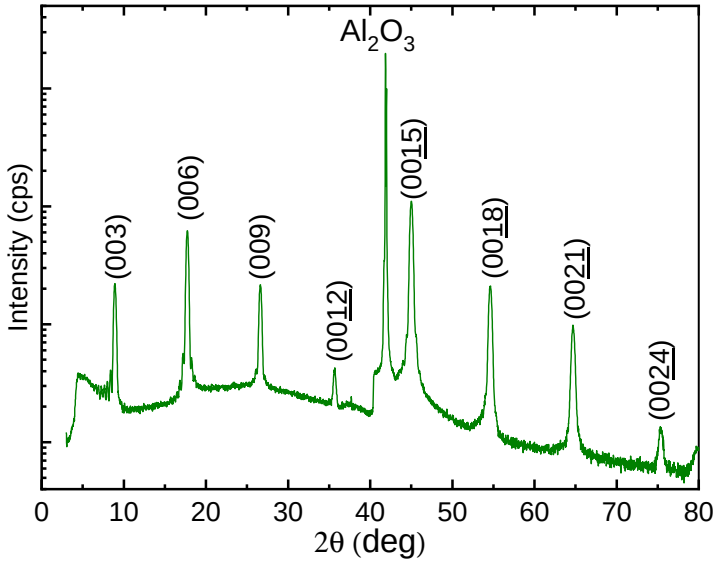


**Figure 4.3: XRD pattern of a $(Bi_{1-x}Sb_x)_2Te_3$ film grown on sapphire.** Only the (00l) peaks (with l=3, 6, 9, 12, 15, 18, 21, 24) are visible which fits the expected rhombohedral crystal structure and epitaxial growth following the crystal structure of the sapphire substrate.

To obtain information about the structural quality of the grown film, x-ray diffraction measurements (XRD) are performed.
Figure 4.3 shows a typical XRD $\theta-2\theta$-scan of a BST film grown on sapphire. Only the (00l) peaks with l=3, 6, 9, 12, 15, 18, 21, 24 are present in the XRD pattern. The peak positions in the pattern of the $(Bi_{1-x}Sb_x)_2Te_3$ film indicate an epitaxial single phase film growth with high crystal quality.

The appearance of Kiessig fringes next to the regular Bragg peaks is an indication for a good quality film growth and high homogeneity. They appear due

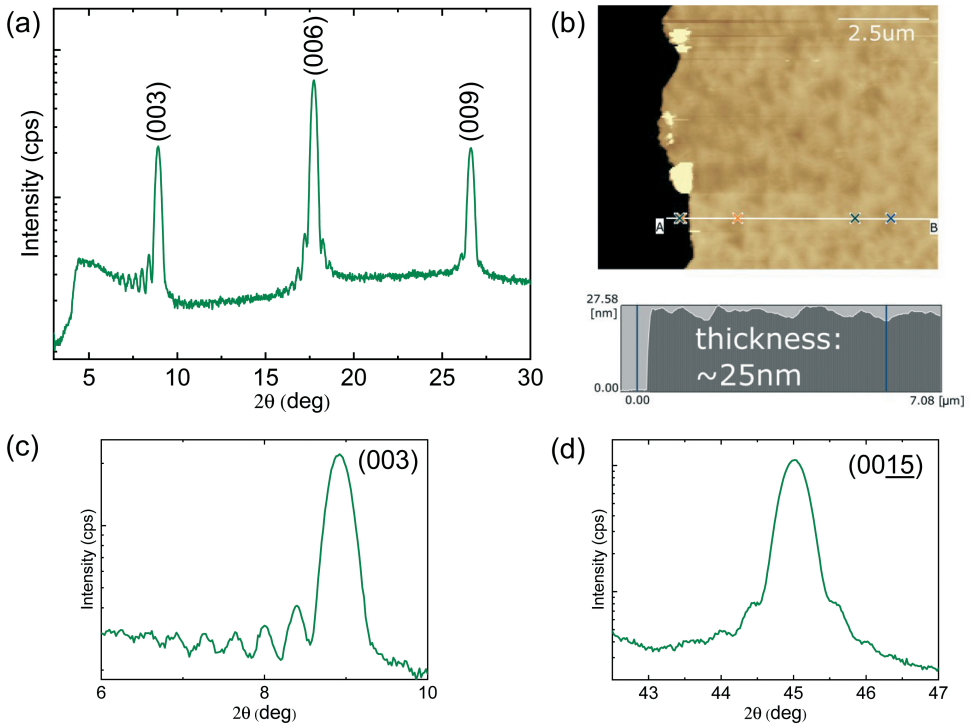


**Figure 4.4: XRD of a $(Bi_{1-x}Sb_x)_2Te_3$ film grown on sapphire.** (a) XRD pattern of the lower angle region from 3° to 30° from Fig. 4.3, (b) AFM image to determine the thickness of the grown film ($t = 25\,\mathrm{nm}$). (c) and (d) show the (003) and (0015) Bragg peaks.

to additional scattering from the interfaces between subsequent film layers and can hence be used to determine the film thickness. Kiessig fringes can be seen in Fig. 4.4. Figure 4.4 (a) shows a zoom of the low angle region of the BST XRD pattern displayed in Fig. 4.3 to emphasize the Kiessig fringes. The XRD patterns depicted in Fig. 4.4 (c) and (d) show the (003) and (0015) peak. The XRD pattern displayed in Fig. 4.4(d) suggests that the Kiessig fringes remain until the (0015) peak. By analyzing the Kiessig fringes next to the (003) peak in Fig. 4.4(c), the thickness of the grown BST can be determined. The angular spacing between the maxima is inversely proportional to the total thickness $t \sim \frac{\lambda}{\Delta(2\Theta)}$, with $\lambda$ as the $K_\alpha$ wavelength of the copper anode used in the XRD system [138].

Thus, we can calculate a film thickness of ∼23 nm, which is in correspondence to the thickness determined by the AFM measurement (see Fig. 4.4(b)). The $c$-lattice parameter of $c = 30.0419\,\text{Å}$ can be extracted from the XRD pattern by using the equations introduced in chapter 3.2.2.

In the process of optimizing the BST growth procedure and in order to explore the family of 3D topological insulators beyond BST, $Bi_2Se_3$ and $Bi_2Te_3$ films

were successfully grown as well. Their respective XRD patterns are displayed in Fig. 4.5 and Fig. 4.6. Just like for the $(Bi_{1-x}Sb_x)_2Te_3$ film, the x-ray diffraction patterns of both materials suggest epitaxial growth which follows the sapphire crystal structure, as shown in Fig. 4.5(a) for $Bi_2Se_3$ and Fig. 4.6(a) for $Bi_2Te_3$. For both materials Kiessig fringes can be observed indicating a homogeneously grown film and the film thickness can be determined to ∼21 nm for $Bi_2Se_3$ and ∼34 nm for $Bi_2Te_3$, which is in good agreement with the thicknesses measured by AFM as shown in Fig. 4.5 (c) and Fig. 4.6 (c). Furthermore the $c$-lattice parameters were extracted from the x-ray patterns as: $c_{Bi_2Te_3} = 30.1956\,\text{Å}$ and $c_{Bi_2Se_3} = 28.4080\,\text{Å}$.

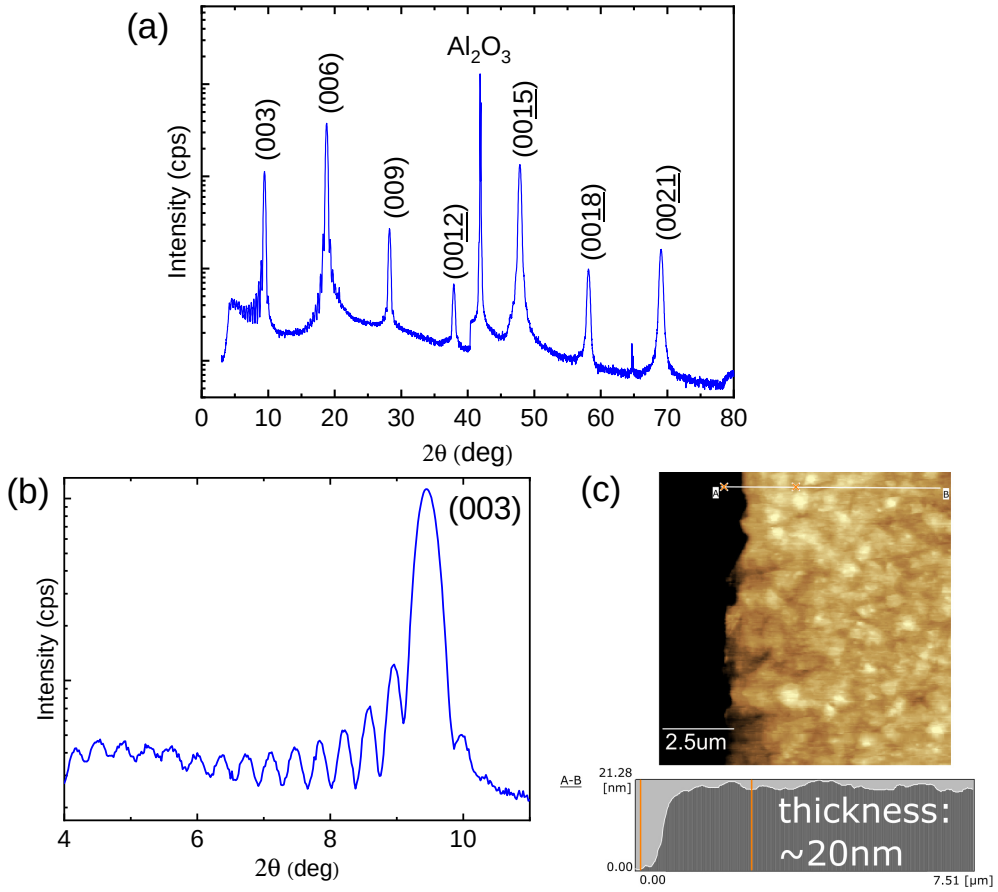


**Figure 4.5: XRD scan of a $Bi_2Se_3$ film grown on sapphire**. (a) The (00l) Bragg peaks are visible, indicating a epitaxial growth of the $Bi_2Se_3$ film following the crystal structure of the sapphire. (b) Zoom on the (003) Bragg peak showing Kiessig fringes. (c) AFM image and height profile to determine the thickness of the grown film.

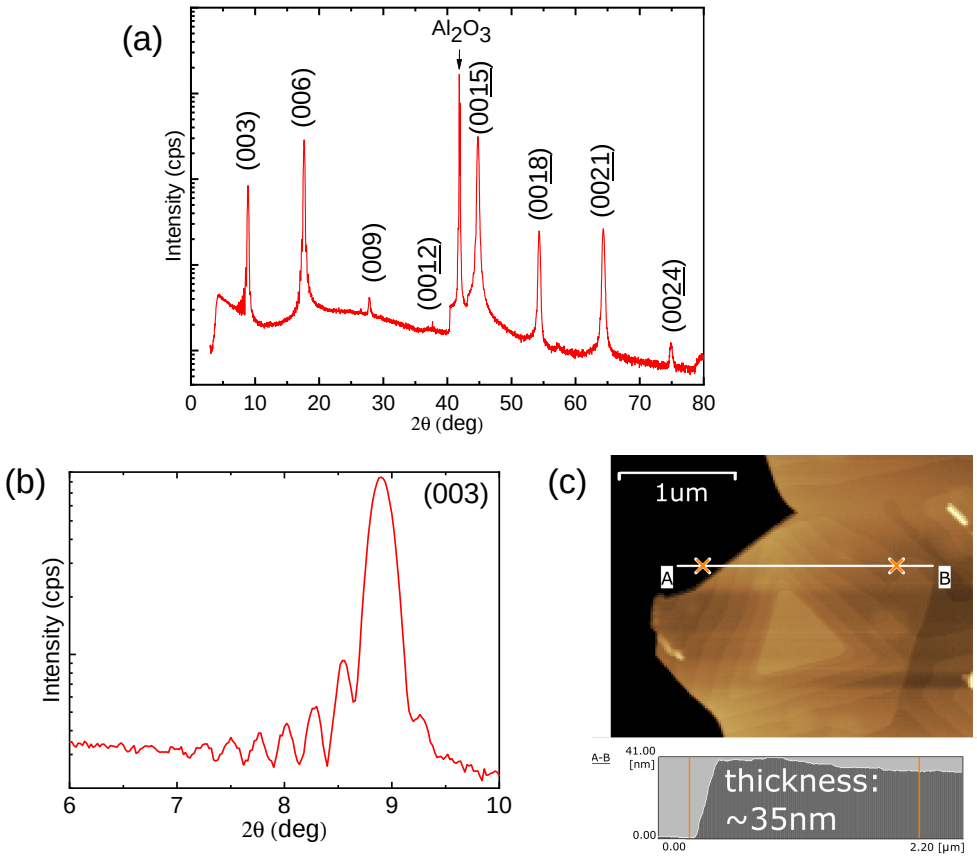


**Figure 4.6: XRD scan of a $Bi_2Te_3$ film grown on sapphire.** (a) The (00l) Bragg peaks are visible, indicating a epitaxial growth of the $Bi_2Te_3$ film following the crystal structure of the sapphire. (b) Zoom on the (003) Bragg peak showing Kiessig fringes. (c) AFM image and height profile to determine the thickness of the grown film.

### 4.2.3 Improving the morphology of the $(Bi_{1-x}Sb_x)_2Te_3$ films

Finding the correct growth temperature is a crucial procedure for MBE growth. The morphology of a MBE-grown BST film is foremost influenced by the substrate temperature. This growth temperature determines the re-evaporation or sticking of the arriving bismuth, antimony and tellurium atoms and their ability to diffuse along the substrate surface (see also chapter 3.1.2). These considerations allow a restricted temperature window to optimize the film growth. Furthermore, the optimization must be done for every MBE chamber and the results can vary from chamber to chamber. The optimization described in the following was performed in the MBE2 chamber.

As previously discussed, the BST films are grown by applying a two-step-growth procedure. With the purpose of finding the optimal starting temperature, a series of $(Bi_{1-x}Sb_x)_2Te_3$ films were grown at a single temperature ranging from 200 °C to 260 °C. This starting temperature is important as it initiates the seed layer of the grown film. The results from these growth are summarized in Fig. 4.7. The structural properties of the grown BST films were studied by atomic force microscopy and x-ray diffraction.

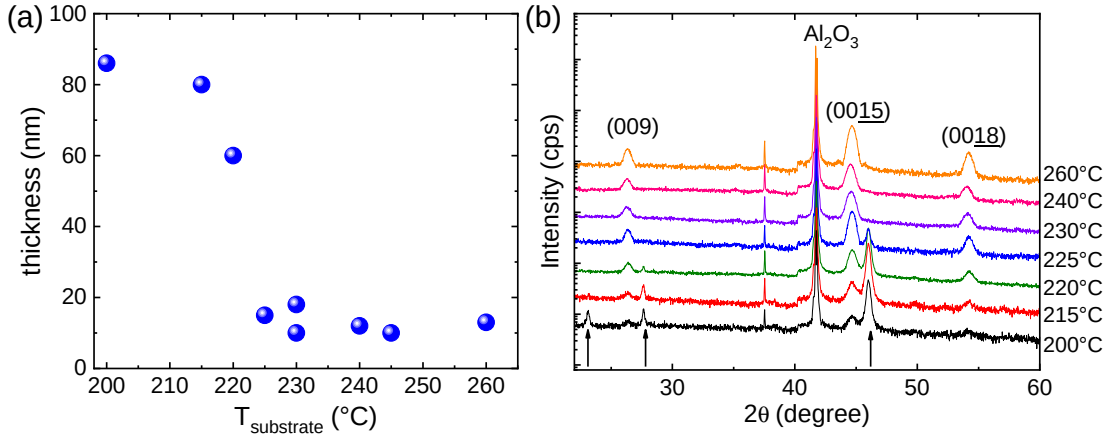


**Figure 4.7: Thickness and XRD study of BST films grown at different substrate temperatures in a single-step growth mode for 30 minutes.** (a) Film thickness dependence of the substrate temperature. Here, the film thickness was determined by AFM. The graph shows a sudden increase in film thickness at a $T_{\mathrm{substrate}}$=230 °C. (b) Corresponding XRD patterns of the BST films. The XRD patterns exhibit only the (00l) peaks for films grown at 230 °C and above. Below 230 °C additional peaks are present, indicating a non-epitaxial growth.

Figure 4.7(a) describes how the film thickness depends on the substrate temperature ranging from 200 °C to 260 °C. The film thickness was determined by atomic force microscopy. The films grown at temperatures between 225 °C and

260 °C all have a similar thickness of ∼15 nm to 20 nm. A sudden increase in film thickness to 60 nm appears at a lower growth temperature of 220 °C, and a thickness of 80 nm at $T_{\mathrm{substrate}}$=200 °C. Corresponding XRD patterns are displayed in Fig. 4.7(b). Here, the spectra of the films which were grown at 230 °C, 240 °C and 260 °C show only the (00l) peaks, suggesting single phase and epitaxial growth. The spectra of the films grown at lower temperatures than 230 °C exhibit additional peaks. This indicates the appearance of a second phase and non-epitaxial growth. The results from the XRD measurements support the thickness dependence presented in Fig. 4.7(a): No epitaxial film growth is achieved for growth temperatures below 230 °C. Tellurium which generally has a high vapor pressure and a low sticking coefficient for temperatures above ∼200 °C [132, 139] might condense at this lower growth temperatures. Furthermore, the mobility of the atoms arriving on the substrate surface is most likely too low to form a single crystalline film.

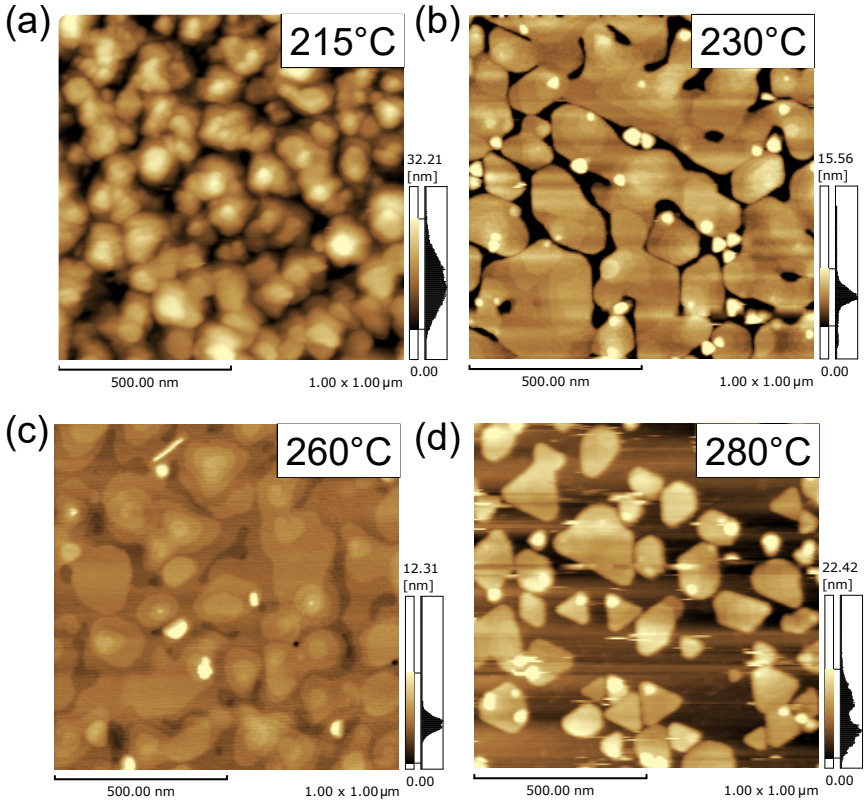


**Figure 4.8: AFM images (1x1 µm) of BST films grown on sapphire for 30 minutes at various temperatures.** (a) $T_{\mathrm{substrate}}$=215 °C: The film exhibits roughness of ∼30 nm; (b) $T_{\mathrm{substrate}}$=230 °C: The film shows interrupted islands; (c) $T_{\mathrm{substrate}}$=260 °C: This film is continuous and has flat terraces; (d) $T_{\mathrm{substrate}}$=280 °C: This film is not continuous, instead disconnected island were grown.

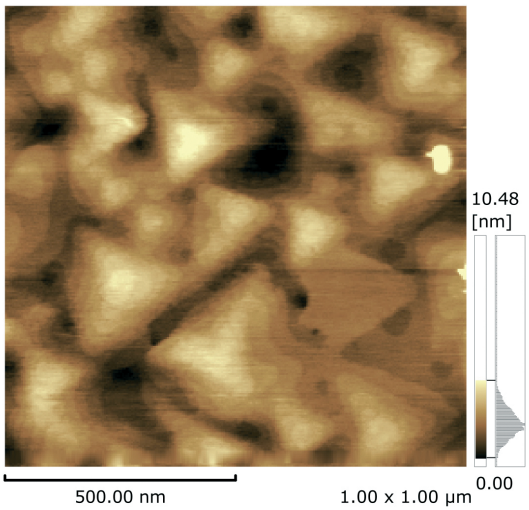


**Figure 4.9: AFM image (1x1 µm) of a BST film grown on sapphire using the two-step growth method.** During growth, the substrate temperature was first ramped from 260 °C to 300 °C in 15 minutes and then kept at 300 °C. In contrast to the film grown at a single temperature of 260 °C, the changed growth procedure improved the morphology. Triangular terraces with sharp edges are clearly visible.

Exemplary AFM pictures of the films grown at 215 °C, 230 °C, 260 °C and 280 °C are displayed in Fig. 4.8. The AFM image in Fig. 4.8 (a) shows a film with a surface roughness of up to 32 nm. The AFM image taken of a BST film grown at 230 °C in Fig. 4.8 (b) is not grown continuously, even though the characteristic terraces structures can be identified. A continuous BST film however was grown at a substrate temperature of 260 °C (see Fig. 4.8(c)). BST films grown at higher temperatures than 260 °C are disconnected. The AFM image measured on a film grown at the highest temperature presented in Fig. 4.8(d) shows isolated BST islands indicating a too high temperature for the incoming atoms to stick on the surface and form a continuous film.
By analyzing the data obtained by AFM and XRD measurements, a growth temperature of 260 °C was identified as a suitable seed temperature for the growth of $(Bi_{1-x}Sb_x)_2Te_3$ films.
To further improve the morphology of the grown film, a second step at a higher temperature is added to the growth procedure. Figure 4.9 shows an AFM image of a BST film grown at a starting temperature of 260 °C. During the growth the substrate temperature was ramped from 260 °C to 300 °C and then kept at 300 °C. Due to the higher mobility of the atoms at the higher temperature, the morphology of the film is evidently improved.
The morphology of the BST film grown at a sole temperature of 260 °C displayed in AFM image Fig. 4.8(c) hints at the formation of the characteristic triangular structure but the terraces are smeared out. The AFM image shown in Fig. 4.9 however presents atomically flat terraces with sharp edges suggesting a high crystal quality.

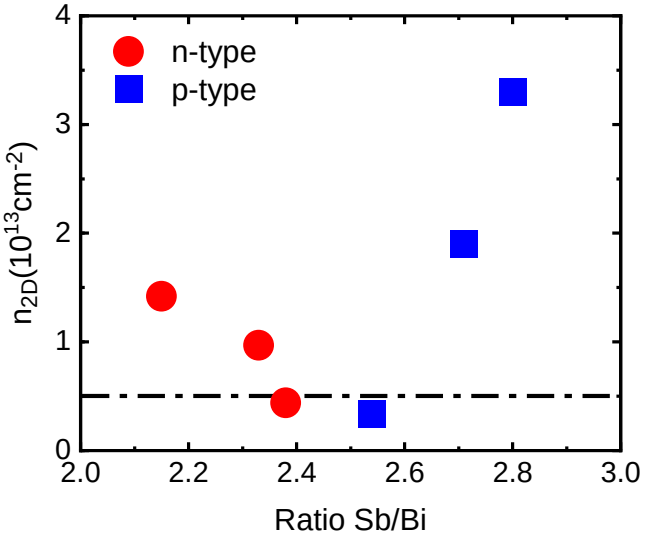


**Figure 4.10: Carrier density as a function of Bi/Sb ratio.** The films were grown at the same conditions and all capped with 3 nm $Al_2O_3$ after growth. The carrier type could be tuned from $n$- to $p$-type. The bulk insulating regime lies below the dashed line.

### 4.2.4 Improving the transport properties

As previously discussed in the introduction of this chapter 4.1, band structure engineering by combining $Bi_2Te_3$ and $Sb_2Te_3$ is a method to achieve bulk insulating $(Bi_{1-x}Sb_x)_2Te_3$ film. By adjusting the Bi/Sb composition ratio during growth, it is possible to tune the Fermi level of the ternary $(Bi_{1-x}Sb_x)_2Te_3$ compound. Figure 4.10 shows the carrier concentration of 15 nm-thin BST films as a function of the Bi/Sb ratio ranging from Bi:Sb of 1 : 2.0 to 1 : 3.0. The composition ratio was determined by the bismuth and antimony flux during the BST growth measured with a beam flux monitor. The carrier concentration was extracted from Hall resistance measurements performed on Hall-bar devices by sweeping the magnetic field in a Physical Properties Measurement System (PPMS) system at 2 K using the ac-lock in technique. All BST films were capped with 3 nm $Al_2O_3$ directly after growth.

It was indeed possible to tune the carrier concentration from $n$-type to $p$-type by adjusting the Bi/Sb ratio. The crossover between $n$- and $p$-type regime is located at a Bi/Sb ratio of approximately 1:2.45. A carrier concentration in the order of $n_{2D} \sim 10^{12}\mathrm{cm}^{-2}$ was achieved, which is generally considered to be bulk-insulating [122]. In the $n$-type regime the lowest carrier concentration is $n_{2D} = 4.4 \times 10^{12}\,\mathrm{cm}^{-2}$ for a Bi:Sb ratio of 1 : 2.38. A carrier concentration of $p_{2D} = 2.5 \times 10^{12}\,\mathrm{cm}^{-2}$ for a Bi:Sb ratio of 1 : 2.54 can be extracted in the $p$-type regime.

Usually after growth, the BST film is cut into several smaller pieces which are then used for various device fabrications. It is important that the film is homogeneously grown across the entire substrate. To confirm the homogeneous growth,

a BST film was grown on a sapphire substrate, which was cut into the biggest possible size to fit on the Eiko-type sample holder. AFM and magneto-transport measurements were performed on several spots across the sample. The results are summarized in Fig. 4.11. Figure 4.11(a) shows the temperature dependence of the sheet resistance which indicates an insulating behavior. The inset shows a photo of the grown film. The film thickness determined by AFM measurements is noted on several positions across the grown film. The thicknesses extracted around the edge of the film are between 14 nm and 16 nm. The film thickness in the middle of the BST sample is slightly larger (19 nm). This points at a slightly lower growth temperature in the middle of the BST film. Since the sapphire substrate is tightly fixed with tantalum clamps on the edge of the substrate, it is likely that the thermal contact between substrate and sample holder is higher at the edge of the sample.

Furthermore, three areas on the sample were selected to investigate the transport properties. The Hall resistances measured in the middle of the sample (blue), at the edge (red) and near a clamp (green) are displayed in Fig. 4.11(b). The three curves show the same $p$-type behavior and the carrier concentrations, which were extracted from this measurement, are all around $n_{2D} = 2 \times 10^{12}\,\mathrm{cm}^{-2}$. This result demonstrates a homogeneous bulk insulating growth even on the largest possible scale.

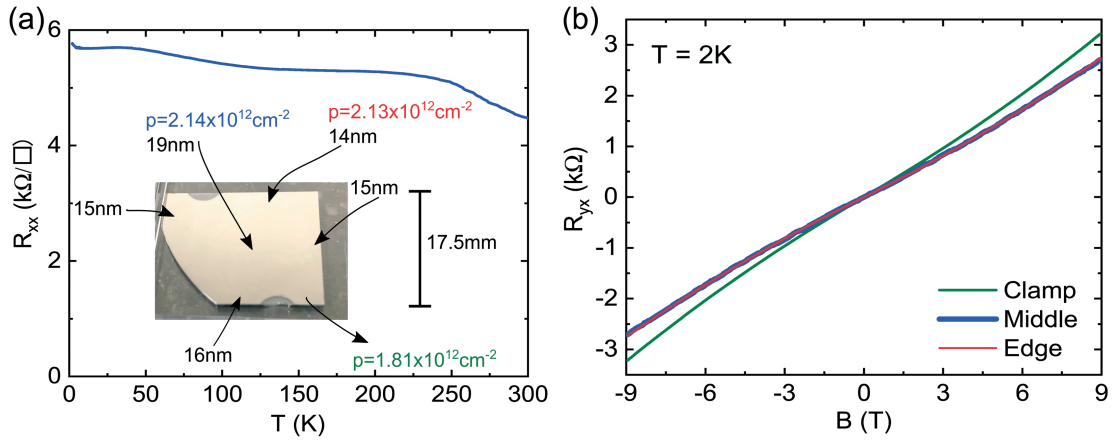


**Figure 4.11: BST growth on a large sapphire substrate to check the homogeneity of the film growth.** (a) The temperature dependence of the sheet resistance indicates an insulating behavior. The inset shows a photo of the grown film. Marked are several positions across the sample on which AFM measurements were performed to determine the thickness. Additionally, three areas in the middle (blue), the edge (red) and near a clamp to fix the substrate on the sample holder (green) are indicated by arrows. (b) Hall resistance measurements performed at the in (a) highlighted areas. All curves show the same p-type behavior and similar carrier concentrations can be extracted.

### 4.2.5 Protective capping of $(Bi_{1-x}Sb_x)_2Te_3$ films

**Introduction**

The conduction in bulk-insulating topological insulator films is dominated by the topological surface states. To preserve these surface states, it is necessary to protect the MBE-grown film from oxidization before exposing them to ambient conditions *ex-situ*. A perfect crystal surface is inert to surface oxidization. However, low dimensional structures and not perfect materials show the formation of an oxide layer upon air exposure. The oxidization process depends on the crystal quality and the growth conditions [140, 141].

In combined studies of magneto-transport and surface sensitive characterization techniques, it was demonstrated that TI thin films which were characterized *in-situ* after growth show different behavior in contrast to TI films which were exposed to ambient conditions. ARPES and XPS measurements revealed that exposing unprotected TI materials to air leads to the filling of the bulk conduction band with electrons, such that the conductivity is no longer carried exclusively by the surface states [142–144]. Contradicting studies claim that a high density of step-edges promotes the formation of an oxide film, while other STM data suggests the same behavior without any prominent features in the morphology [145–147]. The oxidization process involves several steps. Generally, the incoming $O_2$ and $H_2O$ molecules are first absorbed by tellurium at the surface, followed by the oxidization of the first film layer. In the case of $Sb_2Te_3$, this results in the formation of an amorphous antimony oxide layer. Afterwards, the oxide growth continues into deeper film layers [148]. The oxidization kinetics examined by ARPES and XPS studies of $(Bi_{1-x}Sb_x)_2Te_3$ single crystals in the composition range from $x = 0$ ($Bi_2Te_3$) to $x = 1$ ($Sb_2Te_3$) found that the oxidization of the first layer in $Sb_2Te_3$ is much faster than in $Bi_2Te_3$. The behavior of the mixed $(Bi_{1-x}Sb_x)_2Te_3$ crystals is similar to the behavior of $Sb_2Te_3$. The oxide layer growths linearly as a function of time until an oxide thickness of 3 nm is grown and the growth rate decreases. The oxidization speed is further increased in humid air. Volykhov *et al.* [148, 149] found that after an oxidation time of 100 hours in humid air (humidity 44%), the oxide thickness on the surface of a $Bi_2Te_3$ crystal was $\sim$20 Å. The same oxide thickness was found on the surface of a $Sb_2Te_3$ crystals after an oxidation time of only approximately 1 hour [145, 150].

**Characterization of $(Bi_{1-x}Sb_x)_2Te_3$ films capped with $Al_2O_3$**

To protect the grown $(Bi_{1-x}Sb_x)_2Te_3$ films from oxidization, the evaporation of $Al_2O_3$ as a protective layer is an established technique [143, 151]. It is desirable to *in-situ* deposit the $Al_2O_3$ after growth. The lack of a port to mount an additional evaporator at the MBE1 and MBE2 chamber, which are used for the growth of $(Bi_{1-x}Sb_x)_2Te_3$ films, prevents the *in-situ*-evaporation of $Al_2O_3$. To tackle this problem, the film is removed from the MBE load lock and without delay taken into the cleanroom where it is loaded into the atomic layer deposition (ALD) setup to deposit 3 nm of $Al_2O_3$ at 80 °C. A similar process was successfully reported by the Tokura group [86].

Figure 4.12 compares magneto-transport measurements performed on two $(Bi_{1-x}Sb_x)_2Te_3$ films, grown at the same conditions. One film was capped with 3 nm $Al_2O_3$ by ALD deposition ((a) and (b)), while the other film remained unprotected ((c) and (d)). Both films were remeasured several times in a PPMS in the course of up to 26 days to investigate the behavior of magneto-transport properties upon exposure to ambient conditions.

When first measured after growth, both films show the same insulating transport behavior, as indicated by the red curves in the temperature dependence of the sheet resistance in the temperature range between 2 K and 300 K in Fig. 4.12 (a) and (c). First, the sheet resistance $R_{xx}$ increases with decreasing temperature and follows an insulating behavior. An upturn in the sheet resistance can be seen at the lowest temperatures. Here, the bulk carriers freeze out and the conduction is dominated by surface carriers [129, 152]. Both BST films exhibit a similar $n$-type carrier concentration in the Hall resistance of $n_{2D} = 3.41 \times 10^{12}\,\mathrm{cm}^{-2}$ for the $Al_2O_3$ capped and $n_{2D} = 3.81 \times 10^{12}\,\mathrm{cm}^{-2}$ for the pristine film, as extracted from the curves in Fig. 4.12 (b) and (d). These low carrier concentrations suggest a surface dominated conduction in both BST films.

The ALD-capped film still exhibits the same insulating behavior of the sheet resistance in the repeated measurements shown in Fig. 4.12 (a). However, the total values the sheet resistance are shifted, which suggests a change in the mobility of the surface carriers. One can calculate a mobility of $\mu$=464 $\mathrm{cm}^{-2}$/Vs for the first measurement and $\mu$=292 $\mathrm{cm}^{-2}$/Vs for the measurement after 26 days, which explains the change in the sheet resistance. Over the course of 26 days the capped film remains bulk insulating and has an $n$-type carrier concentration of $n_{2D} = 4.2 \times 10^{12}\,\mathrm{cm}^{-2}$, as depicted in Fig. 4.12 (b).

The BST film which was not protected shows typical metallic behavior in the remeasured temperature dependence measurement of the sheet resistance

in Fig. 4.12 (c) already after 6 days. The change in the Hall slope shows a transition from a $n$-type carriers to a mixture of $n$- and $p$-type carriers after 6 days. This non-linear behavior most likely comes from two carriers (surface and bulk) with different mobilities which now contribute to the conduction. The carrier type changed to $p$-type depicted by the positive slope in the measurement performed 24 days after the first measurement with a carrier concentration of $n_{2D} = 1.31 \times 10^{13}\,\mathrm{cm}^{-2}$.

These measurements clearly emphasize that the protected BST film upholds its $n$-type bulk-insulating behavior even after 26 days. The unprotected film however becomes metallic and changes its carrier type from $n$- to $p$-type. In this case, the top surface of the film was not protected from oxidization and the exposure to air changed the electronic structure by shifting the Fermi level of the grown film. The conduction is no longer surface dominated but includes bulk contribution as seen in the higher carrier concentration.

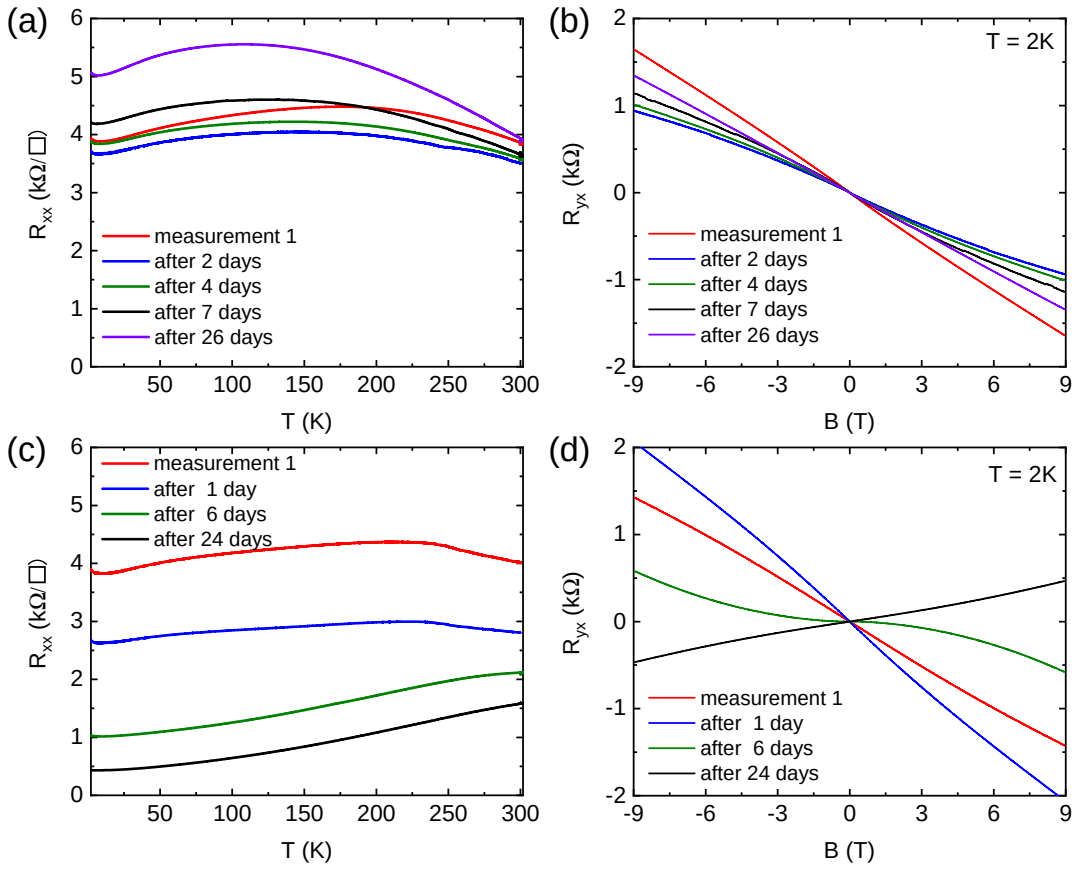


**Figure 4.12: Comparison of the transport properties of a $(Bi_{1-x}Sb_x)_2Te_3$ film which was capped with 3 nm $Al_2O_3$ and a BST film which was not protected.** Both samples where measured several times to see the change in transport properties. (a) Temperature dependence of the sheet resistance and (b) field dependence of the Hall resistance of a capped BST film. (c) Temperature dependence of the sheet resistance and (d) magnetic-field dependence of the Hall resistance of not protected BST film.

### 4.2.6 Electrical gating of a $(Bi_{1-x}Sb_x)_2Te_3$ film

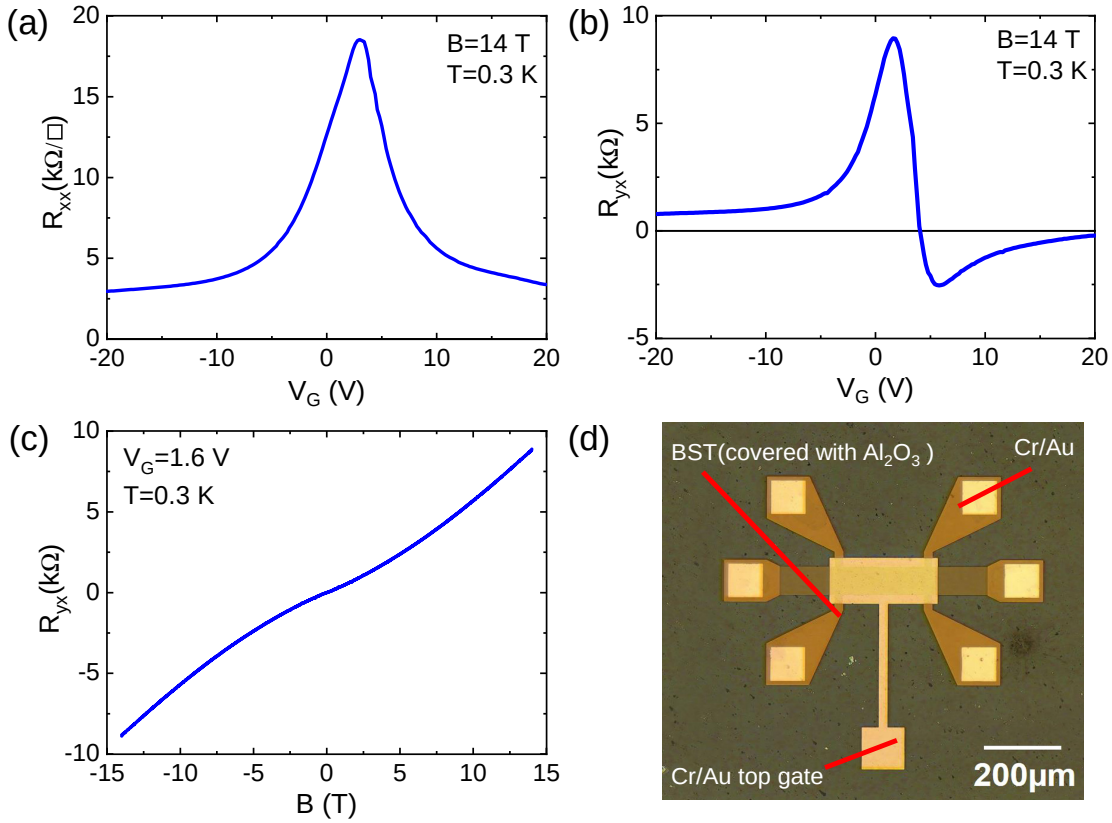


**Figure 4.13: Example of electrical gating of a 8 nm BST film.** (a) Gate voltage dependence of the sheet resistance shows that the Fermi level is tuned through the Dirac point. (b) Gate voltage dependence of the Hall resistance indicates a $n$-type behavior starting at $V_G$=20 V and changing to $p$-type upon scanning the gate voltage in negative direction. (c) Magnetic field dependence of the Hall resistance at $V_G = 1.6$ V. (d) Optical image of the top gating device.

As discussed in the introduction of this chapter 4.1, the control of the Fermi level is essential for topological insulator materials. Electrical gating is, additionally to chemical doping or band structure engineering, a method to fine tune the chemical potential in a wide range [129, 130].

Figure 4.13 presents the results of electrical top-gating of a 8 nm-thin BST film. The $(Bi_{1-x}Sb_x)_2Te_3$ was grown on a sapphire substrate while ramping the temperature from 230 °C to 280 °C within 5 minutes and 10 minutes additional growth at the higher temperature, with a flux ratio Bi:Sb of 1 : 5.6 and 10 times more tellurium flux.

An optical image of the fabricated top gated device is shown in Fig. 4.13(d). The film was patterned into a Hall-bar structure by photolithography and wet-etching. The metal contacts were fabricated by photolithography as well and thermal deposition of 3 nm chromium and 40 nm gold. Afterwards, 40 nm $Al_2O_3$

was deposited by atomic layer deposition (ALD) at 80 °C as a dielectric layer. After opening the windows on the Cr/Au contacts, a top-gate is fabricated as a final step by photolithography and thermal deposition of 33 nm chromium and 40 nm gold.

The magneto-transport measurements were performed in a Helium-3 insert (Oxford Instruments Heliox) in a 14 T-superconducting magnet using the ac-lock in technique. The gate voltage was applied by using a Keithley 2400 source meter.

Figure 4.13(a) and (b) shows the sheet resistance $R_{\mathrm{xx}}$ and the longitudinal resistance $R_{\mathrm{yx}}$ as a function of applied gate voltage $V_{\mathrm{G}}$. The gate voltage was applied in a range of $\pm 20\,\mathrm{V}$ at a base temperature of 0.3 K and a magnetic field of 14 T. The gate-voltage dependence of the sheet resistance $R_{\mathrm{xx}}$ plotted in Fig. 4.13(a) reveals a maximum indicating that the Fermi level is tuned through the Dirac point. The gate voltage dependence of the Hall resistance $R_{\mathrm{yx}}$ in Fig. 4.13(b) indicates $n$-type behavior starting from $V_{\mathrm{G}} = 20\,\mathrm{V}$ and changes to $p$-type upon scanning the gate voltage in negative direction. Hence, by applying a top-gate voltage, the carrier type could be tuned all the way from electron to hole dominated conduction. The magnetic field dependence of the Hall resistance $R_{\mathrm{yx}}$ at $V_{\mathrm{G}} = 1.6\,\mathrm{V}$, which is approximately the Dirac point, in Fig. 4.13(c) shows a slightly non-linear slope. This slight non-linearity probably indicates that the top and bottom surface of the grown film have different carrier concentrations. The top gate on the 8 nm-thin BST film might only tune the chemical potential on the top surface of the film but cannot effectively tune the potential of the bottom surface. In such case, a dual-gate on top and bottom surface of a topological insulator can tune the Fermi level simultaneously on both surfaces [130].

## 4.3 Conclusion and outlook

$(Bi_{1-x}Sb_x)_2Te_3$ films were grown on sapphire substrates using molecular beam epitaxy. The growth conditions were investigated using x-ray diffraction, atomic force microscopy and magneto-transport measurements.

The growth conditions were optimized to obtain high-quality single crystalline films with good morphology. Therefore- a two-step-growth method was established and the start and end growth temperature carefully calibrated. The film growth was further optimized to successfully obtain bulk insulating behavior by changing the ratio between bismuth and antimony. The homogeneity of the grown BST film was demonstrated on a large scale. Furthermore the necessity of protecting the film surface by $Al_2O_3$ capping was investigated and confirmed. Finally, a top-gate device was fabricated on a BST film and the ability to tune the Fermi level was confirmed by applying a gate voltage.

It is prudent to emphasize that the optimization process is always a combination of various parameters. Consequently, changing one parameter, for example the thickness of the film, involves finding a new set of optimized substrate temperature, Bi/Sb ratio and so forth.

The optimized $(Bi_{1-x}Sb_x)_2Te_3$ films have various applications. In the scope of this work they are the basic building block for the magnetically doped topological insulator in chapter 5 and the selective area growth in chapter 7. Additionally, the film were used in other projects such as the etching BST film into nanowires and the investigation of proximitized superconductivity in a $(Bi_{1-x}Sb_x)_2Te_3$ with a layer of palladium on top [153].

# Chapter 5

# MBE growth of magnetically doped topological insulator films

## Contents



Doping a topological insulator with transition metal elements can establish ferromagnetism in a TI and lead to TRS breaking [48, 49]. TRS breaking opens a magnetic exchange gap at the Dirac point in the topological surface states. Tuning the Fermi level into this gap results in the emergence of exotic phenomena such as the quantum anomalous Hall effect (QAHE) which generates disspationless edge current with no external magnetic field needed. This chapter discusses the growth of vanadium-doped $(Bi_{1-x}Sb_x)_2Te_3$ (VBST) films and the optimization process to achieve the QAHE in these films.

## 5.1 Introduction

After the exciting discovery of the quantum Hall effect, with its quantized transverse resistance and simultaneously vanishing longitudinal resistance, it became clear that the technological applications for this effect were limited by the high magnetic fields which were needed to achieve dissipationless edge transport. In the case of the quantum anomalous Hall effect no external magnetic field is needed to observe dissipationless edge transport.

The breaking of time-reversal symmetry in a topological insulator by introducing ferromagnetism into the sample leads to the quantum anomalous Hall effect. Chromium and iron were two of the first elements proposed as possible candidates for magnetic doping [39].

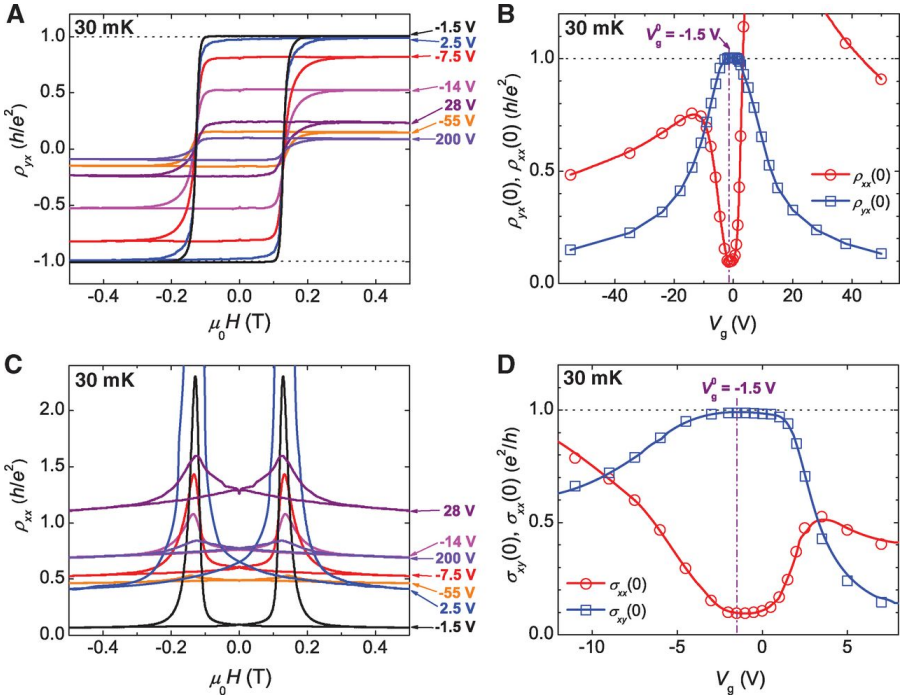


**Figure 5.1: First experimental observation of the quantum anomalous Hall effect in Cr-doped BST at 30 mK** (a) Magnetic field dependence of the transversal resistivity at different gate voltage. (b) Gate voltage dependence of the longitudinal and transverse resistivity at zero field. (c) Magnetic field dependence of the longitudinal resistivity at different gate voltage. (d) Gate voltage dependence of the longitudinal and transverse conductivities at zero field. Reprinted by permission from Science **340**, 6129, pp. 167-170 (2013), Experimental Observation of the Quantum Anomalous Hall Effect in a Magnetic Topological Insulator; C.Z. Chang *et al.*, Copyright (2013), [154]

The opening of a gap at the Γ-point in the topological surface states was first seen by angle-resolved photoemission spectroscopy (ARPES) measurements on iron-doped $Bi_2Se_3$ [156].

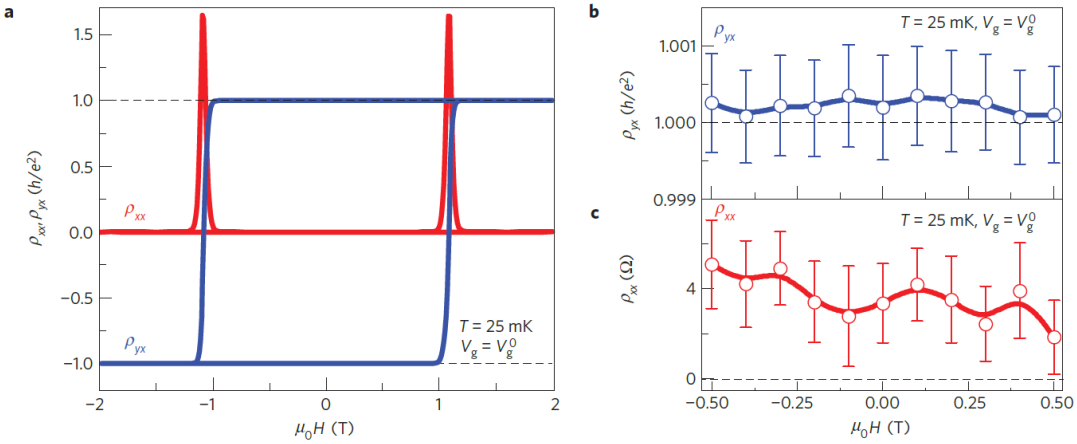


**Figure 5.2: Observation of the quantum anomalous Hall effect in V-doped BST at 25 mK**(a) Magnetic field dependence of the longitudinal and Hall resistance at the charge neutrality point. (b) Magnetic field dependence of $\rho_{xx}$ and $\rho_{yx}$ at low magnetic fields. Reprinted by permission from Springer Nature: Nature Mater **14**,473–477 (2015), High-precision realization of robust quantum anomalous Hall state in a hard ferromagnetic topological insulator ; C.Z. Chang *et al.*, Copyright (2015), [155]

The quantum anomalous Hall effect was first experimentally realized in 5 QL chromium-doped $(Bi_{1-x}Sb_x)_2Te_3$ films grown on $SrTiO_3$ (111) substrates in 2013 [154]. The measurements by the Xue group shown in Fig. 5.1 reveal quantization in units of $e^2/h$ in the transverse resistance while applying a gate voltage of −1.5 V and by this shifting the Fermi level into the surface gap. The longitudinal resistance remains at a value of $\rho_{xx} \sim 2.5\,\mathrm{k}\Omega$ and only vanishes completely after applying a strong perpendicular magnetic field ($B > 10\,\mathrm{T}$). This residual longitudinal resistance is most likely due to inhomogeneously distributed chromium atoms which cause a non-uniform ferromagnetism in the film [157], variable-range hopping [154, 158] or remaining non-chiral edge-states [159, 160]. To demonstrate a quantized sample with no $R_{xx}$ contribution, the film quality had to be improved.

In 2015, the Moodera group achieved the quantum anomalous Hall effect in 4 nm-thin vanadium-doped BST films [155], which have a higher coercive field $H_C$ ($\sim 1\,\mathrm{T}$) and critical temperature $T_C$ than the Cr-doped BST samples and reach a highly ordered ferromagnetic state at zero magnetic field. Here, the more uniformly distributed ferromagnetic order gives a quantization of $\rho_{yx}$ reaching $0.9998e^2/h$ and vanishing $\rho_{xx}$ at 25 mK (see Fig. 5.2). Additionally the Tokura group and Goldhaber-Gordon group reported the quantum anomalous Hall effect achieved in Cr-doped BST showing a longitudinal resistance far lower than

what was achieved in the first measurements of the Moodera group [159, 161, 162].

What all the successful demonstrations of the QAHE have in common is the low temperature regime in which the full quantization of the conductance was achieved. The temperature at which the QAHE is observed is generally below 100 mK, which is several orders lower than the measured $T_C$ of the material and a reported magnetic exchange gap of up to 50 meV [156, 163]. There are various reasons for this behavior, such as impurity channels created by dopants and defects [160] or residual bulk carriers [162].

A way to decrease disorder in the sample and to increase the temperature at which the quantum anomalous Hall effect can be observed, was demonstrated in 2015 by the Tokura group [164]. Mogi *et al.* showed that by growing a 8 nm-thin tri- and penta-layer structure of $(Bi_{0.22}Sb_{0.78})_2Te_3$ and $Cr_{0.46}(Bi_{0.22}Sb_{0.78})_2Te_3$, it was possible to observe a robust quantization up to 0.5 K and $\pm 0.97\,h/e^2$ at 2 K (see Fig. 5.3). This behavior can be explained by the suppression of disorder in the surface states.

Another way to reach a high temperature quantum anomalous Hall effect was brought forward by the theoretically prediction that $MnBi_2Te_4$ is a layered antiferromagnet with septuple van der Waals layers of Te-Bi-Te-Mn-Te-Bi-Te [165]. The intrinsic magnetization in $MnBi_2Te_4$ is expected to open a uniform, large magnetic gap. The temperature at which the QAHE can be observed is increased in this stoichiometric ordered compound. ARPES measurements already confirmed the opening of the magnetic gap [166] and the occurrence of the QAHE at 1.4 K in the intrinsic magnetic topological insulator $MnBi_2Te_4$ was confirmed by experiment [167].

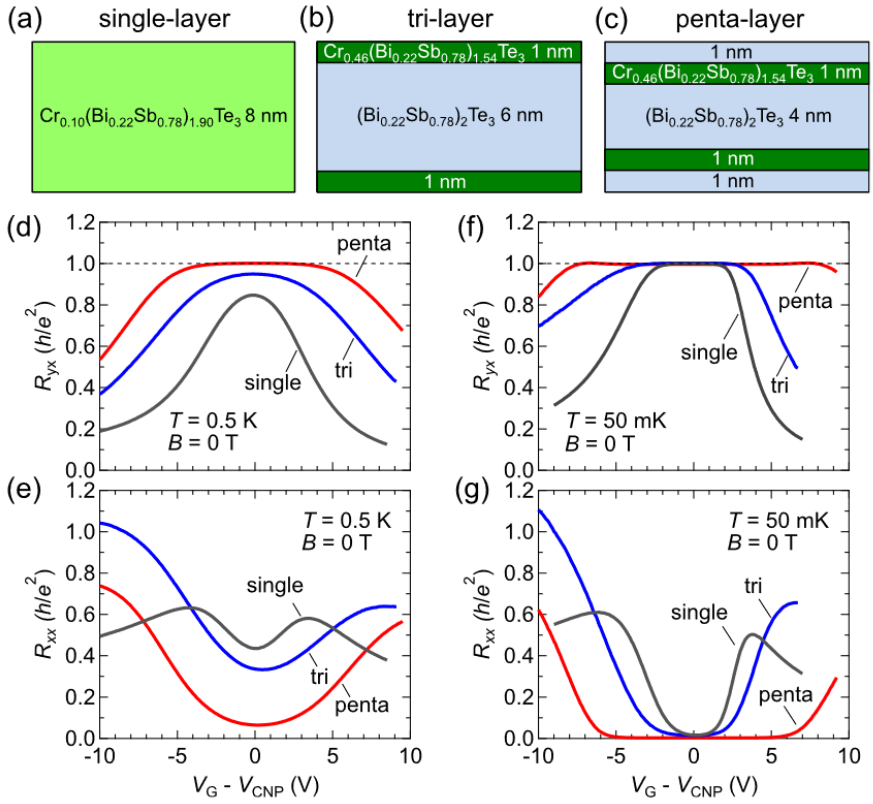


**Figure 5.3: Schematics and measurements of the uniform and modulation magnetic doping structures**(a)-(c) Schematics of the single-, tri- and penta sample structures. (d),(f) Gate voltage dependence of $R_{yx}$ at 0.5 K and 50 mK. (e),(g) Gate voltage dependence of $R_{xx}$ at 0.5 K and 50 mK. Reprinted by permission from: Appl. Phys. Lett **107**,182401 (2015), Magnetic modulation doping in topological insulators toward higher-temperature quantum anomalous Hall effect ; M. Mogi *et al.*, Copyright (2015), [164]

## 5.2 MBE growth and characterization of V-doped BST films

**Optimization of the growth parameters for the MBE growth**

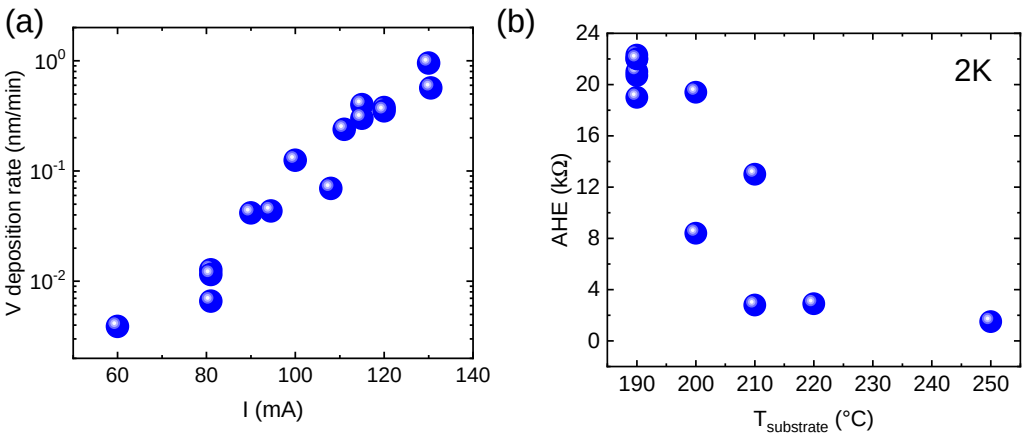


**Figure 5.4: Deposition rate of vanadium and dependence of the anomalous Hall amplitude on the substrate temperature during VBST growth.** (a) Calibration curve for the deposition rate of vanadium as a function of electron beam current of the ebeam evaporator. (b) Dependence of the anomalous Hall amplitude extracted at 2 K on the substrate temperature during VBST growth.

The magnetically doped $(Bi_{1-x}Sb_x)_2Te_3$ (BST) films were grown on InP substrates using the MBE3 UHV-chamber. The substrates were cleaned with acetone and IPA in an ultrasonic bath prior to inserting them into the MBE chamber. The substrates were then annealed to 550 °C in the buffer chamber of the MBE3 system to remove the native oxide layer (see chapter 3.1.3). The prospect of a more robust ferromagnetic order due to the larger coercive field and higher $T_C$ in vanadium-doped BST films compared to those using chromium as a dopant [155] led to the decision to choose vanadium as the magnetic dopant for the BST films grown in the scope of this thesis.

As in the case of undoped $(Bi_{1-x}Sb_x)_2Te_3$ film growth discussed in chapter 4, a careful optimization of the growth parameters for the magnetically doped films has to be carried out. Various growth parameters play an important role, here the optimization of the amount of vanadium dopants and the sample temperature during growth are exemplary discussed. Apart from these two parameters, the thickness of the VBST films [168] and the bismuth-antimony ratio have to be optimized. In order to observe the quantum anomalous Hall effect, the Fermi level has to be tuned into energy gap by changing the Bi/Sb ratio [57]. For films

discussed in this chapter a Bi:Sb ratio of $1 : 3.8 \pm 0.1$ was found to be optimal. In terms of thickness, Feng *et al.* [168] found an lower and an upper limit for the film thickness to reach full quantization of $R_{yx}$. If the film is too thick, surface-dominated conduction is likely to exhibit contributions from the bulk as well. Reducing the thickness of a 3D topological insulator leads to a hybridization of top and bottom surface which opens a gap, such that the system becomes two-dimensional. The size of the hybridization gap $E_g$ has to be smaller than the size of magnetic exchange gap $E_{ex}$ to observe the QAHE [36, 168, 169]. It was found that for film thicknesses $\leq 3$ QL, the hybridization gap exceeds the magnetic exchange gap [168]. Within the scope of this thesis, the film thickness was kept at $\sim$7 nm.

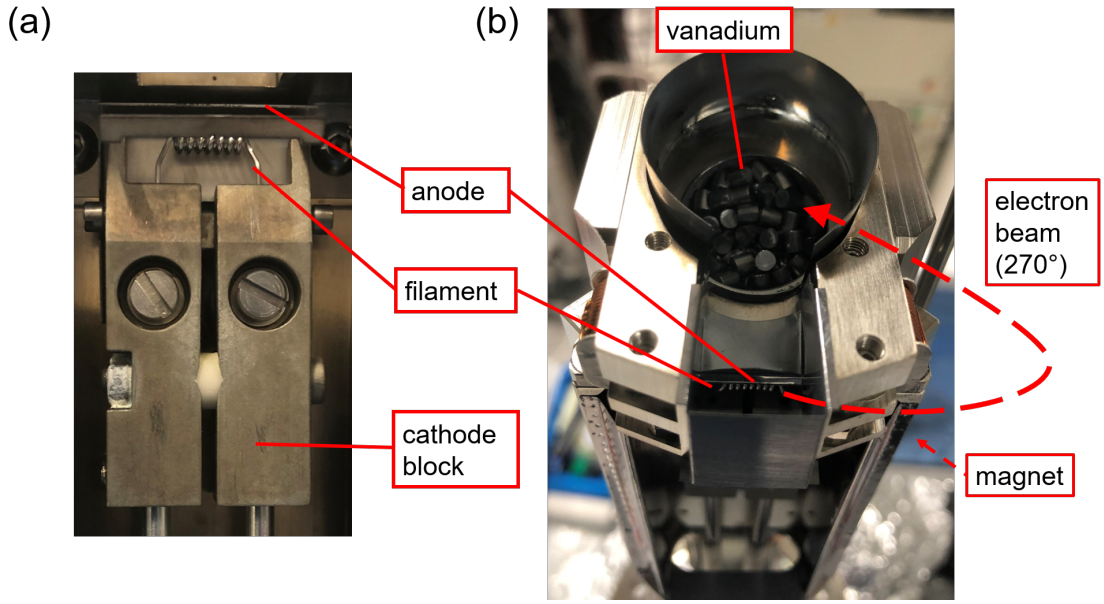


**Figure 5.5: Electron-beam evaporator for the vanadium deposition:** (a) Photo of the front of the electron-beam evaporator with anode, cathode and filament visible. (b) View from top with the evaporant visible and the electron beam sketched. The magnet is fixed on the side of the construction and cannot be seen in this photo.

Due to the high melting point of vanadium ($\sim$1910 °C [170]), an electron-beam evaporator EBVV designed by MBE Komponenten is used for the evaporation. Here, the source material is directly bombarded by high-energy electrons instead of simply heating the material by heat radiation [74]. A photo of the electron-beam evaporator is shown in Fig. 5.5. The tungsten filament is at negative high voltage (−3 kV to −10 kV). Electrons from the hot filament are accelerated by the anode. The cathode shield (−10 kV) prevents the electrons from hitting the anode and instead forces them to take an outer path. A permanent magnet deflects the electron beam by 270° so it bombards the material [171]. The evaporation

rate can be controlled by the electron-beam current and voltage. The amount of vanadium doping cannot be measured by the beam flux monitor since vanadium acts as a gettering material in the MBE chamber [172], such that the pressure in the chamber locally decreases to below the measurable pressure range of $p \sim 10^{-12}$ mbar. To calibrate the deposition rate, a series of vanadium films was grown on sapphire substrates. Figure 5.4(a) shows the growth rate for several such vanadium films. The thickness of the grown films was determined by atomic force microscopy (AFM). The electron beam current was varied between 60 mA and 150 mA, while the applied voltage was always kept at 6 kV. This graph can be used to roughly recalculate the intended number of dopants and additionally should be revisited from time to time to examine whether the growth conditions have changed.

The anomalous Hall effect (AHE) amplitude and the critical temperature $T_{\mathrm{C}}$ are two characteristics to judge the magnetic properties of the grown film, given they measure the ferromagnetic order in the doped film. The anomalous Hall amplitude of the VBST films was measured at 2 K in a PPMS system using a standard Hall bar configuration and the ac-lock in technique while sweeping the magnetic field $\pm 9$ T.

The dependence of the AHE amplitude on the substrate temperature, measured on already optimized samples in terms of thickness, Bi/Sb composition ratio and vanadium concentration, is depicted in Fig. 5.4(b). Here, all samples were grown at the same electron-beam current and voltage, but the growth temperature was varied. The highest value for the anomalous Hall amplitude was measured for VBST films which were grown at a substrate temperature of 190 °C and 200 °C. The amplitude becomes smaller for films grown at higher temperatures. For growth temperatures lower than 190 °C the AFM images present a very rough and holey morphology indicating that these temperatures are too low to grow a single crystalline film with good morphology. Indeed, all samples represented by the blue dots at 190 °C show full quantization of the Hall resistance at 30 mK.

In case of the magnetically doped BST films, the amount of the magnetic dopants has to be carefully tuned. The vanadium concentration has to be large enough to introduce a robust ferromagnetism in the system which can be directly judged by measuring the anomalous Hall effect and the critical temperature $T_{\mathrm{C}}$. A too high vanadium concentration however can introduce magnetic clusters

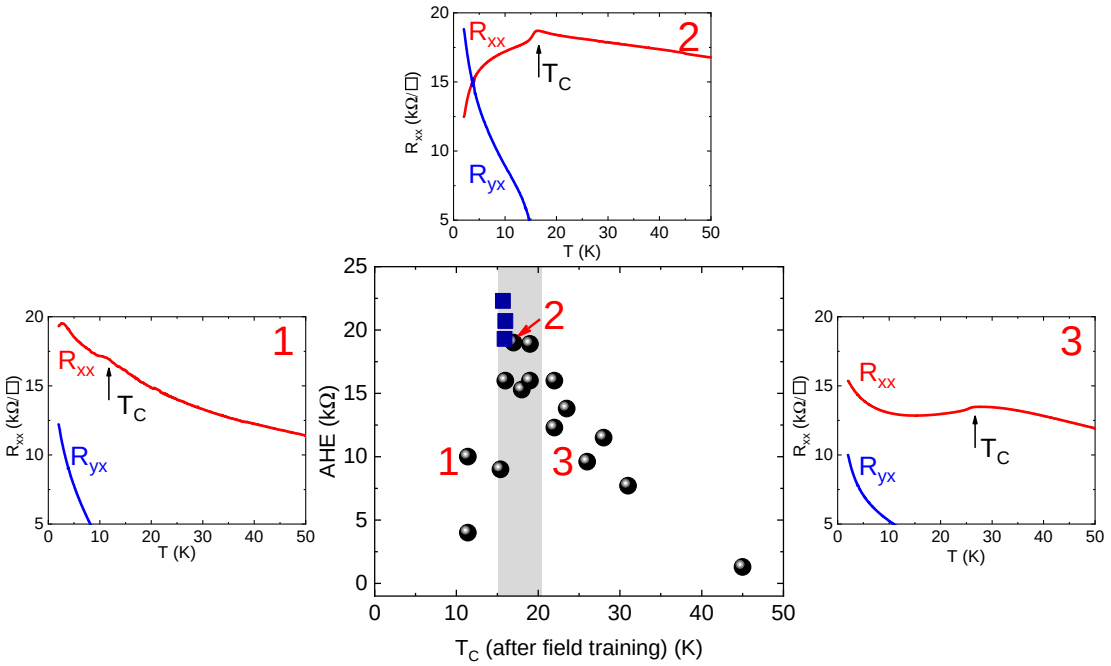


**Figure 5.6: Dependence of the anomalous Hall amplitude on the critical temperature** $T_C$: The middle panel shows the dependence of the anomalous Hall amplitude of the critical temperature $T_C$ determined after field training. The surrounding graphs each show the temperature dependence of the longitudinal resistance $R_{xx}$ (red curve) and the Hall resistance $R_{yx}$ (blue curve) for three samples highlighted by red numbers 1, 2, 3 in the main panel. The samples were all grown 40 minutes at $T_{substrate}$=190 °C and capped with 3 nm of $Al_2O_3$. The current used for the e-beam evaporation of vanadium was different for the three samples: sample 1: I = 66 mA, sample 2: I =67.5 mA and sample 3: I = 70.5 mA.

and by this disorder into the sample. The large, middle panel of Fig. 5.6 shows the anomalous Hall amplitude as a function of critical temperature determined after field training. The grey shaded region highlights a $T_C$ range which was found to be suitable for samples which quantize at temperatures below 100 mK. In fact, the samples represented by the three dark blue squares show quantization of the Hall resistance at 30 mK.

Three exemplary samples were selected and highlighted by red numbers. The three films were all grown 40 minutes at a substrate temperature of $T_{substrate} = 190\,°C$ and capped with 3 nm of $Al_2O_3$ by ALD after growth. The electron-beam voltage was always kept at 6 kV, while the electron-beam current was different for each of the samples (sample 1: $I = 66\,mA$, sample 2: $I = 67.5\,mA$ and sample 3: $I = 70.5\,mA$). The temperature dependence of the longitudinal resistance $R_{xx}$ (red curve) and the Hall resistance $R_{yx}$ (blue curve) is plotted for each sample in the three panels surrounding the middle plot and the critical temperatures are indicated by a black arrow at the transition temperature at which the anomalous

Hall contribution vanishes.

All three samples show a steady increase in the Hall resistance $R_{yx}$ but only sample 2 in the top panel exhibits a continuous decrease in the longitudinal resistance $R_{xx}$ as it is expected for a sample which is in the quantum anomalous Hall state. $R_{xx}$ drops by roughly 30% from its maximum value until the value at the lowest recorded temperature of 2 K. Sample 1 (left panel) also shows a slight decrease of around 1% in the longitudinal resistance, while the $R_{xx}$ curve of sample 3 (right panel) still increases at low temperatures. Given that the electron-beam current and thus the amount of evaporated vanadium used for the growth of sample 3 was the highest among the three samples, it is likely that the disorder created by the vanadium atoms is too large and thus electrons are scattered into the edge channels and prevent an entirely dissipationless edge current. The amount of vanadium in sample 1 is enough to introduce a fully ferromagnetic state with a clear transition temperature $T_C$, but the size of the magnetic gap is most likely too small to observe the quantum anomalous Hall effect even at lower temperatures.

**Protective capping of the grown VBST films**

Similar to the non-doped $(Bi_{1-x}Sb_x)_2Te_3$ films discussed in chapter 4.2.5, the V-doped BST films need to be protected from oxidization. Figure 5.7 shows a comparison of aging effects in transport measurements of VBST films without capping layer and protected by ALD-deposited 3 nm of $Al_2O_3$. Figure 5.7 (a) and (b) depicts the magneto-transport of a non-protected V-doped BST film measured at 2 K in a PPMS setup. The film was remeasured three times over the course of seven days. The first measurement in Fig. 5.7(a) shows a typical hysteretic behavior with a negative slope and an anomalous Hall amplitude of 5.2 kΩ. The characteristics of the film changed significantly over the course of seven days. The second measurement, performed two days after the first one, is displayed in Fig. 5.7(b, red curve) and shows a reversal of the hysteresis loop as well as a more than 10 times smaller anomalous Hall amplitude. The ferromagnetic order in the film has changed evidently as seen by the reversal of the magnetization direction. After seven days the amplitude decreased even further as depicted by the blue curve in Fig. 5.7(b). Furthermore, the sign of the hysteresis loop is reversed again. Consequently, the magnetic properties of the vanadium-doped BST film are clearly altered by the oxidization of the unprotected film.

The vanadium-doped BST film shown in Fig. 5.7(c) was capped with 3 nm $Al_2O_3$ by ALD deposition immediately after removing the sample from the vacuum system. No obvious change is visible in the Hall resistance measurements performed within five days of each other. The coercive field and the anomalous Hall amplitude show the same behavior. These results again underline the necessity to protect every film right after growth.

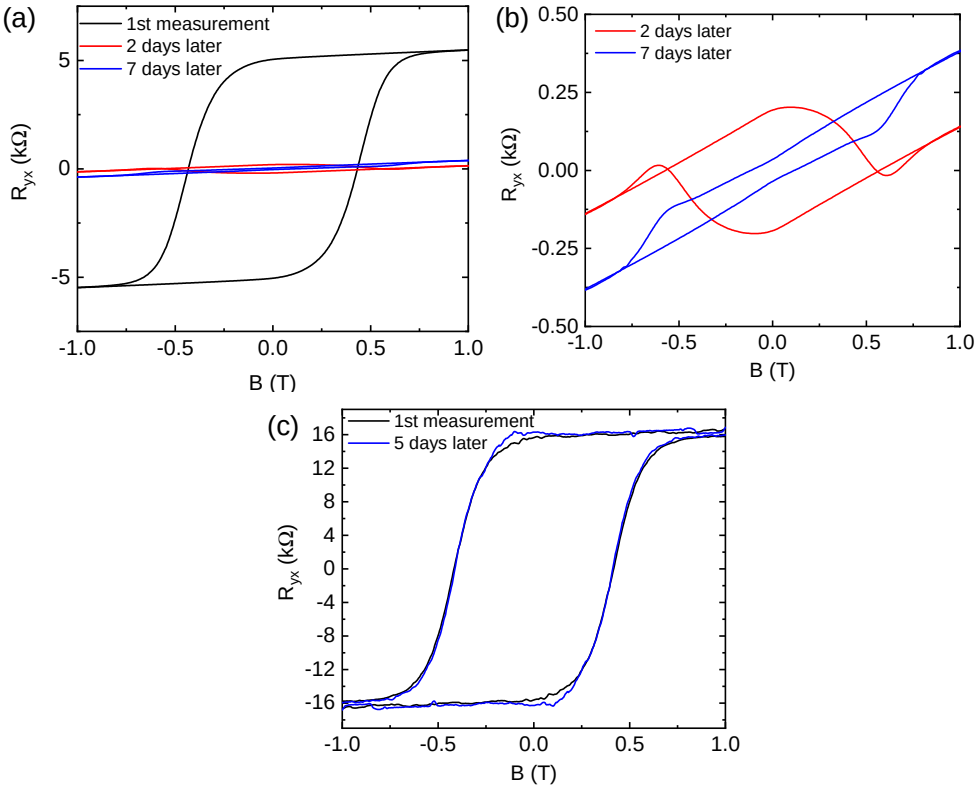


**Figure 5.7: Protective capping of the grown VBST films with ALD deposited $Al_2O_3$:** (a) Hall resistance measurement of a not protected film, with the red and blue curve remeasured 2 and 7 days after the first measurement. (b) Zoom in on the repeated measurements after 2 and 7 days. (c) Magneto-transport measurement of a VBST film which was capped with 3 nm $Al_2O_3$. No obvious change in the measurement of the Hall resistance can be identified over the course of 5 days.

### Growth recipe for the VBST growth

Taking the growth parameters obtained by the optimization process into account, the substrate temperature during growth is kept at $T = 190\,°C$. This optimal substrate temperature is lower than the growth temperature in the case of the undoped BST films. The reasons for this are mainly the different substrate the magnetically doped films are grown on and the different MBE chamber used for the VBST-growth. The heater used in the MBE3 chamber is constructed and positioned differently than the heater used in MBE2 such that the effective growth

temperatures are difficult to compare between the different MBE chambers. High-purity bismuth, antimony, tellurium and vanadium are simultaneously evaporated for 40 minutes with a growth rate of $<0.2\,\mathrm{nm\,min^{-1}}$. Just as for the regular $(Bi_{1-x}Sb_x)_2Te_3$ films, the vanadium-doped BST films are grown under tellurium-rich conditions. The Bi:Sb ratio is kept at $\sim 1:3.8$. The resulting films thickness after the growth is approximately 7 nm. Bismuth, antimony and tellurium are evaporated from standard Knudsen cells. The as-grown films are capped with 3 nm $Al_2O_3$ by atomic layer deposition (ALD). The crystal quality is checked by atomic force microscopy and x-ray diffraction. A typical XRD pattern and AFM image are displayed in Fig. 5.8. The XRD pattern indicates an epitaxial growth along the (00l) direction with no other phase found. A lattice constant of $c = 30.1994\,\text{Å}$ can be extracted from the XRD data. This is slightly larger than the lattice constant obtained for pure $(Bi_{1-x}Sb_x)_2Te_3$ film discussed in chapter 4.2.2, which indicates that vanadium doping leads to a small lattice expansion [154]. The atomic force microscopy image (1x1 µm) shown in Fig. 5.8(b) indicates a high-quality growth with a flat and continuous surface.

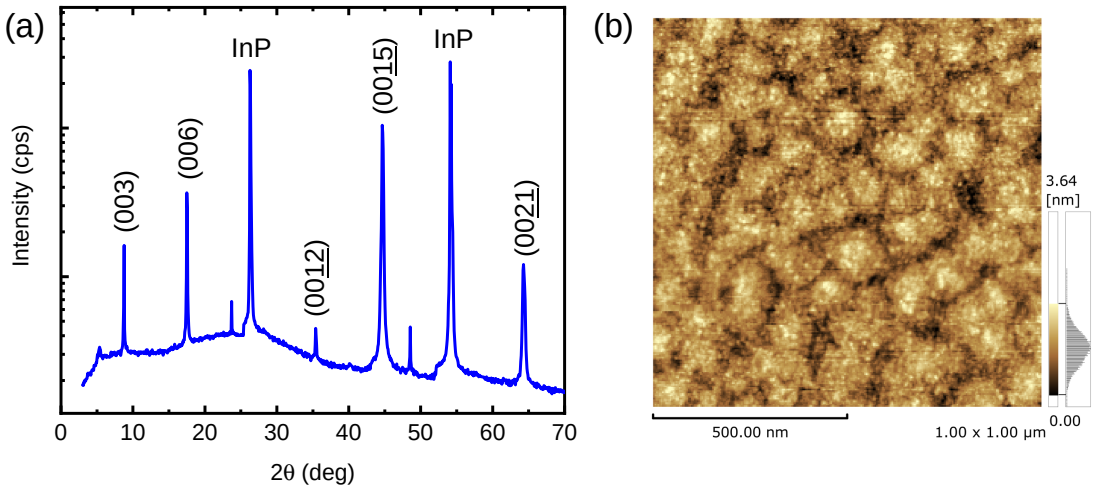


**Figure 5.8: AFM and XRD measurement of V-doped BST films grown on an InP substrate.** (a) The XRD pattern indicates an epitaxial growth along the (00l) direction with the InP peaks present as well. (b) The AFM image (1x1 µm) shows a continuous growth with flat terraces.

## 5.3 Measurement of the quantum anomalous Hall effect

### 5.3.1 Magneto-transport measurement at 2 K

After growth, magneto-transport measurements were performed on all samples at 2 K using a PPMS setup and standard lock-in amplifiers with an applied current of 100 nA.

A typical measurement result is shown in Fig. 5.9. Panel (a) displays the temperature dependence of the sheet resistance. The sheet resistance $R_{\mathrm{xx}}$ increases with decreasing temperature and hence follows an insulating behavior. The transport properties measured in a perpendicular magnetic field for varied temperatures is shown in Fig. 5.9(c) and the hysteresis loop measured at the lowest temperature of 2 K is highlighted in panel (b). From equation 2.17 in chapter 2.2.1, it is already known that the Hall resistance $R_{\mathrm{yx}}$ of a ferromagnetic material consists of an ordinary and an anomalous Hall contribution. Both contributions can be identified in Fig. 5.9 (b) and (c). The anomalous Hall contribution manifests as a hysteresis loop and the ordinary Hall part is described by the straight slope at higher magnetic fields. The square shape of the hysteresis loops indicates a long-range ferromagnetic order introduced by the vanadium dopants with a coercive field of 0.6 T. The negative slope of the ordinary Hall contribution at higher magnetic fields indicates an $n$-type behavior at 2 K. One can extract a carrier concentration of $n_{\mathrm{2D}} = 2.7 \times 10^{12}\, cm^{-2}$ and a mobility of $\mu = 110\, cm^{-2}$/Vs. The low carrier concentration indicates a bulk insulating behavior such that the Fermi level of the film lies in the bulk band gap. The temperature evolution from 300 K to 2 K of the anomalous Hall amplitude is depicted in Fig. 5.9(d). At 2 K, the anomalous Hall amplitude is $R_{\mathrm{AHE}} \sim$19 k$\Omega$, which is already close to the quantized value of $R = 25.81\,\mathrm{k}\Omega$.

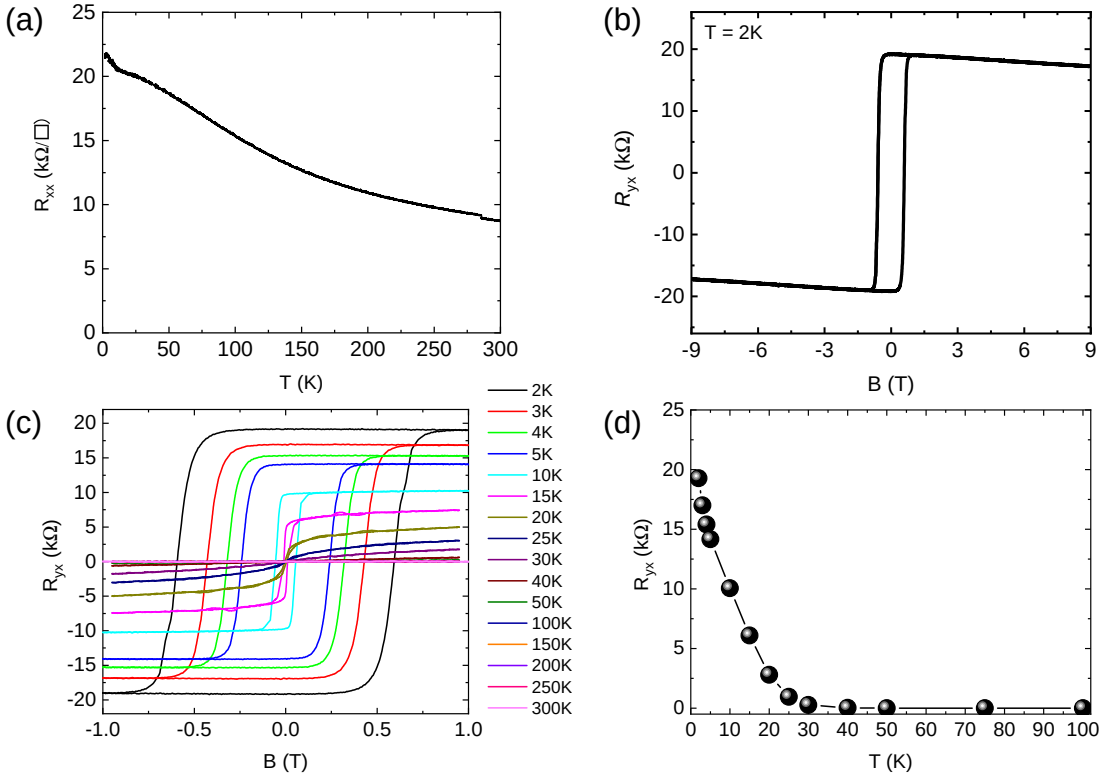


**Figure 5.9: Magneto-transport measurements of a ∼7 nm V-doped BST film at 2 K performed in a PPMS system.** (a) Temperature dependence of the sheet resistance $R_{xx}$. The measurement indicates an insulating behavior. (b) Magnetic field dependence of the Hall resistance $R_{yx}$ at 2 K. The square shape of the hysteresis loops indicates a long-range ferromagnetic order and the anomalous Hall amplitude is ∼19 kΩ. The negative slope of the ordinary Hall contribution at high magnetic fields indicates a n-type behavior with a carrier concentration of $n_{2D}$=2.7 × $10^{12}$ cm$^{-2}$ (c) Anomalous Hall curves: $R_{yx}$ measured by sweeping the field at various temperatures from 2 K to 300 K. (d) Temperature evolution of the anomalous Hall amplitude indicates an AH amplitude of 19 kΩ for the lowest temperature at 2 K and a critical temperature $T_C$ of approximately 25 K to 30 K.

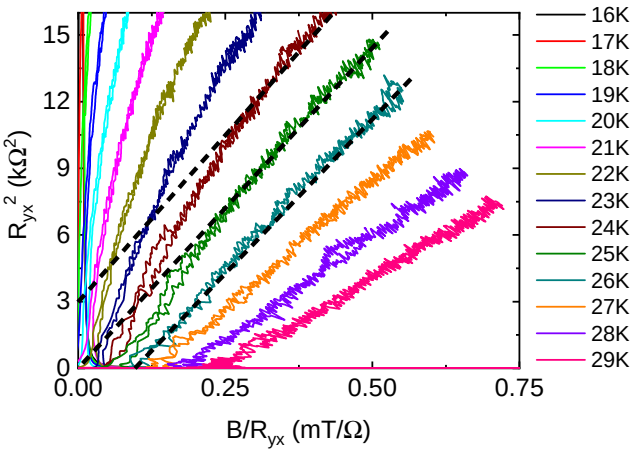


**Figure 5.10: Arrot plot to estimate the Curie temperature $T_C$ of a V-doped BST film.** A critical temperature of $\approx 25\,\mathrm{K}$ is extracted.

### 5.3.2 Determining the critical temperature $T_C$

To determine the Curie temperature $T_C$ of the grown VBST film three methods can be applied.

**(1)** The sample is first trained at 2 K in magnetic field by applying a field of $B = \pm 9\,\mathrm{T}$. This field is sufficient to align all magnetic moments in the V-doped BST film. The now trained sample is warmed up in zero magnetic field until a transition is visible in the longitudinal resistance $R_{xx}$. Above the critical temperature, the anomalous Hall effect vanishes. An exemplary measurement is depicted in Fig. 5.6.

**(2)** The measurement of the anomalous Hall amplitude at various temperatures is another way to define the critical temperature as shown in Fig. 5.9 (c) and (d). The $T_C$ is defined as the temperature at which the anomalous Hall contribution and thus the ferromagnetic state vanishes. Only the linear ordinary Hall contribution is left. This can either be identified by the disappearance of the hysteresis loop at a certain temperature in panel (c) or more clearly in graph (d) which shows the AH amplitudes as a function of temperature [159].

**(3)** Another way to determine the $T_C$ is by measuring Arrot plots [173]. Based on the equation $H = a(T/T_C - 1) + AM^3 + BM^5 + ...$ (for a magnetic field H near $T_C$) which Arrot derived in 1957, the critical temperature is estimated by plotting the square of the magnetization $M^2$ against the ratio of the applied magnetic field and the magnetization H/M. Therefore, further hysteresis loops were measured in close temperature steps near the $T_C$ determined by the magneto-transport measurements in Fig. 5.9(d). Using the relation between the transversal resistance $R_{yx}$ and the magnetic field over $R_{yx}$ given by $R_{yx}^2 = a + bB/R_{yx}$ (with a and b

constants), the Arrot plot is shown in Fig. 5.10. The Curie temperature is the temperature below which the ferromagnetic state appears. When you approach this temperature from above $T_C$, the intercept $a$ changes its sign from negative to positive and the slope $b$ increases. Thus the critical temperature can be extracted from the temperature curve in Fig. 5.10 where a linear fitting curve passes through the origin [155]. In Fig. 5.10 a critical temperature of $T_C \approx 25\,\mathrm{K}$ is extracted. The disadvantage of this method is that the measurement of the various hysteresis loops is far more time consuming than the zero-field warming of the trained film.

### 5.3.3 Observation of the quantum anomalous Hall effect

#### 5.3.3.1 Measurement of the QAHE

Vanadium-doped BST films, which show an anomalous Hall amplitude already close to the quantized resistance value of 25.81 kΩ at 2 K and have a critical temperature and field in the desired range, are further investigated by cooling the sample down to temperatures below 100 mK in a dilution refrigerator.

The grown VBST films are covered with 3 nm $Al_2O_3$, acting as a protective capping layer, and are patterned into a Hall bar geometry using optical lithography. Afterwards, the protective $Al_2O_3$-layer is removed by 50 °C-heated Transene D and the VBST film itself is etched by chemical etching in a $H_2O_2$(35%) 3 : 1 $H_2SO_4$ solution. 5 nm platinum and 45 nm gold ohmic contacts are deposited by sputtering in an UHV chamber. The metal contacts are lifted off by placing the sample in N-Methyl Pyrrolidone (NMP). An optical image of typical Hall bar device with a length of 300 µm and a width of 100 µm is displayed in Fig. 5.11(c).

The VBST film, shown in Fig. 5.9, was characterized in a dilution refrigerator using standard lock-in amplifiers and an applied AC current of 10 nA. The magneto-transport results are shown in Fig. 5.11. Figure 5.11(a) shows the magnetic field dependence of the longitudinal and Hall resistance measured at 30 mK. While sweeping the magnetic field with a rate of 0.02 T min$^{-1}$, the Hall resistance $R_{yx}$ (blue curve) reaches the quantized value of $h/e^2$ ≈25.81 kΩ, while the longitudinal resistance $R_{xx}$ (red curve) becomes zero. $R_{xx}$ increases only at the values of the coercive field at ∼1 T as the magnetization direction is reversed and the QAHE is destroyed. One might notice an additional small increase of $R_{xx}$ around 0 T. This deviation is probably coming from a slight temperature increase when

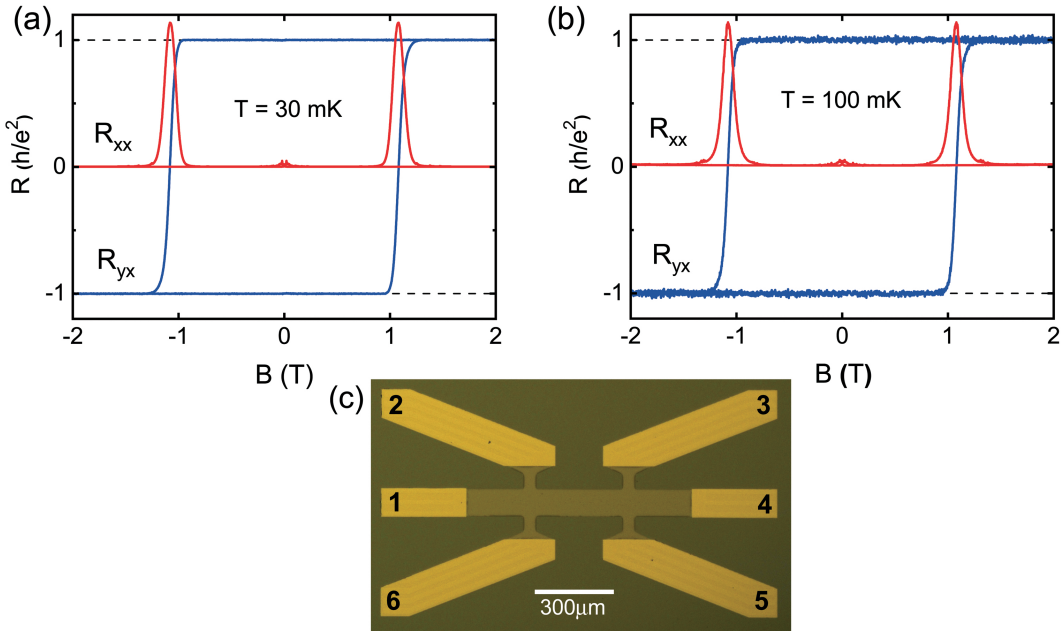


**Figure 5.11: Quantum anomalous Hall effect demonstrated in a V-doped BST film.** (a) The V-doped BST film is quantized at 30 mK. The Hall resistance $R_{yx}$ (blue curve) reaches the quantized value of $h/e^2$ ≈25.81 kΩ, while the transversal resistance $R_{xx}$ (red curve) becomes zero and increases only at the values of the coercive field. (b) The quantum anomalous Hall effect is still observed at 100 mK. (c) Optical image of a typical Hall bar device. Current is applied from contact 1 to 4.

the polarity of the magnetic field is reversed during the field scan [158]. Quantization is still observed at an increased temperature of 100 mK, as can be seen in Fig. 5.11(b). During this measurement, no gate voltage had to be applied in order to observe the quantum anomalous Hall effect. By carefully tuning the Bi/Sb ratio and the amount of vanadium dopants, it was possible to grow insulating VBST films and tune the Fermi level inside of the energy gap.

#### 5.3.3.2 Temperature dependence of the QAHE

Peculiarly, the quantum anomalous Hall effect in magnetically doped topological insulators was in general only observed at temperatures below 100 mK, even though a magnetic exchange gap of up to 28 meV to 50 meV was reported [156, 163]. By co- and modulation doping of TI films the temperature at which the QAHE could be observed was increased up to 2 K [164, 174]. These temperatures are still well below the expected values.

To study the robustness of the quantized state with increasing temperature, the temperature dependence of the conductance was measured on a 100 µm-wide Hall bar. Figure 5.12 shows the temperature dependence of the longitudinal

(red triangles) and transversal (blue points) conductance $G_{xx,yx}$ as a function of $T^{-1}$. The Hall conductance $G_{yx}$ remains at the quantized value of $e^2/h$ until a temperature of approximately 300 mK. The longitudinal conductance $G_{xx}$ can be fitted by an Arrhenius plot for a temperature region between 60 mK to 400 mK. The Arrhenius fitting is used to extract the thermal activation energy $T_0$ of a system. The Arrhenius fit is given by the equation [175]:

$$\sigma_{xx} = \sigma_0 exp(-T_0/T). \tag{5.1}$$

The measured longitudinal conductance $G_{xx}$ (red triangles) follows the exponential Arrhenius fit (black line) down to a temperature of ∼60 mK which points to a thermal activation-type of the temperature dependence [158, 162, 176]. A thermal activation energy $T_0 = 0.5\,\mathrm{K}$ can be extracted from the Arrhenius fit which corresponds to an average magnetic gap size of $k_\mathrm{B}T_0 = 40\,\mu\mathrm{eV}$, with the Boltzmann constant $k_B$. The $T_C$ of this sample is in the order of 20 K which gives a gap size of $k_\mathrm{B}T_\mathrm{C} = 2\,\mathrm{meV}$. Chong *et al.* [177] performed Landau Level-spectroscopy on magnetically-doped topological insulators to investigate the difference in gap sizes. They detect two types of disorder in the material. On the one hand they found evidence for electrostatic disorder. This kind of disorder is caused by a random spatial distribution of bismuth and antimony atoms within the sample. Consequently, a varying Bi/Sb ratio results in random positions of the Fermi level throughout the sample. The other disorder is coming from inhomogeneously distributed magnetic dopants. This magnetic disorder creates a random distribution of the magnetic gap size. The combination of these two disorders can lead to a suppressed size of the gap in the range of two orders from the average gap size in µm-sized regions in the sample.

The deviation of the longitudinal conductance $G_{xx}$ from the Arrhenius fit for temperatures below 60 mK suggests that at lower temperatures not only the surface state electrons carry the conduction, but an additional contribution is present. Variable range hopping (VRH) was suggested as such an electron transport mechanism at low temperatures [154, 158, 176]. Electrons can move by hopping from one localized state to the next near the Fermi energy within an energy range of $k_\mathrm{B}T$ [178]. Given that the electron temperature of the dilution fridge used for the measurements is ∼60 mK, the data obtained at this temperatures is not reliable to make a convincing argument on any low temperature electron transport mechanism.

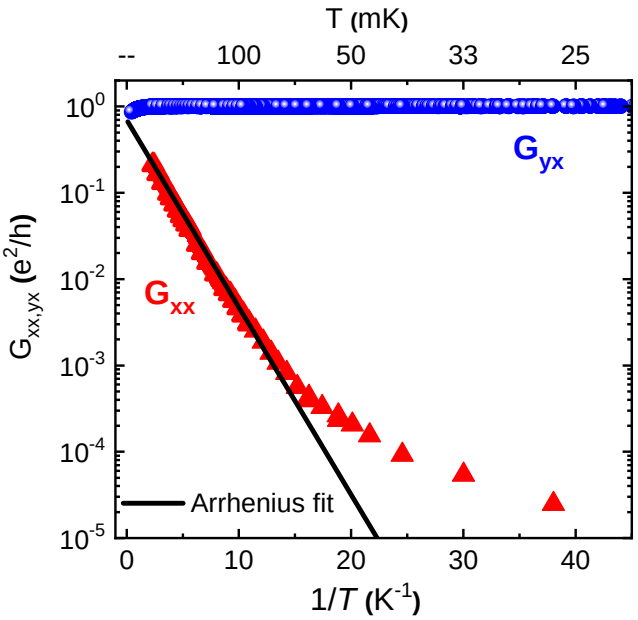


**Figure 5.12:** Temperature dependence of the longitudinal (red points) and transversal (blue points) conductance $G_{xx,yx}$ as a function of $T^{-1}$. The black line is the Arrhenius fitting.

#### 5.3.3.3 Current-induced breakdown of the QAHE

Figure 5.13 shows the current-induced breakdown of the quantum anomalous Hall effect. The longitudinal voltage $V_{xx}$ (red dots) and the transversal voltage $V_{yx}$ (blue dots) are plotted as a function of the current $I_{ac}$ which is send through a Hall bar with a width of 100 µm at 20 mK at zero magnetic field.

The longitudinal voltage $V_{xx}$ starts to deviate from zero at a characteristic current $I_0$. Kawamura *et al.* [158] explain this behavior by stating that in the section in which $V_{xx} = 0$, electrons of counter-propagating edge channels cannot backscatter due to the magnetization-induced gap in the top and bottom surface of the sample. When the current is increased above the critical value $I_0$, the transversal electric field supports the backscattering of electrons. When a current of $I_0 \approx 60\,\mathrm{nA}$ is applied to the VBST film, the quantum anomalous Hall states breaks down. The VBST film discussed in chapter 5.3.3.4 even exhibits a breakdown current of $I_0 \approx 150\,\mathrm{nA}$ and thus has a more robust quantum anomalous Hall state. The breakdown current for chromium-doped BST was measured by Kawamura *et al.* [158] for Hall bar devices with different widths. They observed a higher $I_0$ value for wider Hall bars. For a Hall bar with the same width of 100 µm studied in this work, they found a value for the current-induced breakdown of the QAHE of $I_0 \approx 10\,\mathrm{nA}$ which indicates a less robust QAH state compared to the sample shown in Fig. 5.13.

The measured transversal voltage $V_{yx}$ follows the straight fit of the quantized

voltage (blue line). Additionally, the green triangles show the deviation of $V_{yx}$ from the quantized value. The VBST remains in the quantized regime until a current of $I_{ac}$ ~100 nA is applied which suggests that the Hall voltage is more robust against increasing current than the longitudinal voltage.

To study this behavior, one can apply the Landauer-Büttiker-formalism [179]. A scheme of a Hall bar device which illustrates the characteristic 1D chiral edge channel in the QAH regime is shown in Fig. 5.13(b). Here $\alpha$ denotes the probability of carriers scattering from one edge of the Hall bar to the other edge. This probability is assumed to be the same for both channels. The Landauer-Büttiker formula describes the current $I_i$ which is leaving the i-th contact, as [176, 179–181]:

$$I_i = \frac{e^2}{h} \sum_j (T_{ji} V_i - T_{ij} V_j) \tag{5.2}$$

with the current $I_i$ and the voltage $V_i$ of the i-th contact. $T_{ji}$ is the transmission probability from the j-th to the i-th contact. Equation 5.2 can be rewritten as:

$$I_i = \sum_j G_{ij} (V_i - V_j) \tag{5.3}$$

with the conductance $G_{ij} = \frac{e^2}{h}(\delta_{ij} \sum_k T_{ki} - T_{ij})$.

Equation 5.3 for the current distribution in the Hall bar device shown in Fig. 5.13(b) can be displayed in matrix form as shown in equation 5.4. The current in Fig. 5.13(b) is applied from $I_1$ to $I_4$ ($V_4 = 0$) and contacts 2, 3, 5 and 6 are used as voltage probes ($I_2 = I_3 = I_5 = I_6 = 0$). The current can only travel from one contact to the next in a clockwise manner in the edge state without backscattering. With the scattering probability $\alpha$, the following matrix for the current is obtained:

$$\begin{pmatrix} I_1 \\ I_2 \\ I_3 \\ I_4 \\ I_5 \\ I_6 \end{pmatrix} = \frac{e^2}{h} \begin{pmatrix} 1 & 0 & 0 & 0 & 0 & -1 \\ -1 & 1 & 0 & 0 & 0 & 0 \\ 0 & -(1-\alpha) & 1 & 0 & -\alpha & 0 \\ 0 & 0 & -1 & 1 & 0 & 0 \\ 0 & 0 & 0 & -1 & 1 & 0 \\ 0 & -\alpha & 0 & 0 & -(1-\alpha) & 1 \end{pmatrix} \begin{pmatrix} V_1 \\ V_2 \\ V_3 \\ V_4 \\ V_5 \\ V_6 \end{pmatrix} \tag{5.4}$$

By solving the matrix 5.4 one can calculate that the current is given by $I = I_1 = \frac{e^2}{h}(V_1 - V_6) = \frac{e^2}{h}(1-\alpha)V_1$ and the voltages of the contact 1, 2, 3, 5 and 6 can be extracted as $V_1 = V_2$, $V_3 = (1-\alpha)\,V_1$, $V_5 = 0$ and $V_6 = \alpha\,V_1$.

It is now straightforward to evaluate the longitudinal and transversal resistance of the Hall bar using these equations. The longitudinal resistance is given by:

$$R_{2-3} = R_{6-5} = \frac{\alpha}{e^2/h\,(1-\alpha)}. \tag{5.5}$$

This result indicates that when no scattering probability $\alpha$ from one Hall bar edge to the other is present ($\alpha = 0$), the resistance is zero as expected for the QAHE. However, for $\alpha \neq 0$, the longitudinal resistance deviates from zero. The transversal resistance is given by:

$$R_{2-6} = R_{3-5} = \frac{h}{e^2}. \tag{5.6}$$

The Hall resistance does not depend on the scattering parameter $\alpha$. Consequently, the Hall resistance is more robust against scattering introduced by an electrical field.

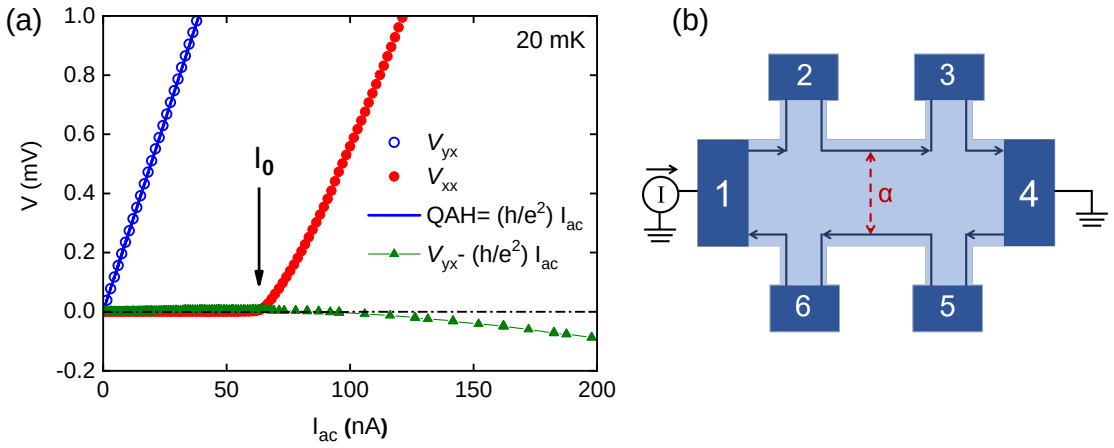


**Figure 5.13: Current dependence of the longitudinal and transversal voltage.** (a) Current dependence of the longitudinal $V_{xx}$ and transversal $V_{yx}$ voltage measured at T=20 mK and zero magnetic field. (b) Scheme of a Hall bar geometry with 6 contacts. In the QAH state, electrons travel in a single chiral edge channel. $\alpha$ is the probability for electrons to scatter from one edge to the other.

#### 5.3.3.4 Measurement of the QAHE on a millimeter-sized Hall bar

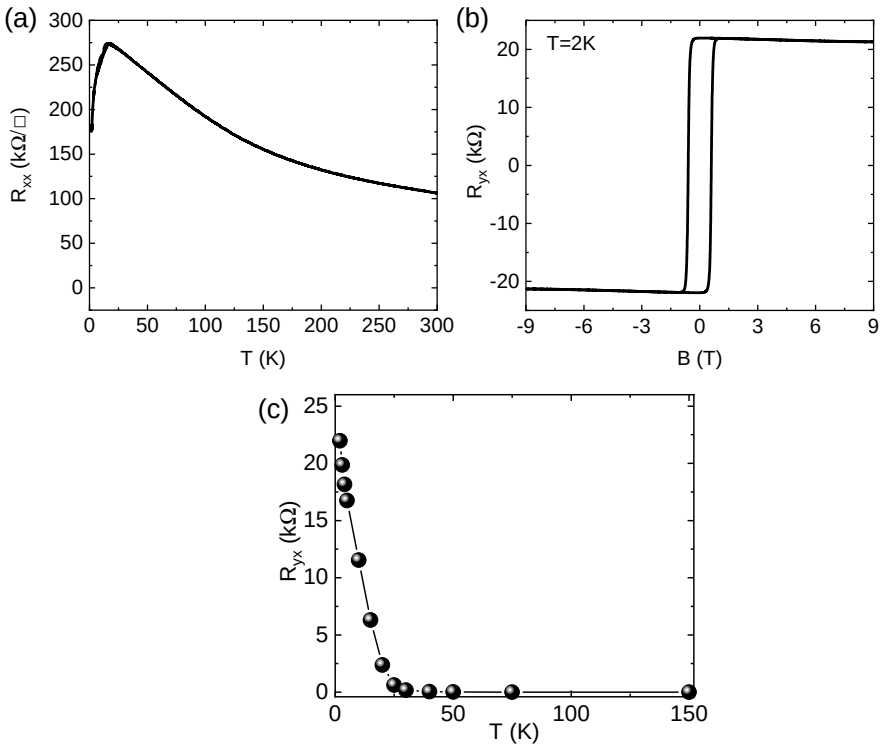


**Figure 5.14: V-doped BST film measured at 2 K.** (a) Measurement of the sheet resistance $R_{\mathrm{xx}}$ has a downturn at low temperatures. (b) Magnetic-field dependence of the Hall resistance $R_{\mathrm{yx}}$. An anomalous Hall amplitude of $\sim$22 kΩ can be extracted. (c) The temperature dependence of the Hall resistance highlights the relatively high anomalous Hall amplitude already at 2 K and a $T_{\mathrm{C}} \approx 30\,\mathrm{K}$ can be extracted.

In order to check the homogeneity of a VBST film on a larger scale than the size of a regular Hall bar, a longer Hall-bar device was fabricated. The vanadium-doped BST film was grown at the same conditions as the film shown in Fig. 5.9 and Fig. 5.11. A Hall-bar device with the same width as the regular Hall bar of 100 µm was fabricated, but the new design includes 26 contacts instead of the usual 6. The individual contacts are spaced 300 µm which corresponds to the length of the regular device and the total length of the device is $L = 3800\,\mu\mathrm{m}$. An optical image of such a ‚snake-like' device is shown in Fig. 5.15(c).
The magneto-transport of the device is first checked at 2 K in a PPMS setup on a Hall bar with width of 100 µm and a length of 1200 µm (contact 5 to contact 13 in Fig. 5.15(c)). The results of this measurement are shown in Fig. 5.14. The temperature dependence of the sheet resistance in panel (a) shows the expected downturn and the magnetic-field dependence of the Hall resistance gives an anomalous Hall amplitude of $\sim$22 kΩ (b). This value can be seen in panel (c) as well and a critical temperature of $T_{\mathrm{C}} \approx 30\,\mathrm{K}$ can be extracted from this graph.

After measuring the magneto-transport properties of the ‚snake-like' device at 2 K, the sample is cooled down to 10 mK and four combinations of contacts along the sample are measured and a current of 80 nA is applied from contact 1 to contact 25. The width of the Hall bar is always 100 µm and the length of each Hall bar is 600 µm. The results are depicted in Fig. 5.15. Panel (a) shows the quantization of all four Hall resistance curves measured across the device. Simultaneously all transversal resistances become zero except for a peak at the coercive field. The temperature dependence of $R_{xx}$ and $R_{yx}$ in Fig. 5.15(b) shows the characteristic behavior of the quantum anomalous Hall effect. The $R_{xx}$ curves all show semiconducting behavior until a drop in resistance occurs at ∼5 K and they enter the quantum Hall state while approaching zero resistance. Simultaneously, the $R_{yx}$ curves stay at zero resistance from room temperature to $T \approx 15\,\mathrm{K}$ where they enter the ferromagnetic state and subsequently advance the quantized value of 25.81 kΩ. The observation that across the sample all measured contact pairs show the same behavior indicates that the vanadium-doped BST film is homogeneously grown and the QAHE is achieved across a millimeter-sized device.

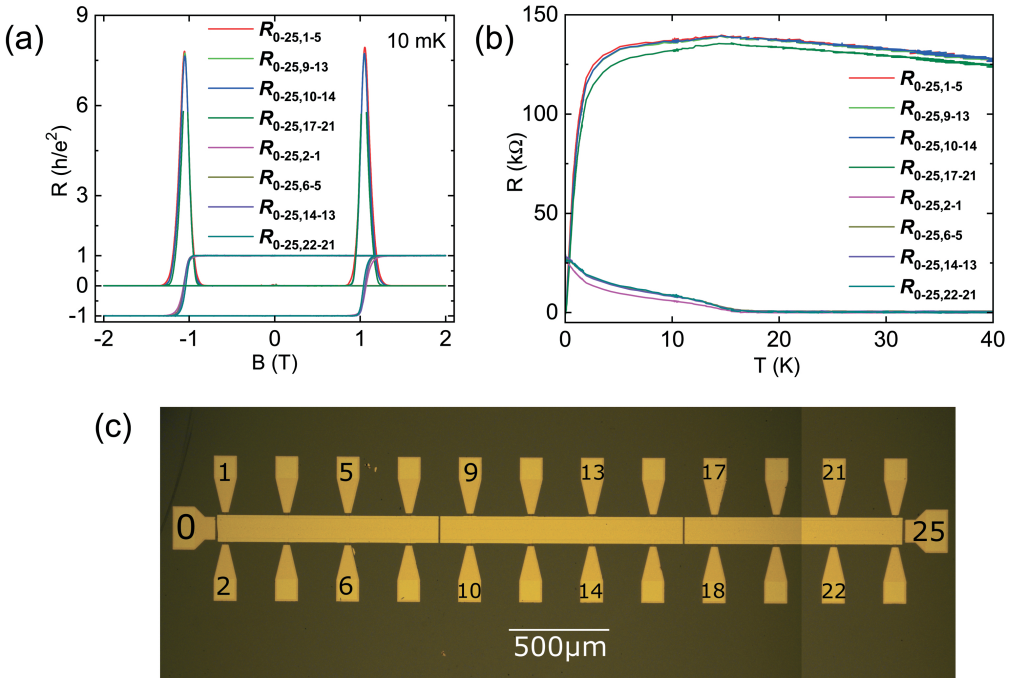


**Figure 5.15: QAHE demonstrated in a V-doped BST film across a long Hall bar device with a width of W=100 µm.** (a) The V-doped BST film is quantized at 10 mK. The Hall resistance $R_{yx}$ and the transversal resistance $R_{xx}$ are measured for four contact configurations across the length of the device. (b) Temperature dependence of $R_{yx}$ and $R_{xx}$. (c) Optical image of the device. Current is applied from contact 0 to 25.

## 5.4 Conclusion and outlook

In this chapter the growth optimization and transport measurements of vanadium-doped $(Bi_{1-x}Sb_x)_2Te_3$ (VBST) films were discussed. After carefully optimizing the growth conditions of the VBST films, the quantum anomalous Hall effect was observed at zero magnetic field and temperatures of 30 mK and 100 mK.

By studying the temperature dependence of the quantum anomalous Hall effect, a Arrhenius-dependence of the longitudinal conductance was observed which suggests a thermal activated behavior until a temperature of 60 mK. A magnetic gap size of 40 µeV was extracted. This gap size is lower than what is expected from the obtained critical temperature and is most likely caused by a combination of electrostatic and magnetic disorder. By applying the Landauer-Büttiker-formalism, the current-induced breakdown of the quantum anomalous Hall effect for the longitudinal and transversal resistances was found to depend on the different robustness against scattering introduced by an electrical field. Furthermore the homogeneity of a grown VBST film in the mm-range was confirmed by observing the quantum anomalous Hall effect across a large ‚snake-like' Hall bar device.

Since for now the quantum anomalous Hall effect is only observed at low temperatures, one of the future goals is to increase the temperature limit. This can be achieved by modulation doping or growing different materials such as $MnBi_2Te_4$, as discussed in the introduction of this chapter.

Samples which show the quantum anomalous Hall effect are moreover building blocks for further applications. Depositing a superconductor on top of a sample which shows the quantum anomalous Hall effect is predicted to host chiral 1D Majorana edge modes [182, 183]. Such experiments were already performed and a half-integer quantized conductance plateau in the two-terminal measurement was claimed to be a signature of Majorana fermions [184]. This interpretation was doubted heavily and the half-integer plateau theoretically and experimentally proven to be not a unique feature for Majorana fermions [185–187]. One future experiment using the quantum anomalous Hall effect is a so called $Z_2$-interferometer, where the magnetically-proximitized topological insulator from the original proposal [188, 189], is going to be replaced by a sample with an intrinsic single edge channel at a FM domain boundary.

# Chapter 6

# Superconductivity in $Sn_{1-x}In_xTe$ thin films grown by molecular beam epitaxy

## Contents



In this chapter the growth of superconducting $Sn_{1-x}In_xTe$ thin films on a $Bi_2Te_3$ buffer layer by molecular beam epitaxy is discussed. Tunneling spectroscopy measurements were performed on the film and a two-gap structure was observed. This observation points to the coexistence of bulk and surface superconductivity. Because of the special properties of the material, the surface superconductivity is bound to be topological.


The following chapter is based on a paper published as:
Andrea Bliesener, Junya Feng, A. A. Taskin, and Yoichi Ando; *Superconductivity in $Sn_{1-x}In_xTe$ thin films grown by molecular beam epitaxy*; Phys. Rev. Materials 3, 101201(R) (2019).


The tunnel-junction devices were fabricated and measured by Dr. Junya Feng.

## 6.1 Introduction

After the discovery of topological insulators, two other topological phases gained interest in recent years: topological crystalline insulators (TCI) and topological superconductors (TSC).

Topological crystalline insulators were first introduced by Liang Fu in 2011 [190]. They are a material class in which the topological surface states are protected by crystal symmetries (such as for example reflection, rotation or mirror symmetry), instead of time-reversal symmetry which is the case for a topological insulator. TCIs cannot be transformed into an ordinary insulator without breaking the crystal symmetries. They have an insulating bulk and chiral gapless states on the surface or on boundaries between the TCI and an ordinary insulator. The crystal symmetries and the orientation of the surface dictate the electronic structure of the topological crystalline insulator [65, 190].

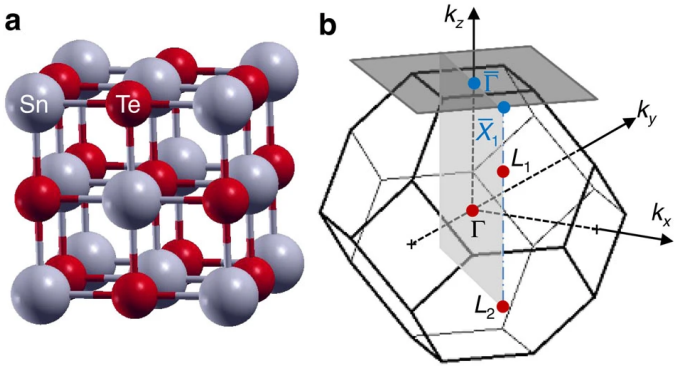


**Figure 6.1: Crystal structure and fcc Brillouin zone of SnTe.** (a) Rocksalt crystal structure of SnTe. (b) Face-centered cubic Brillouin zone showing the plane $\Gamma L_1 L_2$ which is invariant under reflection about the (110) axis and projects onto the $\Gamma X_1$ line in the [001] surface. Reprinted by permission from Springer Nature: Nat Commun **3**, 982 (2012), Topological crystalline insulators in the SnTe material class, Hsieh *et al.*, Copyright (2012), [191]

Hsieh *et al.* [191] predicted the first topological crystalline insulator in 2012 in IV-VI semiconductors, among which SnTe was a candidate. SnTe has a rocksalt crystal structure with four band gaps located at four equivalent $L$ TRIM points in the fcc-Brillouin zone (see Fig. 6.1). The conduction and valence band are inverted at the $L$ points. Since the bands are inverted at an even number of points, SnTe is not a topological insulator within the $Z_2$ classification [191].

The reflection symmetry with respect to the (110) mirror plane is responsible for the topological nature of the material. Topological surface states are also present on the (001) and (111) surface which are normal to the (110) plane due to

the cubic symmetry of SnTe [191]. Intriguingly, different types of surface states were predicted by Liu *et al.* [192] and afterwards confirmed by angle-resolved photoemission spectroscopy (ARPES) measurements [193]. A comparison of the different surfaces is depicted in Fig. 6.2.

ARPES measurements on the (111) surface of SnTe revealed two different types of surface states. One of the four bulk $L$ point is projected onto the surface $\bar{\Gamma}$ point, and the other three bulk $L$ points are projected onto the $\bar{M}$ point of the surface Brillouin zone (see Fig. 6.2). Tanaka *et al.* [193] demonstrated that quantities such as the Dirac velocity $\mathrm{v_D}$ and Dirac energy $\mathrm{E_D}$ differ on both Dirac cones. Additional ARPES measurements on the (001) surface however, present a double Dirac cone structure due to the hybridization of two Dirac cones. Two bulk $L$ points are projected onto the same $\bar{X}$ point of the surface Brillouin zone and lie on the projection of the (110) mirror plane (see Fig. 6.2) [194, 195].

Remarkably, chemically doping SnTe with indium results in superconductivity in $\mathrm{Sn_{1-x}In_xTe}$ [196]. The interplay between the topological nature of the parent material SnTe and superconductivity in In-doped SnTe makes $\mathrm{Sn_{1-x}In_xTe}$ candidate 3D topological superconductor [16, 17]. A hallmark of a 3D topological superconductor is the appearance of gapless Andreev boundstates on the surface [197]. ARPES measurements revealed that the topological surface states arising from the parent material are still preserved after doping SnTe with indium [198].

Transport measurements indicate that topological superconductivity in In-doped SnTe single crystals is only found in an indium doping region of $x \sim 4\%$ when the disorder in the material becomes minimal. It was predicted that in this doping regime the bulk superconducting state can be odd-parity $p$-wave superconductivity [199]. The bulk superconductivity induces a superconducting gap into the surface states by proximity effect [200] similar to the proposal by Fu and Kane [63]. If the disorder is large, the bulk shows even-parity $s$-wave superconductivity. Point-contact spectroscopy on samples with minimal disorder confirmed this behavior by revealing a zero-bias conductance peak (ZBCP) in the bias-voltage dependence of the differential conductance [201]. This appearance is a characteristic for Andreev bound states which are linked to unconventional superconductivity [197].

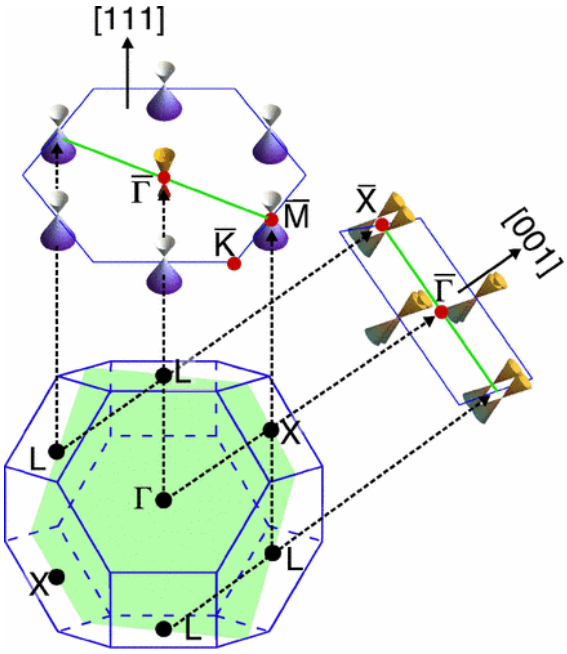


**Figure 6.2:** Schematic of the locations of the Dirac cones on two different SnTe surfaces. The 3D bulk Brillouin zone (with high symmetry points noted) and the projected surface Brillouin zones are shown. Double Dirac cones are present at the $\bar{X}$ points on the (001) surface. On the (111) surface, two different types of surface states are centered at the $\bar{\Gamma}$ and $\bar{M}$ point of the BZ. The green shaded area and line represent the (110) mirror plane. Reprinted figure with permission from Y. Tanaka *et al.*, PRB **88**, 235126 (2013). Copyright 2013 by the American Physical Society; [193]

## 6.2 MBE growth and characterization of $Sn_{1-x}In_xTe$ films

Thin films of $Sn_{1-x}In_xTe$ were grown in the ultrahigh vacuum MBE1 chamber. The films were deposited on a sapphire (0001) substrate which was prepared as described in chapter 3.1.3. The film was grown in two steps: First, $Bi_2Te_3$ was deposited as a buffer layer on the sapphire substrate. Subsequently, a layer of $Sn_{1-x}In_xTe$ was grown on top of the $Bi_2Te_3$ film.

The $Bi_2Te_3$ layer was grown by co-evaporating bismuth and tellurium from Knudsen cells while keeping a growth rate of approximately 1.25 nm min$^{-1}$. During growth, the substrate temperature was ramped from 210 °C to 260 °C within 10 minutes and afterwards kept at 260 °C for additional 10 minutes. The use of $Bi_2Te_3$ as the buffer layer for SnTe-growth in a MBE chamber was established by Taskin *et al.* [202]. Figure 6.3(b) shows the cubic crystal structure of SnTe with the (111) plane highlighted by black triangles. The SnTe (111) plane fits the final hexagonal Te-plane of the $Bi_2Te_3$ quintuple layer (see Fig. 6.3).

During the second growth step, a layer of $Sn_{1-x}In_xTe$ was deposited while co-evaporating indium, tin and tellurium from standard effusion cells. This layer was grown at a substrate temperature of 260 °C and a growth rate of 0.5 nm min$^{-1}$. The grown heterostructure was directly afterwards *in-situ* annealed in the MBE

chamber. This *in-situ* annealing step is crucial to obtain superconducting In-doped SnTe films.

After growth and removing the sample from the MBE chamber, the $Sn_{1-x}In_xTe$ films were characterized *ex-situ*. To confirm a good morphology, the films were studied by atomic force microscopy (AFM). Figure 6.3(a) shows a typical AFM image of a $Bi_2Te_3$ film grown at the same conditions which were used to grow the buffer layer. The high quality of the film is indicated by the clearly visible sharp triangular terraces. Figure 6.3(c) displays the top surface of the $Sn_{1-x}In_xTe$ /$Bi_2Te_3$ heterostructure and shows a continuous, flat film without any holes.

The epitaxial growth and crystal structure were further confirmed by x-ray diffraction (XRD) measurements. A typical XRD pattern is shown in Fig. 6.4. The XRD peaks indicate an epitaxial, single phase growth. The (LLL)-peaks of $Sn_{1-x}In_xTe$ can be identified in the black pattern additionally to the $Bi_2Te_3$ peaks which are shown in the blue spectrum of a bare $Bi_2Te_3$ films for comparison. By analyzing the data, a lattice constant of 0.6310±0.0002 nm can be determined which is comparable to the lattice constant of bulk SnTe of 0.632 nm [203]. The concentration $x$ of indium dopants and the overall composition was analyzed by energy-dispersive x-ray spectroscopy (EDX) in a scanning electron microscope.

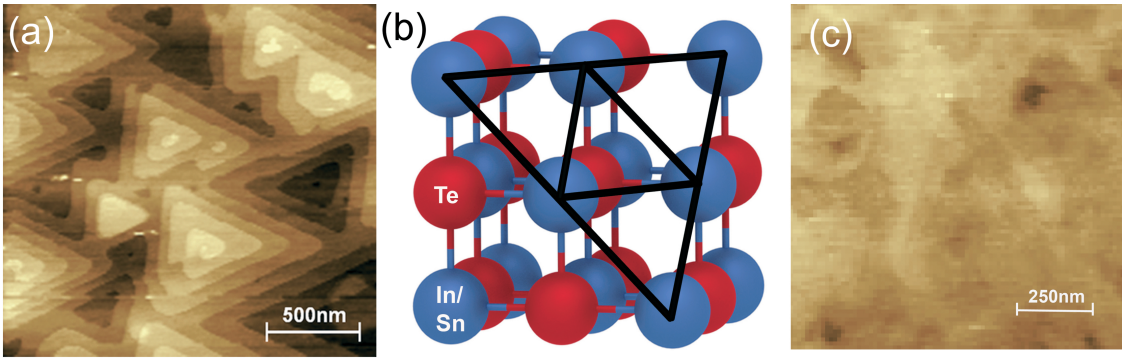


**Figure 6.3: Structural characterization of the grown $Sn_{1-x}In_xTe$ film.** (a) AFM image of the $Bi_2Te_3$ buffer layer. Atomically flat terraces with sharp edge indicate a good morphology. (b) Rocksalt crystal structure of $Sn_{1-x}In_xTe$ with the (111) plane highlighted by the black triangles. (c) AFM image of the flat and continuous top surface of a $Sn_{1-x}In_xTe/Bi_2Te_3$ heterostructure. (modified from [204])

A variety of $Sn_{1-x}In_xTe$ films were grown while optimizing the growth and annealing temperature/time and the indium content. The critical temperatures $T_c$ (defined as the mid-point in the resistive transition) of the films ranged from 0.3 K to 2.0 K.

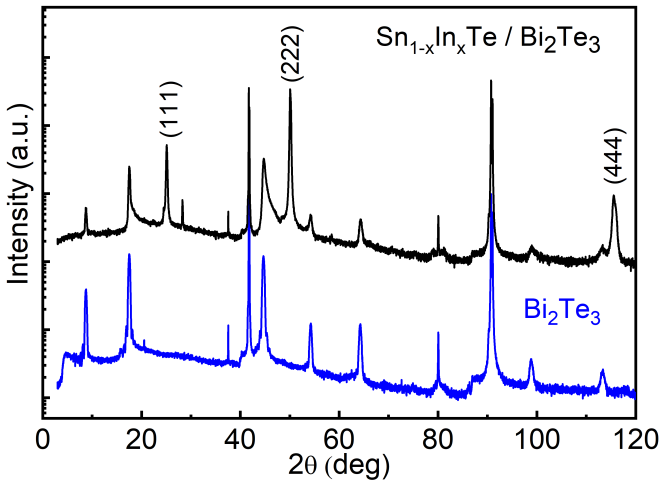


**Figure 6.4: XRD pattern of the $Bi_2Te_3$ buffer layer (blue) and the $Sn_{1-x}In_xTe/Bi_2Te_3$ heterostructure (black).** The (LLL) peaks of the $Sn_{1-x}In_xTe$ are highlighted. (modified from [204])

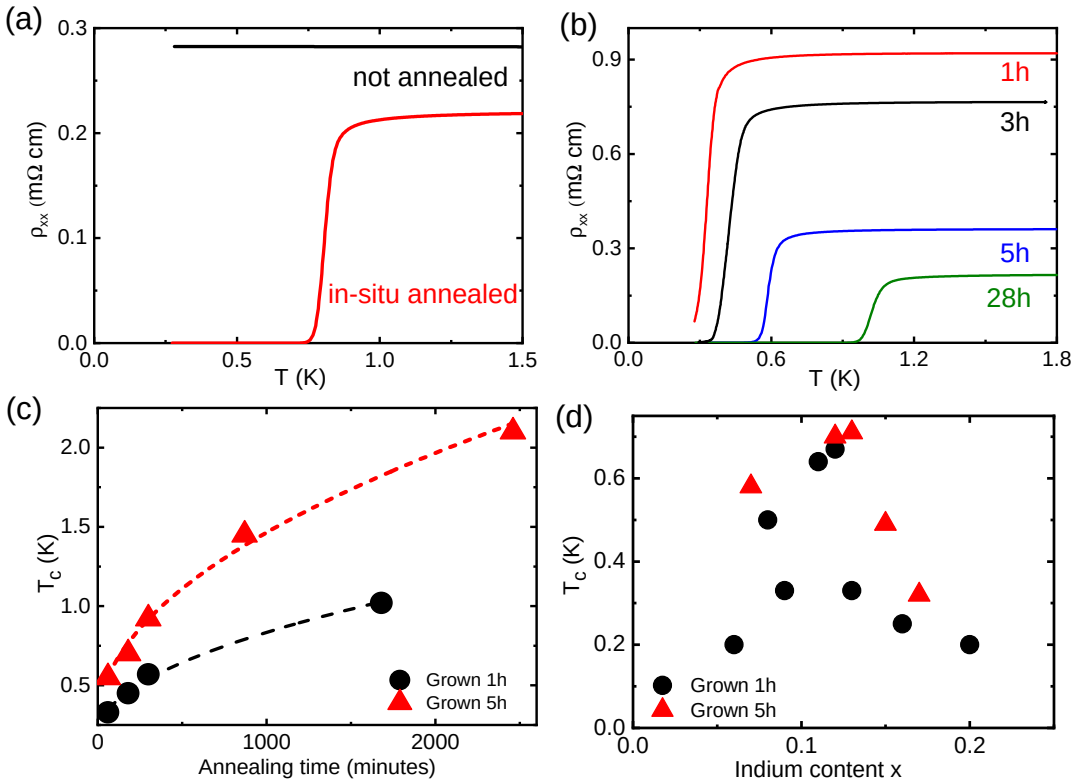


**Figure 6.5: Electrical transport characterization of the grown $Sn_{1-x}In_xTe$ film.** (a) Comparison of the resistivity of an *in-situ* annealed and a not annealed $Sn_{1-x}In_xTe$ film. Only the annealed film shows a superconducting transition. (b) Plot of the temperature dependence of the resistivity of four $Sn_{1-x}In_xTe$ films which were *in-situ* annealed for 1 (red), 3 (black), 5 (blue) and 28 (green) hours at 320 °C. The transition temperature shifts to higher temperatures with longer annealing times. (c) Annealing-time dependence of the critical temperature $T_c$ for films grown 1 (black circles) or 5 (red triangles) hours and annealed for various times. (d) Dependence of the critical temperature $T_c$ on the indium content $x$ for films grown for 1 (black circles) and 5 (red triangles) hours. The curve presents a maximum at around $x = 0.11 - 0.12$. (modified from [204])

Directly after growth, the $Sn_{1-x}In_xTe$ films are generally not superconducting. Only after annealing the samples *in-situ* in the MBE chamber, they become superconducting. Figure 6.5(a) shows a plot of the temperature dependence of the resistivity $\rho_{xx}$ for two $Sn_{1-x}In_xTe$ films. Both films were grown at the same growth conditions, however one film was *in-situ* annealed for 2 hours at 320 °C immediately after growth (red curve), while the other film was not annealed at all (black curve). Only the annealed $Sn_{1-x}In_xTe$ film shows a superconducting transition at $T_c = 0.65\,\mathrm{K}$.

The annealing time plays an important role to increase the critical temperature as depicted in Fig. 6.5(b). Here, different superconducting transitions are shown for films which were grown at the same conditions but annealed for 1 (red), 3 (black), 5 (blue) and 28 (green) hours at 320 °C. A longer annealing time leads to a higher transition temperature $T_c$. This is additionally highlighted in Fig. 6.5(c). This graph shows a comparison of samples for which the $Sn_{1-x}In_xTe$ layer was grown for 1 hour (black) or 5 hours (red) at 260 °C resulting in different film thicknesses. All samples were afterwards *in-situ* annealed for different duration. Again, the transition temperature increases with longer annealing time.

The dependence of the critical temperature on the indium content $x$ in the $Sn_{1-x}In_xTe$ films is shown in Fig. 6.5(d). The $Sn_{1-x}In_xTe$-layer of the films was grown at 260 °C for 1 (black circles) or 5 (red triangles) hours and the samples were afterwards annealed at 260 °C for 1 hour. The dome-shaped curve reveals a maximum at an indium concentration of $x = 0.11 - 0.12$. Generally, the $T_c$ for the presented $x$ values for the $Sn_{1-x}In_xTe$ films is lower than the critical temperature for single crystals with the same $x$ value. This behavior can be understood by comparing the growth conditions for MBE grown films and single crystals. The temperature used for the vapor transport growth of $Sn_{1-x}In_xTe$ single crystals was around 630 °C [199], which is far higher than the temperatures used during the MBE growth.

Since superconductivity is only achieved after annealing, and the critical temperature increases with longer annealing time, a thermal process is most likely involved in changing a non-superconducting into a superconducting film. The indium atoms in the as-grown film presumably sit at non-equilibrium positions and only move to equilibrium positions after thermally activating the atoms by *in-situ* annealing at higher temperatures. In these positions the In-atoms contribute to the superconductivity by providing hole carriers. This kind of thermal process needs an activation energy which depends on a certain temperature and

time.

A summary of the growth and characterization parameters of the samples presented in Fig. 6.5 is displayed in table 6.1. Not only the critical temperature increases with longer annealing, but the carrier concentration $n_{\mathrm{H}}$ (extracted from Hall resistivity measurements) reveals the same behavior. It should be noted the $n_{\mathrm{H}}$-values overestimate the actual hole carrier density $p$ in $Sn_{1-x}In_xTe$, since the measured samples are a heterostructure consisting of typically electron-doped $Bi_2Te_3$ and hole-doped $Sn_{1-x}In_xTe$. The two layers act as parallel channels with hole and electron carriers. The two Hall channels cancel each other which gives a small Hall coefficient $R_{\mathrm{H}}$ and a very large effective charge carrier density $n_{\mathrm{H}} = (eR_{\mathrm{H}})^{-1}$ [205].

| | Annealing temp. (°C) | Annealing time (min) | x | thickness (nm) | $T_c$ (K) | $n_{\mathrm{H}}$ ($cm^{-3}$) |
|---|---|---|---|---|---|---|
| red | 320 | 60 | 0.13 | 55 | 0.33 | 1.4 x $10^{21}$ |
| black | 320 | 180 | 0.13 | 55 | 0.43 | 1.2 x $10^{21}$ |
| blue | 320 | 300 | 0.12 | 45 | 0.59 | 2.2 x $10^{21}$ |
| green | 320 | 1680 | 0.16 | 37 | 1.02 | 5.5 x $10^{21}$ |

**Table 6.1: Summary of the growth parameters and basic characterizations plotted in Fig. 6.5(b).** The $Sn_{1-x}In_xTe$ layer in all of the samples was grown for 1 hour at 260 °C. (modified from [204])

## 6.3 Transport measurements of $Sn_{1-x}In_xTe$ films

The transport measurements of the $Sn_{1-x}In_xTe$ films were performed by measuring a standard Hall bar device in a Helium 3 insert (Oxford Instruments Heliox) in a 14 T-superconducting magnet using the ac-lock in technique.

Tunneling-junction devices were measured in a dry dilution refrigerator (Oxford Instruments Triton 200). The bias voltage was generated by Keithley 2450 source meter together with a voltage divider. The tunneling current was amplified by FEMTO DLCPA-200 current amplifier and measured by a Keithley 2182A nanovoltmeter.

### 6.3.1 Hall bar measurements

The results from the magneto-transport measurements of a standard Hall-bar device on a 170 nm-thick $Sn_{1-x}In_xTe$ film with $x = 0.14$ are shown in Fig. 6.6.

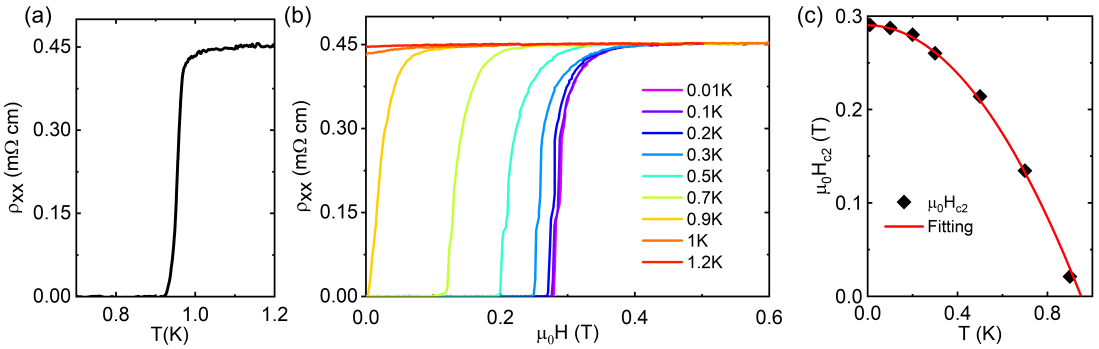


**Figure 6.6:** Results from the Hall bar characterization of a typical $Sn_{1-x}In_xTe$ film. (a) The temperature dependence of the resistivity $\rho_{xx}$ shows a superconducting transition at 0.96 K. (b) Magnetic field dependence of the resistivity at various temperatures. (c) Temperature dependence of the critical field extracted from the curves in (b) with a theoretical WHH-fitting (red curve). A zero-temperature-limit value of $H_{c2}^0 = 0.28\,\mathrm{T}$ can be extracted from this graph. (modified from [204])

The $Sn_{1-x}In_xTe$ film was grown for 5 hours at a temperature of 260 °C and afterwards *in-situ* annealed at 320 °C for 5 hours. Figure 6.6(a) shows the temperature dependence of the longitudinal resistivity $\rho_{xx}$ and a mid-point critical temperature $T_c = 0.96\,\mathrm{K}$ can be extracted. An effective Hall carrier concentration of $n_H \simeq 5\times 10^{20}\,\mathrm{cm}^{-3}$ was derived from the Hall resistance measurements. Keeping in mind that this measurement probes both the usually electron-doped $Bi_2Te_3$ layer and the usually hole-doped $Sn_{1-x}In_xTe$ layer, this is not the carrier concentration of only the $Sn_{1-x}In_xTe$ film, but includes contribution from both layers. However, since the thickness of the $Sn_{1-x}In_xTe$ film is far larger than the $Bi_2Te_3$ film thickness, the obtained $n_H$ value is in close approximation to the actual carrier concentration $p$. Furthermore, the extracted $n_H$ is comparable to the value for superconducting $Sn_{1-x}In_xTe$ single crystals with $x \simeq 0.04$ [199].

The magnetic-field dependence measured at different temperatures is depicted in Fig. 6.6(b). The upper critical field values $H_{c2}$ defined as the midpoint in the resistive transition extracted from this measurement, are plotted in panel (c) as a function of temperature. The temperature dependence can be well fitted by the Werthamer-Helfand-Hohenberg (WHH) theory with [206]

$$\mu_0 H_{c2}^0 = -0.693 T_c (dH_{c2}/dT)_{T=T_c}, \tag{6.1}$$

suggesting a conventional nature of the bulk superconductivity. Furthermore, a zero-temperature-limit value $H_{c2}^0 = 0.28\,\mathrm{T}$ can be extracted from Fig. 6.6(c). This value is in agreement with the value of $H_{c2}^0 = 0.37\,\mathrm{T}$ for a $Sn_{1-x}In_xTe$ single crystal with a similar critical temperature $T_c = 1.2\,\mathrm{K}$, reported by Sasaki *et al.* [201].

### 6.3.2 Tunneling spectroscopy measurements

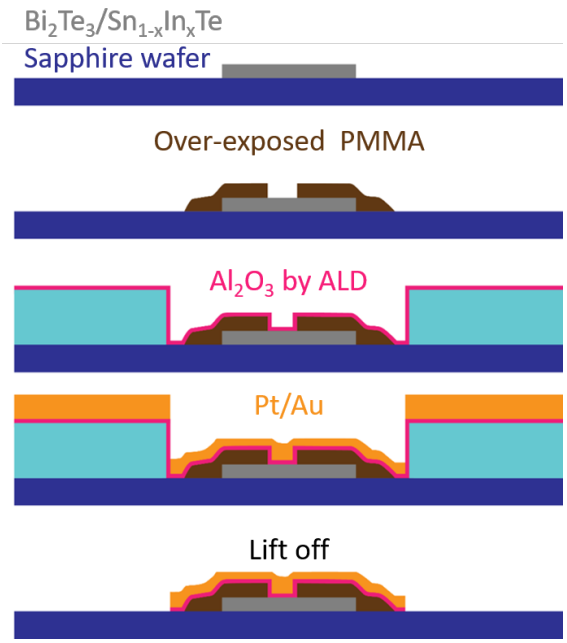


**Figure 6.7: Sketch of the microfabrication scheme of the tunnel-junction device, including:** Etching the film into the desired shape, defining the tunnel-junction-area, deposition of a dielectric $Al_2O_3$ layer, deposition of platinum/gold contacts and final lift-off process. (modified from [204])

A tunnel-junction device was fabricated to further examine the superconducting properties of the $Sn_{1-x}In_xTe$ films. Tunneling spectroscopy probes the density of states (DOS) at the surface, which allows to infer the energy gap in the superconducting state [197].

A scheme of the steps to fabricate a tunnel-junction device is shown in Fig. 6.7. First, 20 µm-thin stripes on the $Sn_{1-x}In_xTe/Bi_2Te_3$ heterostructure were defined by photolithography and etched by argon dry-etching. Afterwards, small windows ($1\times1$, $2\times2$ and $3\times3$ µm$^2$) on the film stripes were defined by electron-beam lithography using over-exposed PMMA (polymethyl methacrylate) to define the tunnel-junction area. Subsequent $O_2$ reactive-ion etching and weak Ar-etching was used to clean the surface of the tunnel-junction area. In a next step, a 0.27 nm-thin $Al_2O_3$ layer was deposited as the tunnel barrier using atomic layer deposition (ALD). The tunnel-junction electrodes were defined by electron-beam lithography and a layer of 2 nm platinum and 120 nm gold was sputtered and subsequently lifted off in acetone to obtain the final device structure. An optical image of the final tunnel-junction device is shown in Fig. 6.8. The tunneling junctions are highlighted by the red squares.

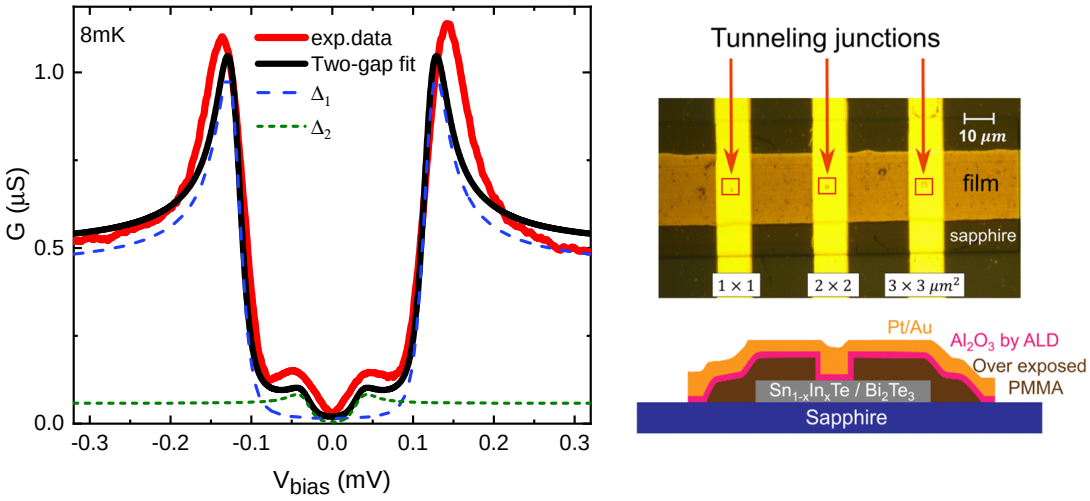


**Figure 6.8: Tunneling spectrum measured at 8 mK and optical picture of the tunnel-junction device** Left: Tunneling spectrum measured at 8 mK (red curve). Two calculated curves for different gaps $\Delta_1$=0.1200±0.0003 meV and $\Delta_2$=0.0324±0.0032 meV (blue and green dashed curve) and the superposition of both gaps (black curve). Right: Optical image of the tunnel-junction device with the tunnel-junction area highlighted by red squares. Below: sketch of the side-view of the tunneling-junction device. (modified from [204])

A tunneling spectrum is shown on the left side of Fig. 6.8. The spectrum was measured at the base temperature of the dilution fridge at 8 mK and at zero magnetic field. Even though the Hall bar measurement points to a conventional superconducting behavior, the surface sensitive tunneling spectrum peculiarly exhibits two gaps, which indicate the presence of two superconducting gaps. Considering the topological nature of the material, the two gaps presumably originate from bulk and surface superconductivity, with the smaller gap stemming from the surface and the larger gap originating from the bulk superconductivity.

To understand this intriguing behavior of the tunneling spectra, the experimental data was fitted with two individual BCS gaps (blue and green dashed lines in Fig. 6.8) using the Dynes formula [207]:

$$G = \frac{\partial I}{\partial V} = G_{\mathrm{N}} \frac{\partial}{\partial V} \int_{-\infty}^{\infty} \rho(E)[f(E) - f(E - eV)]dE, \tag{6.2}$$

where $G_{\mathrm{N}}$ is the normal-state conductance, $f(\mathrm{E})$ is the Fermi function, and $\rho(\mathrm{E})$ is the density of states in the BCS theory given by

$$\rho(\mathrm{E}) = \mathrm{Re}\left[\frac{|\mathrm{E} - \mathrm{i}\Gamma|}{((\mathrm{E} - \mathrm{i}\Gamma)^2 - \Delta^2)^{1/2}}\right]. \tag{6.3}$$

Here, $\Delta$ is the superconducting gap and $\Gamma$ is the non-dimensional broadening

parameter due to a finite quasi-particle lifetime. The parameters used for the calculations are: $\Delta_1$ = 0.1200±0.0003 meV, $\Gamma_1$ = 0.004±0.001, $G_{N,1}$ = 0.447±0.004 $\mu$S and $\Delta_2$ = 0.0324±0.0032 meV, $\Gamma_2$ = 0.0012±0.0004, $G_{N,2}$ = 0.058±0.004 $\mu$S.

The black curve in Fig. 6.8 is the superposition of the two BCS gaps $\Delta_1$ and $\Delta_2$. This fitting curve does not match the experimental data perfectly. This can be explained by considering that the topological surface states of the (111) surface of SnTe consist of two different kind of Dirac cones which might lead to more than two gaps [193, 202].

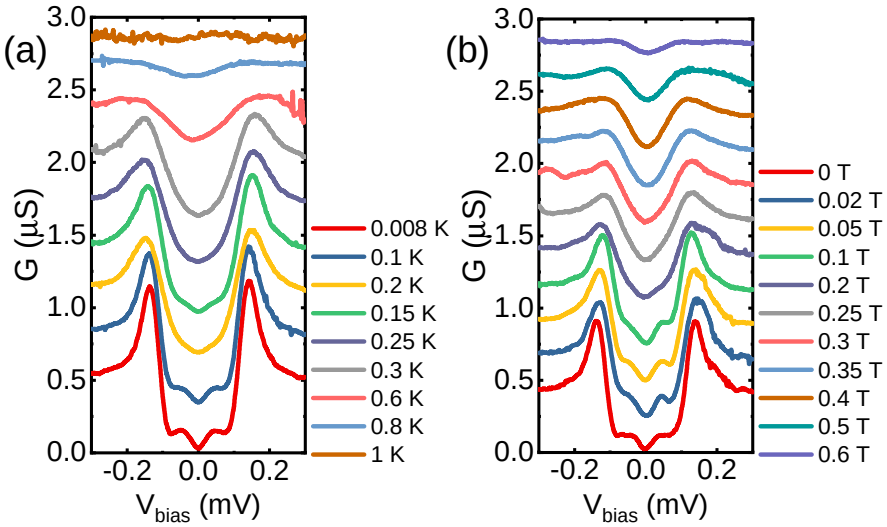


**Figure 6.9: Measurement of the tunneling spectroscopy for various temperatures (a) and magnetic fields (b).** The spectra are offset by 0.23 $\mu$S. adapted from [204])

Figure 6.9 depicts tunnel spectra obtained at various temperatures (a) and magnetic fields (b). The temperature evolution shows a two-gap structure at the lowest temperature of 8 mK. The smaller gap disappears already at 0.2 K, while the larger gap survives until the critical temperature $T_c = 1\,\mathrm{K}$. Above $T_c$, the spectrum shows no gap suggesting that superconductivity is destroyed. Two gaps can as well be identified in the tunnel spectra measured at various perpendicular magnetic fields depicted in Fig. 6.9(b). Here again, the smaller gap vanishes first at around 0.2 T, which is below the critical field $H_{c2} = 0.28\,\mathrm{T}$ at this temperature (compare Fig. 6.6(c)). The larger gap however, is still noticeable above the critical field up to 0.6 T, which suggests that the destruction of superconductivity in magnetic field occurs through the loss of phase coherence.

Figure 6.10 illustrates the results which were obtained by measuring the tunneling spectra of the $Sn_{1-x}In_xTe$ films. The exemplary tunneling spectrum shown in Fig. 6.10(a) reveals the characteristic two-gap structure and the schematic in (b) illustrates the origin of the two gaps. As already discussed in the introduction of

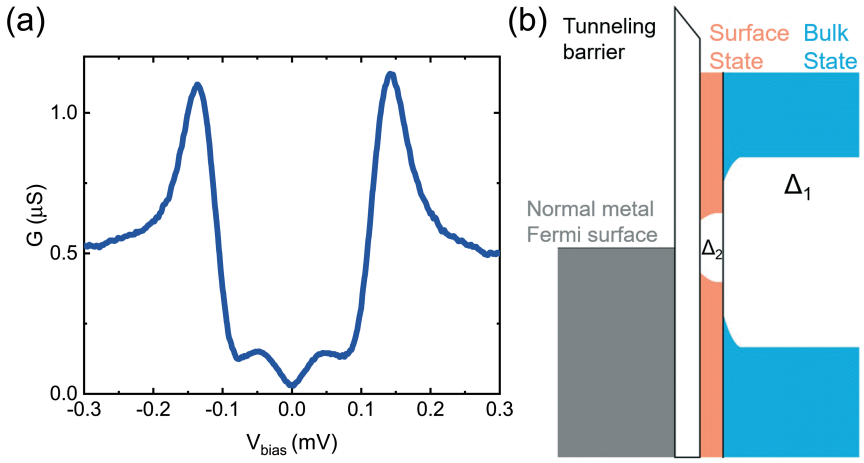


**Figure 6.10: Tunneling spectrum measured at 8 mK and sketch of the corresponding density of states**(a) Tunneling spectrum measured at 8 mK. (b) Illustration of the density of states of the tunneling barrier and the two superconducting gaps $\Delta_1$ and $\Delta_2$. (modified from [204])

this chapter, it was predicted that the superconducting bulk state of $Sn_{1-x}In_xTe$ allows for conventional even-parity $s$-wave and unconventional odd-parity $p$-wave superconductivity. Transferring this to the scheme in Fig. 6.10(b) implies that here the large gap $\Delta_1$ is linked to the $s$-wave bulk superconductivity which introduces superconductivity into the topological surface states ($\Delta_2$) by the proximity effect.

A selection of 16 devices was measured, and only three devices showed a clear two-gap structure as presented in Fig. 6.10(a). These difficulties in reproducing the two-gap structure in the tunneling spectra supports the argument that the small gap stems from the surface states, which are easily disturbed by disorder and are more difficult to access. Furthermore the overall disorder in the sample is an important influence, as was shown for the point spectroscopy measurements performed on $Sn_{1-x}In_xTe$ single crystals by Sasaki *et al.* [201]. Here, only very clean samples with a residual resistivity of $\sim$0.15 m$\Omega$ cm showed a zero-bias conductance peak and thus suggest unconventional superconductivity. The $Sn_{1-x}In_xTe$ film shown in Fig. 6.6 has a residual resistivity of $\sim$0.45 m$\Omega$ cm, which is presumably too high to realize unconventional bulk superconductivity in the grown films.

Fu and Kane discussed in their paper from 2008 [63] similar circumstances to those which were found in $Sn_{1-x}In_xTe$ films. A more detailed description of this work is presented in chapter 2.3.5. In essence, by placing a superconductor on top of a topological insulator, a $s$-wave superconducting gap is introduced into spin-momentum-locked TI surface states by the proximity effect. Fu and Kane

predict that the achieved superconductivity is bound to be of topological origin.

The proximity effect in a normal metal can be achieved by depositing a superconducting layer on top. The quality of the interface between the two materials is hereby of great importance. The proximity effect in case of the $Sn_{1-x}In_xTe$ films takes place within the material itself. The advantage is that the interface which is typically degraded by disorder does not disturb the proximity effect between bulk and surface states. A comparable situation was found in the iron-based superconductor $FeTe_{1-x}Se_x$. Here, it was predicted that the trivial bulk bands induce superconductivity into the surface states which together with their spin-helical texture exhibit topological superconductivity [208]. A zero-bias conductance peak was observed in this material as an evidence for Majorana bound states in the vortex core [209, 210].

## 6.4 Conclusion and outlook

The results presented in this chapter show that high-quality superconducting $Sn_{1-x}In_xTe$ films were successfully grown by molecular beam epitaxy and using $Bi_2Te_3$ as a buffer layer. By measuring the tunneling spectra of the films, a two-gap structure was obtained (see Fig. 6.10). This points to an internal proximity effect where superconductivity is induced into the metallic surface states by the $s$-wave superconducting bulk. Considering the Fu and Kane proposal [63], the superconducting surface states are bound to lead to topological surface superconductivity.

Given that the effective $p$-wave superconducting character of the surface states cannot be probed simply by measuring the tunneling spectra on the $Sn_{1-x}In_xTe$ films, a convincing proof for unconventional superconductivity would be the observation of Majorana zero-modes in the vortex core. This measurement can be performed by scanning tunneling microscopy (STM).

# Chapter 7

# Selective area growth of topological materials

## Contents



This chapter introduces *selective area growth (SAG)* as a new approach of growing low-dimensional topological insulators. To realize this, $Si_3N_4$ is grown on a sapphire substrate and patterned into nanostructures by electron-beam lithography. The defined pattern is afterwards etched into the $Si_3N_4$ layer by reactive ion etching. This pre-patterned substrate is used to selectively grow $(Bi_{1-x}Sb_x)_2Te_3$ nanostructures by molecular beam epitaxy.
The microfabrication of the pre-patterned substrates, as well as the measurements of the nanowires presented in section 7.3.4 were performed by Dr. Oliver Breunig.

## 7.1 Introduction

In order to achieve surface dominated conduction in topological insulators, the bulk contribution has to be minimized. A straightforward approach is to change the surface-to-volume ratio by reducing the dimensions of the topological insulator. Nanowires have a large surface-to-volume ratio and are thus perfect candidates to probe the topological surface states in magnetotransport experiments. Another aspect is that interesting electronic properties arise due to the spatial confinement. Instead of patterning a TI film after MBE growth or synthesizing TI nanowires by crystal growth [211–214], a different technique is introduced in this chapter. The selective growth of a topological insulator film inside of pre-patterned nanostructures is a promising approach to achieve low dimensional structures and observe quantum transport phenomena [215, 216]. During the MBE growth the composition of the TI material and the thickness can be easily controlled. Additionally, the pre-patterned structures have a large flexibility in design. It is easy to simultaneously grow nanowires with different width, networks of nanowires and Hall bar devices.

Quasi-1D nanowires are a platform to study the topological surface states. As an indication for surface transport, the occurrence of Aharonov-Bohm (AB) oscillations in magneto-transport measurements was previously investigated foremost in nanowires grown by vapour-liquid-solid (VLS) growth or synthesized from a solution [214, 217–219]. An ideal TI nanowire exhibits an insulating bulk and hosts topological surface states around the circumference of the wire with spin-momentum locking. Thus, charge carriers encircling the wire with their spin rotating by $2\pi$ pick up a non-trivial Berry phase of $\pi$ which opens up a gap in the surface bands. Now, by applying an external magnetic field $B$ along the length of the nanowire (see Fig. 7.1), surface electrons encircling around the wire, pick up an Aharonov-Bohm phase of $2\pi\phi/\phi_0$, with the magnetic flux $\phi = BS$ through a cross-sectional area $S$ of the nanowire and the magnetic flux quantum $\phi_0 = h/e$ ($h$ = Planck constant, $e$ = electron charge). The magneto-conductance of a TI nanowire is expected to oscillate with a period of $\phi_0 = h/e$. The oscillations have maxima at odd integer multiple of $\phi = \phi_0/2$ and

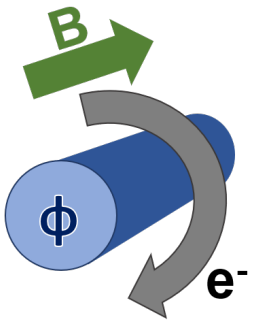


**Figure 7.1:** Sketch of a TI nanowire with magnetic field applied along the length and a charge encircling the circumference.

minima at even integer multiples (including $\phi = 0$). A system described by a Dirac Hamiltonian $H = v\mathbf{p} \cdot \sigma$ ($\sigma$ is the Pauli matrix vector and $v$ is the Fermi velocity) with a single Dirac cone, obeys the anti-periodic boundary conditions $\psi(x, \theta + 2\pi) = \exp(i(2\pi\phi/\phi_0 + \pi))\psi(x, \theta)$. Here, $x$ points in the direction along the nanowire. A flux of $\phi = \phi_0/2$ cancels the Berry phase and a gapless mode is realized in the energy spectrum, as shown in Fig. 7.2 [218, 220, 221].

Proximitizing such a quasi-1D topological insulator nanowire with an $s$-wave superconductor is proposed to give rise to two Majorana zero modes at the ends of the superconducting wire [19, 20]. Implementing a wire based on a 3D topological insulator has a major advantage to wires based on semiconductor. In case of semiconductor nanowires, the chemical potential has to be accurately tuned into a narrow Zeeman gap in an interval of $1\,\mathrm{meV}$ to realize a 1D topological superconductor [222, 223]. A topological insulator nanowire threaded by half a flux quantum realizes a topological phase as long as the chemical potential lies in the bulk band gap ($\mu \approx 200\,\mathrm{meV}$ [224]) and is expected to be robust against non-magnetic disorder [20, 223].
The main challenge lies in the synthesis of truly bulk-insulating wires with good morphology and the realization of a highly transparent interface to the proximitizing superconductor. From the potential synthesis methods, the technique of selective area growth, discussed in the following, stands out due to its good scalability and the potentially good interface to superconductors that could be deposited in an *in-situ* process after the growth.

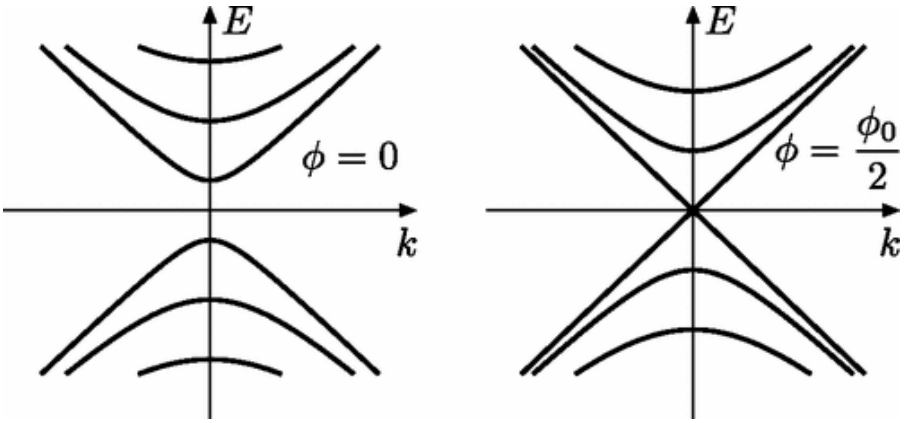


**Figure 7.2: Schematic of the surface state bandstructure of a topological insulator nanowire.** (a) At $\phi = 0$, a gap in the bandstructure is opened due to a $\pi$-Berry phase which an electron picks up by encircling the nanowire. (b) At $\Phi = \Phi_0/2$ a gapless mode is obtained at the Dirac point. Reprinted figure with permission from J.H. Bardason, PRL **105**, 156803 (2010). Copyright 2010 by the American Physical Society; [218]

## 7.2 Preparation of the selective area growth template

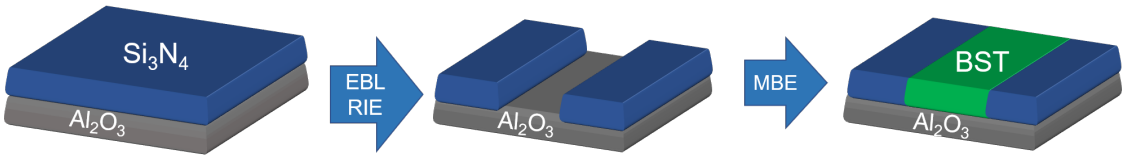


**Figure 7.3: Schematic illustration of the selective area growth process.** First a layer of $Si_3N_4$ is deposited on a sapphire substrate. After patterning the SAG structures by electron beam lithography and etching the trenches in RIE, the template is loaded into the MBE chamber and BST is grown inside of the trenches.

An illustration of the basic steps of the selective area growth process is shown in Fig. 7.3. First, a layer of silicon nitride ($Si_3N_4$) is deposited by hot-wire chemical vapor deposition (CVD) on a sapphire $Al_2O_3$ (0001) substrate. The sample is patterned by electron beam lithography into the desired structure. Therefore, ZEP520A was used as a high resolution positive electron beam resist. A layer of the resist is spincoated at 4000 rpm onto the sample and baked for 3 minutes at 120 °C. To prevent charging effects of the insulating sapphire substrate in the scanning electron microscope, the sample is afterwards spincoated at 3000 rpm with a layer of ESPACER. The desired pattern is fabricated by electron beam lithography in two steps: First structures such as nanowires and Hall bars are exposed with an electron beam voltage of 10 kV and a 10 µm aperture. A dose of 600 pC cm$^{-1}$ and a resolution of 8 nm are the chosen parameters. The nanowire structures are exposed as single lines. Afterwards, the larger structures such as contact pads are written with an aperture of 60 µm. A dose of 32.5 µC cm$^{-2}$ and resolution of 16 nm are used. The sample is developed for 32 s in Oxylene, followed by stopping the development in isopropanol. The structures which are no longer protected by resist are etched by reactive-ion etching (RIE). The $Si_3N_4$ inside of the trenches is etched by $CF_4$ (40 sccm, 40 mTorr, 50 W). The now exposed sapphire surface inside of the trenches is cleaned by two subsequent RIE steps of argon (1 minute, 40 sccm, 40 mTorr, 200 W) and $CF_4$ (1 minute, 40 sccm, 40 mTorr, 150 W). The template is taken out of the RIE and the remaining resist is removed by 50 °C N-Methyl Pyrrolidone (NMP) followed by rinsing the sample in acetone and IPA. The final cleaning step is another treatment in the RIE with oxygen (50 sccm, 40 mTorr, 150 W).

## 7.3 Selective area growth of $(Bi_{1-x}Sb_x)_2Te_3$ films by MBE

### 7.3.1 MBE growth of SAG Hall bar devices

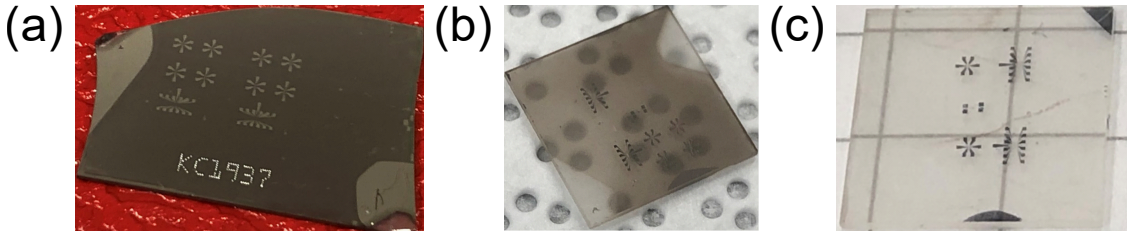


**Figure 7.4: Photos of three different selective area growth attempts.** (a) The BST film was deposited everywhere, inside of the trenches and on top of the $Si_3N_4$. (b) The BST film is still visible on top of the $Si_3N_4$. However, judging by the transparency of the film, it is grown more selective than the film in (a). (c) Fully selective grown BST film.

The aim of the selective area growth (SAG) method is to selectively grow a high-quality $(Bi_{1-x}Sb_x)_2Te_3$ thin film only inside the etched trenches of the pre-patterned substrate, however not on the silicon nitride part of the sample. Additional growth on the $Si_3N_4$ can introduce conduction channels outside of the nanostructures and thus destroy the low dimensionality of the grown film or lead to uncontrollable shunts between leads. To achieve selective growth, the challenge is to optimize the substrate temperature during the MBE growth. The MBE growth is performed by the two-step growth method described in chapter 4.2.1. As in the case of the BST growth on regular sapphire substrates, the pre-patterned substrates are annealed in the MBE2 chamber up to 950 °C and afterwards kept at 400 °C prior to the film deposition.

Figure 7.4 shows three photos of selective area growth attempts. By eye, the different growth results are already evident. The BST film covers the complete sample in Fig. 7.4 (a). The film shown in Fig. 7.4 (b) is already grown more selective, as suggested by the more transparent growth on the $Si_3N_4$ part of the sample. A fully selective grown BST film is presented in the photo in Fig. 7.4 (c). Here, the BST is only grown inside of the trenches and no obvious film growth is visible on top of the $Si_3N_4$. The two silver regions on the upper right and lower middle edge of the sample are the parts where the substrate was fixed with two clamps during the $Si_3N_4$ deposition by hot-wire CVD. Consequently, BST film grows on the sapphire in this region and the film thickness can be measured as a reference by atomic force microscopy.

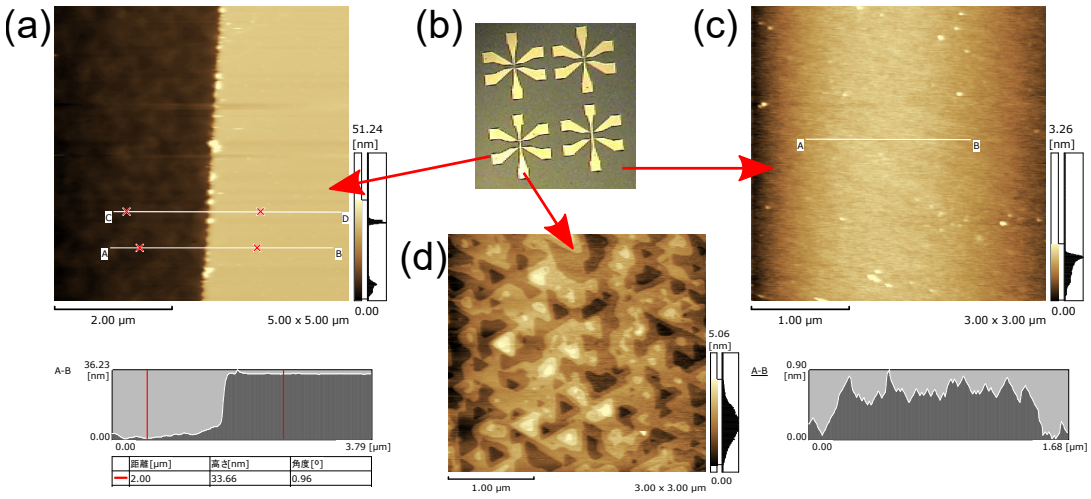


**Figure 7.5: Exemplary AFM images of a fully selectively grown sample.** (a) AFM image (5x5 µm) of the Hall bar pad edge with the BST film shown on the left side and the flat, clean $Si_3N_4$ on the right side of the image. The height profile reveals a flat silicon nitride surface and a height of 34 nm between BST film and $Si_3N_4$. (b) Optical image of the sample to indicate the positions where the different AFM images were taken. (c) AFM image of the $Si_3N_4$ surface, no residues are visible in a 3x3 µm region. The height profile shows a surface roughness of less than 1 nm. (d) AFM image 3x3 µm of the BST film grown inside of a Hall bar pad. The film is flat and continuous and the typical triangles can be identified.

An exemplary atomic force microscopy study of a fully selectively grown $(Bi_{1-x}Sb_x)_2Te_3$ film is presented in Fig. 7.5. This film was grown in the MBE2 chamber with a bismuth-antimony ratio of 1 : 2.85 under tellurium over-pressure as in the case of regular large area BST growth. During the growth, the substrate temperature was ramped with a rate of $\sim$3.5 °C min$^{-1}$ from 255 °C to 300 °C. The film is subsequently grown at the higher temperature of 300 °C for additional 14 minutes. Three different regions on the sample were checked by atomic force microscopy. The AFM image in Fig. 7.5(a) shows the edge of a Hall bar contact pad. The BST film grown inside of the contact pad can be seen on the left side of the image and the $Si_3N_4$ region is located on the right side. There are no residues present on the silicon nitride indicated by the flat height profile below the AFM image. Figure 7.5(c) displays a clean silicon nitride surface with a surface roughness of less than 1 nm, while the AFM image (d) shows a flat, continuous BST film with triangular shapes visible inside of the contact pad. The respective areas in which the AFM images were taken are displayed in the optical microscope picture show in Fig. 7.5(b).

Within the optimized substrate temperature range for this sample, the deposited materials can nucleate and form a continuous BST film on the sapphire

surface inside the pre-patterned structures. BST on top of the silicon nitride part is most likely re-evaporated from the surface due to a too low sticking coefficient on $Si_3N_4$ in this temperature range.

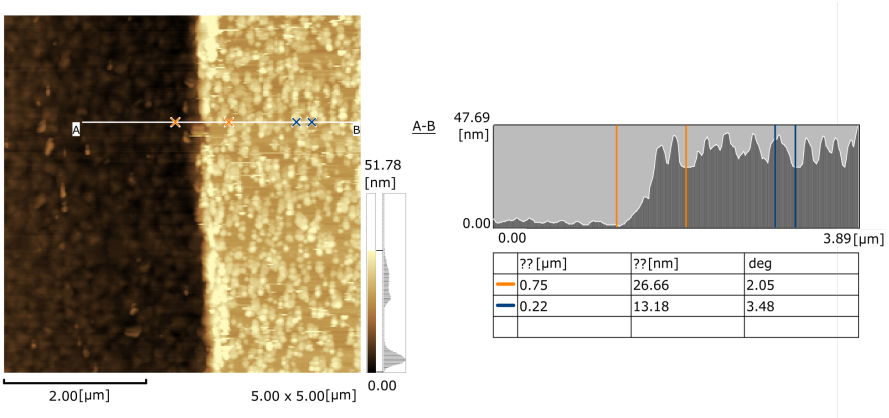


**Figure 7.6: AFM image (5x5 µm) and height profile of a partially selective grown BST film.** This sample was grown at the same substrate temperature as the sample shown in Fig. 7.5. The height profile indicates 13 nm-thin BST film residues on the $Si_3N_4$ surface.

It is prudent to mention that the challenge of this growth method is the reproducibility of the growth parameters. Another SAG growth was performed, using the same growth temperature previously discussed. However the second time, the BST film was not only grown in the trenches but disconnected BST island are also present on top of the $Si_3N_4$, as displayed in the AFM image in Fig. 7.6. The AFM image and height profile show BST island with a height of up to 13 nm on the silicon nitride. The sticking coefficient of the BST on the $Si_3N_4$ was most likely higher due to an effective lower substrate temperature. This indicates that using the same growth temperature does not necessarily guarantee to give the same growth result. The reason for this non-reproducible behavior can most likely be attributed to the way the SAG substrates are mounted on the sample holder. Given that every substrate is individually fixed on the molybdenum sample holder by tightening the screws of the fixing clamps, the thermal contact is slightly different for every sample (see Fig. 7.7). Consequently, the temperature distribution on the substrate varies slightly from sample to sample. Compared to the regular growth of the BST films on 1x1 cm sapphire substrates, the selectivity of the nanostructures appears to be even more temperature sensitive.

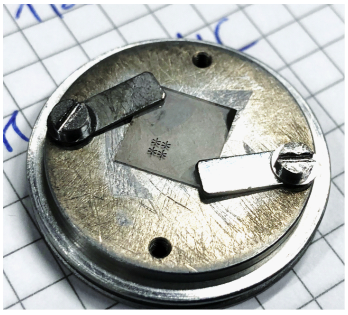

**Figure 7.7:** SAG substrate fixed by Ta-clamps on the Eiko sample holder.

### 7.3.2 Transport measurements of SAG Hall bar devices

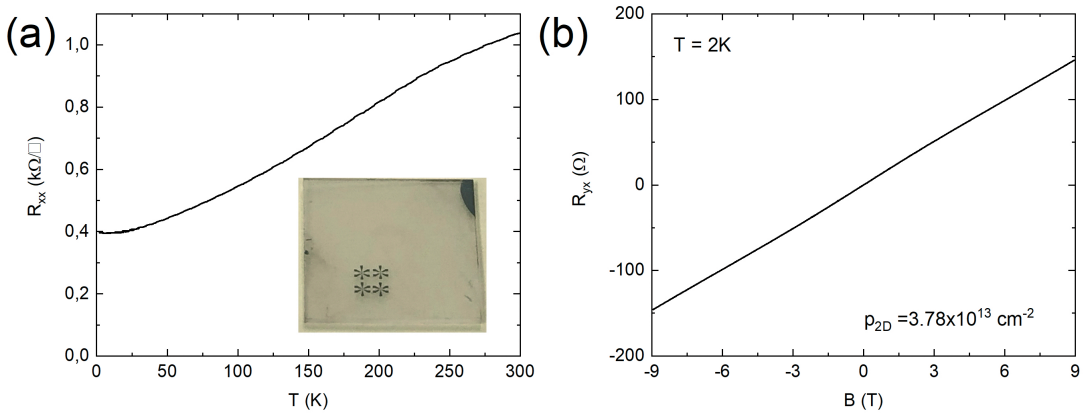


**Figure 7.8: Transport measurement of a fully selective grown BST film.** (a) The temperature dependence of the sheet resistance $R_{xx}$ shows a metallic behavior. A photo of the selectively grown sample is displayed in the inset. (b) The Hall resistance as a function of magnetic field has a positive slope indicating a hole dominated conduction with a carrier concentration of $p_{2D} = 3.78 \times 10^{13}\,\mathrm{cm}^{-2}$.

Besides the morphological properties and the selectivity of the BST growth, the magnetic and electrical properties of the film need to be optimized as it is the case for conventionally grown BST. Consequently, the bismuth-antimony ratio has to be tuned to alter the position of the Fermi level to achieve a bulk-insulating TI film. For such transport measurements, the Hall bar patterns discussed in the previous chapter 7.3.1 are convenient to use. A PPMS setup equipped with a 9 T-magnet was used for the transport characterization.

The magneto-transport measurements on the Hall bar device previously studied by AFM in Fig. 7.5 are depicted in Fig. 7.8. The temperature dependent measurement of the sheet resistance from 300 K to 2 K in Fig. 7.8 (a) reveals a metallic behavior indicated by a decrease of $R_{xx}$ with decreasing temperature. A photo of the selectively grown BST film is displayed in the inset of Fig. 7.8(a). A carrier concentration of $p_{2D} = 3.78 \times 10^{13}\,\mathrm{cm}^{-2}$, extracted from the positive slope of the Hall resistance measurement at 2 K in Fig. 7.8(b), exceeds the value which is attributed to surface dominated transport in the range of $\sim 10^{12}\mathrm{cm}^{-2}$.

A successful bulk-insulating BST film growth is shown in Fig. 7.9. For this growth, the bismuth-antimony ratio was changed to 1 : 2.77 by adding more bismuth compared to the sample shown in Fig. 7.8. The temperature dependence of the sheet resistance $R_{xx}$ in Fig. 7.9(a) shows an insulating behavior of increasing $R_{xx}$ with decreasing temperature. The measurement of the Hall resistance at 2 K

in Fig. 7.9 (b) reveals the BST film to be n-type with a carrier concentration of $n_{2D} = 4.3 \times 10^{12}\,\mathrm{cm}^{-2}$ and a mobility of $\mu = 600\,\mathrm{cm}^2\,\mathrm{V}^{-1}\,\mathrm{s}^{-1}$. This sample was grown only partially selective, as seen in the AFM images in Fig. 7.9. The left AFM image (600x600 nm) was taken inside a Hall bar pad and shows large triangular terraces indicating a high quality BST growth. The right AFM image (5x5 µm) was taken on the edge of the Hall bar pad. Here, growth on top of the $Si_3N_4$ is visible. However, the BST islands on top of the silicon nitride were found to be electrically disconnected by performing a four-terminal-measurement on the $Si_3N_4$ surface. Subsequently, the BST residues on the $Si_3N_4$ surface do not contribute to the conduction inside of the trenches.

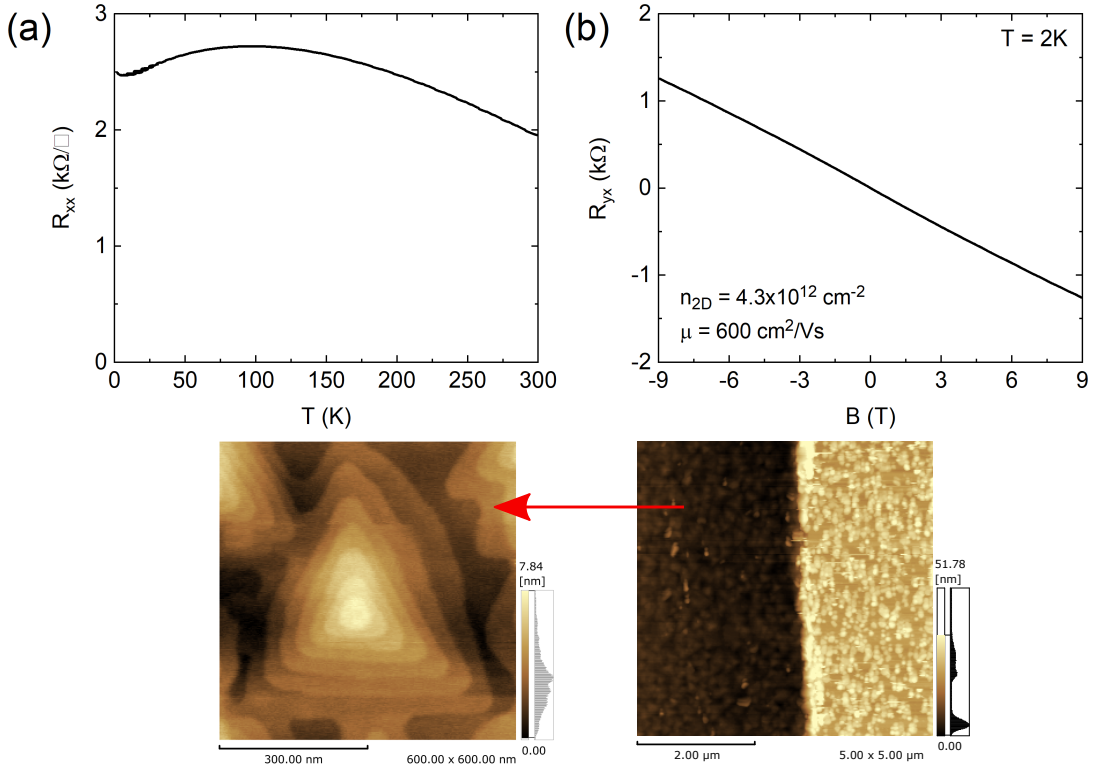


**Figure 7.9: Transport measurement of a bulk insulating SAG BST film.** (a) The temperature dependence of the sheet resistance $R_{xx}$ shows a typical insulating behavior. (b) The Hall resistance has a negative slope indicating a hole dominated conduction with a carrier concentration of $n_{2D} = 4.3 \times 10^{12}\,\mathrm{cm}^{-2}$ and a mobility of $\mu = 600\,\mathrm{cm}^2\,\mathrm{V}^{-1}\,\mathrm{s}^{-1}$. The left AFM image (600x600 nm) was taken inside a Hall bar pad and shows a large triangular terrace. The right AFM image (5x5 µm) was taken on the edge of the Hall bar pad. Isolated film growth on top of the $Si_3N_4$ is visible.

### 7.3.3 MBE growth of SAG nanostructures

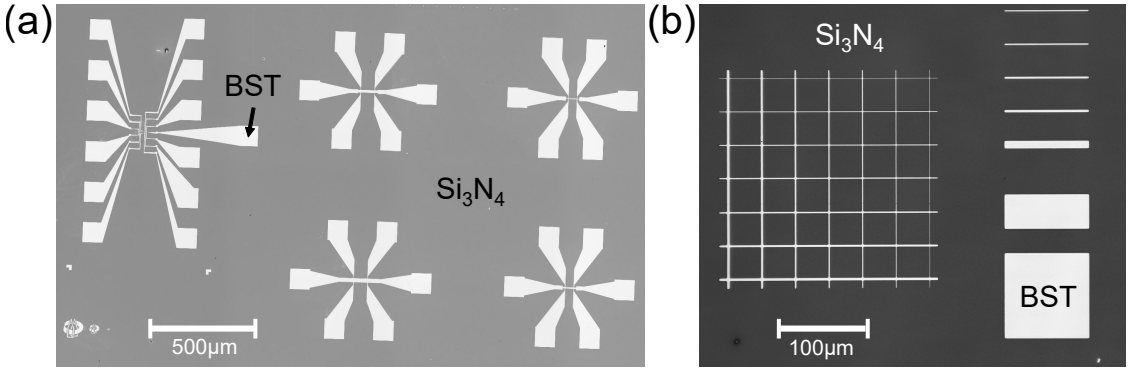


**Figure 7.10: Laser microscope pictures of various nanostructure designs after the MBE growth.** (a) Laser microscope picture of four Hall bars and a nanowire pattern. (b) Nanowire network and nanowires of various thickness. The white region are the trenches with BST growth inside, the dark parts are the silicon nitride regions.

The size of Hall bar devices discussed so far are in the micrometer range. Simultaneously, smaller structures in the nanometer-scale were grown on the same pre-patterned substrates. Figure 7.10 shows two laser microscope pictures of exemplary patterns which were used to selectively grown BST films. In Fig. 7.10(a) a nanowire pattern with various leads and contact pads is shown on the left and four Hall bar device are located on the right side. Figure 7.10 (b) is more focused on nanostructures in form of a nanowire network on the left and nanowires of different widths on the right.

BST films were grown inside of nanowire-patterned structures at various angles from 0° to 360° with respect to the crystal orientation of the sapphire substrate in order to study whether any direction is preferential for the growth of the BST nanowires on the sapphire substrate. A scanning-electron microscope (SEM) image to check the angle dependence is shown in Fig. 7.11. Here, no obvious difference between the individual BST growths at different nanowire angles can be identified. Nanowires of various width down to about $\sim$100 nm were successfully grown, as depicted in the SEM images in Fig. 7.12.

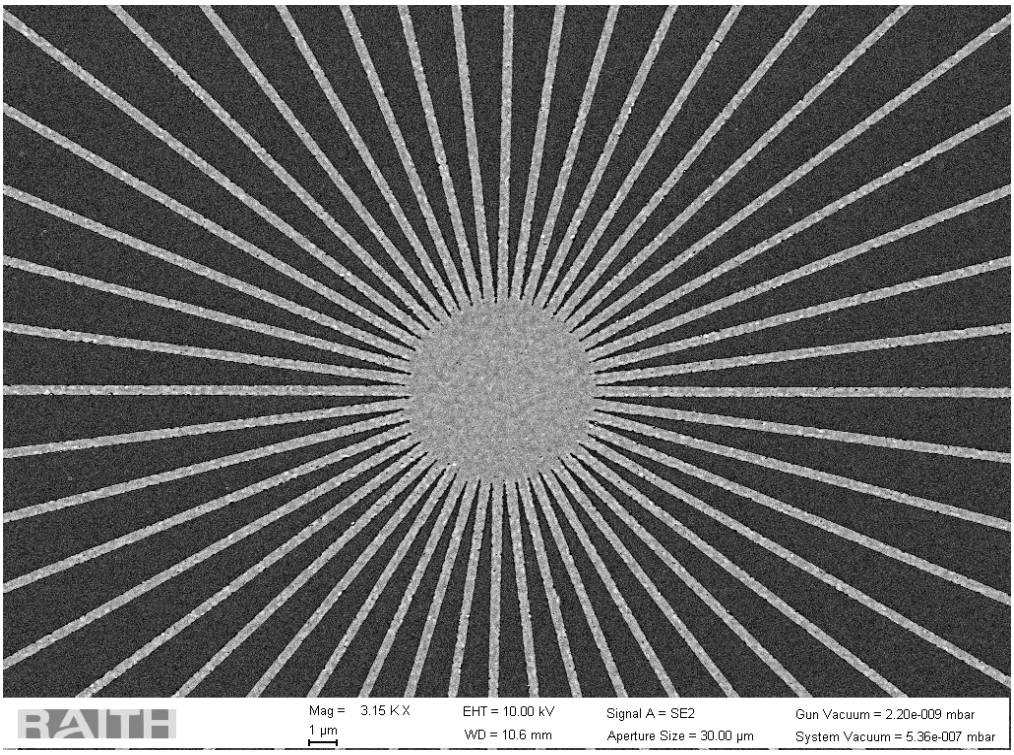


**Figure 7.11: Scanning-electron microscope (SEM) images of selectively grown BST nanowires.** SEM image of selectively grown BST nanowires grown at various angles.

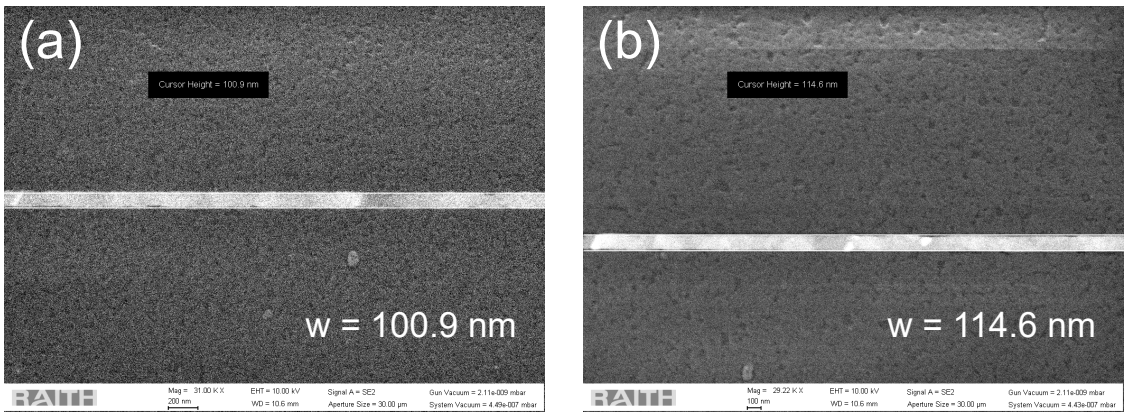


**Figure 7.12: Scanning-electron microscope (SEM) images of selectively grown BST nanowires.** (a) BST nanowire with a width of $w = 100.9\,\mathrm{nm}$. (b) BST nanowire with a width of $w = 114.6\,\mathrm{nm}$.

In order to study the magnetic and electrical properties of nanowires, a more complex pattern was designed. An example of such a nanowire pattern is shown in Fig. 7.13. The lighter regions in the optical image 7.13(a) are the etched areas where a ∼15 nm-thin BST film is grown. The pattern includes a small and a large gate in close proximity to a ∼150 nm-wide nanowire to tune the chemical potential of the BST film (see Fig. 7.13 (a) and (b)). The advantage of this pattern is that the gates consist of grown BST film as well, so no additional microfabrication step is required to add the gates to the nanowire. The AFM image in Fig. 7.13(c) was taken in the region highlighted by the red square in (a). The AFM image and the height profile indicate that the film was selectivity grown only inside the trenches.

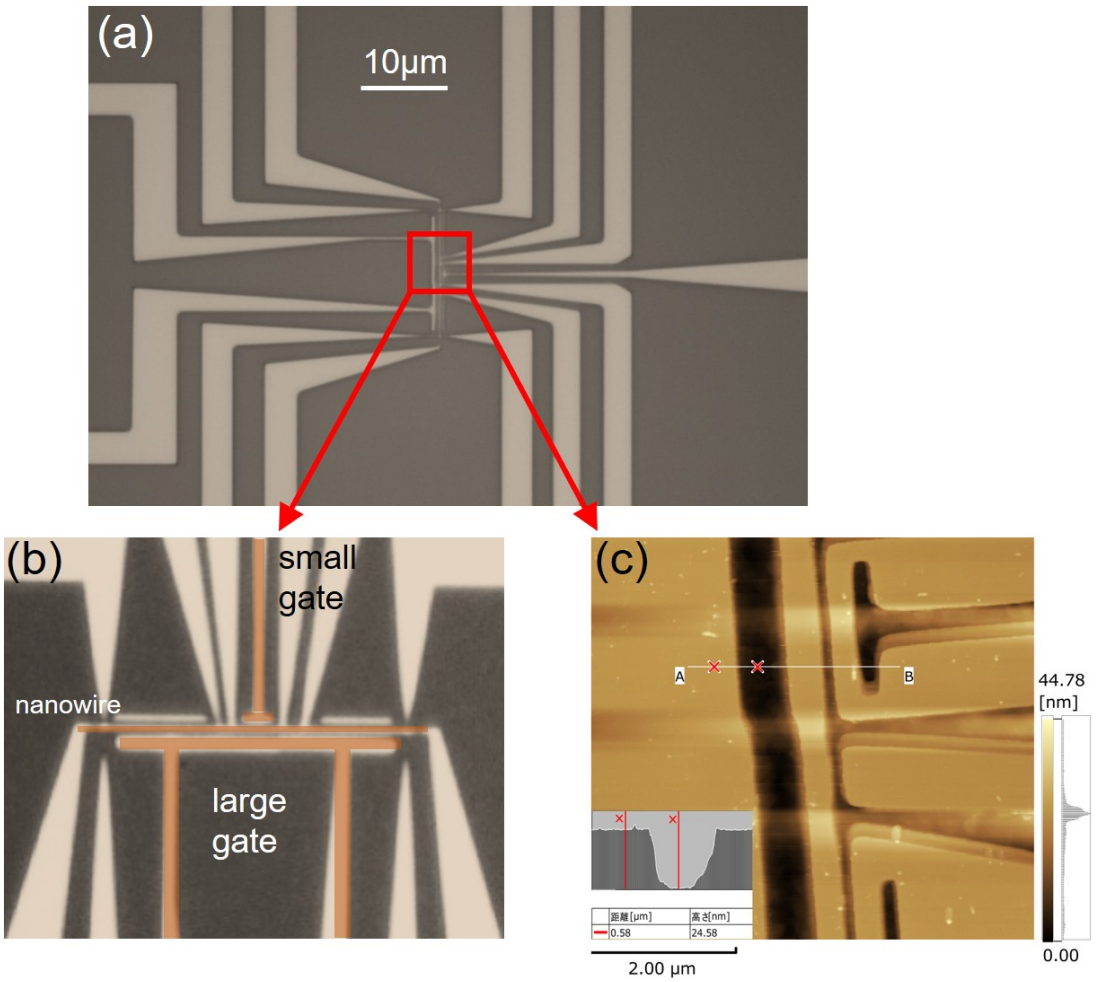


**Figure 7.13: Example of a SAG nanowire design:** (a) Optical image of the nanowire structure. BST is grown in the lighter region in this image. (b) Laser microscope image of the central region of the nanowire design. The ∼150 nm-wide BST nanowire, the small and large gate are highlighted. (c) AFM image and height profile of the central region of the nanowire marked by the red square in (a). The BST is only grown inside the trenches and the silicon nitride part is flat without any residues.

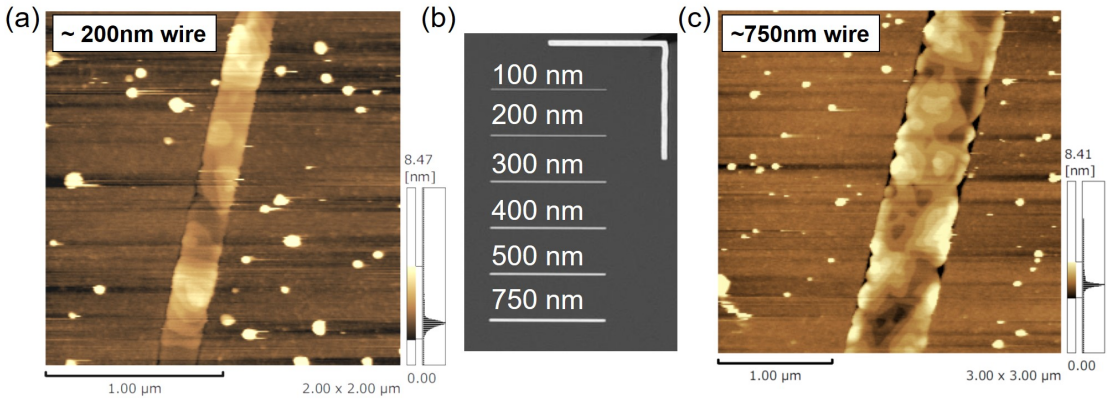


**Figure 7.14: Example of a successful SAG growth using $SiO_2$ as a pattern basis.** Various nanowire sizes were fabricated as depicted by the laser microscope image in (b). The AFM images in (a) (2x2 µm) and (c) (3x3 µm) illustrate the selective, high-quality BST growth of a nanowire with a width of approximately 200 nm and 750 nm.

Other than using silicon nitride as a growth pattern base, silicon dioxide was deposited as well. The selective area growth was successful for pre-patterned $SiO_2$ substrates, however the $SiO_2$ growth itself by magneto-sputtering was less reproducible than growing $Si_3N_4$ by hot-wire CVD. Figure 7.14 shows a selective growth on a silicon dioxide covered substrate. Various nanowire sizes were fabricated as depicted by the laser microscope image in (b). The AFM images in (a) and (c) illustrate the selective, high-quality BST growth of a nanowire with a width of approximately 200 nm and 750 nm. The AFM image in Fig. 7.14 (c) reveals several gaps at the edge of the nanowire. The same behavior can also be seen in the growth on $Si_3N_4$ templates, as shown in Fig. 7.11. In the region of these triangular shaped gaps, two BST growth islands meet but their growth is confined by the nanowire width.

### 7.3.4 Transport measurements of SAG nanostructures

In order to test the gating efficiency of the BST-grown side gates, an additional top gate on top of the approximately 150 nm-wide BST nanowire was fabricated after the SAG growth and characterized by magnetotransport measurements. Figure 7.15 shows optical microscope images of the nanowire pattern design following the MBE growth (a) and after adding an additional top gate to the sample (b). Figure 7.15 (c) shows an AFM image of a contact arm edge with both the BST film on the left side and the $Si_3N_4$ layer visible on the right. Nanometer-sized isolated residues are present on the silicon nitride part. The AFM image in Fig. 7.15 (b) displays the BST film growth inside a trench. The image is slightly blurred due to the fact that it was taken after the sample was covered with 30 nm of $Al_2O_3$ by

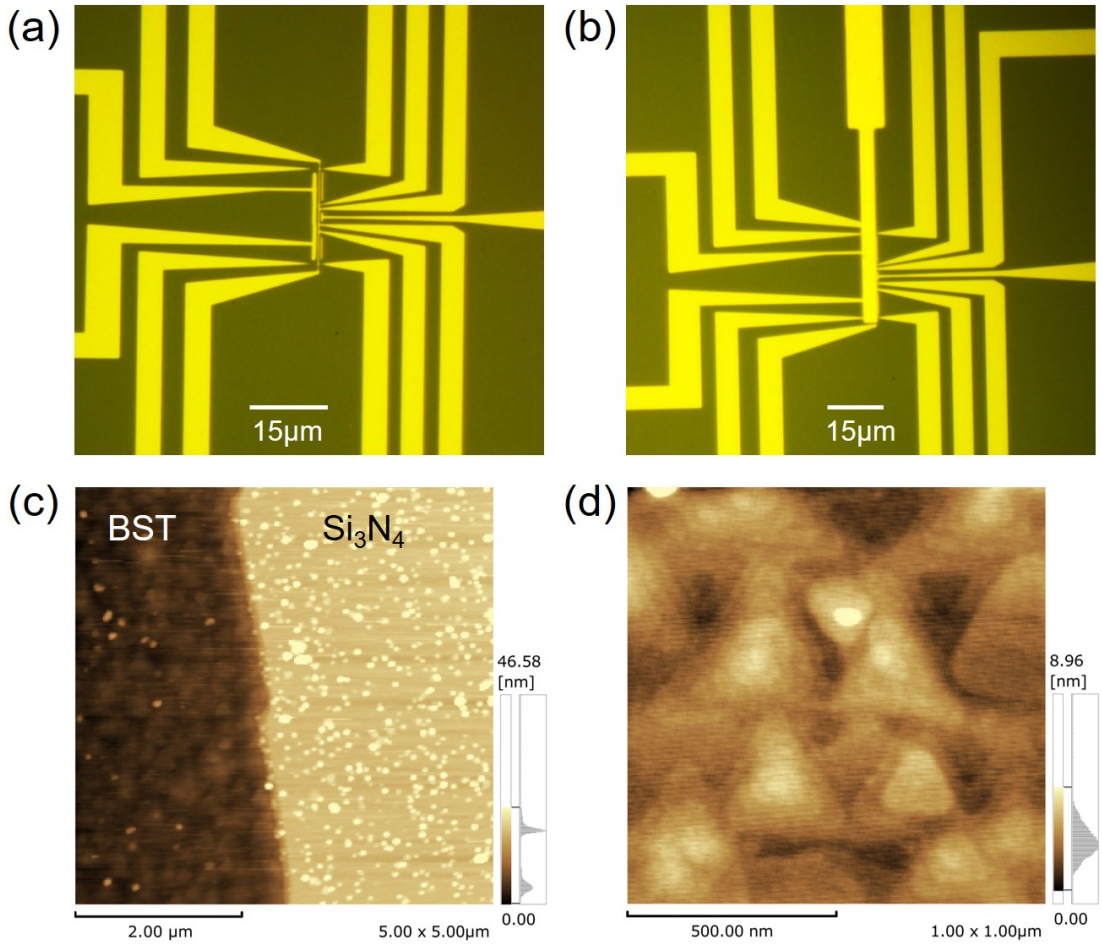


**Figure 7.15: SAG nanowire after the MBE growth** (a) Optical microscope picture of the nanowire pattern after the MBE growth. The yellow region indicates the part where the BST was grown. (b) The same nanowire pattern but now with a top gate added after the MBE growth. (c) AFM image (5x5 µm) of a contact arm edge with both the BST film on the left side and the $Si_3N_4$ layer visible on the right. Nanometer-sized isolated residues are present on the silicon nitride part. (d) AFM image (1x1 µm) of BST grown inside the trench and after growth covered with 30 nm of $Al_2O_3$. A continuous BST film with triangular terraces is shown.

ALD. Even so, a continuous film with triangular terraces is evident, indicating a high quality BST film growth.

Figure 7.16 shows the results of the gating effects for a top-gated Hall bar device (a) and a nanowire (b) fabricated on the same sample. The top-gate voltage dependence of the resistance of the Hall bar is depicted in Fig. 7.16 (a) with an optical image of the device shown as an inset. The gating curve clearly reveals a maximum in resistance at a gate voltage of $\sim$–3.75 V in the up (black curve) and down (red curve) sweep of the voltage. This indicates that by sweeping the top-gate voltage, the dominating carrier type was tuned from $n$-type to

$p$-type (and back) while shifting the Fermi level through the Dirac point in the hole-dominated regime at ∼−3.75 V. Figure 7.16 (b) shows two gating curves obtained by transport measurements of the nanowire. The red gating curve shows the top-gate voltage dependence of the resistance. As in the case of the Hall bar device, by applying a top-gate voltage to the nanowire the position of the Fermi level could be tuned to the Dirac point at ∼−3 V, which is comparable to the measurement of the top-gated Hall bar device shown in Fig. 7.16 (a). This similarity suggests that the film quality and the charge compensation in the $(Bi_{1-x}Sb_x)_2Te_3$ compound hardly depend on the size of the trench in which the film is allowed to grow. Additionally, the gate voltage of two side gates, illustrated in the optical microscope picture in the inset, was simultaneously applied. The side-gating curve is depicted by the blue curve in Fig. 7.16(b). Evidently, the gating efficiency of the side gates is far lower than the efficiency of the top gate. While the top gate can tune the carrier concentration from electron- to hole- dominated regime in the range of −4 V to 4 V, the side gates show no maximum while sweeping the gate voltage from −25 V to 25 V. This behavior suggests that the side gates can only influence the chemical potential of the BST film in a small width-range of the approximately 150 nm-wide nanowire. The top gate covers the top surface of the complete BST nanowire and can consequently affect the chemical potential in the whole width of the approximately 15 nm-thin nanowire.

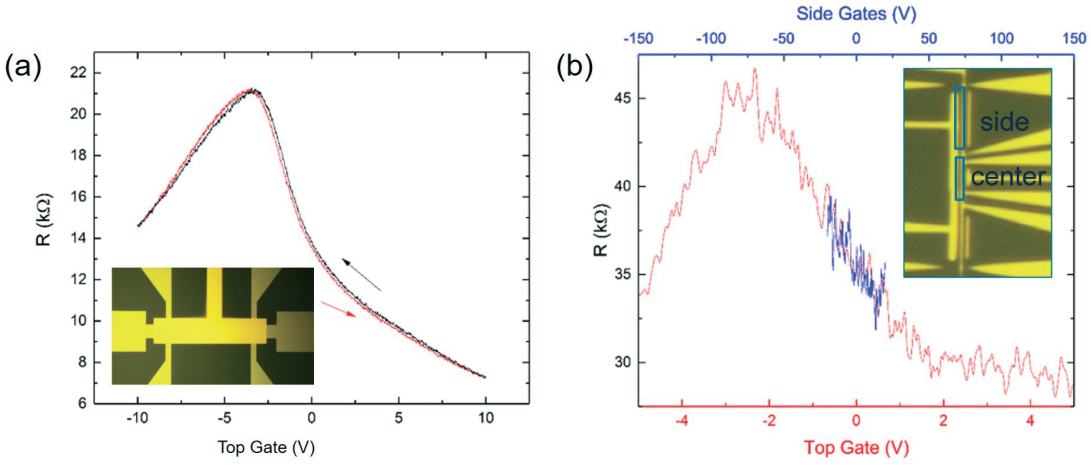


**Figure 7.16: Comparison of the gate efficiency of top and side gates on a SAG nanowire.** (a) Top gate-voltage dependence of the resistance measured on a Hall bar device. The inset show an optical microscope picture the top gated Hall bar device. (b) Comparison of side (blue curve)- and top gate (red curve)-voltage dependence of the resistance measured on a nanowire device. The inset show an optical microscope picture the side gates on the nanowire to indicate their position before the top-gate was added on top.

## 7.4 Conclusion and outlook

The selective area growth technique of $(Bi_{1-x}Sb_x)_2Te_3$ thin films was introduced in this chapter. The successful fabrication of pre-patterned growth substrates and the selective growth of high-quality BST films was shown. Furthermore, the grown BST films could be optimized to be bulk-insulating by tuning the bismuth-antimony ratio. Besides micrometer-sized Hall bar devices, nanostructures were deposited and their electrical properties were studied. In particular the gate efficiency of BST grown side gates in comparison to a top gate added after the film growth was investigated.

The challenge of this growth method was the reproducibility in growth. It was found that almost every pre-patterned substrate had to be grown in an individual growth window in the range of $\pm 10\,^{\circ}\mathrm{C}$. The reason for the non-reproducibility is most likely the way the substrates are fixed on the sample holder. Preliminary growth results from growing the SAG samples in the MBE3 UHV-chamber suggest that the growth is more reproducible in the MBE3 chamber. The sample holders used in the MBE3 chamber require to spot-weld samples on tantalum sample holders as shown in chapter 3.1.1. This most likely gives a more homogeneous temperature distribution on the pre-patterned substrate and is a more reproducible way of fixing the sample.

After establishing the reproducible growth conditions, the next step is to deposit a superconductor on top of the TI nanowire. This is proposed to introduce superconductivity into the TI surface states by the proximity effect and to give rise to two Majorana zero modes at the ends of the superconducting wire [19, 20].

# List of Figures

# Bibliography


[1] F. Bloch, "Über die Quantenmechanik der Elektronen in Kristallgittern", Zeitschrift für Physik **52**, 555–600 (1929).

[2] A. H. Wilson, "The theory of electronic semi-conductors", Proceedings of the Royal Society of London. Series A, Containing Papers of a Mathematical and Physical Character **133**, 458–491 (1931).

[3] K. v. Klitzing, G. Dorda, and M. Pepper, "New Method for High-Accuracy Determination of the Fine-Structure Constant Based on Quantized Hall Resistance", Physical Review Letters **45**, 494–497 (1980).

[4] K. v. Klitzing, "The quantized hall effect", Physica B+C **126**, 242–249 (1984).

[5] Royal Swedish Academy of Sciences, *Popular Science Background: Strange phenomena in matter's flatlands*, 2016.

[6] C. L. Kane and E. J. Mele, "Quantum spin Hall effect in graphene", Physical Review Letters **95** (2005).

[7] C. L. Kane and E. J. Mele, "Z2 topological order and the quantum spin Hall effect", Physical Review Letters **95** (2005).

[8] B. A. Bernevig, T. L. Hughes, and S.-C. Zhang, "Quantum spin Hall effect and topological phase transition in HgTe quantum wells", Science **314**, 1757–1761 (2006).

[9] M. Koenig, S. Wiedmann, C. Brune, A. Roth, H. Buhmann, L. W. Molenkamp, X.-L. Qi, and S.-C. Zhang, "Quantum spin Hall insulator state in HgTe quantum wells", Science **318**, 766–770 (2007).

[10] L. Fu, C. L. Kane, and E. J. Mele, "Topological insulators in three dimensions", Physical Review Letters **98** (2007).

[11] D. Hsieh, D. Qian, L. Wray, Y. Xia, Y. S. Hor, R. J. Cava, and M. Z. Hasan, "A topological Dirac insulator in a quantum spin Hall phase", Nature **452**, 970–974 (2008).

[12] Y. Xia, D. Qian, D. Hsieh, L. Wray, A. Pal, H. Lin, A. Bansil, D. Grauer, Y. S. Hor, R. J. Cava, and M. Z. Hasan, "Observation of a large-gap topological-insulator class with a single Dirac cone on the surface", Nature Physics **5**, 398–402 (2009).

[13] H. Zhang, C.-X. Liu, X.-L. Qi, X. Dai, Z. Fang, and S.-C. Zhang, "Topological insulators in $Bi_2Se_3$, $Bi_2Te_3$ and $Sb_2Te_3$ with a single Dirac cone on the surface", Nature Physics **5**, 438–442 (2009).

[14] Y. L. Chen, J. G. Analytis, J.-H. Chu, Z. K. Liu, S.-K. Mo, X. L. Qi, H. J. Zhang, D. H. Lu, X. Dai, Z. Fang, S. C. Zhang, I. R. Fisher, Z. Hussain, and Z.-X. Shen, "Experimental realization of a three-dimensional topological insulator, $Bi_2Te_3$", Science **325**, 178–181 (2009).

[15] J. Zhang, C.-Z. Chang, Z. Zhang, J. Wen, X. Feng, K. Li, M. Liu, K. He, L. Wang, X. Chen, Q.-K. Xue, X. Ma, and Y. Wang, "Band structure engineering in $(Bi_{1-x}Sb_x)_2Te_3$ ternary topological insulators", Nature Communications **2** (2011).

[16] M. Sato and Y. Ando, "Topological superconductors: a review", Reports on Progress in Physics **80**, 076501 (2017).

[17] X.-L. Qi and S.-C. Zhang, "Topological insulators and superconductors", Reviews of Modern Physics **83**, 1057–1110 (2011).

[18] F. Wilczek, "Majorana returns", Nature Physics **5**, 614–618 (2009).

[19] A. Cook and M. Franz, "Majorana fermions in a topological-insulator nanowire proximity-coupled to an s-wave superconductor", Physical Review B **84** (2011).

[20] A. M. Cook, M. M. Vazifeh, and M. Franz, "Stability of Majorana fermions in proximity-coupled topological insulator nanowires", Physical Review B **86** (2012).

[21] Y. Ando, "Topological insulator materials", Journal of the Physical Society of Japan **82**, 102001 (2013).

[22] J. E. Moore, "The birth of topological insulators", Nature **464**, 194–198 (2010).

[23] R. Gross, *Festkörperphysik* (Oldenbourg, München, 2012).

[24] D. J. Thouless, M. Kohmoto, M. P. Nightingale, and M. den Nijs, "Quantized Hall conductance in a two-dimensional periodic potential", Physical Review Letters **49**, 405–408 (1982).

[25] N. Nagaosa, "Physics: a new state of quantum matter", Science **318**, 758–759 (2007).

[26] P. J. Leek, J. M. Fink, A. Blais, R. Bianchetti, M. Goppl, J. M. Gambetta, D. I. Schuster, L. Frunzio, R. J. Schoelkopf, and A. Wallraff, "Observation of Berry's phase in a solid-state qubit", Science **318**, 1889–1892 (2007).

[27] M. V. Berry, "Quantal phase factors accompanying adiabatic changes", Proceedings of the Royal Society of London. A. Mathematical and Physical Sciences **392**, 45–57 (1984).

[28] M. Z. Hasan and C. L. Kane, "Colloquium: topological insulators", Reviews of Modern Physics **82**, 3045–3067 (2010).

[29] B. A. Bernevig and S.-C. Zhang, "Quantum spin Hall effect", Physical Review Letters **96** (2006).

[30] J. E. Moore and L. Balents, "Topological invariants of time-reversal-invariant band structures", Physical Review B **75** (2007).

[31] L. Fu and C. L. Kane, "Topological insulators with inversion symmetry", Physical Review B **76** (2007).

[32] C. Kittel, *Introduction to solid state physics* (Wiley, Hoboken, NJ, 2005).

[33] E. H. Hall, "On a new action of the magnet on electric currents", American Journal of Mathematics **2**, 287 (1879).

[34] E. Hall, "XVIII. on the "rotational coefficient" in nickel and cobalt", The London, Edinburgh, and Dublin Philosophical Magazine and Journal of Science **12**, 157–172 (1881).

[35] N. Nagaosa, J. Sinova, S. Onoda, A. H. MacDonald, and N. P. Ong, "Anomalous Hall effect", Reviews of Modern Physics **82**, 1539–1592 (2010).

[36] L. P. He, Z. Zhang, J. Pan, X. C. Hong, S. Y. Zhou, and S. Y. Li, "Full superconducting gap in the doped topological crystalline insulator $Sn_{0.6}In_{0.4}Te$", Physical Review B **88**, 014523 (2013).

[37] C.-Z. Chang and M. Li, "Quantum anomalous Hall effect in time-reversal-symmetry breaking topological insulators", Journal of Physics: Condensed Matter **28**, 123002 (2016).

[38] F. D. M. Haldane, "Model for a quantum Hall effect without landau levels: condensed-matter realization of the parity anomaly", Physical Review Letters **61**, 2015–2018 (1988).

[39] R. Yu, W. Zhang, H.-J. Zhang, S.-C. Zhang, X. Dai, and Z. Fang, "Quantized anomalous Hall effect in magnetic topological insulators", Science **329**, 61–64 (2010).

[40] Y. Tokura, K. Yasuda, and A. Tsukazaki, "Magnetic topological insulators", Nature Reviews Physics **1**, 126–143 (2019).

[41] X.-L. Qi, Y.-S. Wu, and S.-C. Zhang, "Topological quantization of the spin Hall effect in two-dimensional paramagnetic semiconductors", Physical Review B **74** (2006).

[42] C.-X. Liu, X.-L. Qi, X. Dai, Z. Fang, and S.-C. Zhang, "Quantum Anomalous Hall Effect in $Hg_{1-y}Mn_yTe$ Quantum Wells", Physical Review Letters **101** (2008).

[43] X.-L. Qi, T. L. Hughes, and S.-C. Zhang, "Topological field theory of time-reversal invariant insulators", Physical Review B **78** (2008).

[44] K. Nomura and N. Nagaosa, "Surface-quantized anomalous Hall current and the magnetoelectric effect in magnetically disordered topological insulators", Physical Review Letters **106** (2011).

[45] K. He, X.-C. Ma, X. Chen, L. Lü, Y.-Y. Wang, and Q.-K. Xue, "From magnetically doped topological insulator to the quantum anomalous Hall effect", Chinese Physics B **22**, 067305 (2013).

[46] R.-L. Chu, J. Shi, and S.-Q. Shen, "Surface edge state and half-quantized Hall conductance in topological insulators", Physical Review B **84** (2011).

[47] X. Kou, Y. Fan, M. Lang, P. Upadhyaya, and K. L. Wang, "Magnetic topological insulators and quantum anomalous hall effect", Solid State Communications **215-216**, 34–53 (2015).

[48] J.-M. Zhang, W. Ming, Z. Huang, G.-B. Liu, X. Kou, Y. Fan, K. L. Wang, and Y. Yao, "Stability, electronic, and magnetic properties of the magnetically doped topological insulators $Bi_2Se_3$, $Bi_2Te_3$, and $Sb_2Te_3$", Physical Review B **88** (2013).

[49] J.-M. Zhang, W. Zhu, Y. Zhang, D. Xiao, and Y. Yao, "Tailoring magnetic doping in the topological insulator $Bi_2Se_3$", Physical Review Letters **109** (2012).

[50] P Kacman, "Spin interactions in diluted magnetic semiconductors and magnetic semiconductor structures", Semiconductor Science and Technology **16**, R25–R39 (2001).

[51] Y.-J. Chien, Z. Zhou, and C. Uher, "Growth and transport properties of $Sb_{2-x}V_xTe_3$ thin films on sapphire substrates", Journal of Crystal Growth **283**, 309–314 (2005).

[52] J. Choi, H.-W. Lee, B.-S. Kim, H. Park, S. Choi, S. Hong, and S. Cho, "Magnetic and transport properties of mn-doped $Bi_2Se_3$ and $Sb_2Se_3$", Journal of Magnetism and Magnetic Materials **304**, e164–e166 (2006).

[53] T. Dietl and H. Ohno, "Dilute ferromagnetic semiconductors: physics and spintronic structures", Reviews of Modern Physics **86**, 187–251 (2014).

[54] M. A. Ruderman and C. Kittel, "Indirect exchange coupling of nuclear magnetic moments by conduction electrons", Physical Review **96**, 99–102 (1954).

[55] K. He, Y. Wang, and Q.-K. Xue, "Quantum anomalous Halll effect", National Science Review **1**, 38–48 (2013).

[56] J. H. van Vleck, *The Theory of Electric and Magnetic Susceptibilities* (Franklin Classics Trade PR, Nov. 11, 2018), 398 pp.

[57] C.-Z. Chang, J. Zhang, M. Liu, Z. Zhang, X. Feng, K. Li, L.-L. Wang, X. Chen, X. Dai, Z. Fang, X.-L. Qi, S.-C. Zhang, Y. Wang, K. He, X.-C. Ma, and Q.-K. Xue, "Thin films of magnetically doped topological insulator with carrier-independent long-range ferromagnetic order", Advanced Materials **25**, 1065–1070 (2013).

[58] X.-L. Qi, T. L. Hughes, S. Raghu, and S.-C. Zhang, "Time-reversal-invariant topological superconductors and superfluids in two and three dimensions", Physical Review Letters **102** (2009).

[59] A. P. Schnyder, S. Ryu, A. Furusaki, and A. W. W. Ludwig, "Classification of topological insulators and superconductors in three spatial dimensions", Physical Review B **78** (2008).

[60] N. Read and D. Green, "Paired states of fermions in two dimensions with breaking of parity and time-reversal symmetries and the fractional quantum Hall effect", Physical Review B **61**, 10267–10297 (2000).

[61] L. Fu and E. Berg, "Odd-Parity Topological Superconductors: Theory and Application to $Cu_xBi_2Se_3$", Physical Review Letters **105** (2010).

[62] Y. S. Hor, A. J. Williams, J. G. Checkelsky, P. Roushan, J. Seo, Q. Xu, H. W. Zandbergen, A. Yazdani, N. P. Ong, and R. J. Cava, "Superconductivity in $Cu_xBi_2Se_3$ and its Implications for Pairing in the Undoped Topological Insulator", Physical Review Letters **104** (2010).

[63] L. Fu and C. L. Kane, "Superconducting proximity effect and Majorana fermions at the surface of a topological insulator", Physical Review Letters **100**, 096407 (2008).

[64] Y. Ando, "48th IFF Spring School, Forschungzentrum Jülich: Lecture notes on Topological Superconductors", in (2017).

[65] Y. Ando and L. Fu, "Topological crystalline insulators and topological superconductors: from concepts to materials", Annual Review of Condensed Matter Physics **6**, 361–381 (2015).

[66] H. K. Onnes, "Further experiments with liquid helium. c. on the change of electric resistance of pure metals at very low temperatures etc. IV. the resistance of pure mercury at helium temperatures", in *Through measurement to knowledge* (Springer Netherlands, 1991), pp. 261–263.

[67] W. Meissner and R. Ochsenfeld, "Ein neuer Effekt bei Eintritt der Supraleitfähigkeit", Die Naturwissenschaften **21**, 787–788 (1933).

[68] F. London and H. London, "The electromagnetic equations of the supraconductor", Proceedings of the Royal Society of London. Series A - Mathematical and Physical Sciences **149**, 71–88 (1935).

[69] J. Bardeen, L. N. Cooper, and J. R. Schrieffer, "Microscopic theory of superconductivity", Physical Review **106**, 162–164 (1957).

[70] J. Bardeen, L. N. Cooper, and J. R. Schrieffer, "Theory of superconductivity", Physical Review **108**, 1175–1204 (1957).

[71] M. Tinkham, *Introduction to superconductivity* (Dover Pubn Inc, June 1, 2004), 454 pp.

[72] S. Blügel, *Topological Matter - Topological Insulators, Skyrmions and Majoranas lecture notes of the 48th IFF Spring School 2017* (Forschungszentrum Jülich GmbH, Zentralbibliothek, Verlag, Jülich, 2017).

[73] S. Kruchinin, *Modern aspects of superconductivity : theory of superconductivity* (World Scientific, 2011).

[74] R. F. C. Farrow, *Molecular beam epitaxy : applications to key materials* (Noyes Publications, Park Ridge, N.J, 1995).

[75] H. Lüth, *Solid surfaces, interfaces and thin films* (Springer-Verlag, Heidelberg New York, 2010).

[76] T. A. Flaim and P. D. Ownby, "Observations on bayard–alpert ion gauge sensitivities to various gases", Journal of Vacuum Science and Technology **8**, 661–662 (1971).

[77] M. Herman, *Molecular Beam Epitaxy : Fundamentals and Current Status* (Springer Berlin Heidelberg, Berlin, Heidelberg, 1989).

[78] M. Herman, *Epitaxy : Physical Principles and Technical Implementation* (Springer Berlin Heidelberg, Berlin, Heidelberg, 2004).

[79] G. Cao, *Nanostructures and nanomaterials: synthesis, properties and applications* (Imperial College Press, Apr. 1, 2004), 448 pp.

[80] A. Koma, "New epitaxial growth method for modulated structures using van der waals interactions", Surface Science **267**, 29–33 (1992).

[81] A. Koma, "Van der waals epitaxy for highly lattice-mismatched systems", Journal of Crystal Growth **201-202**, 236–241 (1999).

[82] X. F. Kou, L. He, F. X. Xiu, M. R. Lang, Z. M. Liao, Y. Wang, A. V. Fedorov, X. X. Yu, J. S. Tang, G. Huang, X. W. Jiang, J. F. Zhu, J. Zou, and K. L. Wang, "Epitaxial growth of high mobility $Bi_2Se_3$ thin films on CdS", Applied Physics Letters **98**, 242102 (2011).

[83] L. He, F. Xiu, X. Yu, M. Teague, J. Wanjun, Y. Fan, X. Kou, M. Lang, Y. Wang, G. Huang, N.-C. Yeh, and K. L. Wang, "Surface-dominated conduction in a 6 nm thick $Bi_2Se_3$ thin film", Nano Letters **12**, 1486–1490 (2012).

[84] S. Borisova, J. Kampmeier, M. Luysberg, G. Mussler, and D. Grützmacher, "Domain formation due to surface steps in topological insulator $Bi_2Te_3$ thin films grown on Si (111) by molecular beam epitaxy", Applied Physics Letters **103**, 081902 (2013).

[85] O. Caha, A. Dubroka, J. Humlíček, V. Holý, H. Steiner, M. Ul-Hassan, J. Sánchez-Barriga, O. Rader, T. N. Stanislavchuk, A. A. Sirenko, G. Bauer, and G. Springholz, "Growth, structure, and electronic properties of epitaxial bismuth telluride topological insulator films on $BaF_2$ (111) substrates", Crystal Growth & Design **13**, 3365–3373 (2013).

[86] R. Yoshimi, A. Tsukazaki, Y. Kozuka, J. Falson, K. Takahashi, J. Checkelsky, N. Nagaosa, M. Kawasaki, and Y. Tokura, "Quantum Hall effect on top and bottom surface states of topological insulator $(Bi_{1-x}Sb_x)_2Te_3$ films", Nature Communications **6** (2015).

[87] Z. Zeng, T. A. Morgan, D. Fan, C. Li, Y. Hirono, X. Hu, Y. Zhao, J. S. Lee, J. Wang, Z. M. Wang, S. Yu, M. E. Hawkridge, M. Benamara, and G. J. Salamo, "Molecular beam epitaxial growth of $Bi_2Te_3$ and $Sb_2Te_3$ topological insulators on GaAs (111) substrates: a potential route to fabricate topological insulator p-n junction", AIP Advances **3**, 072112 (2013).

[88] X. Liu, D. J. Smith, J. Fan, Y.-H. Zhang, H. Cao, Y. P. Chen, J. Leiner, B. J. Kirby, M. Dobrowolska, and J. K. Furdyna, "Structural properties of $Bi_2Te_3$ and $Bi_2Se_3$ topological insulators grown by molecular beam epitaxy on GaAs(001) substrates", Applied Physics Letters **99**, 171903 (2011).

[89] A. A. Taskin, S. Sasaki, K. Segawa, and Y. Ando, "Achieving surface quantum oscillations in topological insulator thin films of $Bi_2Se_3$", Advanced Materials **24**, 5581–5585 (2012).

[90] C. Weyrich and M. Droegeler and J. Kampmeier and M. Eschbach and G. Mussler and T. Merzenich and T. Stoica and I. E. Batov and J. Schubert and L. Plucinski and B. Beschoten and C. M. Schneider and C. Stampfer and D. Grützmacher and Th. Schäpers, "Growth, characterization, and transport properties of ternary $(Bi_{1-x}Sb_x)_2Te_3$ topological insulator layers", Journal of Physics: Condensed Matter **28**, 495501 (2016).

[91] L. He, X. Kou, and K. L. Wang, "Review of 3d topological insulator thin-film growth by molecular beam epitaxy and potential applications", physica status solidi (RRL) - Rapid Research Letters **7**, 50–63 (2013).

[92] D. Zhang, Y. Wang, and Y. Gan, "Characterization of critically cleaned sapphire single-crystal substrates by atomic force microscopy, XPS and contact angle measurements", Applied Surface Science **274**, 405–417 (2013).

[93] D. Zhang and Y. Gan, "Recent progress on critical cleaning of sapphire single-crystal substrates: a mini-review", Recent Patents on Chemical Engineering **6**, 161–166 (2014).

[94] S. Hashmi, *Reference module in materials science and materials engineering* (Elsevier, Amsterdam, 2015).

[95] W. M. Lau, R. N. S. Sodhi, and S. Ingrey, "Thermal desorption of oxides on InP", Applied Physics Letters **52**, 386–388 (1988).

[96] A. Guivarc'h, H. L'Haridon, G. Pelous, G. Hollinger, and P. Pertosa, "Chemical cleaning of InP surfaces: oxide composition and electrical properties", Journal of Applied Physics **55**, 1139–1148 (1984).

[97] Shimadzu, *Scanning probe microscope instruction manual hardware* (Sept. 2014).

[98] M. Baykara and U. Schwarz, "Atomic force microscopy: methods and applications", in *Encyclopedia of spectroscopy and spectrometry* (Elsevier, 2017), pp. 70–75.

[99] B. D. Cullity, *Elements of x-ray diffraction* (Prentice Hall, Upper Saddle River, NJ, 2001).

[100] W. Demtröder, *Experimentalphysik 3: Atome, Moleküle und Festkörper* (Springer Berlin Heidelberg, Berlin, Heidelberg, 2010).

[101] J. Goldstein, *Scanning electron microscopy and x-ray microanalysis* (Springer US, Boston, MA, 2003).

[102] R Jenkins, *Practical x-ray spectrometry* (Springer US, New York, NY, 1982).

[103] R. W. Johnson, A. Hultqvist, and S. F. Bent, "A brief review of atomic layer deposition: from fundamentals to applications", Materials Today **17**, 236–246 (2014).

[104] M. J. Biercuk, D. J. Monsma, C. M. Marcus, J. S. Becker, and R. G. Gordon, "Low-temperature atomic-layer-deposition lift-off method for microelectronic and nanoelectronic applications", Applied Physics Letters **83**, 2405–2407 (2003).

[105] F. Yang, S. Ghatak, A. A. Taskin, K. Segawa, Y. Ando, M. Shiraishi, Y. Kanai, K. Matsumoto, A. Rosch, and Y. Ando, "Switching of charge-current-induced spin polarization in the topological insulator $BiSbTeSe_2$", Physical Review B **94** (2016).

[106] Ultratech, *Installation and User Manual - Savannah S100, S200, S300 Atomic Layer Deposition Systems* (2013).

[107] G. N. Parsons, S. M. George, and M. Knez, "Progress and future directions for atomic layer deposition and ALD-based chemistry", MRS Bulletin **36**, 865–871 (2011).

[108] R. Shul, *Handbook of advanced plasma processing techniques* (Springer Berlin Heidelberg, Aug. 28, 2000), 672 pp.

[109] H. Jansen, H. Gardeniers, M. de Boer, M. Elwenspoek, and J. Fluitman, "A survey on the reactive ion etching of silicon in microtechnology", Journal of Micromechanics and Microengineering **6**, 14–28 (1996).

[110] *Oxford Instruments Plasma Technology - Plasma Pro80 - Instructions for Use*, Issue 18 (Dec. 2015).

[111] R. A. Boudreau and S. M. Boudreau, *Passive micro-optical alignment methods* (Taylor & Francis Ltd., Oct. 3, 2018), 416 pp.

[112] F. Pobell, *Matter and methods at low temperatures* (Springer Berlin Heidelberg, Berlin, Heidelberg, 1992).

[113] N. H. Balshaw, *Practical cryogenics : an introduction to laboratory cryogenics* (Oxford Instruments, Scientific Research Division, Eynsham, 2012).

[114] K. Uhlig, "Dry dilution refrigerator with 4He-1K-loop", Cryogenics **66**, 6–12 (2015).

[115] Z. Alpichshev, J. G. Analytis, J.-H. Chu, I. R. Fisher, Y. L. Chen, Z. X. Shen, A. Fang, and A. Kapitulnik, "STM imaging of electronic waves on the surface of $Bi_2Te_3$: topologically protected surface states and hexagonal warping effects", Physical Review Letters **104** (2010).

[116] Y.-Q. Li, K.-H. Wu, J.-R. Shi, and X.-C. Xie, "Electron transport properties of three-dimensional topological insulators", Frontiers of Physics **7**, 165–174 (2011).

[117] S. Barua and K. P. Rajeev, "Status of surface conduction in topological insulators", AIP Advances **4**, 017135 (2014).

[118] J. Xiong, Y. Luo, Y. Khoo, S. Jia, R. J. Cava, and N. P. Ong, "High-field Shubnikov–de Haas oscillations in the topological insulator $Bi_2Te_2Se$", Physical Review B **86** (2012).

[119] Z. Ren, A. A. Taskin, S. Sasaki, K. Segawa, and Y. Ando, "Large bulk resistivity and surface quantum oscillations in the topological insulator $Bi_2Te_2Se$", Physical Review B **82** (2010).

[120] H. Steinberg, D. R. Gardner, Y. S. Lee, and P. Jarillo-Herrero, "Surface state transport and ambipolar electric field effect in $Bi_2Se_3$ nanodevices", Nano Letters **10**, 5032–5036 (2010).

[121] N. Bansal, Y. S. Kim, M. Brahlek, E. Edrey, and S. Oh, "Thickness-Independent Transport Channels in Topological Insulator $Bi_2Se_3$ Thin Films", Physical Review Letters **109** (2012).

[122] M. Brahlek, N. Koirala, N. Bansal, and S. Oh, "Transport properties of topological insulators: band bending, bulk metal-to-insulator transition, and weak anti-localization", Solid State Communications **215-216**, 54–62 (2015).

[123] G. Zhang, H. Qin, J. Teng, J. Guo, Q. Guo, X. Dai, Z. Fang, and K. Wu, "Quintuple-layer epitaxy of thin films of topological insulator $Bi_2Se_3$", Applied Physics Letters **95**, 053114 (2009).

[124] Y. S. Hor, A. Richardella, P. Roushan, Y. Xia, J. G. Checkelsky, A. Yazdani, M. Z. Hasan, N. P. Ong, and R. J. Cava, "$p$-type $Bi_2Se_3$ for topological insulator and low-temperature thermoelectric applications", Physical Review B **79** (2009).

[125] D. Hsieh, Y. Xia, D. Qian, L. Wray, J. H. Dil, F. Meier, J. Osterwalder, L. Patthey, J. G. Checkelsky, N. P. Ong, A. V. Fedorov, H. Lin, A. Bansil, D. Grauer, Y. S. Hor, R. J. Cava, and M. Z. Hasan, "A tunable topological insulator in the spin helical Dirac transport regime", Nature **460**, 1101–1105 (2009).

[126] A. A. Taskin, Z. Ren, S. Sasaki, K. Segawa, and Y. Ando, "Observation of Dirac holes and electrons in a topological insulator", Physical Review Letters **107** (2011).

[127] J. Chen, H. J. Qin, F. Yang, J. Liu, T. Guan, F. M. Qu, G. H. Zhang, J. R. Shi, X. C. Xie, C. L. Yang, K. H. Wu, Y. Q. Li, and L. Lu, "Gate-voltage control of chemical potential and weak antilocalization in $Bi_2Se_3$", Physical Review Letters **105** (2010).

[128] D. Kong, W. Dang, J. J. Cha, H. Li, S. Meister, H. Peng, Z. Liu, and Y. Cui, "Few-layer nanoplates of $Bi_2Se_3$ and $Bi_2Te_3$ with highly tunable chemical potential", Nano Letters **10**, 2245–2250 (2010).

[129] F. Yang, A. A. Taskin, S. Sasaki, K. Segawa, Y. Ohno, K. Matsumoto, and Y. Ando, "Top gating of epitaxial $(Bi_{1-x}Sb_x)_2Te_3$ topological insulator thin films", Applied Physics Letters **104**, 161614 (2014).

[130] F. Yang, A. A. Taskin, S. Sasaki, K. Segawa, Y. Ohno, K. Matsumoto, and Y. Ando, "Dual-gated topological insulator thin-film device for efficient fermi-level tuning", ACS Nano **9**, 4050–4055 (2015).

[131] J. Zhang, X. Feng, Y. Xu, M. Guo, Z. Zhang, Y. Ou, Y. Feng, K. Li, H. Zhang, L. Wang, X. Chen, Z. Gan, S.-C. Zhang, K. He, X. Ma, Q.-K. Xue, and Y. Wang, "Disentangling the magnetoelectric and thermoelectric transport in topological insulator thin films", Physical Review B **91** (2015).

[132] A. Mzerd, D. Sayah, G. Brun, J. C. Tedenac, and A. Boyer, "Crystal growth and sticking coefficient of $Bi_2Te_3$ thin films on Si(111) substrate", Journal of Materials Science Letters **14**, 194–197 (1995).

[133] G. Fuchs, P. Melinon, F. S. Aires, M. Treilleux, B. Cabaud, and A. Hoareau, "Cluster-beam deposition of thin metallic antimony films: cluster-size and deposition-rate effects", Physical Review B **44**, 3926–3933 (1991).

[134] T. Ginley, Y. Wang, and S. Law, "Topological insulator film growth by molecular beam epitaxy: a review", Crystals **6**, 154 (2016).

[135] R. Murri, ed., *Silicon based thin film solar cells* (Bentham Science Publishers, 2013).

[136] J. Krumrain, G. Mussler, S. Borisova, T. Stoica, L. Plucinski, C. Schneider, and D. Grützmacher, "MBE growth optimization of topological insulator $Bi_2Te_3$ films", Journal of Crystal Growth **324**, 115–118 (2011).

[137] C. I. Fornari, P. H. O. Rappl, S. L. Morelhão, and E. Abramof, "Structural properties of $Bi_2Te_3$ topological insulator thin films grown by molecular beam epitaxy on (111) $BaF_2$ substrates", Journal of Applied Physics **119**, 165303 (2016).

[138] U. Pietsch, V. Holy, and T. Baumbach, *High-resolution x-ray scattering* (Springer-Verlag GmbH, Sept. 1, 2004).

[139] A. Mzerd, D. Sayah, J. C. Tedenac, and A. Boyer, "Effect of substrate temperature on crystal growth of $Bi_2Te_3$ on single crystal $Sb_2Te_3$", Journal of Materials Science Letters **13**, 301–304 (1994).

[140] R. J. Macedo, S. E. Harrison, T. S. Dorofeeva, J. S. Harris, and R. A. Kiehl, "Nanoscale probing of local electrical characteristics on MBE-grown $Bi_2Te_3$ surfaces under ambient conditions", Nano Letters **15**, 4241–4247 (2015).

[141] D. Kong, J. J. Cha, K. Lai, H. Peng, J. G. Analytis, S. Meister, Y. Chen, H.-J. Zhang, I. R. Fisher, Z.-X. Shen, and Y. Cui, "Rapid surface oxidation as a source of surface degradation factor for $Bi_2Se_3$", ACS Nano **5**, 4698–4703 (2011).

[142] K. Hoefer, C. Becker, D. Rata, J. Swanson, P. Thalmeier, and L. H. Tjeng, "Intrinsic conduction through topological surface states of insulating $Bi_2Te_3$ epitaxial thin films", Proceedings of the National Academy of Sciences **111**, 14979–14984 (2014).

[143] P. Ngabonziza, M. P. Stehno, H. Myoren, V. A. Neumann, G. Koster, and A. Brinkman, "Gate-tunable transport properties of in situ capped $Bi_2Te_3$ topological insulator thin films", Advanced Electronic Materials **2**, 1600157 (2016).

[144] X. Wang, G. Bian, T. Miller, and T.-C. Chiang, "Fragility of Surface States and Robustness of Topological Order in $Bi_2Se_3$ against Oxidation", Physical Review Letters **108** (2012).

[145] L. V. Yashina, J. Sánchez-Barriga, M. R. Scholz, A. A. Volykhov, A. P. Sirotina, S. N. Vera, M. E. Tamm, A. Varykhalov, D. Marchenko, G. Springholz, G. Bauer, A. Knop-Gericke, and O. Rader, "Negligible surface reactivity of topological insulators $Bi_2Se_3$ and $Bi_2Te_3$ towards oxygen and water", ACS Nano **7**, 5181–5191 (2013).

[146] J. H. Hwang, J. Park, S. Kwon, J. S. Kim, and J. Y. Park, "Role of oxidation on surface conductance of the topological insulator $Bi_2Te_2Se$", Surface Science **630**, 153–157 (2014).

[147] C. R. Thomas, M. K. Vallon, M. G. Frith, H. Sezen, S. K. Kushwaha, R. J. Cava, J. Schwartz, and S. L. Bernasek, "Surface Oxidation of $Bi_2(Te,Se)_3$ Topological Insulators Depends on Cleavage Accuracy", Chemistry of Materials **28**, 35–39 (2015).

[148] A. A. Volykhov, J. Sánchez-Barriga, M. Batuk, C. Callaert, J. Hadermann, A. P. Sirotina, V. S. Neudachina, A. I. Belova, N. V. Vladimirova, M. E. Tamm, N. O. Khmelevsky, C. Escudero, V. Pérez-Dieste, A. Knop-Gericke, and L. V. Yashina, "Can surface reactivity of mixed crystals be predicted from their counterparts? A case study of $(Bi_{1-x}Sb_x)_2Te_3$ topological insulators", Journal of Materials Chemistry C **6**, 8941–8949 (2018).

[149] A. A. Volykhov, L. V. Yashina, T. S. Zyubina, V. I. Shtanov, V. S. Neudachina, R. Püttner, and A. S. Zyubin, "Comparative reactivity of AIVBVI compounds in their reactions with dioxygen", Russian Journal of Inorganic Chemistry **56**, 1284–1289 (2011).

[150] H. M. Benia, C. Lin, K. Kern, and C. R. Ast, "Reactive chemical doping of the $Bi_2Se_3$ topological insulator", Physical Review Letters **107** (2011).

[151] M. Lang, L. He, F. Xiu, X. Yu, J. Tang, Y. Wang, X. Kou, W. Jiang, A. V. Fedorov, and K. L. Wang, "Revelation of topological surface states in $Bi_2Se_3$ thin films by in situ al passivation", ACS Nano **6**, 295–302 (2011).

[152] M. Liu, C.-Z. Chang, Z. Zhang, Y. Zhang, W. Ruan, K. He, L. li Wang, X. Chen, J.-F. Jia, S.-C. Zhang, Q.-K. Xue, X. Ma, and Y. Wang, "Electron interaction-driven insulating ground state in $Bi_2Se_3$ topological insulators in the two-dimensional limit", Physical Review B **83** (2011).

[153] M. Bai, F. Yang, M. Luysberg, J. Feng, A. Bliesener, G. Lippertz, A. A. Taskin, J. Mayer, and Y. Ando, "Novel self-epitaxy for inducing superconductivity in the topological insulator $(Bi_{1-x}Sb_x)_2Te_3$", Physical Review Materials **4** (2020).

[154] C.-Z. Chang, J. Zhang, X. Feng, J. Shen, Z. Zhang, M. Guo, K. Li, Y. Ou, P. Wei, L.-L. Wang, Z.-Q. Ji, Y. Feng, S. Ji, X. Chen, J. Jia, X. Dai, Z. Fang, S.-C. Zhang, K. He, Y. Wang, L. Lu, X.-C. Ma, and Q.-K. Xue, "Experimental observation of the quantum anomalous Hall effect in a magnetic topological insulator", Science **340**, 167–170 (2013).

[155] C.-Z. Chang, W. Zhao, D. Y. Kim, H. Zhang, B. A. Assaf, D. Heiman, S.-C. Zhang, C. Liu, M. H. W. Chan, and J. S. Moodera, "High-precision realization of robust quantum anomalous Hall state in a hard ferromagnetic topological insulator", Nature Materials **14**, 473–477 (2015).

[156] Y. L. Chen, J.-H. Chu, J. G. Analytis, Z. K. Liu, K. Igarashi, H.-H. Kuo, X. L. Qi, S. K. Mo, R. G. Moore, D. H. Lu, M. Hashimoto, T. Sasagawa, S. C. Zhang, I. R. Fisher, Z. Hussain, and Z. X. Shen, "Massive Dirac fermion on the surface of a magnetically doped topological insulator", Science **329**, 659–662 (2010).

[157] K. He, "The quantum Hall effect gets more practical", Physics **8** (2015).

[158] M. Kawamura, R. Yoshimi, A. Tsukazaki, K. S. Takahashi, M. Kawasaki, and Y. Tokura, "Current-driven instability of the quantum anomalous Hall effect in ferromagnetic topological insulators", Physical Review Letters **119** (2017).

[159] X. Kou, S.-T. Guo, Y. Fan, L. Pan, M. Lang, Y. Jiang, Q. Shao, T. Nie, K. Murata, J. Tang, Y. Wang, L. He, T.-K. Lee, W.-L. Lee, and K. L. Wang, "Scale-invariant quantum anomalous Hall effect in magnetic topological insulators beyond the two-dimensional limit", Physical Review Letters **113** (2014).

[160] C.-Z. Chang, W. Zhao, D. Y. Kim, P. Wei, J. Jain, C. Liu, M. H. Chan, and J. S. Moodera, "Zero-field dissipationless chiral edge transport and the nature of dissipation in the quantum anomalous Hall state", Physical Review Letters **115** (2015).

[161] J. G. Checkelsky, R. Yoshimi, A. Tsukazaki, K. S. Takahashi, Y. Kozuka, J. Falson, M. Kawasaki, and Y. Tokura, "Trajectory of the anomalous Hall effect towards the quantized state in a ferromagnetic topological insulator", Nature Physics **10**, 731–736 (2014).

[162] A. Bestwick, E. Fox, X. Kou, L. Pan, K. L. Wang, and D. Goldhaber-Gordon, "Precise quantization of the anomalous Hall effect near zero magnetic field", Physical Review Letters **114** (2015).

[163] I. Lee, C. K. Kim, J. Lee, S. J. L. Billinge, R. Zhong, J. A. Schneeloch, T. Liu, T. Valla, J. M. Tranquada, G. Gu, and J. C. S. Davis, "Imaging Dirac-mass disorder from magnetic dopant atoms in the ferromagnetic topological insulator $Cr_x(Bi_{0.1}Sb_{0.9})_{2-x}Te_3$", Proceedings of the National Academy of Sciences **112**, 1316–1321 (2015).

[164] M. Mogi, R. Yoshimi, A. Tsukazaki, K. Yasuda, Y. Kozuka, K. S. Takahashi, M. Kawasaki, and Y. Tokura, "Magnetic modulation doping in topological insulators toward higher-temperature quantum anomalous Hall effect", Applied Physics Letters **107**, 182401 (2015).

[165] J. Li, Y. Li, S. Du, Z. Wang, B.-L. Gu, S.-C. Zhang, K. He, W. Duan, and Y. Xu, "Intrinsic magnetic topological insulators in van der Waals layered $MnBi_2Te_4$-family materials", Science Advances **5**, eaaw5685 (2019).

[166] M. Otrokov, I. Rusinov, M. Blanco-Rey, M. Hoffmann, A. Vyazovskaya, S. Eremeev, A. Ernst, P. Echenique, A. Arnau, and E. Chulkov, "Unique Thickness-Dependent Properties of the van der Waals Interlayer Antiferromagnet $MnBi_2Te_4$ Films", Physical Review Letters **122** (2019).

[167] Y. Deng, Y. Yu, M. Z. Shi, Z. Guo, Z. Xu, J. Wang, X. H. Chen, and Y. Zhang, "Quantum anomalous Hall effect in intrinsic magnetic topological insulator $MnBi_2Te_4$", Science **367**, 895–900 (2020).

[168] X. Feng, Y. Feng, J. Wang, Y. Ou, Z. Hao, C. Liu, Z. Zhang, L. Zhang, C. Lin, J. Liao, Y. Li, L.-L. Wang, S.-H. Ji, X. Chen, X. Ma, S.-C. Zhang, Y. Wang, K. He, and Q.-K. Xue, "Thickness dependence of the quantum anomalous Hall effect in magnetic topological insulator films", Advanced Materials **28**, 6386–6390 (2016).

[169] Y. Zhang, K. He, C.-Z. Chang, C.-L. Song, L.-L. Wang, X. Chen, J.-F. Jia, Z. Fang, X. Dai, W.-Y. Shan, S.-Q. Shen, Q. Niu, X.-L. Qi, S.-C. Zhang, X.-C. Ma, and Q.-K. Xue, "Crossover of the three-dimensional topological insulator $Bi_2Se_3$ to the two-dimensional limit", Nature Physics **6**, 584–588 (2010).

[170] J. F. Smith, "Melting point of vanadium", Bulletin of Alloy Phase Diagrams **5**, 339–339 (1984).

[171] *Dr. Eberl MBE-Komponenten GmbH; Vertical UHV E-Beam evaporator with rotary shutter on DN63CF, EBVV63 - Operating instructions* (Dec. 2009).

[172] K Jousten, *Handbook of vacuum technology* (Wiley-Blackwell, Weinheim, 2008).

[173] A. Arrott, "Criterion for ferromagnetism from observations of magnetic isotherms", Physical Review **108**, 1394–1396 (1957).

[174] Y. Ou, C. Liu, G. Jiang, Y. Feng, D. Zhao, W. Wu, X.-X. Wang, W. Li, C. Song, L.-L. Wang, W. Wang, W. Wu, Y. Wang, K. He, X.-C. Ma, and Q.-K. Xue, "Enhancing the quantum anomalous Hall effect by magnetic codoping in a topological insulator", Advanced Materials **30**, 1703062 (2017).

[175] M. Furlan, "Electronic transport and the localization length in the quantum Hall effect", Physical Review B **57**, 14818–14828 (1998).

[176] E. J. Fox, I. T. Rosen, Y. Yang, G. R. Jones, R. E. Elmquist, X. Kou, L. Pan, K. L. Wang, and D. Goldhaber-Gordon, "Part-per-million quantization and current-induced breakdown of the quantum anomalous Hall effect", Physical Review B **98** (2018).

[177] Y. X. Chong, X. Liu, R. Sharma, A. Kostin, G. Gu, K. Fujita, J. C. S. Davis, and P. O. Sprau, "Severe Dirac Mass Gap Suppression in $Sb_2Te_3$-Based Quantum Anomalous Hall Materials", Nano Letters **20**, 8001–8007 (2020).

[178] B. Jeckelmann, "The quantum Hall effect and its application in metrology", Proceedings of the International School of Physics Enrico Fermi **146**, 263–290 (2001).

[179] M. Büttiker, "Absence of backscattering in the quantum Hall effect in multiprobe conductors", Physical Review B **38**, 9375–9389 (1988).

[180] S. Datta, *Electronic transport in mesoscopic systems* (Cambridge University Press, Cambridge, UK New York, 1997).

[181] H. Bruus and K. Flensberg, *Many-body quantum theory in condensed matter physics: an introduction* (Oxford University Press, 2004).

[182] X.-L. Qi, T. L. Hughes, and S.-C. Zhang, "Chiral topological superconductor from the quantum Hall state", Physical Review B **82** (2010).

[183] J. Wang, Q. Zhou, B. Lian, and S.-C. Zhang, "Chiral topological superconductor and half-integer conductance plateau from quantum anomalous Hall plateau transition", Physical Review B **92** (2015).

[184] Q. L. He, L. Pan, A. L. Stern, E. C. Burks, X. Che, G. Yin, J. Wang, B. Lian, Q. Zhou, E. S. Choi, K. Murata, X. Kou, Z. Chen, T. Nie, Q. Shao, Y. Fan, S.-C. Zhang, K. Liu, J. Xia, and K. L. Wang, "Chiral Majorana fermion modes in a quantum anomalousHall insulator–superconductor structure", Science **357**, 294–299 (2017).

[185] W. Ji and X.-G. Wen, "$\frac{1}{2}(e^2/h)$ Conductance Plateau without 1D Chiral Majorana Fermions", Physical Review Letters **120** (2018).

[186] Y. Huang, F. Setiawan, and J. D. Sau, "Disorder-induced half-integer quantized conductance plateau in quantum anomalous Hall insulator-superconductor structures", Physical Review B **97** (2018).

[187] M. Kayyalha, D. Xiao, R. Zhang, J. Shin, J. Jiang, F. Wang, Y.-F. Zhao, R. Xiao, L. Zhang, K. M. Fijalkowski, P. Mandal, M. Winnerlein, C. Gould, Q. Li, L. W. Molenkamp, M. H. W. Chan, N. Samarth, and C.-Z. Chang, "Absence of evidence for chiral Majorana modes in quantum anomalous Hall-superconductor devices", Science **367**, 64–67 (2020).

[188] A. R. Akhmerov, J. Nilsson, and C. W. J. Beenakker, "Electrically detected interferometry of Majorana fermions in a topological insulator", Physical Review Letters **102** (2009).

[189] L. Fu and C. L. Kane, "Probing neutral Majorana fermion edge modes with charge transport", Physical Review Letters **102** (2009).

[190] L. Fu, "Topological crystalline insulators", Physical Review Letters **106**, 106802 (2011).

[191] T. H. Hsieh, H. Lin, J. Liu, W. Duan, A. Bansil, and L. Fu, "Topological crystalline insulators in the SnTe material class", Nature Communications **3** (2012).

[192] J. Liu, W. Duan, and L. Fu, "Two types of surface states in topological crystalline insulators", Physical Review B **88**, 241303 (2013).

[193] Y. Tanaka, T. Shoman, K. Nakayama, S. Souma, T. Sato, T. Takahashi, M. Novak, K. Segawa, and Y. Ando, "Two types of Dirac-cone surface states on the (111) surface of the topological crystalline insulator SnTe", Physical Review B **88**, 235126 (2013).

[194] Y. Tanaka, T. Sato, K. Nakayama, S. Souma, T. Takahashi, Z. Ren, M. Novak, K. Segawa, and Y. Ando, "Tunability of thek-space location of the Dirac cones in the topological crystalline insulator $Pb_{1-x}Sn_xTe$", Physical Review B **87** (2013).

[195] Y. Tanaka, Z. Ren, T. Sato, K. Nakayama, S. Souma, T. Takahashi, K. Segawa, and Y. Ando, "Experimental realization of a topological crystalline insulator in SnTe", Nature Physics **8**, 800–803 (2012).

[196] A. S. Erickson, J.-H. Chu, M. F. Toney, T. H. Geballe, and I. R. Fisher, "Enhanced superconducting pairing interaction in indium-doped tin telluride", Physical Review B **79**, 024520 (2009).

[197] S. Kashiwaya, H. Kashiwaya, K. Saitoh, Y. Mawatari, and Y. Tanaka, "Tunneling spectroscopy of topological superconductors", Physica E: Low-dimensional Systems and Nanostructures **55**, 25–29 (2014).

[198] T. Sato, Y. Tanaka, K. Nakayama, S. Souma, T. Takahashi, S. Sasaki, Z. Ren, A. A. Taskin, K. Segawa, and Y. Ando, "Fermiology of the Strongly Spin-Orbit Coupled Superconductor $Sn_{1-x}In_xTe$: Implications for Topological Superconductivity", Physical Review Letters **110**, 206804 (2013).

[199] M. Novak, S. Sasaki, M. Kriener, K. Segawa, and Y. Ando, "Unusual nature of fully gapped superconductivity in In-doped SnTe", Physical Review B **88**, 140502 (2013).

[200] P. Hosur, P. Ghaemi, R. S. K. Mong, and A. Vishwanath, "Majorana modes at the ends of superconductor vortices in doped topological insulators", Physical Review Letters **107**, 097001 (2011).

[201] S. Sasaki, Z. Ren, A. A. Taskin, K. Segawa, L. Fu, and Y. Ando, "Odd-parity pairing and topological superconductivity in a strongly spin-orbit coupled semiconductor", Physical Review Letters **109**, 217004 (2012).

[202] A. A. Taskin, F. Yang, S. Sasaki, K. Segawa, and Y. Ando, "Topological surface transport in epitaxial SnTe thin films grown on $Bi_2Te_3$", Physical Review B **89**, 121302 (2014).

[203] N. Haldolaarachchige, Q. Gibson, W. Xie, M. B. Nielsen, S. Kushwaha, and R. J. Cava, "Anomalous composition dependence of the superconductivity in In-doped SnTe", Physical Review B **93**, 024520 (2016).

[204] A. Bliesener, J. Feng, A. A. Taskin, and Y. Ando, "Superconductivity in $Sn_{1-x}In_xTe$ thin films grown by molecular beam epitaxy", Physical Review Materials **3** (2019).

[205] C. M. Hurd, *The Hall effect in metals and alloys* (Plenum Press, New York, 1972).

[206] N. R. Werthamer, E. Helfand, and P. C. Hohenberg, "Temperature and Purity Dependence of the Superconducting Critical Field,$H_{c2}$. III. Electron Spin and Spin-Orbit Effects", Physical Review **147**, 295–302 (1966).

[207] R. C. Dynes, V. Narayanamurti, and J. P. Garno, "Direct measurement of quasiparticle-lifetime broadening in a strong-coupled superconductor", Physical Review Letters **41**, 1509–1512 (1978).

[208] P. Zhang, K. Yaji, T. Hashimoto, Y. Ota, T. Kondo, K. Okazaki, Z. Wang, J. Wen, G. D. Gu, H. Ding, and S. Shin, "Observation of topological superconductivity on the surface of an iron-based superconductor", Science **360**, 182–186 (2018).

[209] J.-X. Yin, Z. Wu, J.-H. Wang, Z.-Y. Ye, J. Gong, X.-Y. Hou, L. Shan, A. Li, X.-J. Liang, X.-X. Wu, J. Li, C.-S. Ting, Z.-Q. Wang, J.-P. Hu, P.-H. Hor, H. Ding, and S. H. Pan, "Observation of a robust zero-energy bound state in iron-based superconductor Fe(Te,Se)", Nature Physics **11**, 543–546 (2015).

[210] D. Wang, L. Kong, P. Fan, H. Chen, S. Zhu, W. Liu, L. Cao, Y. Sun, S. Du, J. Schneeloch, R. Zhong, G. Gu, L. Fu, H. Ding, and H.-J. Gao, "Evidence for Majorana bound states in an iron-based superconductor", Science **362**, 333–335 (2018).

[211] F. Xiu, L. He, Y. Wang, L. Cheng, L.-T. Chang, M. Lang, G. Huang, X. Kou, Y. Zhou, X. Jiang, Z. Chen, J. Zou, A. Shailos, and K. L. Wang, "Manipulating surface states in topological insulator nanoribbons", Nature Nanotechnology **6**, 216–221 (2011).

[212] M. Tian, W. Ning, Z. Qu, H. Du, J. Wang, and Y. Zhang, "Dual evidence of surface Dirac states in thin cylindrical topological insulator $Bi_2Te_3$ nanowires", Scientific Reports **3** (2013).

[213] L. A. Jauregui, M. T. Pettes, L. P. Rokhinson, L. Shi, and Y. P. Chen, "Magnetic field-induced helical mode and topological transitions in a topological insulator nanoribbon", Nature Nanotechnology **11**, 345–351 (2016).

[214] F. Münning, O. Breunig, H. F. Legg, S. Roitsch, D. Fan, M. Rößler, A. Rosch, and Y. Ando, "Quantum confinement of the Dirac surface states in topological-insulator nanowires", Nature Communications **12** (2021).

[215] J. Kampmeier, C. Weyrich, M. Lanius, M. Schall, E. Neumann, G. Mussler, T. Schäpers, and D. Grützmacher, "Selective area growth of $Bi_2Te_3$ and $Sb_2Te_3$ topological insulator thin films", Journal of Crystal Growth **443**, 38–42 (2016).

[216] D. Rosenbach, N. Oellers, A. R. Jalil, M. Mikulics, J. Kölzer, E. Zimmermann, G. Mussler, S. Bunte, D. Grützmacher, H. Lüth, and T. Schäpers, "Quantum Transport in Topological Surface States of Selectively Grown $Bi_2Te_3$ Nanoribbons", Advanced Electronic Materials **6**, 2000205 (2020).

[217] H. Peng, K. Lai, D. Kong, S. Meister, Y. Chen, X.-L. Qi, S.-C. Zhang, Z.-X. Shen, and Y. Cui, "Aharonov-Bohm interference in topological insulator nanoribbons", Nature Materials **9**, 225–229 (2009).

[218] J. H. Bardarson, P. W. Brouwer, and J. E. Moore, "Aharonov-Bohm oscillations in disordered topological insulator nanowires", Physical Review Letters **105** (2010).

[219] S. Cho, B. Dellabetta, R. Zhong, J. Schneeloch, T. Liu, G. Gu, M. J. Gilbert, and N. Mason, "Aharonov-Bohm oscillations in a quasi-ballistic three-dimensional topological insulator nanowire", Nature Communications **6** (2015).

[220] J. H. Bardarson and J. E. Moore, "Quantum interference and Aharonov–Bohm oscillations in topological insulators", Reports on Progress in Physics **76**, 056501 (2013).

[221] Y. Zhang, Y. Ran, and A. Vishwanath, "Topological insulators in three dimensions from spontaneous symmetry breaking", Physical Review B **79** (2009).

[222] A. Y. Kitaev, "Unpaired Majorana fermions in quantum wires", Physics-Uspekhi **44**, 131–136 (2001).

[223] M. Franz, "Majorana's wires", Nature Nanotechnology **8**, 149–152 (2013).

[224] C. Reinhoffer, Y. Mukai, S. Germanskiy, A. Bliesener, G. Lippertz, A. Uday, A. A. Taskin, Y. Ando, Z. Wang, and P. H. M. van Loosdrecht, "Relaxation dynamics of the optically driven nonequilibrium states in the electron- and hole-doped topological-insulator materials $(Bi_{1-x}Sb_x)_2Te_3$", Physical Review Materials **4** (2020).

# Acknowledgments

Even though only my name appears on the cover of this work, I must thank many people who played a great part in finishing this thesis.
First of all, I would like to thank my supervisor Prof. Yoichi Ando for giving me the opportunity to work and learn in his group. His dedication to science and attitude towards work set up the highest example and motivated me to always give my best and never give up.
Furthermore, I would like to thank Prof. Thomas Lorenz for being my second reviewer. I hope it is in my favor that he overtook me in our institute's Bundesliga betting game on the day I must hand in this thesis. Thank you to Prof. Achim Rosch for taking over the thesis committee chair.

I cannot thank Dr. Alexey Taskin enough for his patience, motivation and guidance. I am grateful for everything he has taught me about MBE growth and transport measurements. In the past 4+ years, I probably spent more time with Alexey than with anyone else and I always enjoyed our passionate discussions about science, politics or movies.
Special thanks to the other two members of Team MBE: Gertjan Lippertz and Anjana Uday. I enjoyed all the time we got to spent together in and outside of the lab.

The Ando group has grown rapidly since I started my PhD work. At the beginning of my work Lionel Andersen, Dr. Fan Yang and Dr. Zhiwei Wang were a huge help to get me settled in the group and in the lab. In the past years, a lot of other PhD students joined the group and shared good and bad times with me. Special thanks to Mahasweta Bagchi for all our chats while eating chocolate, Mengmeng Bai for always rushing to help me and panda discussions, Matthias Rößler for all his epic pep talks and the best time in Japan, Felix Münning for all the brilliant (and not so brilliant) jokes and Poojitha Umesh for delicious Indian food and great talks about dogs.
Apart from fellow PhD students, I was also lucky to share my time in and outside the lab with many excellent PostDocs: Dr. Jens Brede, Dr. Oliver Breunig, Dr. Junya Feng, Dr. Dingxun Fan and Dr. Yongjian Wang all contributed to this work. Jens is doomed to share an office with rather chatty people (including me...)

who are constantly visited by other chatty people. I admire him for enduring it like a champ. I am grateful Oliver initiated the SAG project and that he agreed to be a member of my defense committee. He was the first person to properly welcome me into the Ando group and since then has continued to support me. Without Junya the work on $Sn_{1-x}In_xTe$ probably would not have ended up in such a nice paper (also the stories about his daughters always brighten up my day). Thank you to Dingxun for teaching me a lot about cleanroom work and microfabrication and measurements and ebeam evaporation and so much more. The MBE growth would not have been possible without Yongjian who always perfectly prepared the source materials. Dr. Richard Bounds, Dr. Christian Dickel and Dr. Jakob Schluck all joined later during my PhD and even though our scientific overlap mostly consisted of them nagging me for BST films (except Jakob who kindly provided epic memes without asking for BST in return), they all are an immense enrichment for the Ando group. I appreciate Rich and (especially) Chris for constantly trying to explain to me what a qubit is.

I call myself lucky to have found great colleagues and friends outside of my own work group. Thank you to everyone at the red floor for many great Mensa lunches, DPG conferences and further shenanigans over the years.
My boys from the Friday morning SFB-Meeting - Niels Ehlen, Yannic Falke and Robin Bernhardt - made sure that every week ended on a high note with lots of stimulating discussion about physics, YouTube videos or donkeys. Dr. Johannes Engelmayer had the answers to all my questions about how to write and ‚LaTeX' a thesis. Thank you to one of my favourite conference buddies, Dr. Henry Legg, for proofreading parts of the theory and nanowire section. Linda Kerkhoff finished her PhD at roughly the same time and I am glad we could share the experience. I am particularly grateful for Lena Wysocki who was there for me through the ups and downs of my PhD, and who always had a good advice in every situation.

I wish to thank all the people from the electrical and mechanical workshop of the II. Institute of Physics. Especially Andreas Freimut and Sebastian Knappe who patiently built every molybdenum/tantalum construction for me. Klaus Lehmann, Christian Honerlage and Harald Lüttgen kindly dealt with every unusual Japanese electronics and circuit diagram. I also wish to pay my special regards to our own group technicians Lucie Hamdan and Timur Zent who make all our scientific lives so much easier every day. The same goes for Dr. Harald Kierspel who always had a good advice on everything and patiently helped me deal with many peculiar purchasing orders. I'm very grateful for Dr. Ralf Müller

who was my partner in crime in countless rounds of Kinder Uni, Junior Uni, Senioren Uni and a few very special Zoom experiments through out the years. I probably would not have seriously considered applying for a PhD position without the encouragement of Carmen Handels who made me aware of open PhD positions in the Ando group and afterwards always took great care of me.

I appreciate the funding and support to attend many excellent conferences during my PhD work. Thank you to the ML4Q office (Konstantinia Baroutas, Dr. Marian Barsoum, Dr. Magdalena Baer Radermacher, Dr. Beate Saal and Dr. Philipp Wilking), the CRC 1238 office (Clara Berthet and Dr. Thomas Koethe) and the Bonn-Cologne Graduate School for Physics and Astronomy BCGS. Dr. Petra Neubauer-Guenther of the BCGS already encouraged me during a school work experience to become a physicist.

Few people know the road I had to travel to get to this point in life. Among them Sabrina and Mirjam who have been my friends for over 20 years. Especially the crazy trips all over Europe to watch some English lads play guitar were a much-needed diversion from the lab work. Especially Mirjam has been there for me through it all. Thanks to all my friends who still invite me to their birthday parties, even though 90% of the time I had to cancel because I had to wrap a vacuum chamber with aluminum foil.

Mein größter Dank gilt meiner Familie. Meine Paten Helene, Rudi und Roswitha, sowie mein Onkel Henni sind immer für mich da. Insbesondere meine Eltern Anneliese und Jürgen haben mich immer unterstützt und diese Doktorarbeit ist genauso ihr Verdienst wie meiner.

*But in the end journey's brought joys that outweigh the pain. - Frank Turner*

# Abstract

In the scope of this thesis, four different topological materials grown by molecular beam epitaxy are investigated. The MBE growth conditions have to be optimized for each of the materials. The structural properties of the grown films are studied using x-ray diffraction (XRD), atomic force microscopy (AFM) and energy-dispersive x-ray spectroscopy (EDX). Low-temperature magneto-transport measurements are performed to characterize the magnetic and electrical properties of the samples.

The topological insulator $(Bi_{1-x}Sb_x)_2Te_3$ (BST) serves as a basic building block for several applications in this work. The morphology of the grown BST film is improved by optimizing the growth conditions such as growth temperatures, elemental material fluxes, growth duration, etc., and by employing special growth methods like a two-step deposition technique. The optimal growth conditions are found by measuring the film morphology by atomic force microscopy and using x-ray diffraction to confirm the epitaxial and single-phase growth mode. Bulk-insulating BST films with surface carrier dominated conduction and carrier concentrations as low as $10^{12}\mathrm{cm}^{-2}$ are obtained by varying the bismuth-antimony ratio. Furthermore, the necessity of protecting the top surface of the MBE grown film with a capping layer is established. A 3 nm-thin $Al_2O_3$ which is deposited by atomic layer deposition (ALD), can protect the BST film from oxidization.

A robust ferromagnetic order is successfully achieved by doping $(Bi_{1-x}Sb_x)_2Te_3$ with vanadium. The magnetic-field dependence of the Hall resistance is investigated and both, the ordinary Hall effect and the anomalous Hall effect are revealed by the observed hysteresis loops. By extracting the critical temperature and anomalous Hall amplitude from the transport measurements at 2 K, the amount of vanadium dopants and the optimal growth temperature are specified. Most significantly, the quantum anomalous Hall effect is observed in the vanadium-doped BST films. As expected, the longitudinal resistance vanishes and the Hall resistance reveals the quantized value of 25.81 kΩ when measuring the magnetic-field dependence at 30 mK. The quantized resistance is still preserved at 100 mK. Furthermore, the current-induced breakdown and the temperature stability of the quantum anomalous Hall effect are investigated.

Apart from topological insulators, their superconducting relatives recently attracted a significant interest. $Sn_{1-x}In_xTe$ is predicted to be candidate topological superconductor. Thin $Sn_{1-x}In_xTe$ films are grown on a $Bi_2Te_3$ buffer layer by molecular beam epitaxy. It is found that the films only can be turned into a superconducting state after annealing them *in-situ* in the MBE chamber right after growth. The critical temperature depends on the annealing time and temperature suggesting a thermal activation process for the superconducting properties. Tunnel-junction devices are fabricated on the films and surface-sensitive tunneling spectra are measured. Even though measurements on regular Hall bar devices suggest conventional superconductivity a peculiar behavior is revealed by the tunneling spectroscopy. Here, a two-gap structure is observed which points to the coexistence of bulk and surface superconductivity. Because of the special properties of the material the surface superconductivity is bound to be topological.

Finally, nano-scaled $(Bi_{1-x}Sb_x)_2Te_3$ films are grown by the selective area growth (SAG) method. A $Si_3N_4$ film is deposited on a sapphire substrate and afterwards patterned into nanostructures by electron-beam lithography and etched by reactive-ion etching. The pre-patterned substrate is used to selectively grow $(Bi_{1-x}Sb_x)_2Te_3$ nanostructures in the molecular beam epitaxy chamber. The selective growth of the BST films is achieved by optimizing the growth temperature such that film growth takes place only inside the pre-patterned structures and not on top of the $Si_3N_4$ layer. Again, by tuning the bismuth-antimony ratio a bulk-insulating film growth is confirmed by magneto-transport measurements on selectively grown Hall bar devices. Furthermore, the efficiency of two different kind of gates fabricated on a BST nanowire is compared. It is found that the gating efficiency of an after growth fabricated top gate is higher than the efficiency of selectively grown BST-side gates.

# Kurzzusammenfassung

In dieser Arbeit werden vier verschiedene topologische Materialien untersucht, die mittels Molekularstrahlepitaxie (MBE) gewachsen wurden. Die MBE Wachstumsbedingungen wurden für jedes einzelne Material optimiert. Die strukturellen Eigenschaften der gewachsenen Filme werden mittels Röntgendiffraktometrie (XRD), Rasterkraftmikroskopie (AFM) und energiedispersive Röntgenspektroskopie (EDX) untersucht. Die magnetischen und elektrischen Eigenschaften der Proben werden durch Transportmessungen analysiert.

Der topologische Isolator $(Bi_{1-x}Sb_x)_2Te_3$ (BST) bildet die Grundlage für mehrere behandelte Anwendungen in dieser Arbeit. Die Morphologie der gewachsenen BST Filme wird verbessert, indem die Wachstumsbedingungen optimiert werden. Dazu gehören unter anderem die Wachstumstemperatur, die jeweiligen Materialmengen, die Wachstumsdauer und das Anwenden spezieller Wachstumsmethoden wie des Zwei-Stufen-Wachstums. Die optimalen Wachstumsbedingungen wurden gefunden, indem die Morphologie in einem Rasterkraftmikroskop untersucht und das epitaktische und Ein-Phasen Wachstum per Röntgendiffraktometrie bestätigt wurde. Durch Variation des Bismuth-Antimon Verhältnis der BST Filme, wurden Filme synthetisiert, in denen die Leitfähigkeit von Oberflächenzuständen dominiert wird und die Ladungsträgerdichten im Bereich von $10^{12}\text{cm}^{-2}$ liegen. Außerdem wird die Notwendigkeit einer Schutzschicht auf der Oberfläche der MBE gewachsenen Filme untersucht. Hierbei wurde festgestellt, dass ein 3 nm-dünner $Al_2O_3$ Film, der durch Atomlagenabscheiden (ALD) gewachsen wurde, ausreicht, um den Film vor Oxidation zu schützen.

Eine robuste ferromagnetische Ordnung wird erfolgreich realisiert, indem BST Filme mit Vanadium versetzt werden. Die Magnet Feldabhängigkeit des Hall Widerstandes wurde untersucht, und es können sowohl der klassische Hall Effekt, als auch der anomale Hall Effekt in den gemessenen Hystereschleifen identifiziert werden. Die Vanadium-Dotierung und Wachstumstemperatur werden optimiert, indem die kritische Temperatur und die Amplitude des anomalen Hall Effektes aus Transportmessungen bei 2 K bestimmt werden. Besonders hervorzuheben ist das Erreichen des Quanten anomalen Hall Effektes in

den Vanadium-dotierten BST Filmen. Wie erwartet, verschwindet der Längswiderstand und der Hall Widerstand quantisiert bei 25.81 kΩ, wenn die Magnetfeldabhängigkeit bei 30 mK und ebenso bei 100 mK gemessen wird. Außerdem wird der strominduzierte Zusammenbruch und die Temperaturabhängigkeit des Quanten anomalen Hall Effektes untersucht.

Neben den toplogischen Isolatoren haben ihre supraleitenden Verwandten ebenfalls für reges Interesse gesorgt. Es wurde vorausgesagt, dass $Sn_{1-x}In_xTe$ ein Kandidat für einen topologischen Supraleiter ist. Dünne Filme werden mittels Molekularstrahlepitaxie auf einer $Bi_2Te_3$-Zwischenschicht gewachsen.
Die $Sn_{1-x}In_xTe$ Filme sind nur dann supraleitend, wenn sie sofort nach dem Wachsen *in-situ* in der MBE Kammer weiter erhitzt werden. Die kritische Temperatur hängt dabei von der Dauer und der Temperatur des Erhitzens ab, was auf einen thermischen Aktivierungsprozess hindeutet. Ein Tunnelkontakt wird auf dem Film fabriziert und oberflächenempfindliche Tunnelspektroskopie gemessen. Obwohl die Untersuchung von normalen Hall bar-devices auf konventionelle Supraleitung hindeutet, zeigen die Tunnelspektroskopie Messungen ein unerwartetes Verhalten. Hierbei wurden zwei Bandlücken gefunden, die auf die Koexistenz von Supraleitung an der Oberfläche und im Inneren des Materials hindeutet. Bedenkt man die topologische Natur der Proben, ist die Oberflächensupraleitung zwangsläufig topologisch.

Zudem werden $(Bi_{1-x}Sb_x)_2Te_3$ Nanostrukturen selektiv gewachsen. Ein $Si_3N_4$ Film wird zunächst auf einem Saphir Wafer aufgedampft und anschließend durch Elektronenstrahllithographie und selektivem Ätzen in Nanostrukturen strukturiert. Diese vorstrukturierten Substrate werden verwendet, um $(Bi_{1-x}Sb_x)_2Te_3$ Nanostrukturen in der MBE Kammer zu wachsen. Hierbei wird das selektive Wachsen durch das Optimieren der Wachstumstemperatur erreicht, wobei der Film nur innerhalb der Nanostrukturen wächst, nicht aber auf der $Si_3N_4$-Schicht. Erneut wird das Bismut-Antimon Verhältnis variiert, um eine oberflächendominierte Leitungen zu erreichen, was durch das Messen der Transporteigenschaften von Hall bar devices bestätigt wird. Außerdem werden die Transporteigenschaften von Nanodrähten untersucht. Hierbei wird die Effizienz von Side-Gates, die aus selektiv gewachsenen BST Filmen bestehen, und einem Top-Gate, das nach dem Wachstum zusätzlich auf dem Nanodraht angebracht wurde, verglichen. Das Top Gate erreicht hierbei eine höhere Gating-Effizienz.

# Publikationen

The following publications are not included in this thesis.

- Boris V. Senkovskiy, Markus Pfeiffer, Sayed Khalil Alavi, **Andrea Bliesener**, Jingyi Zhu, Samuel Michel, Alexander V. Fedorov, Raphael German, Dirk Hertel, Danny Haberer, Luca Petaccia, Felix R. Fischer, Klaus Meerholz, Paul H. M. van Loosdrecht, Klaas Lindfors, Alexander Grüneis ; *Making Graphene Nanoribbons Photoluminescent*; Nano Lett. 2017, 17, 7, 4029–4037 (2017).

- Martin G. Hell, Yannic Falke, **Andrea Bliesener**, Niels Ehlen, Boris V. Senkovskiy, Thomas Szkopek, Alexander Grüneis ; *Combined Ultra High Vacuum Raman and Electronic Transport Characterization of Large-Area Graphene on $SiO_2$*; pssb volume 255, Issue 12 (2018).

- Lena Wysocki, Ramil Mirzaaghayev , Michael Ziese, Lin Yang, Jörg Schoepf, Rolf B. Versteeg, **Andrea Bliesener**, Johannes Engelmayer, András Kovács, Lei Jin, Felix Gunkel, Regina Dittmann, Paul H. M. van Loosdrecht, Ionela Lindfors-Vrejoiu ; *Magnetic coupling of ferromagnetic $SrRuO_3$ epitaxial layers separated by ultrathin non-magnetic $SrZrO_3$/$SrIrO_3$*; Appl. Phys. Lett. 113, 192402 (2018).

- Lena Wysocki, Jörg Schoepf, Michael Ziese, Lin Yang, András Kovács, Lei Jin, Rolf B. Versteeg, **Andrea Bliesener**, Felix Gunkel, Lior Kornblum, Regina Dittmann, Paul H. M. van Loosdrecht, Ionela Lindfors-Vrejoiu ; *Electronic Inhomogeneity Influence on the Anomalous Hall Resistivity Loops of $SrRuO_3$ Epitaxially Interfaced with 5d Perovskites*; ACS Omega 2020, 5, 11, 5824–5833 (2020).

- Mengmeng Bai, Fan Yang, Martina Luysberg, Junya Feng, **Andrea Bliesener**, Gertjan Lippertz, A. A. Taskin, Joachim Mayer, Yoichi Ando ; *Novel self-epitaxy for inducing superconductivity in the topological insulator $(Bi_{1-x}Sb_x)_2Te_3$*; Phys. Rev. Materials 4, 094801 (2020).

- Chris Reinhoffer, Yu Mukai, Semyon Germanskiy, **Andrea Bliesener**, Gertjan Lippertz, Anjana Uday, A. A. Taskin, Yoichi Ando, Zhe Wang, Paul H. M. van Loosdrecht ;*Relaxation dynamics of the optically driven nonequilibrium states in the electron- and hole-doped topological-insulator materials* ($Bi_{1-x}Sb_x)_2Te_3$; Phys. Rev. Materials 4, 124201 (2020).

# Erklärung zur Dissertation

Ich versichere, dass ich die von mir vorgelegte Dissertation selbständig angefertigt, die benutzten Quellen und Hilfsmittel vollständig angegeben und die Stellen der Arbeit - einschließlich Tabellen, Karten und Abbildungen -, die anderen Werken im Wortlaut oder dem Sinn nach entnommen sind, in jedem Einzelfall als Entlehnung kenntlich gemacht habe; dass diese Dissertation noch keiner anderen Fakultät oder Universität zur Prüfung vorgelegen hat; dass sie - abgesehen von unten angegebenen Teilpublikationen -noch nicht veröffentlicht worden ist, sowie, dass ich eine solche Veröffentlichung vor Abschluss des Promotionsverfahrens nicht vornehmen werde. Die Bestimmungen der Promotionsordnung sind mir bekannt. Die von mir vorgelegte Dissertation ist von Prof. Dr. Yoichi Ando betreut worden.

Andrea Bliesener
Köln, den 21.12.2020

**Teilpublikationen:**

**Andrea Bliesener**, Junya Feng, A. A. Taskin, and Yoichi Ando; *Superconductivity in $Sn_{1-x}In_xTe$ thin films grown by molecular beam epitaxy*; Phys. Rev. Materials 3, 101201(R) (2019).